

STRUCTURAL DESIGN OF IONIC LIQUIDS FOR PROCESS OPTIMISATION

A thesis submitted in fulfilment of the requirements for the degree of
Doctor of Philosophy (Chemistry)

Haihui Joy Jiang

School of Chemistry
The University of Sydney
September 2018

Declaration

This is to certify that to the best of my knowledge; the content of this thesis is my own work. This thesis has not been submitted for any degree or other purposes. I certify that the intellectual content of this thesis is the product of my own work and that all the assistance received in preparing this thesis and sources have been acknowledged.

Haihui Joy Jiang

Authorship Attribution Statement

Chapter 1, 3 and 4 of this thesis contains some figures and results that have been published (or submitted):

- Jiang, H. J.; FitzGerald, P. A.; Dolan, A.; Atkin, R.; Warr, G. G., Amphiphilic Self-assembly of Alkanols in Protic Ionic Liquids. *The Journal of Physical Chemistry B* **2014**, *118* (33), 9983-9990.
- Jiang, H. J.; Imberti, S.; Atkin, R.; Warr, G. G., Dichotomous Well-defined Nanostructure with Weakly Arranged Ion Packing Explains the Solvency of Pyrrolidinium Acetate. *The Journal of Physical Chemistry B* **2017**, *121* (27), 6610-6617.
- Jiang, H. J.; Atkin, R.; Warr, G. G., Nanostructured Ionic Liquids and Their Solutions: Recent Advances and Emerging Challenges. *Current Opinion in Green and Sustainable Chemistry* **2018**, *12*, 27-32.
- Jiang, H. J.; Imberti, S.; Simmons, B. A.; Atkin, R.; Warr, G. G., Structural Design of Ionic Liquids for Optimizing Aromatic Dissolution. *ChemSusChem*. Published Online (9th Oct **2018**)

In these cases, I carried out the experiments, analysed the data and wrote the draft of the manuscript.

In addition to the statements above, in cases where I am not the corresponding author of a published item, permission to include the published material has been granted by the corresponding author.

Haihui Joy Jiang

As supervisor for the candidature upon which this thesis is based, I can confirm that the authorship attribution statements above are correct.

Gregory G. Warr

Abstract

Ionic liquids (ILs) are designer solvents with tuneable cationic and anionic structures. To optimise solvent performance, we seek an understanding of the structure of neat ILs, their mixtures and solutions. In this thesis, we propose structural factors that are key to realising the designer solvent promise of ILs. We highlight their potential for translation to new generations of low-cost and environmentally sustainable cation and anion motifs for large-scale applications.

Starting from a systematic comparison among primary and secondary ammonium ILs, the unusual liquid nanostructure of pyrrolidinium ILs explains its versatile solvent properties. Neutron diffraction combined with simulation shows a bi-continuous network of polar and apolar domains with disordered arrangements of functional groups, enabling the solubilisation of a wide range of solutes. In the context of biomass processing, we explore how an aromatic solute dissolves in protic ILs. Results highlight the geometry of the cation and solvent amphiphilicity. Based on key solvent-solute interactions, we present a framework for the design of IL structure to minimize competition and to enhance driving forces for aromatic extraction. Choline amino-acid ILs and their water mixtures show great promise as low-cost biocompatible solvents.

ILs as solvents have the rare ability to promote amphiphilic self-assembly of molecules, such as n-alkanols, that are not conventionally considered as amphiphilic surfactants in water. This self-assembly creates nanostructure that can significantly change solvent properties, such as the ability to solubilise molecules of varying polarity. We investigate the structure of complex solutions using a combination of small-angle X-ray scattering (SAXS), small-angle neutron scattering (SANS), invariant analysis, and neutron diffraction combined with Empirical Potential Structural Refinement (EPSR) simulation technique. We rationalise how protic IL-supported self-assembly can be controlled over solute polarity, packing geometry and formulation.

The design of ILs as solvents is not restricted to pure ionic species. We demonstrate new categories of ILs based on molecular complexation around metal cations. Mixtures of lithium salts and polyoxoethylene non-ionic surfactants show micellar and liquid-crystalline structure at RT. Surfactants self-assemble in inorganic salts as they do in protic ILs or water, with predictable phase behaviours rationalised by the surfactant packing parameter. Further, we show mixtures of paramagnetic salts and low-volatile solvents as magnetic ionic liquids. Our structural understanding of ILs and their mixtures creates opportunities for formulating new types of nanomaterials and facilitates the design of future solvents for process optimisation.

Acknowledgements

My sincerest thank you to my supervisor, Professor Gregory G. Warr, for his guidance and encouragement. He has inspired me to pursue my passion, helped me to grow in all aspects of my life and to achieve what is otherwise impossible. It has been an honour working with him, learning from him, and taking this journey with him and his team. Thank you for believing in me and providing me with wonderful opportunities over the years. Thank you for being one of the most influential people in my life.

I would like to thank Professor Gregory G. Warr and Professor Rob Atkin for leading the team to conduct experiments overseas, and for valuable discussions on project planning and manuscript preparation. Thank you to Dr Silvia Imberti and Dr Tristan Youngs for training on simulation, and for their assistance in performing neutron diffraction experiments at Rutherford Appleton Laboratory, UK. Thank you to Dr Kathleen Wood at ANSTO for her assistance in collecting neutron scattering data.

Thank you to Professor George M. Whitesides for hosting me at Harvard University and for intriguing conversations. Thank you to Dr Daniel J. Preston, Dr Maral Mousavi and other members of Whitesides' Group for fruitful collaboration. Thank you to Dr Paul A. FitzGerald and other members of Warr's Group for their continuous support.

I acknowledge the following scholarships and awards received during my PhD –

- Henry Bertie and Florence Mabel Gritton Postgraduate Research Scholarship (2015-2018)
- RJW Le Fèvre Research Travelling Scholarship (Gordon Research Conference, 2016)
- Enzo Ferroni Award (30th Conference on the European Colloid and Interfacial Society, 2016)
- RJW Le Fèvre Student Lectureship (2017)
- Bruce Veness Chandler Research Scholarship in Food Chemistry (2017)
- AAS-SIEF Fellowship (67th Lindau Nobel Laureate Meeting, 2017)
- Teaching Fellowship (The University of Sydney, 2017)
- SCI Messel Travel Bursary (Harvard University exchange, 2018)
- Harvard Mobility Scheme and Sydney Nano Institute Fund (Harvard University exchange, 2018)

CHAPTER 1

INTRODUCTION

This thesis describes investigations into the structure and properties of protic ionic liquids, either neat or as solvents with additives. We explore structural factors that contribute to their performance in applications such as formulating nanomaterials, biomass treatment, and lithium-ion batteries. Depending on the cation-anion combination, certain ionic liquids induce molecular self-assembly at the nanoscale, forming micellar, bi-continuous and liquid-crystalline structures. Liquid structures are analysed by polarising microscope, X-ray and neutron scattering experiments, and supported by simulations. This study establishes correlations between molecular structure, intermolecular interactions, liquid nanostructure and solvent performance. It develops strategies for controlled constructions at the nanoscale, and systems with potential industrial benefits.

1.1 Ionic Liquids as Designer Solvents

Solvents are crucial for modern society, and their global market is expected to reach over USD 30 billion by 2020.¹ Solvents are important for synthesis and preparation (of paints, foods and medicines), processing (of minerals, biofuels and surface coatings), energy storage and transportation. Conventional solvents consist of water, alcohols, hydrocarbons, ethers, chlorinated and ketones. Apart from water, all of these solvents present safety, health and environmental concerns, such as high flammability, volatility, toxicity in organs and nerve systems,² while solvent-free systems are relatively expensive.³ Besides, solvent effects vary from system to system.⁴

The choice of solvent depends on the physicochemical demands of the application and the solute types. For example, a reaction of a water-like and an oil-like substrate occurs at the interface between two immiscible liquids, with the reaction rate optimised by increasing their interfacial area.⁵ Similarly, a solvent for dissolution of biomass must have the capacity to simultaneously solvate polar and apolar groups.⁶ Variable solvent design is key to meet future technology.

‘If you want to understand the function, study structure!’ said Francis H. Crick.⁷ Arrangements and interactions among liquid molecules are closely related to the structure and nanostructure of solvents. Liquids feature properties of both solid and gas. However, its structure is the least understood. Historically, the liquid is interpreted to be homogeneous, coherent and

irregular.⁸ Recent studies show that it is possible for liquids to have defined bulk and interfacial structures.⁹⁻¹⁰

Ionic liquids (ILs) are pure salts with low melting points. Composed entirely of ions,¹¹ ILs possess many attractive and environmentally-friendly properties, including high thermal stability and negligible vapour pressure. Their excellent solubilising capacity for solutes of different polarities¹²⁻¹⁵ has led to their adoption as designer solvents, where liquid properties are readily tunable by varying cation and anion structure.¹⁶ From synthesis to catalysis, from electrochemistry to colloid science, ILs have repeatedly demonstrated performance advantages over molecular solvents.¹⁷⁻¹⁹

There are two major classes of ILs: aprotic ILs and protic ILs.^{15, 20} Figure 1.1 shows structures of representative cations and anions. Aprotic ILs contain an alkyl-substituted cation, such as phosphonium, pyrrolidinium, imidazolium (Im^+) and pyridinium, paired with an aprotic anion, such as hexafluorophosphate (PF_6^-), tetrafluoroborate (BF_4^-), halide (Cl^- , Br^- or I^-), thiocyanate (SCN^-) and carboxylate. Protic ILs contains a cation with labile protons, such as primary ammonium, secondary pyrrolidinium (Pyrr^+) and quaternary cholinium (Ch^+), paired with either an aprotic or a protic anion, such as nitrate (NO_3^-), hydrogen sulfate (HSO_4^-) and amino acids. Protic ILs are formed by proton transfer from a Brønsted acid to a Brønsted base. In contrast, multistep reactions for preparing aprotic ILs lead to lower energy efficiencies, higher costs and limited scalability for industrial applications.

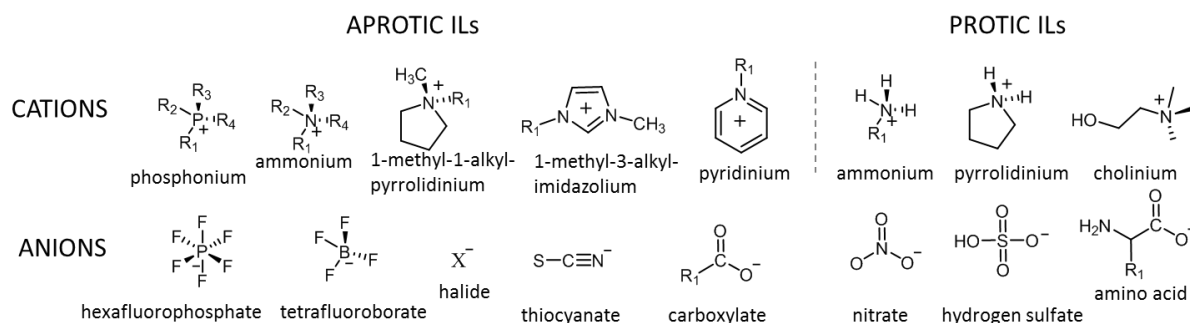


Figure 1.1 Chemical structures of representative cations and anions used in aprotic and protic ionic liquids.

To design economically and environmentally viable solvents, our study focuses on protic ILs for their ease of synthesis, simplicity, stability and low toxicity.²¹ Without the use of fluoros anions, we discuss the structure of traditional alkylammonium, alkylnolammonium and pyrrolidinium ILs with or without solutes, structural implications on aromatic dissolution, and abilities of these ILs in formulating nanomaterials. Choline amino-acid ILs are naturally derived and tolerant to water, therefore, we study the structure of these biocompatible ILs, their water mixtures, and with the addition of a solute in the context of biomass processing.

1.2 Structure and Nanostructure

One of the most striking features of ionic liquids (ILs) is the widespread occurrence of amphiphilic nanostructure.^{20, 22} Far more than simply being low melting-point salts, most ILs are structurally heterogeneous on the nanoscale; the features of this structure are highly variable, but controllable through e.g. polar/apolar structure and composition, charge density, and H-bonding capacity of the cation and anion. This amphiphilic nanostructure is manifested in the bulk liquid as well as near macroscopic interfaces, affecting the physical properties of pure ILs, as well as their performance as solvents and in liquid mixtures. The ability to control properties via nanostructure through structural variation of cations and anions has prompted research spanning process technology, synthesis and catalysis, biotechnology, pharmaceuticals, electrochemistry, analytics and functional materials.²³

X-ray and neutron scattering studies over the past decade have shown how the amphiphilicity of cations and anions determines the bulk structure of ILs.²⁴ Amphiphilic nanostructure arises when the alkyl chain length (or another non-polar moiety) is too long to be accommodated by the charged groups, which in turn depends on the nature of the charged group. Thus, ILs with sterically hindered (e.g. N-alkyl-N-methylpyrrolidinium) or delocalised (e.g. N-alkyl-N'-methylimidazolium) charges develop amphiphilic nanostructure above n-butyl chains.²⁵⁻²⁶ In protic alkyl ammonium ILs, cation with a short ethyl chain is sufficient to form nanostructure, since the charges on IL head groups are more localised and exposed.²⁷ The bulk amphiphilic nanostructure is controlled mainly by Coulombic forces expelling non-polar groups. Simple packing constraints, similar to those used in surfactant self-assembly, then determine the overall arrangement of polar and non-polar domains.²⁸ A dense H-bond network, once thought to be critical for the amphiphilic nanostructure, is not necessary, and in fact H-bonding plays a secondary role to electrostatics even in protic ILs.²⁹⁻³⁰ It is noteworthy that the amphiphilic nanostructure of protic ILs is not found in their H-bonding molecular precursors, which are homogeneous.³¹ ILs with a hydrocarbon cation and fluorocarbon anion have even more complex liquid nanostructure, consisting of segregated polar, hydrocarbon and fluorocarbon domains.³² Figure 1.2 shows liquid how nanostructure is affected by ion type for three representative protic ILs, with corresponding X-ray scattering patterns.

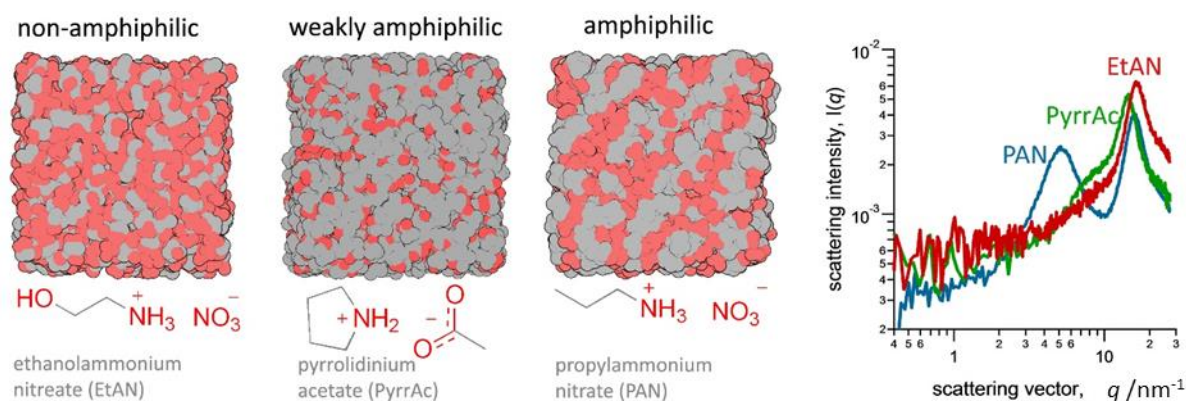


Figure 1.2 Emergence of amphiphilic nanostructure in protic ILs, as determined from neutron diffraction and X-ray scattering.^{29, 33} Longer alkyl moieties on cations are expelled into nonpolar domains, with overall liquid nanostructure influenced by cation and anion structure, packing of polar/apolar sub-volumes, and H-bonding capacity

AFM studies have shown the existence of distinct surface and near-surface amphiphilic nanostructures that differ from, but are related to the bulk structure, and these can also be controlled by varying ion structure.³⁴ The bulk isotropic nanostructure of the IL becomes increasingly anisotropic as the polar and non-polar domains align parallel to the macroscopic interface in response to geometric constraints, and its charge and chemical composition. The structure of ILs near a solid surface is important for diverse applications from electrodeposition to lubrication.³⁵⁻³⁶

The existence of degrees of amphiphilic nanostructure renders ILs structurally more akin to microemulsions than conventional molecular solvents, which requires a paradigm shift beyond current ideas of uniform solvent polarity. Traditional methods based on a partition coefficient ($\log P$) or a solvatochromic dye yield a single parameter describing an average solvent environment. The three-parameter Kamlet-Taft approach, which characterizes solvents according to their polarizability (π^*), hydrogen-bond acidity (α) and hydrogen-bond basicity (β) is widely used to compare ILs to other green solvents.³⁷ Amphiphilic nanostructure disrupts the interpretation of such experiments due to selective solvation or partitioning of probes between polar and apolar domains within the IL itself. Partitioning studies of homologous series of poly(oxyethylene)-*n*-alkyl ether surfactants showed that the alkyl chains experienced a more-or-less average of the polar and non-polar environment, the ethoxy groups were exclusively located within the polar domains of IL nanostructure. Likewise, different choices of solvatochromic probe give rise to different polarity scales of ILs.³⁸⁻³⁹

With recent advances in computation methodologies, multi-scale studies of IL nanostructure are redefining the concept of solvent polarity.⁴⁰ Atomistic *ab initio* calculations, such as Density Functional Theory, probe intra- and intermolecular interactions in detail, with a computation capacity up to a few ion pairs. To explore IL structure at the nanoscale, methods such as Molecular Dynamics accommodate hundreds of ion pairs with statistical information on atom-atom pair correlations. Most

neat ILs have domain sizes that fall within this length scale. However, if the system of interest includes a dissolved polymer, surfactant self-assembly structures, or dispersed nanoparticles, it is currently necessary to use coarse-grained methods with compromises on the atomic resolution.

X-ray and neutron scattering have proven to be powerful experimental tools for studying nanostructured ionic liquids with and without solutes.²⁴ However, the nanostructure of ILs is less-well defined than, for example, aqueous surfactant micelles, and cannot be accurately described by geometric models such as spheres, ellipsoids or bilayers. Flexible models or simulation methods to fit experimental data over wide length scales will emerge.

The “green credentials” of many conventional (*i.e.* imidazolium) ILs have recently been subjected to well-deserved scrutiny. Their high synthesis cost and reliance on fluororous components compromise the advantages of negligible vapour pressure, and limits the potential for sustainable exploitation of the performance advantages of the amphiphilic nanostructure. To achieve broad uptake, ILs must be both economical and environmentally-friendly. Instead of using aprotic ILs which typically cost over USD \$50 kg⁻¹, protic ILs can be as cheap as USD \$1.25 kg⁻¹, significantly lowering the industrial processing cost.⁴¹ Adding a molecular co-solvent such as water or alcohols further reduces solvent cost, while preserving structural features and functionality of the neat IL.⁴²⁻⁴³ Moreover, ILs made from renewable starting materials are of environmental interest and with potential biomedical uses.⁴⁴ These include amino-acid based ILs and the related but distinct deep eutectic solvents (DESs).

In this context, it is important to note that some ILs, both aprotic and protic, have been shown to retain amphiphilic nanostructure in the presence of significant amounts of water. Aggregation of cation alkyl tails, driven by preferential anion-water interactions, largely preserves liquid nanostructure up to at least 25 wt% water in imidazolium ILs.⁴⁵⁻⁴⁶ Protic ethylammonium nitrate-water mixtures (as well as ethylammonium formate-glycerol) at 50% v/v also exhibit comparable amphiphilic nanostructure as pure ILs, but with a modified structure due to the different polar/apolar volume fractions.^{42, 47} Incorporation of the amphiphilic butanoate anion changes packing constraints, rendering the IL more like a catanionic surfactant. This affects how nanostructure changes on upon water dilution.⁴⁸ (At the limit, many long-chain analogues of ammonium, pyridinium and imidazolium ILs are of course cationic surfactants that form micelles in water.) Adding water into ILs reduces their cost, often with the additional benefit of lowering viscosity, thereby retaining or improving performance. Biomass pre-treatment is an important example of using ILs as a processing solvent, which involves water as a by-product, and therefore the chosen ILs must be water compatible.

Other simple solutes can have surprisingly complex effects. For example, amphiphilic and non-amphiphilic protic ILs have been shown to undergo starkly different, ion-specific, structural changes

in the presence of dissolved salts.⁴⁹⁻⁵⁰ Chloride weakens amphiphilic nanostructure by selectively binding to the ammonium charge centre. Lithium – solvated by the nitrate anion – weakens existing nanostructure but, perversely, induces it for marginally amphiphilic cations. Similar observations were found in aprotic imidazolium and pyrrolidinium ILs with the bis(trifluoromethanesulfonyl)imide (TFSI) anion.⁵¹ As heterogeneity affects the transport mechanisms of various solutes in ILs,⁵² these short-range effects on amphiphilic nanostructure can have macroscopic implications, e.g. for the performance of ILs as electrolytes for Li-ion batteries.

Addition of more complex solutes or molecular components can dramatically modify nanostructure. Many nanostructured ILs are miscible with medium chain length n-alkanols, accommodating their hydroxyl groups into polar nano-domains containing IL charged groups, while stabilizing the non-polar domains that can be substantially swollen by the alkanol, and may lead to substantially longer-range periodic order than the IL alone (see Figure 1.3),^{43, 53-54} bringing these binary mixtures even closer in concept to conventional microemulsions. Additional components may then dissolve into or swell polar or non-polar domains. This behaviour is unlike water and other polar molecular solvents, in which alkanols cannot self-assemble. The pre-existing amphiphilic nanostructure is essential.

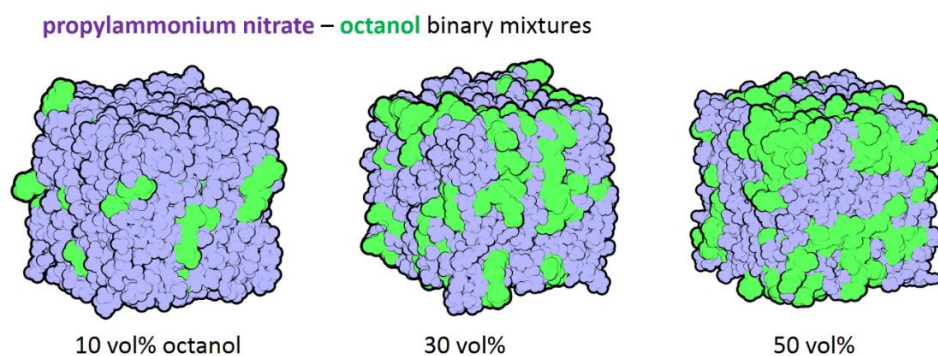


Figure 1.3 Structure of propylammonium nitrate/n-octanol mixtures from neutron diffraction, showing the development of octanol tail-rich non-polar domains stabilised by the IL's amphiphilic nanostructure⁵³

1.3 Exploiting Nanostructure in Applications

ILs are important solvents for the processing of various biomaterials, such as lignocellulosic biomass, microalgae, and coal, from which a range of chemical compounds including lipids, biopolymers, aromatics and other small molecules are extracted. Badgujar *et al.* identified many individual structural factors that govern lignocellulosic biomass dissolution including IL anion (H-bond basicity), IL cation structure, functional group, cation size, and side chain length, as well as Kamlet-Taft solvation properties.⁵⁵ Many of these factors also determine the extent and nature of IL amphiphilic nanostructure.

Microalgae are another rich potential sustainable source to produce fuels and other chemicals. Lipid extraction by ILs has been investigated, including exploiting their water miscibility to bypass costly dewatering and drying stages needed with most current solvents.⁵⁶ Although much of the detailed mechanism remains unknown, including the chemical roles of IL and water, ILs are known to facilitate lipid extraction by disrupting cell structure, including lipid bilayers. Two recent studies have shown that the stability of phospholipid vesicle bilayers depends on amphiphilicity of ILs.⁵⁷⁻⁵⁸ Non-amphiphilic ILs preserve lipid bilayers, whereas amphiphilic ILs with longer alkyl chains disrupts lipid bilayers.

In the synthesis of both inorganic materials and organic compounds, mechanisms, selectivity, and rates can also be controlled by IL steric factors, H-bonding, solvophobic interactions, ion self-assembly and clathrate formation.⁵⁹ Here also the amphiphilic nanostructure of ILs, which resemble self-assembled nanoreactors, has been implicated as a determining feature.⁶⁰ We expect nanodomains to bring otherwise immiscible reactants into contact, to facilitate a cascade reaction (e.g. from polar reactants, to amphiphilic intermediates, to apolar products), and to allow easy separations. Beyond a static picture of the amphiphilic nanostructure, understanding the dynamics of assembly/disassembly and the relative “stiffness” of polar and apolar nanodomains⁶¹ will help to realise the full potential of ILs as designer solvents for a diverse range of chemical processes.⁶²

Systematically studying ILs with a variety of model solutes would enable the rational design of ILs by identifying key solvent-solute interactions and extending the “like dissolves like” rule to amphiphilically nanostructured solvents.²⁹

At the solid-IL interface, the strong interaction of imidazolium-based ILs with carbon nanomaterials leads to confined ion layers on graphene sheets and in carbon nanotubes.⁶³ Nanomaterials and functional surfaces have been templated via ion self-assembly.⁶⁴⁻⁶⁵ On metal

electrodes, the ion-surface interactions and therefore the near-surface IL structure controls the size and morphology of the deposit.⁶⁶

The majority of the ILs studied for processing biomaterials are imidazolium-based, due to their commercial availability.⁶⁷ More sustainable processes will be achieved with lower cost and more environmentally friendly solvents, such as protic ILs prepared by one-step synthesis, biocompatible solvents such as amino-acid ILs⁶⁸ and DESs, as well as utilising mixtures with water and other benign molecular solvents where suitable.

Cholinium ILs with amino acid anions and their water mixtures have been investigated for extraction from sources ranging from fruit peel,⁶⁹ to straw,⁷⁰ to coals.⁷¹ Some correlation with anion basicity, charge density, or local structure have been identified,⁷² but a fuller understanding awaits systematic studies that correlate performance with structural variation. The diversity of naturally-occurring (and synthetic amino acid) structures includes potentially amphiphilically nanostructured ILs and their solutions, but how this may correlate to process efficiency remains an open question.

Deep eutectic solvents (DESs) are two- (or more) component systems comprising at least a hydrogen bond donor and acceptor, one of which is often a salt. They share many of the structural features and advantageous characteristics of ILs and IL solutions for synthesis and processing applications.⁷³ The most widely-studied DES – choline chloride/urea – is formed from naturally-occurring components, and retains its underlying structure up to 40 wt% water.⁷⁴ Such water-compatible DES are potential candidates for applications such as biomass processing. The changes in properties observed on replacing urea by ethylene glycol and glycerol highlights the importance of hydrogen bond donor-to-acceptor ratio and strengths.⁷⁵ To date, the majority of DESs studied are non-amphiphilic, with hydrogen bonding and Coulomb forces governing bulk structure. Recent studies have shown not only that it is possible to design DESs analogous to protic IL – solvent mixture with amphiphilic nanostructure, but that they exhibit similar structures and tunability across diverse properties,⁷⁶⁻⁷⁷ both in bulk and at interfaces.⁷⁸ The structural understanding of ILs is a decade ahead of DESs, and exciting questions are to be answered. DESs allow sustainable and efficient separations in oil and gas industries, with a selective solubility of small aromatics, acidic gases such as CO₂ and H₂S.⁷⁹ Ionic liquid-formulated hybrid solvents containing amine have similar functions for CO₂ capture.⁸⁰ Future research should further strengthen the nanostructure/ property correlation between DESs and protic ILs.

The nanostructure of ILs differs substantially from both molecular solvents and simple molten salts. Although the understanding of factors that affect nanostructure in first-generation ILs is relatively mature, some outstanding challenges for modelling intermediate and long-range structures

remain. A better understanding of the structural and dynamic coupling between length scales will enable better *a priori* design of ILs and improve process efficiency.

The translation of the understanding of IL nanostructure into more environmentally benign, lower cost, and sustainable components (protic ILs, mixtures, bio-based ILs and DESs) will enable the advantages of ILs to be exploited more widely and in larger scale applications utilising the next generation of solvent technology. This will complement structure and application-oriented performance studies, such as examining ILs with dissolved model solutes, alongside multi-scale simulations.

1.4 Systems of Interest

In this thesis, we investigate the relationship among IL molecular structure, bulk nanostructure, solvent-solute interactions and its performance in applications, such as biomass processing and formulating water-free surfactant-free microemulsions, as explained below. The focus is on the structural behaviour of ionic liquids with different cationic and anionic structures and amphiphilicity. This facilitates a rational design of ILs to solubilise solutes with various molecular shapes, functional groups, and polarities.

1.4.1 ILs and biomass processing

Lignocellulosic biomass is the most abundant source of carbon on the planet and is potentially 100% renewable.⁸¹ Figure 1.4 shows major fractions of biomass, which include carbohydrate polymers (40% cellulose, 30% hemicellulose) and aromatic polymers (25% lignin).⁸² Mostly found within plant cell walls, lignocellulose has strong intermolecular interactions to serve as biological support. Among all three components, lignin has the highest tolerances to both chemical and physical conditions, preventing the overall structure from decomposition and separation. To utilise this renewable resource, commercially viable procedures for biomass extraction are in need.

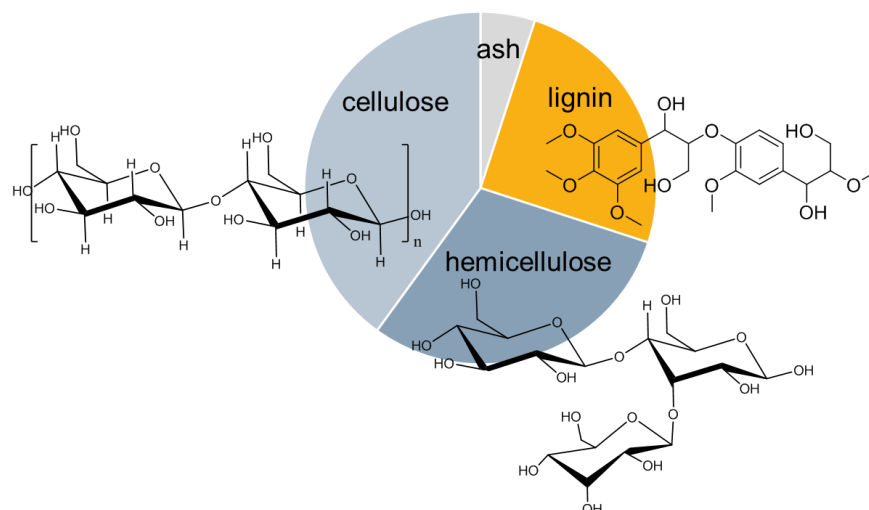


Figure 1.4 Composition of lignocellulosic biomass and representative polymer structures.

Current methods include ammonia fibre expansion, dilute acid, steam explosion, autohydrolysis and an organic solvent.⁸³ These processes all associate with disadvantages, outweighing products' industrial benefits. There is no biomass pre-treatment available today that can sustainably process a diverse range of feedstock at high yields. Only recently, protic ILs were integrated as solvents for the extraction of lignin.^{41, 84} Protic ILs are less expensive compared to previously studied aprotic class, while the extraction can be equally effective. A structural understanding of IL-aromatic mixtures will facilitate targeted and economic designs for industrial uses.

To choose a representative structure of lignin for studying solvent-solute interactions, we analyse the structure of its monomers and decomposition products. Figure 1.5a shows the structure of three lignin monomers, *p*-coumaryl, coniferyl and sinapyl alcohols, which are methoxylated to various degrees.⁸⁵ Lignin aromatic cores incorporate these lignols in the form of phenyl propanoids, namely *p*-hydroxyphenyl (H), guaiacol (G) and syringyl (S) units. The percentage content of H, G and S units (and therefore the number of methoxy groups) vary across different types of biomass (i.e. hardwood, softwood, grasses).

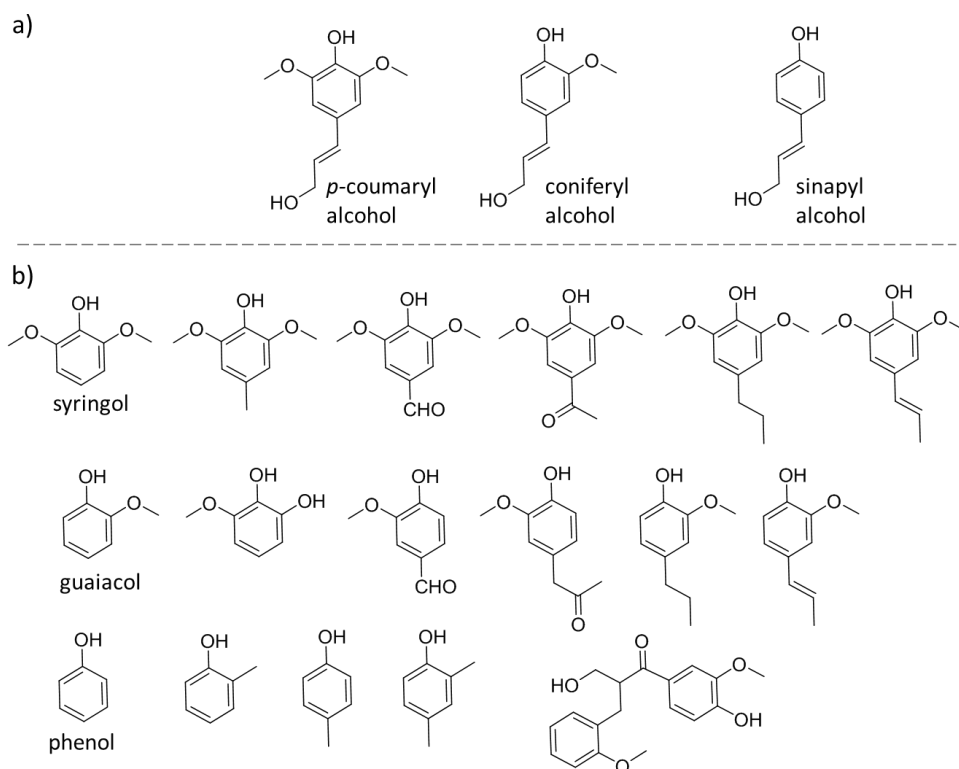


Figure 1.5 The chemical structure of a) lignin monomers and b) decomposition products of lignin through chemical treatments.

Figure 1.5b shows the structure of possible aromatic products resulted from common lignin depolymerisation methods. Acid or base hydrolysis produces derivatives of syringol (2,6-dimethoxyphenol) and guaiacol (2-methoxyphenol) derivatives.⁸⁶ Metal-based catalysis generates methylphenols (cresols), or methoxyphenols with a hydrocarbon sidechain that is either saturated or unsaturated.⁸⁷⁻⁸⁸ Despite the difference in position of substitution and small variations in functional groups, these small aromatic products share the common parental structure of phenol and guaiacol.

In Chapter 3, we discuss the solvent structure of pyrrolidinium and alkylammonium ionic liquids and how they dissolve aromatic molecules in the context of lignin extraction. We choose guaiacol as a model solute, since its structure is representative to major lignin decomposition products shown in Figure 1.5b. The structural understanding of key interactions with the methoxy group and the phenol group of guaiacol molecules is transferrable to guaiacol derivatives and small aromatic compounds in general.

1.4.2 ILs induced microemulsions

The traditional definition of a microemulsion is “a dispersion made of water, oil, and surfactant(s) that is an isotropic and thermodynamically stable system with dispersed domain diameter varying approximately from 1 to 100nm, usually 10 to 50 nm”.⁸⁹ In other words, one or several amphiphilic compounds (surfactants) induce the miscibility of two otherwise immiscible

liquids (water and oil), forming a macroscopically homogenous but nanoscopically heterogenous mixture. In the 1970s and 1980s, there were intense investigations of microemulsions, as aqueous systems of low interfacial tension substantially enhance the recovery of crude oil from wells.⁹⁰ When the price of oil fell in the mid-1980s, the application of microemulsions has shifted towards drug delivery,⁹¹⁻⁹² reaction medium for nanoparticle synthesis,⁹³⁻⁹⁴ and polymerisations.⁹⁵

Recently, Prévost *et al.* proposed a new definition of microemulsions, in which *flexible*, *rigid* and *ultra-flexible* microemulsions are the three categories classified based on the rigidity of the amphiphilic monolayer that separated the water and the oil domain at the nanoscale.⁹⁶ In *flexible microemulsions*, the amphiphilic component may be a non-ionic surfactant (i.e. the alkyloligoethylene oxide C_nE_m type), a double chain surfactant which forms reverse microemulsions, or a combination of a surfactant with a cosurfactant forming quaternary microemulsions. Co-surfactants are medium-chain alcohols that increase the flexibility of the amphiphilic monolayer and the extent of solubilization, which are requirements for the formation of a microemulsion. In *rigid microemulsions*, interfaces are stiffer, and the concentration of surfactants is higher. Their phase boundaries and scattering spectra are almost insensitive to temperature change.

The nanostructure of *ultra-flexible microemulsions* is investigated only recently when a substantial amount of research activities demonstrates the possibility of formulating microemulsion-type structure without using conventional surfactants.^{43, 97-107} An ultra-flexible microemulsion contains a polar, an apolar and a weakly amphiphilic component that is not considered as a surfactant. Such surfactant-less mixtures have no compact surfactant monolayer to separate two immiscible liquids.¹⁰²⁻¹⁰⁴ Instead, weakly amphiphilic molecules slightly accumulate at the polar-apolar interface without forming a well-defined monolayer. Unlike classical microemulsions, the scattering of ultra-flexible microemulsions has no peak, nor a clear Porod decay at high angles.⁹⁹ Details of scattering experiments and analysis will be discussed in Chapter 2.

In 1916, Neuberg defined hydrotropes as compounds that increase the solubility of sparingly soluble organic substances in water.¹⁰⁸ Kunz *et al.* recently reviewed ternary mixtures of water-hydrotrope-hydrophobic substances, which are structured at the nanoscale.¹⁰⁹ Hydrotropes form pronounced aggregation in the presence of a hydrophobic solute, but the aggregation is weak without a hydrophobic solute. This unique behaviour of hydrotropes distinguishes themselves from surfactants.

An example of ultra-flexible microemulsions is the water-ethanol-octanol ternary mixture, in which ethanol is a hydrotrope acting as the weakly amphiphilic component.^{97, 104, 106} Figure 1.6 illustrates the weak structuration with snapshots from a Molecular Dynamics simulation.¹⁰⁴ There is a

continuous water-rich domain with ethanol molecules solubilised randomly. Octanol molecules segregate into separate domains with a radius of about 2nm, with enhanced concentration of ethanol at the water-octanol interface. These nano-aggregates are distinct from critical fluctuations of an unstructured ternary fluid, which are changes in molecular concentrations and occur near the critical point. Ethanol molecules form interfaces in the water-ethanol-octanol system. Light scattering studies show that the fluctuations near the critical point are formed by well-defined aggregates alternating between oil-rich and oil-poor domains.¹⁰⁷

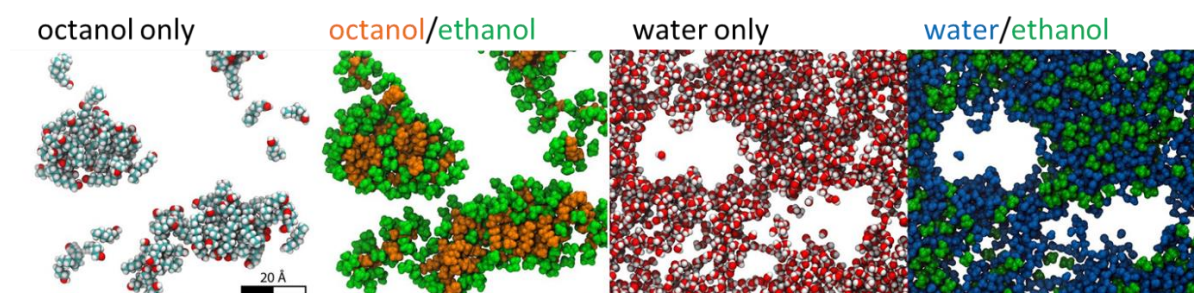


Figure 1.6 Snapshots of the water-ethanol-octanol system from molecular dynamics, reproduced from reference ¹⁰⁴ with permission. Copyright (2018) National Academy of Sciences. All four snapshots are extracted (selectively) from the same simulation box. Molecular labels were colour-coded and shown on top of each snapshot. The second snapshot shows ethanol molecules (green) that interact strongly with the octanol molecules. The mixture is macroscopically homogeneous and thermodynamically stable.

Protic ILs support conventional surfactants to form micelles, liquid crystals and microemulsions.¹¹⁰⁻¹¹² More interestingly, amphiphilic protic ILs themselves show surfactant-like behaviours. A previous study shows that protic IL induces self-assembly of n-alkanols, which are only weakly amphiphilic and do not segregate otherwise.⁴³ It is possible to substitute the surfactant component of a conventional microemulsion with an amphiphilic ionic liquid. However, the structure of these ternary mixtures has not been explored. A nanostructured fluid without the presence of surfactant is exciting. Moreover, non-amphiphilic protic ILs is structurally similar to a polar solvent, such as water. Whether or not a non-amphiphilic protic IL can substitute water or the polar component in formulating microemulsions is in question. The structural insight of ILs' amphiphilic and non-amphiphilic potential will open up many opportunities, including controlled construction at nanoscales and highly functional materials.

Our approach is to utilise three scattering techniques at different length scales, with each giving a new piece of information. At the atomic level, we use neutron diffraction combined with a simulation technique to generate high-resolution pictures of individual interaction and correlation. On the other hand, both small angle X-ray and neutron scattering experiments (SAXS/SANS) are with relatively low resolution, looking at nano- to mesoscopic structures. The analysis is customised to suit

the nature of individual experiments. Hypotheses and conclusions drawn from each experiment are analysed cooperatively to ensure consistency and to obtain a more comprehensive understanding.

1.4.3 Overview

This thesis is divided into four sections; Introduction (Chapter 1), Methods (Chapter 2), Results and Discussion (Chapters 3-5), and Conclusions (Chapter 6). The introduction gives a brief overview of nanostructured ionic liquids and their solutions. The Methods section describes the chemicals, experimental techniques and theories behind the analysis used throughout this work. Chapter 3 discusses the design factor of ILs and their aqueous solutions for aromatic dissolution, in the context of lignin extraction. Chapter 4 presents a matrix of IL-induced microemulsions without the presence of water or surfactant. Chapter 5 explores two special categories of ILs: an amphiphilic extension of solvate ionic liquids, in which non-ionic surfactants self-assembles in lithium salts, forming micellar and liquid-crystalline structures (Section 5.1); and paramagnetic ILs (Section 5.2). Finally, Chapter 6 brings all the research together and discusses the conclusions of this project regarding the structural design of ionic liquids for process optimisation.

CHAPTER 2

METHODS

Our overall approach begins with the synthesis of ionic liquids with systematic variation of cations and anions (Figure 2.1). Since many protic ionic liquids are hygroscopic, drying procedures, storage methods and purity checks are important. Systems involved are typically multi-component, and each shows different phase behaviour. Therefore, determining the solubility of solutes in ILs and phase boundaries of mixtures is a crucial step before structural studies. We use polarising microscopy and X-ray scattering as preliminary scanning techniques, followed by small-angle neutron scattering (SANS) with invariant analysis, and neutron diffraction combined with a simulation method—Empirical Potential Structural Refinement (EPSR). Further analysis was performed using routines with specialised functions (DLPUTILS). Each technique provides structural information at a different length scale. Depending on the characteristics of ILs, other experiments such as magnetic susceptibility and contact-angle measurements were performed.

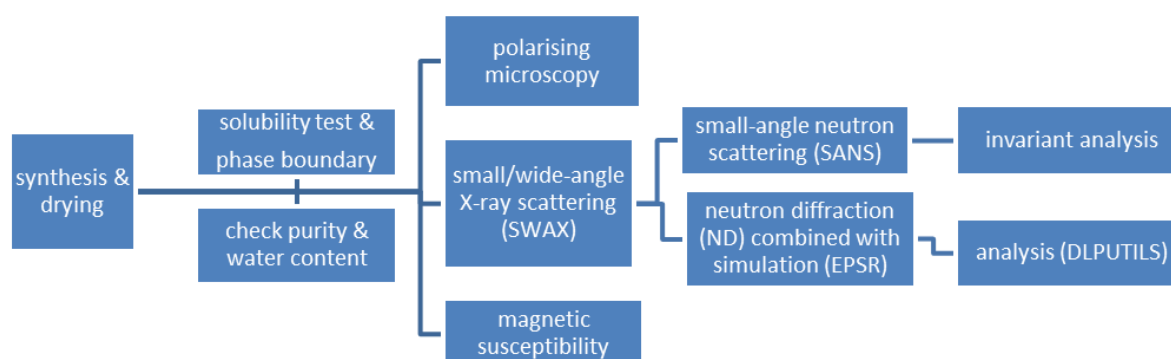


Figure 2.1 A flowchart of our project approach

2.1 Synthesis of Ionic Liquids

A range of ionic liquids was synthesised via acid-base neutralisation, summarised in Table 2.1. Depending on the stability of IL precursors and the resulting product, details of the synthesis can vary. In this section, we discuss experimental details of making alkylammonium ILs, acetate-based ILs, amino-acid based ILs, solvate ILs and magnetic ILs.

Table 2.1 A list of ionic liquids synthesised with their corresponding starting materials and sources.

	ETHYLAMINE (SIGMA)	ETHANOLAMINE (MERCK)	PROPYLAMINE (ACROS)	PYRROLIDIN E (FLUKA)	CHOLINE HYDROXIDE (SIGMA)
NITRIC ACID (AJAX)					
ACETIC ACID (VWR)					
LYSINE (SIGMA)					
ASPARTIC ACID (FLUKA)					

2.1.1 Alkylammonium ILs

Ethylammonium nitrate, ethanolammonium nitrate, and propylammonium nitrate were prepared based on previously published procedures.¹¹⁰ All alkylammonium ILs were synthesised by slow titration of the relevant amine base into the relevant acid (Table 2.1). The reaction was maintained below 10 °C in an ice bath. The pH of aqueous solutions of ILs was maintained in between 5 and 6, preventing the formation of amine-related impurities. Products were dried first to less than 5 wt% water content on a rotary evaporator, followed by drying under N₂ at 120 °C over 12 hours. Water contents were measured by Karl Fischer titration to be less than 0.2 wt% (typically much lower) for these ILs after drying. Note that the non-substituted ammonium nitrate and the secondary pyrrolidinium nitrate are both explosives and avoided in this project.¹¹³

2.1.2 Acetate-based ILs

Acetic acid is a relatively weak acid (pK_a = 4.76). ILs with an acetate anion thus contain a small amount of acetic acid in equilibrium with a relatively weak base such as pyrrolidine (pK_a=11.27). Drying acetate-based ILs (such as pyrrolidinium acetate) under high vacuum or at high temperature leads to an unbalanced ratio between the acid and the base. Below are our synthetic methods modified from published literature.¹¹⁴⁻¹¹⁵

Pyrrolidinium Acetate

PyrrAc samples were synthesised via acid–base neutralisation from neat reagents in 1:1 mol ratio. Although we mentioned pyrrolidine as a relatively weak base, it is stronger than alkylamines, pyridine, or imidazole. H-PyrrAc was synthesized using pyrrolidine (Fluka, > 99%) and acetic acid

(VWR, > 99.9%). D4-PyrrAc was synthesised from D4-acetic acid (Cambridge Isotopes, D99.5%) and hydrogenous pyrrolidine. D8-PyrrAc was synthesised from D8-pyrrolidine (Cambridge Isotopes, D98%) and hydrogenous acetic acid. Reactions were maintained at just above the melting temperature of the mixture (20 °C at the beginning, then gradually decrease to 5°C using an ice bath). Vacuum drying was avoided as the acid:base ratio changes under low pressure. Water contents were measured to be in between 0.4 and 0.6 wt% by Karl Fischer (Metrohm) volumetric titration. Over the period of a two-month experiment, the maximum water content was 0.9 wt%, which is equivalent to a water:ion ratio of 1:30. According to our structural study of protic IL–water mixture, such water content is unlikely to influence the present interpretation.⁴² The amide content was monitored by ¹H NMR 300 MHz (Bruker) on regularly collected samples. Ionic liquid peaks were observed at 1.80–2.05 ppm (anions) and 3.15–3.35 ppm (cations), with D₂O as the solvent ($\delta_{\text{solvent}} = 4.75$ ppm). In the case of amide formation, we expect to see downfield shifts, observing peaks at 2.05–2.10 ppm and 3.30–3.60 ppm, respectively. Exchangeable protons of PyrrAc were detected near 9.0–11.5 ppm. PyrrAc samples are stable at room temperature with negligible amide content that is below the detection limit (1.0 mol%) after one month.

Cholinium Acetate

Cholinium acetate (ChAc) was prepared here by dropwise addition of choline hydroxide (Sigma, 46 wt% in water) into acetic acid (VWR, >99.9%) in a 1:1 molar ratio. To remove water, the sample was kept on a rotary evaporator (10 mbar) at 70 °C for 4 hours before drying under a high vacuum (0.05 mbar) overnight. Since cholinium hydroxide is a strong base ($\text{pK}_a = 13.9$), the electrostatic interaction is stronger in ChAc compared to PyrrAc. Drying ChAc under a moderate vacuum (10mbar) is not a concern as it is for PyrrAc. The sample was measured by ¹H NMR to determine the acid-base ratio after drying under high vacuum (0.05mbar). Based on NMR results, a corresponding amount of acid was added to reach a 1:1 acid:base molar ratio. The sample was mixed at 85 °C for 30 min. The melting point of ChAc was measured to be 80 °C, similar to literature value.¹¹⁶ The purity of ChAc was checked by ¹H and ¹³C NMR spectroscopy. ChAc-water mixtures (1:5 molar ratio, various deuterations) were prepared, which have a melting temperature below RT. The water content of ChAc-water samples was confirmed by Karl-Fischer ($\pm 0.1\text{wt}\%$).

2.1.3 Amino acid-based ILs

The synthetic method of cholinium lysinate (ChLys) was modified from published literature.¹¹⁷ A choline hydroxide solution (Sigma, 46 wt% in water) was diluted to 10 wt%, and added dropwise to L-lysine monohydrate powder (>97%, Sigma) with stirring, at 1:1 molar ratio at RT overnight. Water was removed under reduced pressure at 40 °C. The acid-base ratio was checked by ¹H-NMR, and a

small amount of the base or the acid was added and stirred to balance the acid:base ratio. The IL was stirred and dried under high vacuum (0.05 mbar, 5 days) to further reduce the water content to < 0.5 wt%. ChLys and ChAc were mixed with water (at 1:5 molar ratio, with various deuterations) for neutron experiments.

2.1.4 Ion Exchange

To prepared deuterated choline amino-acid based ILs and their mixtures for neutron experiments, d9-choline chloride (d9-ChCl) was exchanged into d9-choline hydroxide (d9-ChOH). Before use, ion exchange resins (Amberlite IRA-400 for hydroxide, 25mL) were washed with concentrated NaOH aqueous solutions five times. Silver test (0.2M AgNO₃ and 0.25M HNO₃ in water) was done to ensure a negligible amount of chloride residue remained on the resin. Flame photometry showed that the concentration of sodium was below 12ppm. Resins were rinsed with deionised water until its pH reached neutral, then loaded onto a small column (1cm radius) with deionised water as the eluent. An aqueous solution of d9-ChCl (0.5g solid in 10mL of solvent) was loaded as the sample. All basic eluents with ChOH (pH > 7.5) were collected and combined. Water was partially removed on a rotary evaporator (30 mbar, 40°C) and the volume was reduced to 30mL. A known volume fraction of the obtained ChOH solution (e.g. 1.00 mL out of 30.0 mL) was titrated with a standard acid solution (e.g. 0.01M HNO₃), showing a yield of 95%. The concentration of the ChOH solution was calculated based on the titrated yield, and used for the synthesis of d9-choline amino-acid ILs following procedures described in Section 2.1.3.

2.1.5 Proton-Deuterium Exchange

Fully hydrogenous ILs were prepared using hydrogenous reagents following procedures described above. Fresh deuterium oxide D₂O (Sigma, 99%) was added to a hydrogenous IL in a 10:1 molar ratio. For example, 1 mole of PAN has 3 moles of exchangeable hydrogens, requiring 15 moles of D₂O for each exchange. A D₂O-IL mixture was dried on a rotary evaporator, followed by high-vac. The exchange was performed four times for each IL. ¹H-NMR experiments reveal that, on average, 95% exchangeable hydrogens were replaced with deuterium.

2.1.6 Solvate ILs and Solvate Surfactants

Tetraglyme (>99%), triglyme (>99%), triethylene glycol (>99%) and tetraethylene glycol (>99%) along with lithium nitrate (LiNO₃, >99.9%), lithium bis(trifluoromethane)sulfonimide (LiTFSI, >99.9%), and lithium trifluoromethanesulfonate (LiOTf, >99.9%) were purchased from Sigma Aldrich. Lithium salts were dried in a vacuum oven at 100 °C for 3 hours, then stored in a glove box before use.

Polyoxyethylene alkyl ether nonionic surfactants, C_nE_m , of various alkyl chain lengths, n , and degrees of ethoxylation, m , were purchased from Nikkol or Fluka. Purity was verified by reverse-phase HPLC.

The solvate ILs and solvate surfactants were synthesised by mixing stoichiometric quantities of lithium salt and glyme or glycol or a non-ionic surfactant under nitrogen at 50 °C for 4 hours with stirring. Samples were cooled back to RT upon dissolution and stored in a vacuum desiccator. The water content of individual samples was verified by Karl Fischer titration before use.

2.1.7 Magnetic ILs

Paramagnetic salts, $Mn(NO_3)_2 \cdot 4H_2O$ and $Fe(NO_3)_3 \cdot 9H_2O$, were mixed with triglyme (G_3), tetraglyme (G_4), EtAN (>99.8% synthesized), and PAN (>99.8% synthesized), respectively at a 1:1 molar ratio. Mixtures were stirred and heated gently at 50 °C to accelerate the dissolution of inorganic salts, then cooled back to RT and equilibrated overnight to ensure thermal stability without precipitation of crystals before measurements.

2.2 Miscibility and Phase Behaviour

2.2.1 Two-component Systems

Samples were prepared by mass in 2 mL glass vials at 5 wt% intervals. Miscibility/solubility was determined after 30 minutes equilibration and confirmed after one week. Immiscible/insoluble samples were identified when observing phase separation, or optical turbidity when mechanically agitated.

2.2.2 Three-component Systems

Starting from a single-phase region, two-component samples were prepared by mass in 2mL glass vials at approximately 10 wt% intervals. Phase boundaries were determined by titration of a third component into the solution at 2 wt% intervals until cloudiness appeared. Samples were mixed by mechanical agitation on a Vortex mixer for three minutes, bath sonication for 30s, followed by equilibration for 10min-24hrs. Alternatively, ternary mixtures within the two-phase region were prepared, mixed and left to equilibrate and separate into two liquid layers for 72 hours. The composition of each layer was analysed by 1H -NMR 300MHz integration. All measurements were done at 25°C.

The phase behaviour for ternary mixtures is most easily represented at a single temperature by ternary phase diagrams such as in Figure 2.2. In ternary phase diagrams, each corner of the triangle

represents a pure component, the edges represent two-component (binary) mixtures and the body of the triangle represents three component mixtures.

In the water-PAN-octanol ternary system, PAN is miscible with both water and n-octanol in all compositions, whereas water and n-octanol are almost completely immiscible. The area bounded by the blue curve represents the two-phase region. In other words, if the three components are mixed in these proportions, they will separate into two immiscible phases with one phase rich in n-octanol and the other rich in water. The composition of any point is read by drawing three lines parallel (not perpendicular) to the three edges of the triangle and reading off the amount for each component. For example, the sample shown in Figure 2.2A contains 50wt% water, 20wt% PAN and 30wt% octanol.

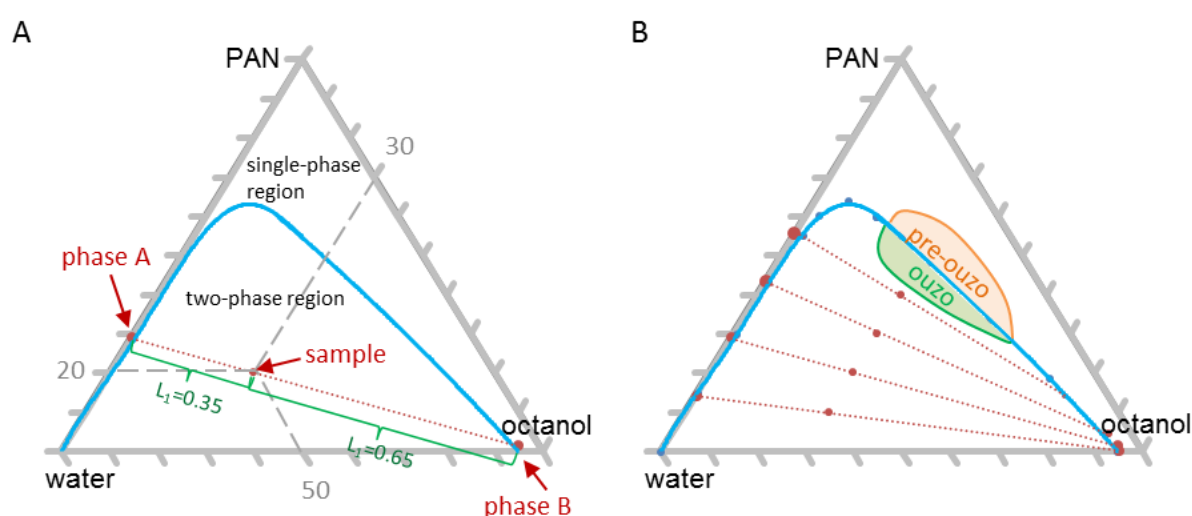


Figure 2.2 Ternary phase diagrams (wt%) of the water–PAN–octanol system at 298K (for details see Chapter 4). A) a schematic diagram for determining sample compositions, tie-lines, and phase boundaries by NMR. B) ouzo and pre-ouzo regions relative to the direction of tie-lines. Red dots represent data from NMR; Blue dots represent data from titration. Experimental errors are represented by the radius of data points. The green area is the ouzo region, and the orange area is the pre-ouzo region.

The red dotted lines in the two-phase region are tie-lines, which give both the composition and the quantity of each of the two phases for compositions anywhere along the line. Tie-lines were determined by $^1\text{H-NMR}$ analysis of separated layer compositions at equilibrium. The quantity of each phase is determined by the lever rule, which gives the amount of phase A as the fractional length of the tie-line to phase B. In Figure 2.2A, the sample is 0.35 unit (L_1) away from sample A, and 0.65 unit (L_2) away from sample B (i.e. this sample is made 35% along the tie-line from phase A). Therefore, it contains $(100\% - 35\% = 65\%)$ phase A and 35% of phase B.

A critical point is a composition at which two liquid phases have the same density and refractive indices. In ternary phase diagrams, trends in tie-lines lead to the critical point, where volumes and compositions of two phases become equal (i.e. the length of the tie-lines approaches zero). An ‘ouzo’ region (shown in green in Figure 2.2B) is a two-phase region near the critical point.¹¹⁸

With a slight excess of the amphiphilic component (PAN in this system), a single-phase region is formed, designated the 'pre-ouzo' region (shown in orange). Within this region, the scattering grows corresponding to the growth of the liquid nanostructure, which is distinct from a critical density fluctuation.¹¹⁹ Ternary solutions in the pre-ouzo region are excellent solubilisers.¹²⁰

2.3 Polarising Microscopy

Polarised light microscopy analyses the molecular order in heterogeneous systems, using basic optical properties such as refraction and absorption.¹²¹ Birefringence is anisotropy of the refractive index, whereas dichroism is anisotropy of the absorption coefficient. These two optical anisotropic properties are consequences of long-range molecular order that is within the visible spectrum of 390-700 nm, such as that found in liquid crystals.¹²²

The light from the microscope bulb passes through a polarising film that transmits light with a specific polarisation parallel to the direction of the filter. The light then passes through the sample and into a second polarising film which is perpendicular to the first, i.e. crossed polarisers. If there has been no change to the light between the first and second films, no light will pass through, as shown in Figure 2.3a.¹²³

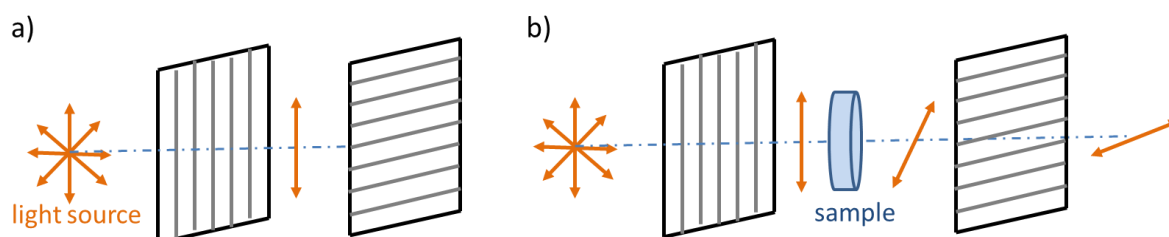


Figure 2.3 a) A polarising film orients the light (direction of oscillation is indicated by arrows). A second polarising film rotated 90° prevents any light from passing through. b) An anisotropic (or birefringent) sample rotates the plane of polarisation so that light can pass through the second polarising film and can be observed.

Polarising optical microscopy is a useful tool for identifying phases formed by surfactants. There are two broad categories of phases formed by surfactants: isotropic and anisotropic, based on their refraction of light. Isotropic phases are structurally the same in three orthogonal directions (e.g. a cubic phase) and will not affect the plane of polarisation of light passed through it. Therefore, if an isotropic phase is placed between two crossed polarisers it will appear dark.

On the other hand, anisotropic phases cause double refraction, splitting light into different axes (where the speed of light is different) and will rotate the plane of polarisation, as shown in Figure 2.3b. Therefore, when an anisotropic phase (e.g. a hexagonal phase) is placed between crossed polarisers it will appear bright and birefringent.

Distinguishing between anisotropic phases is based on observing characteristic ‘textures’ of birefringence through a microscope. The correlation of particular phases with particular textures has been well established.¹²⁴ Figure 2.4 gives example textures of a hexagonal and lamellar phases respectively.

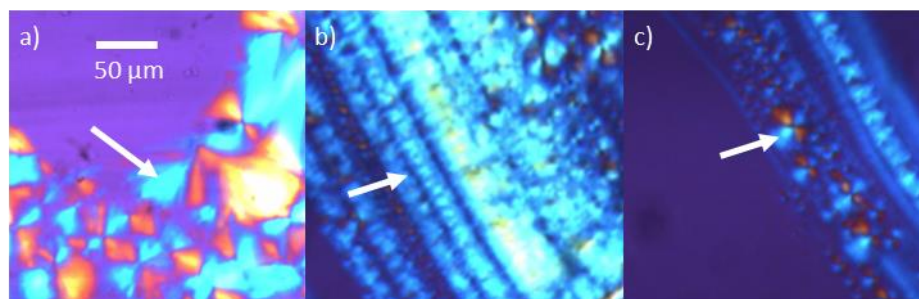


Figure 2.4 Polarising optical micrographs show a) a hexagonal phase with a fan-like texture in a $C_{10}E_4$ - $LiNO_3$ -water mixture. b) a swollen lamellar phase with a myelinic texture in a $C_{10}E_3$ - $LiNO_3$ -water mixture, and c) a lamellar phase with Maltese crosses, which is a characteristic of vesicle formation, in a $C_{10}E_3$ - $LiNO_3$ -water mixture.

The identification of Maltese crosses and myelinic figures (Figure 2.4b-c) are especially of interest to this investigation. Maltese crosses are textures characteristic of multilamellar vesicles, due to their radially smectic structure, and were used in this project to demonstrate vesicle formation. Myelinic figures are indicative of a swollen lamellar phase.¹²⁵⁻¹²⁶

2.4 Magnetic Susceptibility

Magnetic susceptibility (χ) measures the magnetic properties of a material, and it is determined from $M = \chi H$, where M is the magnetic moment measured by a magnetometer and H is the applied magnetic field.¹²⁷ Information on whether a material is attracted to or repelled out of a magnetic field has implications for the material structure and practical applications. A paramagnetic substance has a greater-than-zero magnetic susceptibility, meaning it is attracted by a magnetic field. A diamagnetic material has a less-than-zero magnetic susceptibility, meaning it is repelled by a magnetic field. Neither paramagnetic nor diamagnetic materials retain the magnetic properties when the external field is removed. In contrast, ferromagnetic materials with large positive susceptibility retain their magnetic properties after the removal of the external field.

Magnetic ionic liquid samples with a known mass were loaded into a polypropylene (Formolene® 4100N) sample holder that snaps into a brass half-tube for measurement. To prevent sample loss, parafilm was wound around the join of the two halves of the polypropylene sample holder. Magnetic susceptibility data were collected on a Quantum Design VersaLab magnetometer, measured at 298K in the magnetic field ranging between -30,000 and +30,000 Oe.

2.5 Scattering Experiments

Small-angle scattering (SAS) is a technique based on the scattering of incident radiation after interacting with the material (Figure 2.5). In most cases, the scattering angle is small ($0.1\text{-}10^\circ$). SAS experiments are powerful in providing structural information, by measuring the scattering intensity as a function of scattering vector, q , given by:

$$q = \frac{4\pi}{\lambda} \sin \frac{\theta}{2} \quad [1]$$

Where λ is the wavelength of the incident radiation, and θ is the angle at which the beam is scattered. Bragg's equation defines:

$$q = \frac{2\pi}{d} \quad [2]$$

where the scattering vector q is inversely proportional to the distance between the scattering planes.

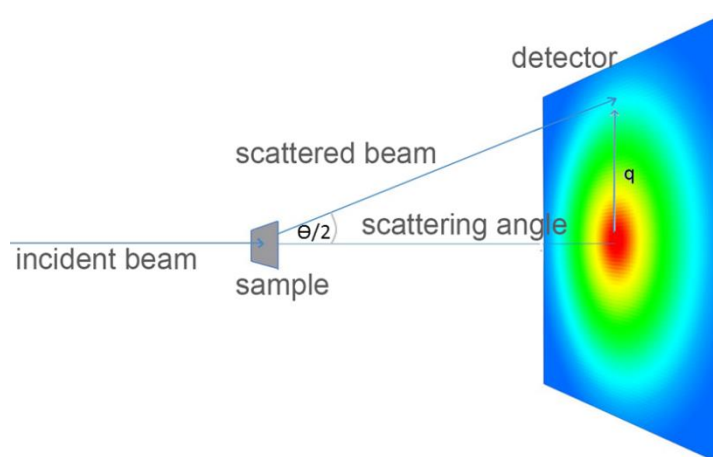


Figure 2.5 A schematic diagram of the process of scattering experiments. A 2D detector measures the number of particles (either X-ray or neutron) at different values of the scattering vector, q .

A structural periodicity will cause a constructive interference, leading to an increase in the scattering intensity at an angle related to the repeating distance. Ideal crystalline substances are characterised by well-defined Bragg peaks in scattering profiles. In comparison, this project mainly investigates liquid samples that do not possess strong ordering. As a result, the intensity varies with the scattering angle, forming relatively broad peaks.

2.5.1 Small and Wide-Angle X-ray Scattering

The X-ray scattering profile depends on the variation in electron density between different atoms of the sample. In this project, small and wide-angle X-ray scattering (SAXS) is used as a primary

screening technique to identify structural changes as a function of composition. The scattering vector q ranges from 3 \AA^{-1} to 0.03 \AA^{-1} , which corresponds to approximately 2 \AA to 200 \AA in real space.

SAXS was performed on an Anton Paar SAXSess instrument with a point source ($\text{CuK}\alpha$, 1.541 \AA). A single image plate was used and radially averaged with normalisation to a direct beam intensity of 1. Empty cell scattering was subtracted, and all patterns were calibrated to water. Before SAXS/WAXS experiments, sample purity was confirmed to be $> 99\%$ by $^1\text{H-NMR}$ 300MHz. All measurements were conducted at $25 \text{ }^\circ\text{C}$ with 1mm quartz capillaries for five minutes per sample.

2.5.2 Small Angle Neutron Scattering

2.5.2.1 Introduction

In contrast to X-ray scattering, where radiation interacts with electrons, neutrons interact with nuclei of atoms. Therefore, they can distinguish between different isotopes, most notably hydrogen and deuterium. This allows the study of complex multiphase systems by isotopic substitution. In this project, small angle neutron scattering (SANS) experiments are designed with a q range from 0.7 \AA^{-1} to 0.01 \AA^{-1} , corresponding to 9 \AA to 600 \AA in real space.

For neutrons, the scattering length density (SLD), is defined as:

$$SLD = \frac{\sum_{i=1}^n b_i}{v_m} \quad [3]$$

$$\text{and } v_m = \frac{N_A \cdot \rho}{M_w} \quad [4]$$

where b_i is the bound coherent scattering length of the atom_{*i*} in a molecule: and v_m is the molecular volume, which is calculated based on density ρ , molecular weight M_w , and the Avogadro constant N_A .

To further derive the SLD of the individual functional group, we refer to Edward's Equation:¹²⁸

$$V_M = 16.63n + 32.57 \quad [5]$$

where V_M (mL/mol) is the molar volume for an alkyl tail, and n is the number of methylene units and the constant (32.57) accounts for the volume of the terminal methyl group.

Edward's equation approximates the volume of a hydrocarbon tail in liquid mixtures. Assuming there is no volume change during mixing, the partial volume of the individual functional group is calculated accordingly. Note that results from Edward's equation are comparable to Gruen's

volume of chains in amphiphilic aggregates, with negligible differences (<1%) at RT.¹²⁹ The densities of hydrogenous compounds were experimentally measured by a densitometer.

SLDs for all components used in this study are shown in Table 2.2. Values were calculated using the National Institute of Standards and Technology (NIST) SLD calculator.

Table 2.2 SLD values from NIST SLD calculator¹³⁰ for all components used in this study. These values are used for subsequent invariant analysis.

Component	Chemical Formula	Density (g/cm ³)	SLD (10 ⁻⁶ Å ⁻²)
Water	H ₂ O	1.00	-0.56
heavy water	D ₂ O	1.11	6.36
Ethanol	C ₂ H ₆ O	0.79	-0.35
D6-ethanol	C ₂ D ₆ O	0.89	6.10
ethanol head	OH	1.85	1.35
D1-ethanol head	OD	1.96	8.18
ethanol tail	C ₂ H ₅	0.59	-0.66
D5-ethanol tail	C ₂ D ₅	0.69	5.71
EtAN	C ₂ H ₈ N ₂ O ₄	1.38	1.70
D4-EtAN	C ₂ H ₄ D ₄ N ₂ O ₄	1.42	4.48
EtAN charged	NH ₃ NO ₃	1.67	3.16
D3-EtAN charged	ND ₃ NO ₃	1.73	7.12
EtAN tail	C ₂ H ₅ O	1.05	0.06
D1-EtAN tail	C ₂ H ₄ OD	1.09	1.53
PAN	C ₃ H ₁₀ N ₂ O ₃	1.16	1.01
D3-PAN	C ₃ H ₇ D ₃ N ₂ O ₃	1.19	2.86
PAN charged	NH ₃ NO ₃	2.00	3.80
D3-PAN charged	ND ₃ NO ₃	2.08	8.57
PAN tail	C ₃ H ₇	0.66	-0.57
Octanol	C ₈ H ₁₈ O	0.82	-0.32
D1-octanol	C ₈ H ₁₇ OD	0.83	0.08
D17-octanol	C ₈ D ₁₇ OH	0.93	6.43
octanol head	OH	1.86	1.36
D1-octanol head	OD	1.99	8.30
octanol tail	C ₈ H ₁₇	0.76	-0.42
D17-octanol tail	C ₈ D ₁₇	0.87	6.73
octane	C ₈ H ₁₈	0.70	-0.52
D18-octane	C ₈ D ₁₈	0.81	6.42
toluene	C ₇ H ₈	0.87	1.03
D8-toluene	C ₇ D ₈	0.95	5.68
cyclohexane	C ₆ H ₁₂	0.78	-0.28
D12-cyclohexane	C ₆ D ₁₂	0.89	6.69

2.5.2.2 Experimental Procedures

SANS was performed at the QUOKKA beamline¹³¹ at Bragg Institute (ANSTO, Australia) using 1mm path-length cylindrical Hellma Cells. A neutron wavelength of 5 Å was used with sample-to-detector distances of 1.3m and 8m, to provide a q range of 0.01 to 0.7 Å⁻¹. Raw SANS data were reduced to 1D in IGOR Pro with reduction procedure provided by NIST modified for uses on QUOKKA.¹³²

2.5.2.3 Invariant Analysis

In the system with clear interface between particles and surrounding solvent, Porod's law states the scattering intensity becomes proportional to q^{-4} , as q tending to infinity.¹³³

Porod's law defines:

$$I(q) \approx \frac{2\pi}{q^4} \rho^2 S, \quad (q \rightarrow \infty) \quad [6]$$

where S is the particle surface; q is the scattering vector, and ρ is the scattering length density of the system.

Porod's invariant is an important overall value computed from the scattering experiment. The invariant depends only on the particle volume, not on its form.¹³⁴ The experimental invariant Q^*_{exp} is defined as:

$$Q^*_{\text{exp}} = \int_0^{\infty} I(q) q^2 dq \quad [7]$$

where $I(q)$ is the scattering intensity after background subtraction, and q is the scattering vector.

The scattering background is calculated based on Porod's Law of $I(q)q^4 \propto q$. The integration range is approximated by plotting $I(q)q^2$ against q .

For an incompressible, two-domain system, the theoretical invariant Q^*_{theory} is defined as:

$$Q^*_{\text{theory}} = 2\pi^2 \Delta\rho^2 \varphi(1-\varphi) \quad [8]$$

where φ is the volume fraction of domain_A, $(1-\varphi)$ is the volume fraction of domain_B, and $\Delta\rho$ is the contrast difference calculated based on the total SLD of domain_A (ρ_A) and domain_B (ρ_B):

$$\Delta\rho = |\rho_A - \rho_B| \quad [9]$$

This assumes each domain is homogeneous, and the domain SLD is calculated based on individual SLDs and corresponding volume fractions of its components. However, if one of the two domains is not homogeneous and contains aggregates of a specific species, the theoretical invariant calculated based on Equations [8] and [9] may not match with the experimental invariant. In this case, we consider a three-domain system¹³⁵:

$$Q^*_{\text{theory}} = 2\pi^2 \times (\varphi_A(\rho_A - \bar{\rho})^2 + \varphi_B(\rho_B - \bar{\rho})^2 + \varphi_C(\rho_C - \bar{\rho})^2) \quad [10]$$

where A, B, and C represent three types of domains within the sample, and $\bar{\rho}$ is the average SLD of the sample, calculated by:

$$\bar{\rho} = \varphi_A \rho_A + \varphi_B \rho_B + \varphi_C \rho_C \quad [11]$$

In Chapter 4, our invariant analysis starts from a two-domain model (based on Eq 8 and 9) to fit all contrasts simultaneously. By minimising the percentage difference between theoretical and experimental invariant, this model outputs a distribution of each component across the domains. In the case of which the two-domain model does not fit well to the experimental invariant, a three-domain model (based on Eq 10 and 11) is setup for further fitting.

2.5.3 Neutron Diffraction

2.5.3.1 Introduction

The neutron diffraction instrument at Rutherford Appleton Laboratory (UK) is a time-of-flight diffractometer designed for investigating liquids and amorphous materials. It measures the static structure factor, $S(q)$, over a wide-angle range ($50 - 0.2 \text{ \AA}^{-1}$). This generates a high-resolution picture of atomic correlations as well as medium-range periodicities.

The analysis of SANS is based on SLD, as defined previously in Eq 3–5. In contrast, neutron diffraction detects scattering by individual atoms, without referring to a molecular or regional volume. In neutron diffraction experiments, the scattered radiation amplitude, $A(q)$, from an array of N point atoms at positions R_1 to R_N is given by:

$$A(q) = \sum_j b_j \exp(iq \cdot R_j) \quad [12]$$

where b_j is the scattering length of atom $_j$, and q is the scattering vector defined in Eq 1.

The structure factor, $S(q)$, is the scattered intensity per unit atom, defined as:

$$S(q) = \frac{1}{N} |A(q)|^2$$

$$S(q) = \frac{1}{N} \sum_{\alpha\beta} b_\alpha b_\beta \exp[iq \cdot (R_\alpha - R_\beta)] \quad [13]$$

Experimentally, atomic correlations of complex liquids are difficult to unravel. This is because diffraction measurement is an average of all the partial structure factors that characterise the sample.¹³⁶ In this project, we systematically deuterate different functional groups to highlight specific interactions. As neutron scattering amplitude is dependent on the isotope, this enables the extraction of partial structure factors from diffraction data.

2.5.3.2 Experimental Procedures

Sample containers are made of $\text{Ti}_{0.68}\text{Zr}_{0.32}$ alloy, which is both chemically inert and null scattering. These flat plate cans have dimensions of $35 \times 35\text{mm}^2$, 1mm path length, and 1mm wall thicknesses, with a known atom density, $0.0541 \text{ atoms}/\text{\AA}^3$.

Diffraction experiments were conducted at 298K under vacuum on instrument SANDALS.¹³⁷ The sample chamber was left to equilibrate for 10 minutes before measurements, and the temperature was maintained by a Julabo FP50 temperature controller. Before loading, diffraction measurements were made on the empty containers, empty instrument and a vanadium standard sample for data correction and normalisation. The sample was weighed before and after measurements to ensure no evaporation had occurred. The net run time for each system was eight hours.

2.5.3.3 Data Reduction

Neutron diffraction data are treated by GUDRUN,¹³⁸ a program for correcting raw neutron total scattering data to differential cross section. GUDRUN performs the following corrections: 1) normalisation to the incident flux; 2) absorption and multiple scattering corrections; 3) Ti-Zr can subtraction; 4) normalisation to absolute units with a vanadium reference; 5) correction of single atom scattering and inelastic scattering by hydrogen.

2.5.4 Empirical Potential Structural Refinement

2.5.4.1 Introduction

Empirical potential structural refinement (EPSR) is a technique that communicates computer simulation with experimental measurements. It is a 3D modelling method designed for molecular liquids and disordered systems.¹³⁹⁻¹⁴² Previously, Reverse Monte Carlo (RMC) has been used to generate the structure of both disordered and crystalline materials combined with diffraction data.¹⁴³⁻¹⁴⁴ Although EPSR and RMC are analogous methods, the reference potential in RMC is limited to a hard-core repulsive term,¹⁴⁵ whereas in EPSR, the reference potential serves to incorporate and test assumptions about how the atoms may be interacting.¹⁴¹ The empirical potential represents the perturbation to the reference potential needed to obtain a fit to the data, and it is accumulated over many iterations via fitting coefficients.¹⁴⁶ EPSR yields a best description of the experimentally-determined scattering patterns, hence the structure and the geometry, without giving explicit information about bond energies. The algorithm to run EPSR is shown in Figure 2.6, and can be summarized in seven steps, as described below.

(1) Like most conventional simulation techniques, we first need to input known properties of the sample, including structure, density, composition, and a reference potential, $U_{\alpha\beta}^0(r)$, into the simulation box (Figure 2.6). With all input references, EPSR iterates a direct Monte Carlo simulation of a molecular system. This means, whether the simulation accepts the movement of molecules or not depends on how it changes the total potential energy of the box. The movement is rejected, unless the total potential energy U decreases, or if the following is true:

$$\exp\left(\frac{-\Delta U}{k_B T}\right) > \text{random number } (0 - 1) \quad [14]$$

The simulation runs until it reaches the thermodynamic equilibrium with minimum potential energy U .

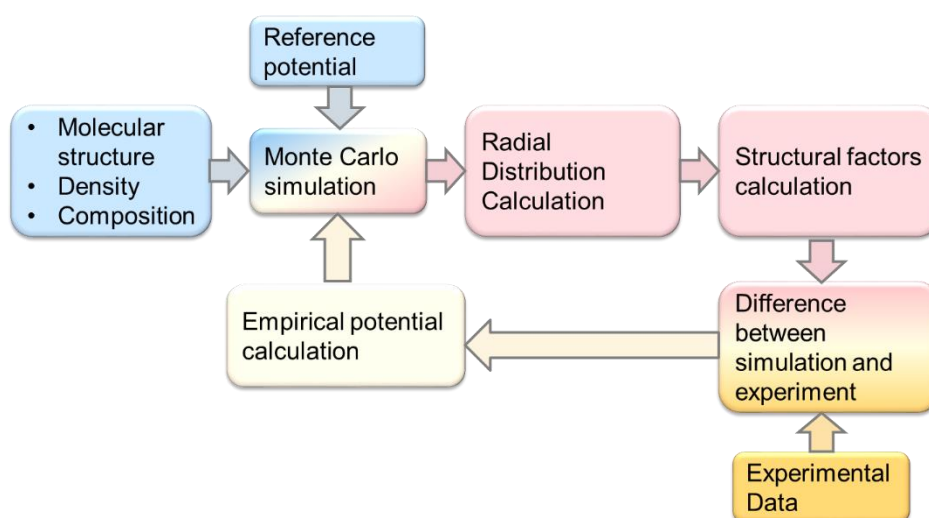


Figure 2.6 A schematic diagram of empirical potential structural refinement (EPSR): blue, initial references; red, EPSR calculations; orange, experimental input.

(2) A set of simulated partial structure factors, $S_{\alpha\beta}^s(q)$, was generated.

(3) Based on neutron diffraction experiment, total structure factors derived from data, $S^D(q)$, can be further derived into partial structure factors $S_{\alpha\beta}^D(q)$ and partial pair correlation functions $g_{\alpha\beta}(r)$:

$$S^D(q) = \sum_{\alpha\beta} (2 - \delta_{\alpha\beta}) c_{\alpha} c_{\beta} b_{\alpha} b_{\beta} S_{\alpha\beta}^D(q) \quad [15]$$

$$S_{\alpha\beta}^D(q) - 1 = 4\pi\rho \int_0^{\infty} r^2 [g_{\alpha\beta}(r) - 1] \frac{\sin(qr)}{qr} dr \quad [16]$$

where c is the atomic concentration, b is the scattering length, ρ is the atomic density.¹⁴¹

From these experimental measurements, the atom-atom pair potential of mean force, $U_{\alpha\beta}(r)$, could be generated based on:

$$U_{\alpha\beta}(r) = -k_B T \ln(g_{\alpha\beta}(r)) \quad [17]$$

$U_{\alpha\beta}(r)$ are experimental pairwise potentials that contain information arising from many-body cooperative effects, such as the packing of molecules in the material. With a reasonable “first guess” potential from the simulation, $U_{\alpha\beta}(r)$ were used to indicate where the simulation need to be modified to improve agreement with a measured set of $g_{\alpha\beta}(r)$. Further, these empirical potentials can be expanded into a series of Poisson functions:

$$U(r) = k_B T \sum_k C_k p_{n_k}(r, \sigma_r) \quad [18]$$

where C_k are real and can be positive or negative, and σ_r is a width function.

With a 3-D Fourier transformation to q -space, $U(r)$ can be correlated to the diffraction data as a function of q :

$$U(q) = \sum_k C_k p_{n_k}(q, \sigma_q) \quad [19]$$

In this case, C_k can be estimated from the diffraction data by fitting a series of $U(q)$ functions.

(4) The Empirical Potential Structure Refinement (EPSR) process compares the experimental atom-atom structure factors, $S_{\alpha\beta}^D(q)$, with the simulated atom-atom structure factors $S_{\alpha\beta}^S(q)$, and derive a difference function:

$$\Delta(q) = \sum_k C_k p_{n_k}(q, \sigma_q) \quad [20]$$

The fit to an experimental data set, $F_i(q)$, is a weighted sum over pairs of atoms of the relevant simulated structure factors:

$$F_i(q) = \sum_{j=1,N} w_{ij} S_j(q) \quad [21]$$

where i is the data set, j is the $\alpha\beta$ pair. The task is to invert the matrix of w_{ij} and refine the empirical potential that is driving the simulation of the experimental data.¹⁴¹

(5) EPSR continues to run the simulation using this new potential to equilibrium.

(6) EPSR refines the simulation by repeating steps (2), (4) and (5) until C_k becomes very small and the empirical potential (U) ceases to change. At the end of the refinement, the simulated partial structural factors agree with the experimental partial structural factors, shown below:

$$S_{\alpha\beta}^S(q) = S_{\alpha\beta}^D(q) \quad [22]$$

(7) EPSR continues to run the converged (or refined) simulation and accumulate ensemble information.

EPSR allows a comparison between the theory and the experiment. It adjusts the potential between molecules accordingly. The idea of this refinement process is to realise missing features in theory, to rationally improve the model, and to agree with the experiment. The degree of adjustment

is manually controlled, preventing unrealistic constraints. The advantage of using EPSR is to visualise complex systems at an atomic level. Its output has excellent reliability, with sufficient theoretical support as well as quantitative agreements with experimental data.

2.5.4.2 The Pair Correlation Function $g(r)$

One important structural characteristic is $g(r)$, known as the pair correlation function, defined as:

$$g(r) = \frac{\rho(r)}{\rho} \quad [23]$$

where $\rho(r)$ is the local density of atoms at a distance r from an atom at the origin: and ρ is the average density of atoms in the whole system.

A more detailed expression is the partial pair correlation function, $g_{ij}(r)$. This gives information on the probability to find an atom j in a shell dr at the distance r of a reference atom i (Figure 2.7A). Because $g_{ij}(r)$ is a normalised function, results are relative to the probability of finding such correlation on average. When comparing two different systems, a peak with higher intensity does not necessarily mean a higher coordination number. Instead, it suggests a stronger correlation compared to the bulk.

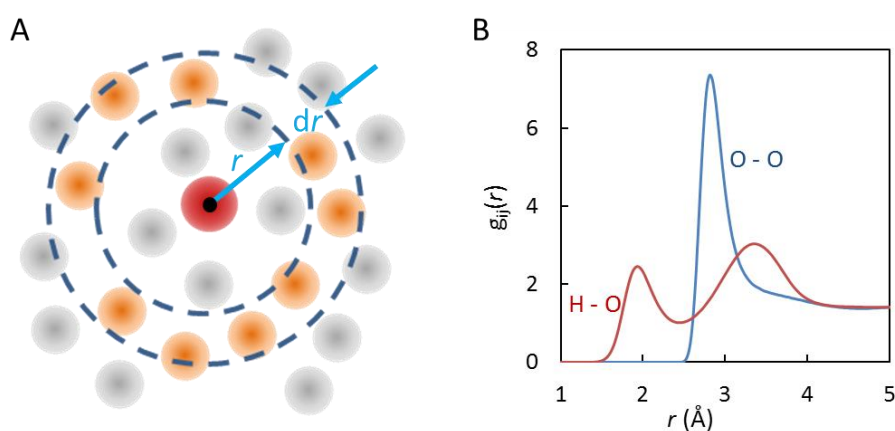


Figure 2.7 A) a schematic diagram of $g(r)$, the radial distribution function. The red centre represents the reference atom i , and the surrounding atoms represent atom type j . B) examples of $g_{ij}(r)$ functions of oxygen-oxygen and hydrogen-oxygen correlations in the water-PAN-octanol system.

Figure 2.7B show examples of pair correlations between water molecules in one of our ternary mixtures. There are peaks in the hydrogen-oxygen correlation, indicating two separate ranges of correlation distances. In comparison, the oxygen-oxygen correlation has one peak, indicating a single-range correlation distance. The hydrogen-oxygen correlation peak at shorter distances (1.5 – 2.4 Å) falls into the hydrogen bonding range. This gives us information on hydrogen bonding distances between water molecules in our mixture.

2.5.4.3 Coordination Numbers

Based on $g(r)$ functions, it is possible to calculate the number of atoms that coordinate a given atom at the origin. This is called the coordination number, $N(r_{\min}, r_{\max})$, and is defined relative to a given distance range, r_{\min} to r_{\max} , after integrating over all the directions of r :

$$N(r_{\min}, r_{\max}) = 4\pi\rho \int_{r_{\min}}^{r_{\max}} r^2 g(r) dr \quad [24]$$

Coordination numbers in a multicomponent system are defined in an exactly analogous manner:

$$N_{\alpha\beta}(r_{\min}, r_{\max}) = 4\pi\rho_{\beta} \int_{r_{\min}}^{r_{\max}} r^2 g_{\alpha\beta}(r) dr \quad [25]$$

where $N_{\alpha\beta}$ is the number of β -type atoms around an α -type atom at the origin.

In general, $N_{\alpha\beta}(r_1, r_2) \neq N_{\beta\alpha}(r_1, r_2)$ for different density coefficients. Moreover, coordination numbers are sensitive to sample composition as well as correlation strength. Within the same system, a comparison of coordination numbers distinguishes between dominant and negligible pair correlations.

2.5.4.4 Tri-molecular angular distribution

The triangles function in EPSR calculates the distribution of angles for triplets of atoms, which satisfy the defined distance constraints. In our project, this function is particularly useful for calculating H-bonding distances. Using the correlation among water molecules as an example, the H-O \cdots H bond angle distribution would be of interest. This gives information on the probability of finding a given H-O \cdots H bond angle, and if most are bent, linear, or both. Hydrogen bonding distances are defined based on the observed peak positions in $g(r)$ functions.

2.5.4.5 The Spatial Density Function

The spatial density function (SDF)¹⁴⁷ describes the spatial arrangement of species relative to one another. The atom type at the origin needs to be sufficiently well defined with a set of coordinate axes, typically as part of a molecule with at least three atoms. The species at the origin of the coordinate system is at a particular orientation, given by the Euler angles $\omega_1 = (\varphi_1, \theta_1, \chi_1)$ ¹⁴⁸, shown in Figure 2.8A. To understand how the second species at orientation $\omega_2 = (\varphi_2, \theta_2, \chi_2)$ is distributed relative to the first species, SDF gives information on how the other species is situated around the centre (i.e. the density of the second species as a function of r , for a given reference).

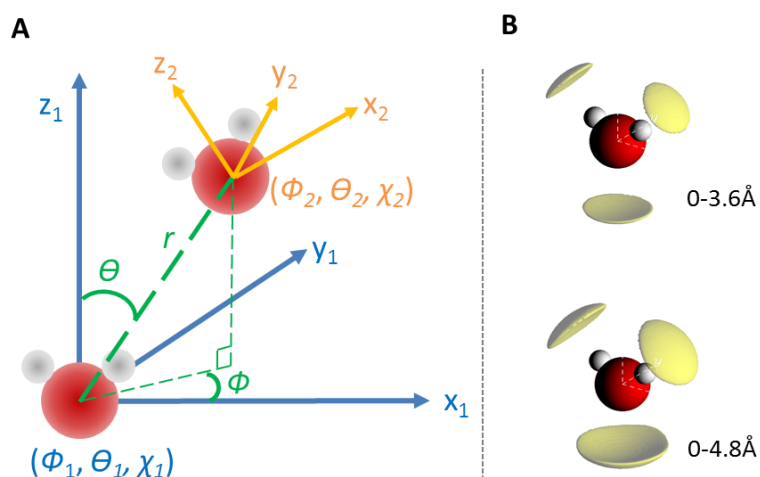


Figure 2.8 Geometric distribution of water molecules around a reference water molecule. A) A schematic diagram of the spatial coordinates of species₂ (top) around species₁ (bottom). B) 3D density plots based on spatial coordinates of water molecules. Lobes represent are 20% probability surfaces, which represent the most likely geometric distribution of water oxygen atoms around a reference water molecule.

Using the correlation between water oxygens as an example, Figure 2.8B shows SDF plots over two ranges of distances, in which yellow lobes represent the most probable locations of finding another oxygen atom around a reference water molecule. In this case, oxygen atoms either go next to the hydrogens or go to the bottom of the oxygen. Increasing the correlation distance from 3.6 Å to 4.8 Å shows no significant change in geometric distribution.

2.5.4.6 Cluster Analysis

Cluster analysis calculates the size of clusters (or semi-continuous networks) of molecules, with given information on one or specific sites on the molecule and intermolecular distance criteria. Using water as an example, one could examine the distribution of cluster size by defining the distance between two oxygen atoms.

Figure 2.9 shows water-glycerol mixtures at different concentrations, the size distribution of water clusters and glycerol clusters.¹⁴⁹ Simulation snapshots, shown in Figure 2.9A, helps to visualise the distribution of glycerol (in grey) and water (in red) respectively, where X_g represents the fraction of glycerol. Figure 2.9B shows that percolating water clusters appear (shown by red data points to the right of the blue percolation threshold) in all concentrations apart from $X_g = 0.80$. Similarly, percolating glycerol clusters are found at all concentrations of $X_g \geq 0.25$ (shown by black data points to the right of the blue percolation threshold). Therefore, there is a bi-percolating mixture at $0.25 < X_g < 0.50$ (both red and black data points to the right of the blue line).

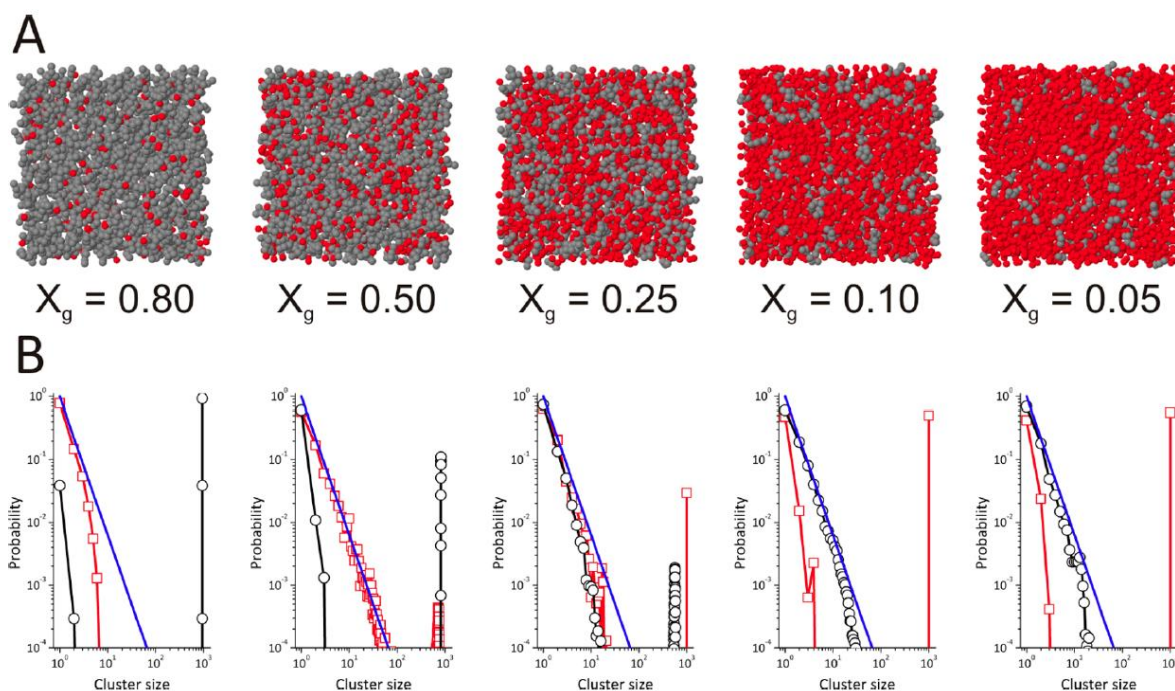


Figure 2.9 Cluster analysis of water-glycerol mixtures, taken from reference¹⁴⁹ with permission. Copyright 2018 American Chemical Society. A) Experimentally refined simulation snapshots show only glycerol-carbon (grey) and water-oxygen atoms (red) at different concentrations (where X_g is the fraction of glycerol). B) Cluster size distributions for water (red) and glycerol (black), compared to the 3D percolation threshold (blue).

2.5.5 Further analysis (DLPUTILS)

DLPUTILS is a collection of utilities for calculations and manipulation from Molecular Dynamic trajectories with codes in DL_POLY format.¹⁵⁰ DLPUTILS utilities have special capacities that are complementary to current routines available within EPSR. With the format conversion of EPSR trajectories (with xyz-style codes), we can use DLPUTILS to analyse hydrogen bonding types and correlations between cyclic and aromatic molecules based on the experimentally refined simulation.

2.5.5.1 H-bonding types and distribution map

Between a hydrogen bond donor species (e.g. an amine) and a hydrogen bond acceptor species (e.g. a carboxylate group), five types of hydrogen bonds discussed in this work are shown in Figure 2.10, including single, bidentate, bifurcated, bridge and multi hydrogen bonds. To calculate the percentage distribution of different hydrogen bonding types, H-bonding distances, donor species (with specific H-donating atomic sites) and acceptor species (with specific H-accepting atomic sites) were defined.

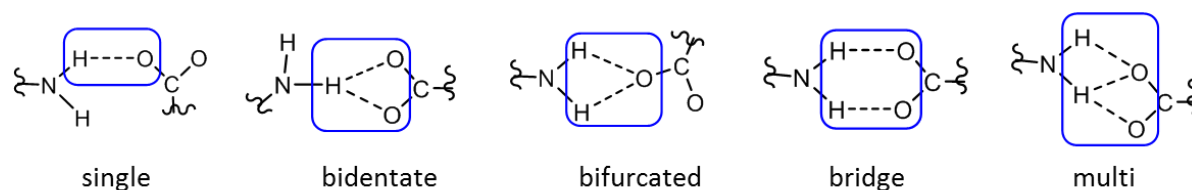


Figure 2.10 Schematics of different hydrogen bonding types

In the context of analysing ionic liquids, depending on the geometry of the ions as well as the donor-acceptor ratio, different types of hydrogen bonds were observed. A 3D distribution map of H-bonding angle and H-bonding distances could be generated. This combines the information of correlation distance functions $g(r)$ with angular functions $g(\theta)$.

2.5.5.2 Ring-ring correlations

Similar to the analysis of hydrogen bonding angles, a distribution map of correlation distance and correlation angle between two species can be applied to cyclic and aromatic species. Using the correlation between two benzene ring as an example, Figure 2.11A shows four common correlations. The angle between the normal to the aromatic plane, θ , is demonstrated in Figure 2.11B. Parallel orientations are defined by $\theta \approx 0^\circ (\pm 10^\circ)$, and perpendicular orientations by $\theta \approx 90^\circ (\pm 10^\circ)$.

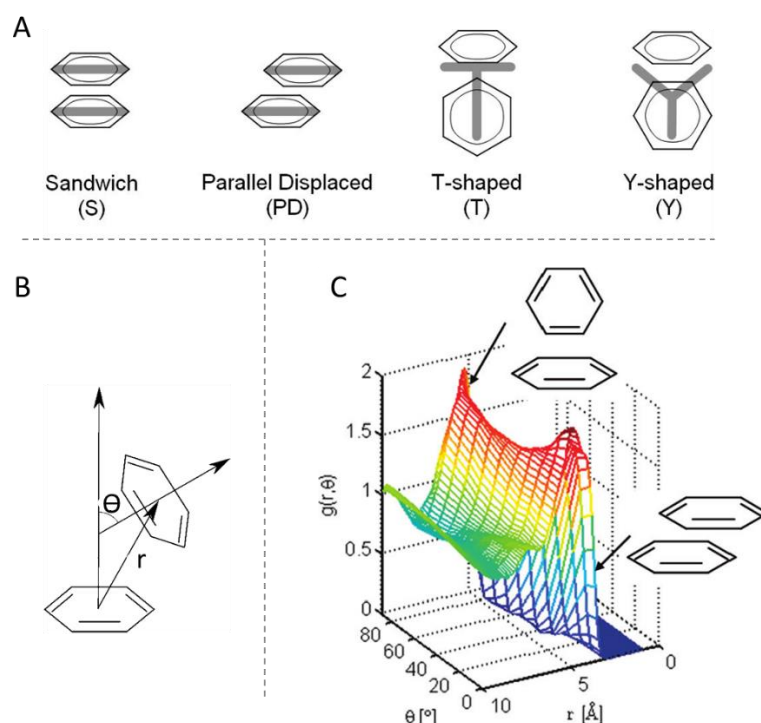


Figure 2.11 Correlations between two aromatic rings, taken from reference¹⁰ with permission. Copy right 2018 American Chemical Society. A) four types of geometric correlations; B) a diagram showing the definition of θ , the minimum angle between the normals to the aromatic planes; C) an angular radial distribution map for toluene, $g(r, \theta)$.

Figure 2.11C shows an angular radial distribution map of toluene molecules based on experimentally refined simulation results.¹⁰ It shows toluene has a very weak preference for parallel arrangements of molecules. The main maximum is at 5.05 Å for $\theta \approx 0^\circ$ (parallel) and 5.25 Å for $\theta \approx 90^\circ$ (perpendicular).

CHAPTER 3 ILS FOR BIOMASS PROCESSING

Biomass processing is one of the key applications of ILs. To optimise the performance of a solvent, it is important to understand the structure of the solvent as well as solvent-solute interactions. In this chapter, we will discuss the unusual liquid nanostructure of four ionic liquids, including pyrrolidinium acetate (PyrrAc), propylammonium nitrate (PAN), cholinium acetate (ChAc), cholinium lysinate (ChLys), with the addition of water and an aromatic solute, guaiacol. Figure 3.0 shows chemical structures of these ILs.

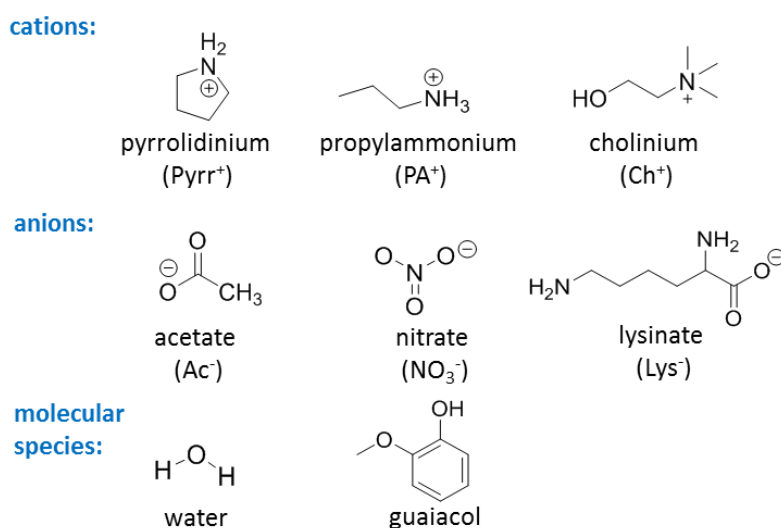


Figure 3.0 Structures of ions and molecular species studied in this chapter.

Starting from PyrrAc, we examine the arrangement of groups in the polar and apolar domains, compare our observations to previously studied alkylammonium, imidazolium and pyridinium ionic liquids, and identify unique structural characteristics of PyrrAc that determines its function as an electrolyte and as a lignin extraction solvent. With the addition of an aromatic solute, we determine key solvent-solute interactions, compare PyrrAc with a poor lignin extraction solvent, PAN, and construct a design framework for aromatic dissolution in protic ionic liquids.

With a structural understanding of primary (PAN) and secondary (PyrrAc) ionic liquids, we study quaternary ionic liquids, including choline acetate (ChAc) and choline lysinate (ChLys). In addition to a geometric comparison among cations, we look at the role of the anion, from inorganic nitrate, to acetate, to complex structures with amino groups. To rationalise how water acts as a co-solvent with these biocompatible ILs, we compare neat ChLys to its water mixture. Further adding

guaiacol as a model lignin residue, we compare an excellent solvent (ChLys) to a good solvent (PyrrAc) for lignin extraction, arriving at recommendations for future solvent design.

3.1 Primary and Secondary Ammonium Ionic Liquids

Pyrrolidinium protic ionic liquids have recently been shown to have outstanding potential as solvents or electrolytes in a range of applications. Pyrrolidinium acetate (PyrrAc) shows particular promise for the extraction of lignin from lignocellulosic biomass when compared to benchmark pyridinium and imidazolium systems.^{114, 151} C₂C₁im acetate has been extensively studied for use in biorefineries with a variety of biomass types,¹⁵²⁻¹⁵³ suggesting PyrrAc would be an economically-attractive alternative. PyrrAc has also shown good potential as an acid-catalyzed reaction environment.¹⁵⁴ Several pyrrolidinium ILs have a wide electrochemical window compared to other protic ILs, making them suitable candidate electrolytes in capacitors, fuel cells, and lithium-ion batteries.¹⁵⁴⁻¹⁵⁶ In the context of this work, Margulis *et al.* have also shown the impact of ionic liquid nanostructure on the transport of both neutral and charged species.^{52, 157-158}

Here we seek to understand how the liquid structure of PyrrAc determines its performance in these diverse applications, and what design features are desirable for other ionic liquids. PyrrAc in many ways is a bridge between N-substituted pyridinium, imidazolium aprotic ILs and primary alkylammonium protic ILs, which retains the high synthetic atom efficiency of protic ILs and good potential for large-scale uptake. Unlike pyrrolidinium nitrate, which is an energetic material,¹¹³ the acetate is a stable and benign anion. As pyrrolidine is a stronger base than alkylamines, pyridine or imidazolium, pyrrolidinium ($pK_a = 11.27$) will be much less deprotonated by acetate than other protic cations.¹⁵⁹⁻¹⁶⁰ Thus, pyrrolidinium acetate is expected to have a high ionicity and therefore have the potential to electrostatically drive polar/apolar segregation between the charge centres and ring carbons.

We determine the liquid structure of PyrrAc at high resolution by neutron diffraction. Results are analysed by empirical potential structure refinement (EPSR), which simultaneously converges a Monte-Carlo simulation to diffraction patterns of multiple, isotopically-substituted (H/D) samples, as discussed in Section 2.5.4. To make a systematic comparison between PyrrAc to previously studied alkylammonium protic ILs, first we investigate how a secondary ammonium differs from primary ammonium cations; As a secondary ammonium cation, pyrrolidinium has a lower capacity to form the dense, extended, three-dimensional, H-bond network that has been implicated in the structure and properties of other protic ILs,¹⁶¹⁻¹⁶³ and amphiphilic nanostructure in general.^{31, 164} Second, we explore how acetate differs from nitrate and formate anions. Lastly, we examine how the saturated

pyrrolidinium ring affects liquid structure compared to both a primary ammonium chain and to an aromatic ring.

Figure 3.1 shows the neutron diffraction data as structure factors, $S(q)$, for PyrrAc isotopomers in the range $0.0 < q < 20.0 \text{ \AA}^{-1}$, as well as atomic notions of PyrrAc used in this section. Varying the H/D isotopic composition creates three neutron contrasts: hydrogenous H-PyrrAc, d_4 -PyrrAc with deuterated acetate and partially deuterated exchangeable amine protons, and d_8 -PyrrAc with a deuterated cation ring. This distinguishes between protons with different hydrogen-bonding capacities. Simultaneous fitting to all contrasts shows good agreement between experimental data (dots) and EPSR calculation (solid lines). The slight disagreement at $q = 2-3 \text{ \AA}^{-1}$ is an artefact, which exists in all three contrasts and did not change during the refinement process. Therefore this did not influence the final analysis. Scattering patterns at all contrasts have high q peaks $> 1.5 \text{ \AA}^{-1}$, corresponding to combinations of inter- or intra-ionic correlations.

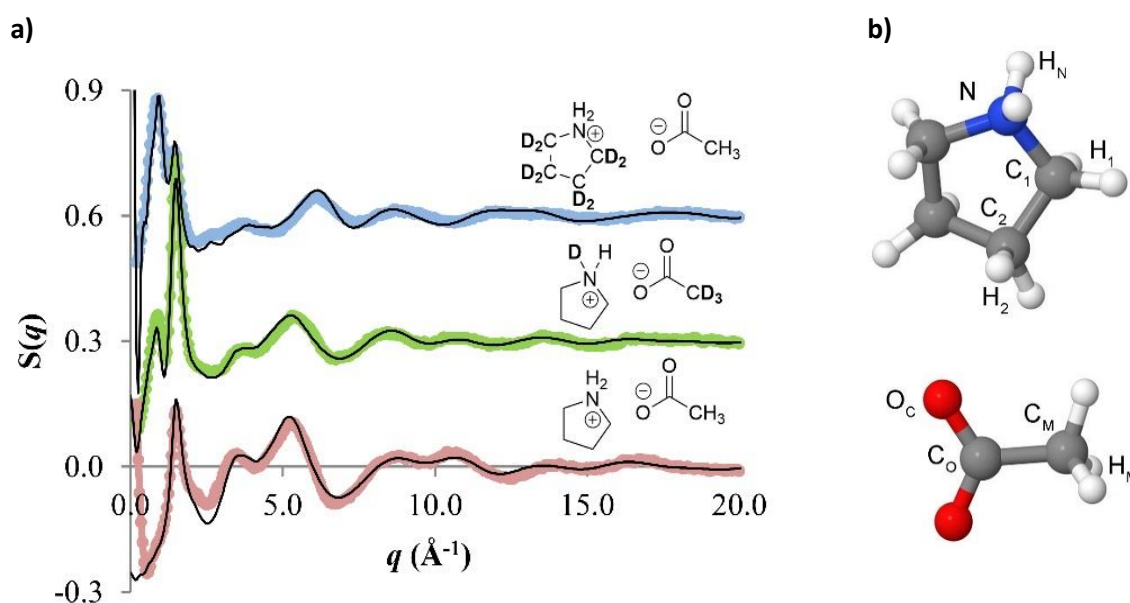


Figure 3.1 a) Neutron diffraction experimental (coloured dots) and EPSR fitted (solid line) structure factors, $S(q)$, as a function of the wave vector, q , for three isotopomers of PyrrAc. b) atomic labels of PyrrAc used in this section.

All three samples exhibit a pronounced Bragg peak at $q = 1.5 \text{ \AA}^{-1}$, corresponding to a nearest-neighbour (cation-anion) spacing of 4.2 \AA ($= 2\pi/q$). The other striking feature in Figure 2 is the presence of a peak at low q , visible in both partially-deuterated samples, d_8 - and d_4 - PyrrAc. For both contrasts, this low- q peak lies at 0.90 \AA^{-1} corresponds to a periodicity of 7.0 \AA , which is a combination of charge alternation and polar-apolar alternation.¹⁶⁵ Further analysis is required to distinguish among these correlations. In the case of an amphiphilic nanostructure, this repeat distance is smaller than the $10.0 - 10.2 \text{ \AA}$ periodic nanostructure seen in ethylammonium (EA^+) protic ILs.^{30, 33}

Figure 3.2 shows representative snapshots of the simulation boxes captured after convergence to the experimental neutron diffraction results, with all atoms in standard atomic colours. Figure 3.2b shows the same snapshot, but with polar and apolar groups highlighted. This allows the visualisation of how polar and apolar groups are distributed through the liquid. Apolar groups occupy a higher volume fraction than polar groups, and clearly form a continuous apolar domain. The distribution and connectivity of polar groups are less clear. Figure 3.2c shows snapshots through the simulation box of the locations of the polar ($>NH_2^+$ and $-CO_2^-$) and non-polar (C_4H_8 and $-CH_3$) groups; The extended connectivity of the non-polar groups is clear, but the polar domains are more isolated by comparison.

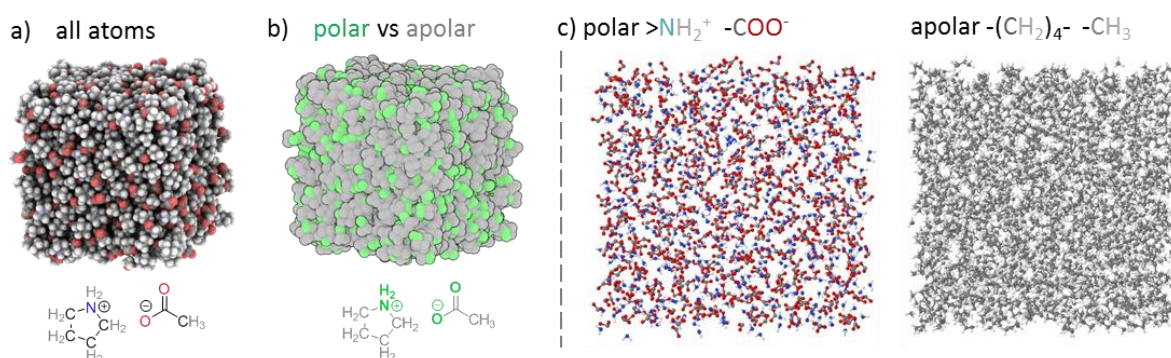


Figure 3.2 a) Representative snapshot of simulation box with 460 ion pairs converged to neutron diffraction patterns, in standard atomic colours; b) Snapshot derived from Figure 3a, with polar groups in green and apolar parts in grey; c) shows separately the polar and non-polar moieties, respectively, of both the cations and anions.

To look at atomic details in the polar region, Figure 4a shows partial pair correlation functions, $g_{ij}(r)$, between the H-bond donor and acceptor (H_N-O_C) and the corresponding charged centres ($N-C_O$) on the cation and anion. $g_{ij}(r)$ describe the radially-averaged distance-dependence of atom-atom correlations, obtained from the converged EPSR simulation. A peak in $g_{ij}(r)$ corresponds to a preferred correlation distance between atoms i and j and is strongest for nearest-neighbour correlations between cation-anion charged groups at short distances. The sharp peak at 2.38 Å in the ammonium H and anion O pair (H_N-O_C) correlation function represents the most probable H-bond distance. Between oppositely charged centres ($N-C_O$) there is also a peak, meaning that there is a strong cation-anion correlation due to Coulombic interactions.

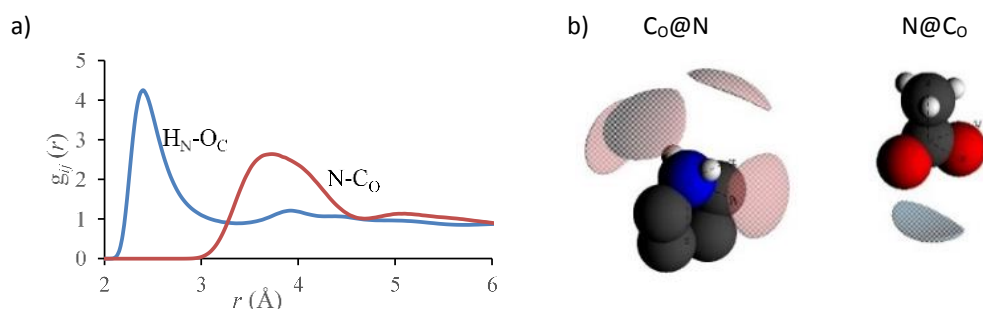


Figure 3.3 a) $g_{ij}(r)$ functions of PyrrAc in the polar region. b) Spatial distribution function (SDF) plots showing 20% probability surfaces for anion carboxyl carbon around cation ammonium, and for cation ammonium around anion carboxyl.

The anisotropy of nearest-neighbour distributions between charged groups is shown in Figure 3.3b in the form of the spatial distribution function (SDF). Lobes represent the most-probable arrangements of nearest-neighbours up to maximum radial distances corresponding to the first minimum in the corresponding $g_{ij}(r)$. Figure 3.3b ($C_O@N$) shows that the centre of the acetate carboxyl group is preferentially found in well-defined orientations around the ammonium group away from the saturated ring. There are two different types of preferred site, and each has two symmetry-equivalent lobes: in one the carboxyl group sits opposite the pyrrolidinium ring, but on either side of the ammonium centre. In the other, the carboxyl sits to the side of ammonium at possible H-bonding sites. The complementary cation@anion ($N@C_O$) distribution, shows a single preferred arrangement for the ammonium group that is highly localized between two acetate oxygens, opposite the acetate methyl. This spatial arrangement of ammonium around the carboxylic group is similar to that seen previously in a formate protic IL, except that probability lobe is smaller here,³⁰ and is similar to the three-lobe structure seen for ammonium charge centres around the more symmetric nitrate anion.³³

Figure 3.4a shows the cation-anion hydrogen bond angle distribution in PyrrAc, compared to primary ammonium protic ILs including ethylammonium formate (EAF), ethylammonium nitrate (EAN) and propylammonium nitrate (PAN).¹⁶² These protic ILs all show a broad distribution of angles, with the majority lying in between 90-170°. This means that H-bonds in these ILs are mostly bent. Figure 3.4b shows the hydrogen bonds in PyrrAc separated by type based on the spatial distribution of atoms as 25.6% single, 14.4% bidentate, 27.2% bifurcated, 0.1% bridged and 32.7% multi-contact interactions. According to bond-length/bond-angle distribution maps for the three main types, the majority of which are within the range of 2.2-2.8 Å and 110-170°. As H_N-O_C distance increases, there is a shift towards lower bond angles for all H-bond types. Not even the single H-bonds are predominantly linear at short distances. The distribution of bifurcated H-bonds lies at lower bond angles for a given bond length than either single or bidentate bonds. Note, however, that these classifications are based solely on N, H_N and O_C positions in the converged simulations and not on any

energetic measure. The distribution of bidentate H-bonds thus includes a population of single H-bonds in which distal O_C s have simply rotated near to H_N .

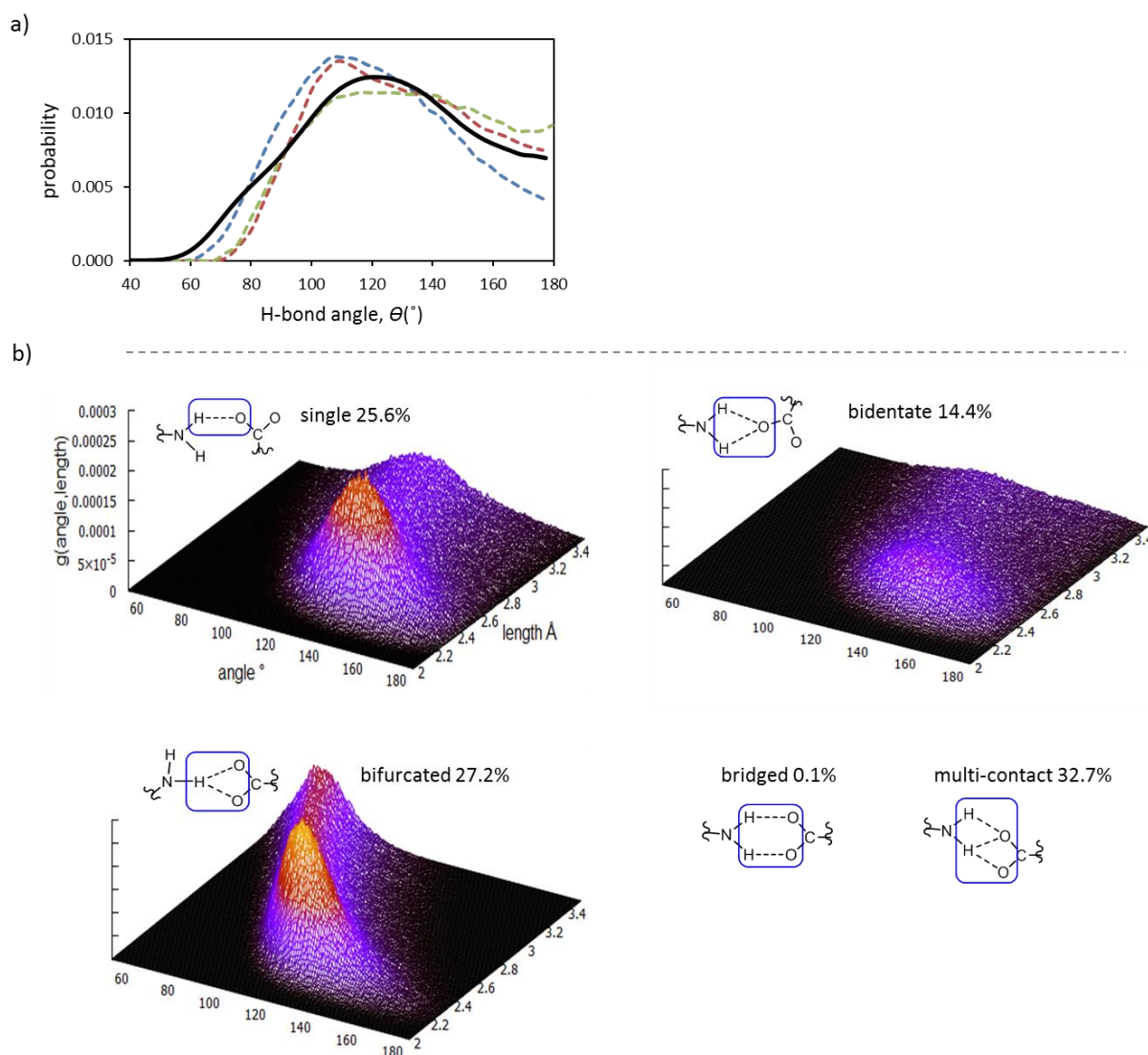


Figure 3.4 a) Hydrogen bond angle distribution of $N-H\cdots O_C$ (black), defined by bond lengths ($H_N\cdots O_C < 3.4 \text{ \AA}$), compared to EAF (blue), EAN (red) and PAN (green).¹⁶² b) Hydrogen bond angle-distance distribution maps with classification labelled.

These results highlight that the ionic arrangements in PyrrAc are dominated by electrostatic attractions between charges on the ammonium cation and carboxylate anion. Instead of forming a linear H-bonding network, the bond angle is distorted to accommodate closer approach of opposite charges.

Table 3.1 compares key hydrogen bond characteristics of the current and our previous studies on protic ILs, including PyrrAc, EAF, EAN and PAN. There also the local ion arrangements and H-bond network structure were found to be a consequence of the balance between Coulombic forces that drive polar-apolar nano segregation, and the packing geometry of ions.¹⁶² A different donor-acceptor

ratio in PyrAc means variations in a geometric arrangement. Although all four ILs have long and bent H-bond, the coordination number of anion around cation varies significantly. Despite the structural similarity between acetate and formate anions, the H-bond geometry in PyrAc is more similar to PAN than EAF.

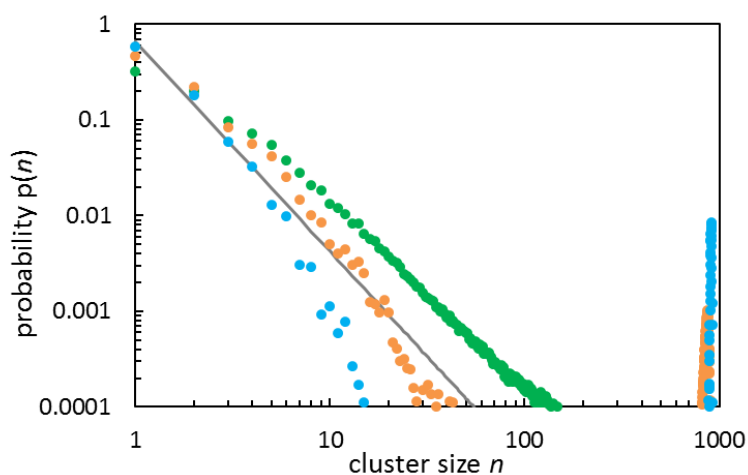
Table 3.1 Average H-bond properties of protic ionic liquids. Data for ethylammonium formate (EAF), ethylammonium nitrate (EAN) and propylammonium nitrate (PAN) were extracted from previous work.¹⁶²

	donor: acceptor	Length (Å)	Angle (°)	Coord # (range Å)	Type
PyrAc	2:2	2.43	120	1.8 (0-3.25)	Single/bifurcated
EAF	3:2	2.45	110	2.7 (0-3.25)	Bi/trifurcated
EAN	3:3	2.41	107	1.6 (0-3.00)	Bifurcated
PAN	3:3	2.37	117(broad)	2.1 (0-3.00)	Bifurcated

To quantitatively assess the micro-segregation among polar groups in the ionic liquid, cluster analysis was used over thousands of iterations of the converged simulation box to calculate the probability, $p(n)$, of finding a cluster of size n . Details of cluster analysis were discussed in Section 2.5.4.6. The results are shown in Figure 3.5. We perform three series of analysis on the same PyrAc system: The first series (green) shows the distribution of “standard” H-bonds, defined by a distance between an H-donor (H_N) and an H-acceptor (O_C) less than 2.8 Å and bond angles between 90° and 180° (cf. Figure 3.4). The green series lies slightly above the predicted random 3-dimensional percolation threshold, derived from the probability function¹⁶⁶ (shown as a solid line), meaning that standard hydrogen bonds form a network that lies on the percolation threshold.

If we expand the definition to incorporate “distorted” H-bonds (up to 3.4Å, and angles from 60-180°, shown in orange), then the fraction of small clusters ($n < 30$) decreases markedly and falls well below the percolation threshold. This decrease is offset by a population of large clusters on the right-hand side lying above the percolation threshold, which represents a continuous (simulation box spanning) network of polar groups that are not all connected by standard H-bonds.

This interpretation is substantiated by a cluster analysis of the electrostatic network, defined by a correlation distance between cation (N) and anion (C_O) charge centres, shown in blue. Here the nearest-neighbour cutoff distance is determined from the first minimum in the $N-C_O g_{ij}(r)$ (Figure 3.3a). The cluster distribution parallels that of the expanded H-bond series and also produces a peak on the right-hand side. This means electrostatic interactions alone form a continuous network, with more than 99% of ions forming part of a single large cluster that lies far above the percolation threshold. This means that PyrAc has a continuous polar domain with alternating charges, and it is primarily Coulombic in its origin. The hydrogen bond network within the polar domain is not continuous.



Series	Correlation	Length (Å)	H-bond Angle (°)
Standard H-bond	H _N – O _C	0 - 2.8	90 - 180
Standard & distorted H-bond	H _N – O _C	0 - 3.4	60 - 180
Electrostatic	N – C _O	0 - 4.7	-

Figure 3.5. Cluster analysis of polar groups in PyrAc, where probability $p(n)$ is the fraction of clusters with size n defined by nearest-neighbour distances and bond angles between different atom types derived from partial pair-correlation functions, $g_{ij}(r)$ (see text); black line is the theoretical percolation threshold $p(n) = n^{-2.2}$, normalized to $\sum p=1$, see reference ¹⁶⁶.

Knowing the structure in the polar region, we further look into interactions in the apolar region. Figure 3.6a shows key atomic partial pair correlation functions, $g_{ij}(r)$, among hydrocarbons. The $g_{ij}(r)$ function between acetate methyl carbons (C_M-C_M) has a peak near 4 Å, which is more pronounced than between terminal carbons of Pyr⁺ (C_2-C_2). There is a stronger apolar-apolar correlation among the anions than among the cations. Acetate methyl groups are also correlated with a cation ring carbon (C_M-C_2), producing a peak with equal intensity to C_M-C_M . This suggests mixed association rather than the formation of distinct apolar regions of cation and anion.

Spatial distribution plots of apolar groups further support these conclusions. As shown in Figure 3.6b, there is a conventional ‘tail-tail’ arrangement of acetate ions. The acetate methyl group seems to induce an amphiphilic character in the anion not seen previously in structurally similar formate protic ILs; Extrapolating this trend, we would expect much stronger anion-induced nanostructure with longer alkanoate ILs.¹⁶⁷⁻¹⁶⁸ Although adding an extra level of complexity to the interactions, we note that this kind of anion association has also been reported previously for ILs with analogous fluorosulfonate anions, which in this case did yield separate hydrocarbon and fluorocarbon regions.¹⁶⁹⁻¹⁷⁰

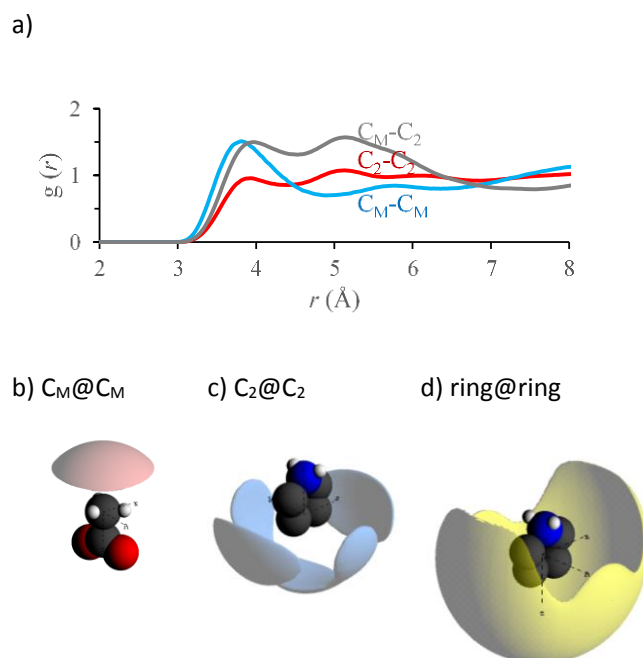


Figure 3.6 a) $g_{ij}(r)$ functions of selected hydrophobic groups of PyrrAc, showing correlation strength at a given distance. Also shown are spatial distribution function (SDF) plots showing 20% probability surfaces among b) anion methyl groups c) C_2 (bottom) carbons of the cation ring d) the cation ring geometric centres

Association between cation ring carbons is shown through the $C_2@C_2$ distribution in Figure 3.6c. Although these probability lobes are not quite isotropic and exhibit some preferred orientations, they surround the sides and at the bottom of the cation ring and do not extend around the ammonium head group. This strong, amphiphilic association between pyrrolidinium rings is underscored by Figure 3.6d, which shows the spatial distribution of the geometric centres of cation rings. The most probable position of finding a second ring from a reference ring is around the carbon side of the cation (i.e. the relatively apolar region), and far away from the charged ammonium group. The ring-centre spatial distribution is essentially the complement of the anion spatial distribution (Figure 3.3b) around the cation charge.

This suggests that, although there is an association between nonpolar rings, there is no preferred specific arrangement for adjacent cation rings in PyrrAc, such as stacking. Figure 3.7 confirms that cation rings in PyrrAc do not adopt any preferred arrangement at any correlation distance by showing the angular radial distribution function, $g(r, \theta)$, where θ is the angle between the normals to each ring. Details of the angular radial distribution function were discussed in Section 2.5.5.2. Here, the distribution is relatively flat with only small oscillations across all angles at short distances and confirms that there is no strong preference towards any specific alignment between adjacent rings.

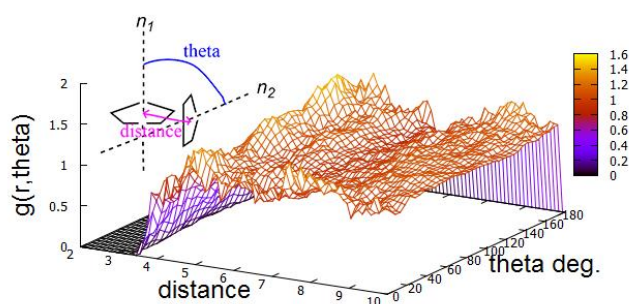


Figure 3.7. Angular radial distribution function plot for pyrrolidinium ring-centre—ring-centre, $g(r,\theta)$, where r is the distance (\AA) between the centre of two rings and θ is the angle between the normal for cation ring-approximated planes shown on the right. The analysis was performed using DLPUTILS.¹⁷¹

For aromatic liquids like benzene or pyridinium- and imidazolium-based aprotic ILs, π - π stacking is an important intermolecular interaction that can give rise to parallel and T-shaped orientations of neighbouring aromatic rings.^{10, 172} However with saturated pyrrolidinium cations, there are no such strong intermolecular interactions between rings, and steric effects are insufficient to induce any preferred arrangements.

The liquid structure of PyrrAc qualitatively recapitulates the amphiphilic nanostructure seen in primary alkylammonium protic ILs, but highlights some important distinctive features. Cluster analysis has revealed that strong, Coulombic interactions between charged groups drive the segregation of uncharged groups and leads to the formation of a bicontinuous, system-spanning network of interpenetrating polar and non-polar domains. Within the polar domains, the H-bond network is limited to a distribution of finite clusters within the extended polar domain. The H-bonds themselves are predominantly long and bent, accommodating electrostatics. Amphiphilic nanostructure remains a feature of this protic IL, even though the density of H-bond donors and acceptors in the secondary ammonium cation and acetate anion is lower than in previously-studied systems.

The key difference between PyrrAc and previously-studied primary alkylammonium protic ILs is packing in the apolar region. Pyrr⁺ cation rings are less ordered within the apolar domains than their primary alkylammonium counterparts; Figure 3.6b highlights the lack of strong end-to-end correlations between ring C₂ carbons,^{33, 173-174} showing instead a high degree of ring intercalation. PyrrAc thus forms apolar domains that are thinner than the combined length of two cation rings, giving rise to the smaller observed periodic spacing for PyrrAc (7.0 \AA) in comparison to EAN (10.0 \AA) in their neutron diffraction patterns. Unlike nitrate or formate, the acetate methyl group contributes to the amphiphilic nanostructure of PyrrAc.

The relative sizes of the polar and nonpolar part of an IL define a packing geometry ($a_{\text{alkyl}}/a_{\text{polar}}$), similar to the packing parameter used for surfactants.¹⁷⁵⁻¹⁷⁶ Linear protic ILs of similar molecular lengths, such as ethylammonium nitrate and formate, have packing parameters of $a_{\text{alkyl}}/a_{\text{polar}} \sim 1$, forming a bicontinuous sponge-like structure, built up from a locally *bilayer-like* arrangement of cations oriented tail-tail with their terminal methyls opposite each other, and a mean curvature of the polar/apolar interface near zero.³⁰ The larger non-polar volume in PyrAc at near-constant alkyl length and polar group size, yielding $a_{\text{alkyl}}/a_{\text{polar}} > 1$, gives rise to an inverted structure, analogous to a bicontinuous microemulsion near its transition to discrete water-in-oil droplets.¹⁷⁷⁻¹⁷⁹

Phenolic compounds, such as lignin decomposition products, are challenging solutes because they consist of small polar and apolar domains. Many other ionic liquids have bicontinuous nanostructure,²² but with ordered polar and apolar domains that become more ordered as the cation is made more amphiphilic.^{174, 180} These well-defined ion arrangements do not easily adjust to incorporate solutes of closely associated polar and hydrophobic groups, resulting in a high energetic cost. PyrAc, on the other hand, has well-defined nanostructure but the arrangements of groups within the polar and apolar domains are flexible, and therefore can readily adapt to the structure of phenolic compounds with minimal energetic cost; i.e. with less disruption to their existing disordered structure.^{43, 53} Likewise, the distorted and adaptable H-bond network of PyrAc facilitates the dissolution and solvation of other polar groups including lithium and other ions.¹⁵⁶

3.2 Design of ILs for Optimising Aromatic Dissolution

To understand the key design features of protic ILs that determine solubility selectivity of small aromatic compounds at the atomic level, we utilise neutron diffraction to compare the bulk structure of two protic ILs containing a dissolved model lignin residue, guaiacol (2-methoxyphenol), in the context of biomass processing. Structural details of lignin, its monomers and decomposition products were discussed in Chapter 1. We investigate how protic ILs solubilise phenolic compounds and alike, key solvent-solute interactions in the polar region and the less-polar region of ILs, the effect of IL nanostructure, and considerations for biomass dissolution.

3.2.1 Ammonium ILs with an aromatic solute

The secondary cell walls of lignocellulosic biomass are primarily composed of cellulose, hemicellulose and lignin. Lignocellulosic biomass is potentially an abundant and renewable source of biofuels,¹⁸¹⁻¹⁸² and as such the polysaccharide portion has attracted significant research interest as a source of pentoses and hexoses suitable for fermentation. However, the economic viability of a biorefinery requires conversion of the lignin fraction into high-value chemicals¹⁸³ such as vanillin and a wide variety of phenolic products.¹⁸⁴⁻¹⁸⁵

Lignin is an aromatic polymer that is difficult to dissolve and decompose.¹⁸⁶ Moderately polar molecular solvents and solutions are currently used for lignin extraction from biomass, ranging from, e.g., DMF and DMSO, to aliphatic alcohols and glycols, ketones, esters and carboxylic acids,¹⁸⁷ but all these have significant drawbacks, ranging from toxicity to evaporative losses during processing.

Ionic liquids (ILs) have recently emerged as effective solvents for lignin extraction.^{114, 183} The current benchmark, 1-ethyl-3-methylimidazolium acetate (C_2C_1imOAc), has a good yield but is not economically viable due to its high cost (>USD 50 kg⁻¹) and processing temperatures above 100 °C.¹⁸⁸⁻¹⁹⁰ ILs currently finding use in the chemical industry combine protic cations with a mineral acid anion¹⁸³ to form protic ILs, which are an order of magnitude cheaper. Both secondary and tertiary alkylammonium protic ILs performed comparably to C_2C_1imOAc for lignin extraction, but at a fraction of the cost (USD 1.25 kg⁻¹),⁴¹ although monoethylammonium protic ILs were found to be less effective.

Our understanding of the mechanisms underlying the extraction of aromatics with protic ILs is in its infancy. Using lignin extraction as an example, the performance of protic ILs is usually considered, like molecular solvents, in terms of solvent polarity or anion basicity, but these average indicators do not account for molecular-level factors that are hypothesised to control the solubility of individual residues in protic ILs.²² Most protic ILs have an amphiphilic nanostructure consisting of polar and non-polar domains that percolate through the liquid.¹⁹¹ The solubility of aromatic species in

protic ILs will depend on interactions between its aromatic rings and their substituents with either the polar and apolar phases, which are completely unexplored at the molecular level. This means that pathways to optimising ion structures cannot be identified rationally.

In this section, we use neutron diffraction to compare the solution structure of guaiacol (2-methoxy-phenol), a model depolymerisation product of lignin,¹⁹² in two protic ILs at the molecular level. The protic ILs selected for study are a propylammonium nitrate (PAN), which has a primary cation, and pyrrolidinium acetate (PyrrAc), which comprises a secondary cation, and is one of the more promising protic IL lignin solvents due to its high extraction yield and low processing temperature.¹¹⁴ Guaiacol is fully miscible in both protic ILs, and is a model lignin depolymerisation product that is also representative of many substituted small aromatic compounds such as anisole, aniline, anethole, and other phenol derivatives. Structural understanding of how these small aromatics dissolve in protic ILs has broad applicability to the design of task-specific solvents for lignin dissolution and transformation.

Neutron diffraction with hydrogen/deuterium isotopic substitution (see Appendix 1 and 2) yields multiple contrasts for each chemical system. The liquid nanostructure of pure PAN¹⁷³ and PyrrAc¹⁹³ have been described previously. PAN has a pronounced liquid nanostructure and well-defined ion arrangements. PyrrAc also exhibits amphiphilic nanostructure, but the ion arrangements within the structure are less well defined than for PAN.

Here we have examined solutions of guaiacol in PyrrAc at 10 and 25wt%, and in PAN at ten wt%. Figure 3.8 shows neutron diffraction patterns as structure factors $S(q)$ for PyrrAc-guaiacol and PAN-guaiacol mixtures in the range $0.0 < q < 10.0 \text{ \AA}^{-1}$, as well as atomic notations of PAN and guaiacol used in this section. Varying the H/D isotopic substitution creates four contrasts, as shown in Appendix A1 and A2. Contrast variation distinguishes among protons with different hydrogen bonding capacities. After simultaneously fitting to all four contrasts, all IL-guaiacol systems show good agreement between experimental data (dots) and EPSR calculation (solid lines).

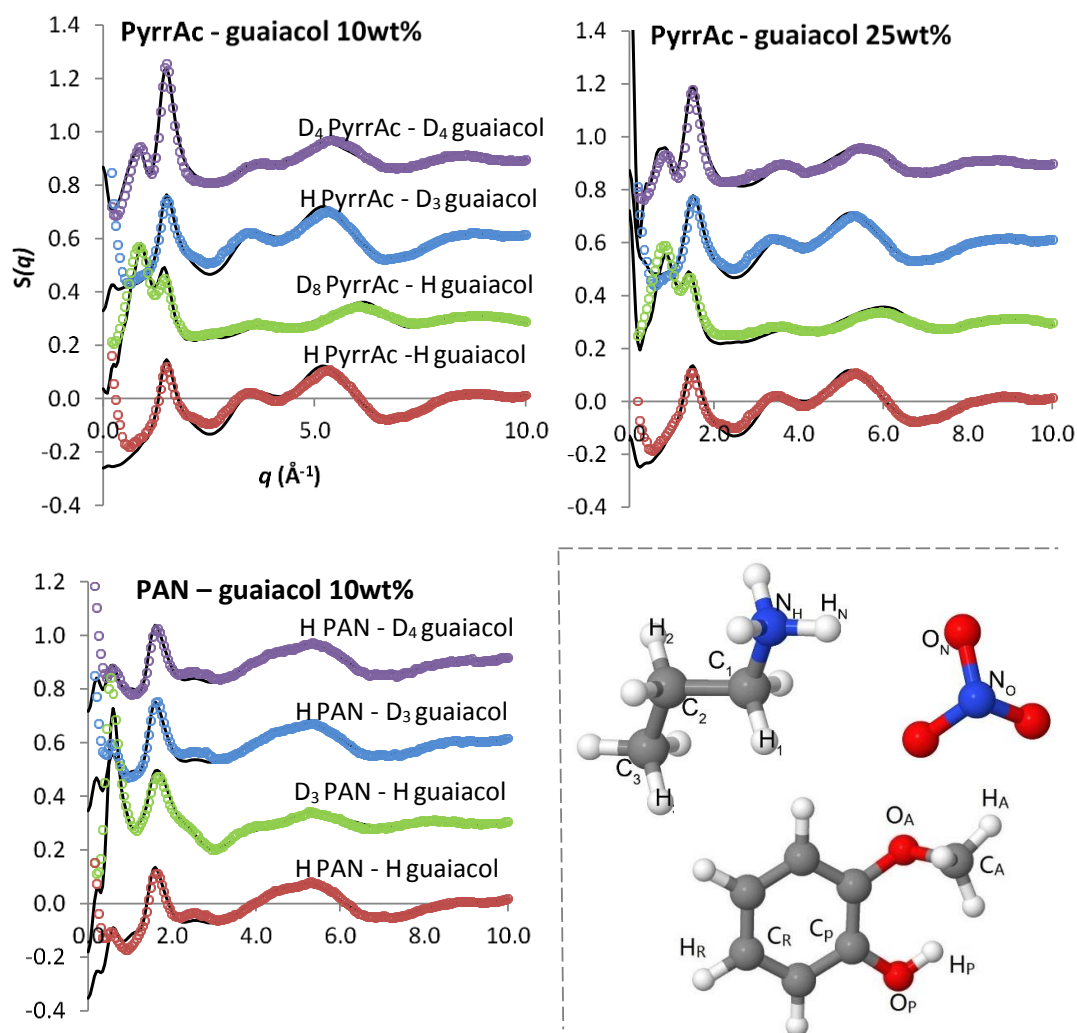


Figure 3.8 Experimental (dots) and EPSR fitted (solid line) structure factor as a function of q for IL-guaiacol (10 and 25wt%) mixtures; atomic labels of PAN and guaiacol used in this section.

In PyrrAc-guaiacol systems, scattering patterns at all contrasts have high q peaks $> 1.5 \text{ \AA}^{-1}$, corresponding to combinations of inter- or intra-ionic correlations. H-rich contrasts, H-PyrrAc H-guaiacol and H-PyrrAc D_3 -guaiacol are almost identical, suggesting the methoxy group of guaiacol is evenly distributed in the liquid mixture. From 15wt% to 25wt% guaiacol, there is no significant change in the scattering pattern for all contrasts. This indicates a negligible change in liquid structure as guaiacol content increases.

In the PAN-guaiacol system, the d_3 PAN-guaiacol contrast gives a strong Bragg peak at 0.55 \AA^{-1} , corresponding to a real space repeat spacing of 11.4 \AA . In pure PAN, this peak appears at lower q of 0.53 \AA^{-1} which corresponds to a larger repeat spacing of 11.9 \AA .¹⁷³ The addition of 10wt% guaiacol slightly reduces the periodicity of the PAN nanostructure. This observation is similar to adding propylammonium chloride salt to PAN without causing a significant change in the bulk nanostructure.⁴⁹

Figure 3.9 shows key correlations functions, $g_{ij}(r)$, involving H-bond acceptors and donors, including cation-anion, anion-guaiacol (with either phenol H or aromatic H), cation-guaiacol (with either phenol O or methoxy O), and guaiacol-guaiacol (via either phenol-phenol or phenol-methoxy interactions).

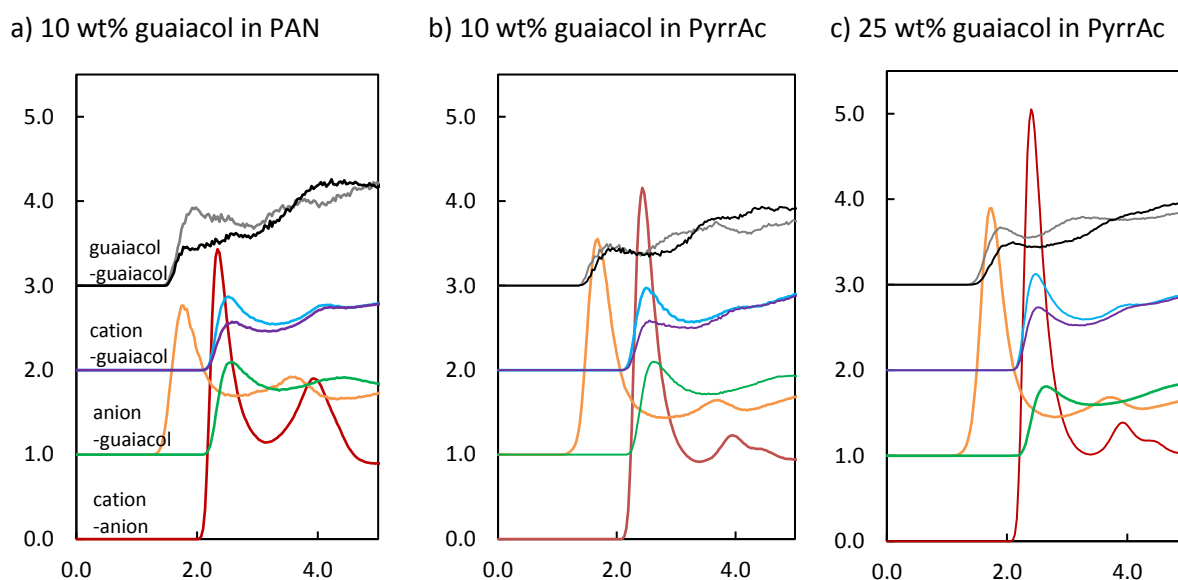


Figure 3.9. Key atom-atom correlation functions in a) PAN-guaiacol and b-c) PyrrAc-guaiacol. Correlations were colour-coded as cation-anion H_N-O_C/O_N , anion-phenol O_C/O_N-H_P , anion-aromatic O_C/O_N-H_R , cation-phenol H_N-O_P , cation-methoxy H_N-O_A , phenol-phenol H_P-O_P and phenol-methoxy H_P-O_A .

In either PAN or PyrrAc, the cation-anion (H_N-O_C or H_N-O_N) correlation has the sharpest and most intense peak at short distances, followed by the anion-phenol correlation, which is stronger in PyrrAc (O_C-H_P) than in PAN (O_N-H_P). The cation-phenol (H_N-O_P) correlation has a much less intense peak compared to the anion-phenol correlation. Note that an anion can also interact with a guaiacol aromatic hydrogen (O_C/O_N-H_R), and a cation can also interact with a guaiacol methoxy oxygen (H_N-O_A). However, the methoxy oxygen (O_A) and the aromatic hydrogen (H_R) are not our focus, as their correlations are much weaker compared to the predominant correlations discussed. Guaiacol-guaiacol correlations, including phenol-phenol (H_P-O_P) and phenol-methoxy (H_P-O_A), are weak as the intensity of short-distance peaks is less than 1, meaning the probability of finding such correlations is lower than the bulk average. This means the guaiacol-guaiacol H-bond is negligible at short distances, leading to an even distribution of guaiacol in either PyrrAc or PAN.

When increasing solute concentration from 10wt% to 25wt% in PyrrAc, the peak positions in $g_{ij}(r)$ stay, and peak intensities change slightly. This means that the type of interaction remains, with slight variation in coordination numbers as changing the solvent-solute molar ratio. There is no significant change in solvent structure as going from 10wt% to 25wt% of guaiacol.

The atomic arrangements within the liquid were found to be independent of concentration, although better statistics were achieved at 25 wt%. This method unambiguously determines the locations of hydrogens and the corresponding part of the molecule in a sample, enabling the identification of intermolecular interactions that drive dissolution. Using Empirical Potential Structure Refinement (EPSR) to model and simultaneously fit solutions with identical chemical composition but different H/D substitutions, the liquid structure is determined with near-atomic resolution. We will correlate IL geometry, H-bonding capacity and amphiphilicity to solvent performance.

3.2.2 Solvent-solute interactions in the polar region

In both PAN-guaiacol and PyrrAc-guaiacol the dominant correlations are between polar groups on the cation ($-\text{NH}_3^+$ or $>\text{NH}_2^+$), the anion ($-\text{COO}^-$ or NO_3^-) and the guaiacol phenol group, all of which are capable of H-bonding (Figure 3.9). Figure 3.10 compares the details of hydrogen bond arrangements for guaiacol in PyrrAc (top row) and PAN (bottom row).

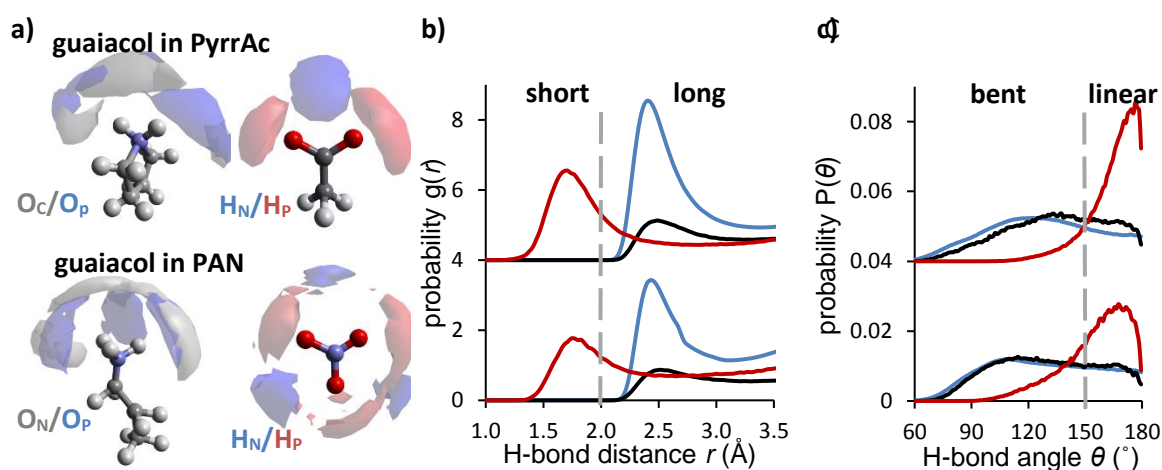


Figure 3.10 Key H-bond atomic arrangements for 25 wt% guaiacol in PyrrAc (top) and PAN (bottom). Three interactions are colour-coded: **cation-anion**, **cation-guaiacol** and **anion-guaiacol**. A) 20% probability surfaces for the *competitive* arrangement of H-bond acceptors of the anion (O_C on acetate or O_N on nitrate) and phenol oxygen (O_P) of guaiacol around cations (left), and *complementary* arrangement of H-bond donors from the ammonium cation (H_N) and guaiacol phenol (H_P) around the anions (right); B) corresponding bond length and C) bond angle distribution, distinguishing short, straight from long, bent bonds.

Figure 3.10a shows the spatial arrangement the most probable 20% of H-bond acceptors around cations and H-bond donors around anions. The H-bond acceptors of the anion and phenol oxygen of guaiacol form two lobes above and around Pyrr⁺, and three lobes around PA⁺. However, there is essentially no difference between the locations of phenol and the anion acceptor atoms, which compete for the cation. In contrast, the H-bond donors of the ammonium cation (H_N) and guaiacol phenol (H_P) occupy different spatial locations around both nitrate and acetate anions. In PyrrAc, the cation charged group is preferentially located between anion oxygens due to electrostatics,

so the H_N atoms form a lobe in this region. This leaves H-bonding positions available near each donor O_C, resulting in two symmetrical lobes corresponding to linear H-bonds to H_P. This is also clearly seen in the H-bond angle distribution (Figure 3.10c) which is sharply peaked near 180° for C-O_C-H_P, whereas the C-O-H_N bond angle distributions of anion and guaiacol phenol around the cation are both less well-defined, with broad peaks from 90-150°.

The same behaviour is seen around nitrate in PAN, but with three-fold symmetry. The cation H-bond donors lie between O_N, while the guaiacol occupies the vacant linear positions. The peak at 180° in Figure 3.10c is less pronounced.

Partial pair-correlation functions (Figure 3.10b) show that linear anion-guaiacol preferred bond length of 1.7 Å is also much shorter than both the cation-anion and cation-guaiacol H-bond lengths of 2.4 - 2.5 Å, indicating a much stronger interaction. (A statistical summary of H-bond properties is available in Appendix 3.) This is similar to previous results for H-bonding in pure primary alkylammonium protic ILs.¹⁶² The competition for H-bonding sites around the cation, but differences around the anion, is consistent with earlier reports that the species of the anion is more important than the cation for biomass dissolution.¹⁵¹

3.2.3 Solvent-solute interactions in the apolar region

Both PyrrAc and PAN are amphiphilically nanostructured liquids,^{173, 193} which is known to enhance miscibility with various alkanols.^{53, 194-195} The structure of their apolar domains may, therefore, contribute to the miscibility of guaiacol with both PyrrAc and PAN. Figure 3.11 shows correlation functions among the less-polar groups, including the terminal carbon of the propylammonium cation (C₃), the bottom carbon of the pyrrolidinium ring (C₂), and the aromatic carbon of the guaiacol molecule (C_R). Results indicate relatively strong associations between the terminal carbons of propylammonium cations, and weak associations between the bottom carbons of pyrrolidinium and with the aromatic ring of guaiacol.

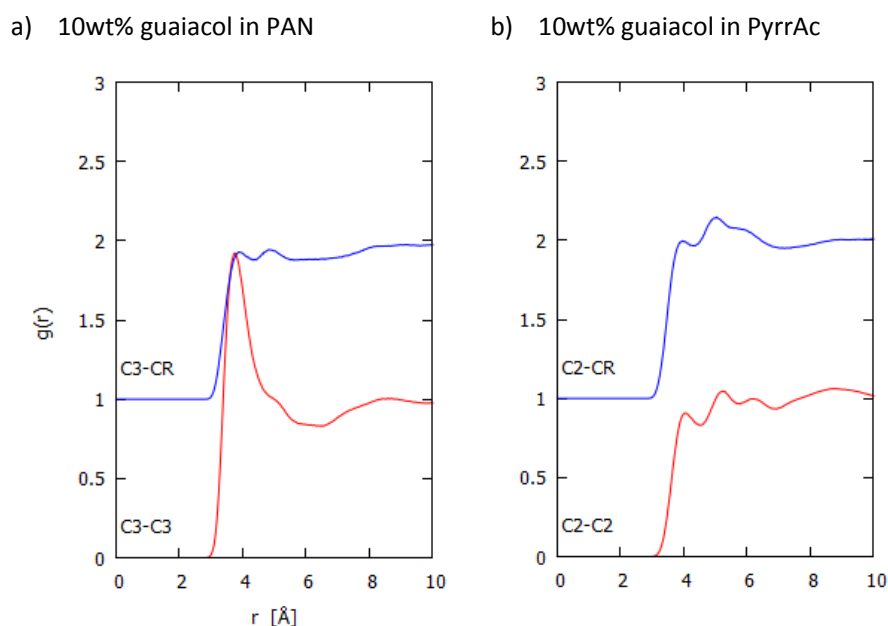


Figure 3.11 Key atom-atom correlation functions in a) PAN-guaiacol and b) PyrrAc-guaiacol. Correlations were colour-coded as cation-cation C₃-C₃ or C₂-C₂, and cation-guaiacol C₃-C_R or C₂-C_R.

Figure 3.12 shows the most probable locations of both the cation terminal methyl (C₃) and the centre of mass of the guaiacol aromatic ring (Ar) around representation propylammonium cation. The C₃ methyl locations are consistent with the bulk liquid structure of PAN,¹⁷³ in which the cation alkyl chains segregate into a tail-to-tail or bilayer-like sponge arrangement. The guaiacol aromatic ring occupies similar, but less well defined, positions, consistent with its solubilisation into apolar regions. Around a reference guaiacol molecule, the cation terminal methyl group shows similar distribution as a guaiacol ring, with no site-specific interaction observed.

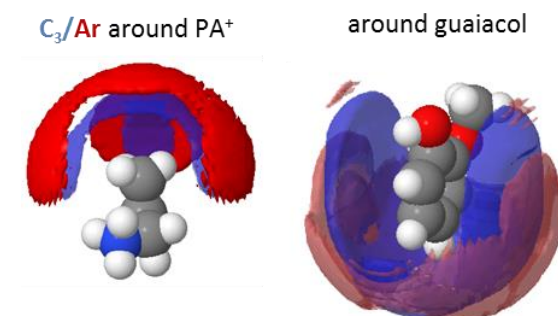


Figure 3.12 Geometric arrangements around the propylammonium cation (left) and around the guaiacol molecule (right). Coloured surfaces represent most probable distributions (20%) around reference molecules. Blue surfaces represent the terminal carbon (C₃) of the propylammonium cation and red surfaces represent the geometric centre of the guaiacol ring.

Figure 3.13 shows the relative distribution of the centres of mass of pyrrolidinium and guaiacol apolar rings as a function of distance and orientation. As seen in pure PyrrAc,¹⁹³ the distribution of Pyrr⁺ rings is almost independent of angular orientation, suggesting no preferred alignment or stacking of cations. The spatial probability distribution (inset) of Pyrr⁺ rings is similarly homogeneous, but also

highlights the amphiphilic association of these non-polar groups into domains segregated from the polar ammonium cation and acetate anion. In contrast, guaiacol-guaiacol correlations show a strong propensity for face-to-face (parallel) stacking of aromatic rings. Surprisingly, Pyrr⁺-guaiacol ring correlations also exhibit preferred parallel alignment. This is likely to be a packing preference of the planar guaiacol ring, considering the absence of strong intermolecular interactions. Such steric constraints may also underpin the preferential orientation of guaiacol rings. These results suggest that, in contrast to PAN, the absence of preferential orientation of the Pyrr⁺ rings in the apolar domain mean they can solvate the guaiacol and rearrange into a favourable conformation with minimal energetic cost.

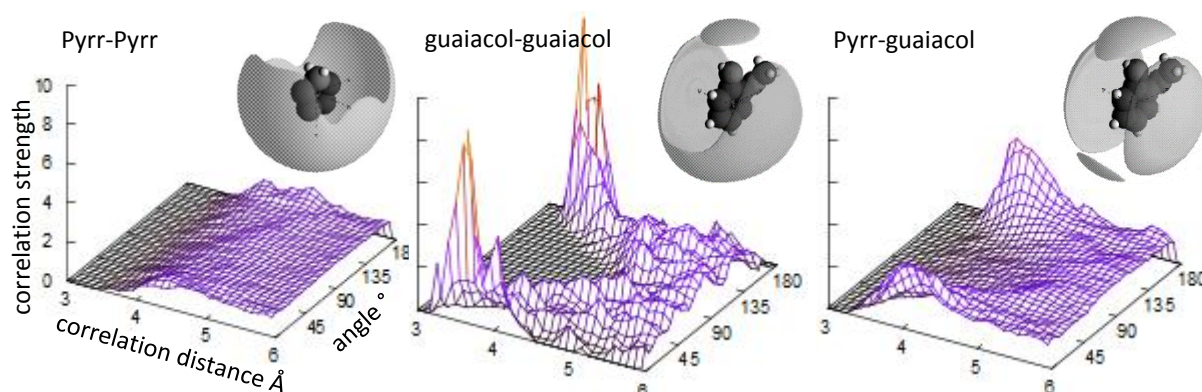


Figure 3.13. Ring-ring angular distribution maps, derived from the angle between the normal of two rings and the distance between geometric centres.

3.2.4 Solvent nanostructure

Figure 3.14 shows representative snapshots of the EPSR simulation of 25 wt% guaiacol in (a) PyrrAc and (b) PAN, converged to the experimental neutron diffraction patterns, with IL polar head groups, apolar hydrocarbons and guaiacol molecules labelled in different colours. PAN displays a sponge-like bicontinuous solvent structure with near-equal volumes of interpenetrating polar and non-polar domains. In PyrrAc, apolar groups take up the major volume, forming a continuous apolar domain. The liquid structures are consistent with those previously reported for pure PAN and PyrrAc.^{173, 193} In both ILs, guaiacol is evenly distributed throughout the solvent with no segregation, and is in contact with both the polar and the apolar domains as inferred from the preceding analysis.

The extent of the H-bond network may be quantified by cluster analysis, shown in figure 3.14c, which reveals the probability of finding a cluster with size n , consisting nearest neighbours within cation-anion H-bond range (<2.8 Å, from Figure 3.10). Whereas PyrrAc exhibits a distribution of finite clusters close to that expected for a random percolation threshold, PAN almost exclusively forms clusters that span the simulation box, indicating a continuous H-bonding network of ammonium and nitrate ions. The dense, three-dimensional H-bond network of PAN with three donors and three

acceptors per ion pair stabilises the continuous polar network. In PyrAc, with only two donors and two acceptors, no such network forms. This parallels the H-bonding conditions required for molecular solvents to exhibit a solvophobic effect and induce micelle formation.¹⁶⁴

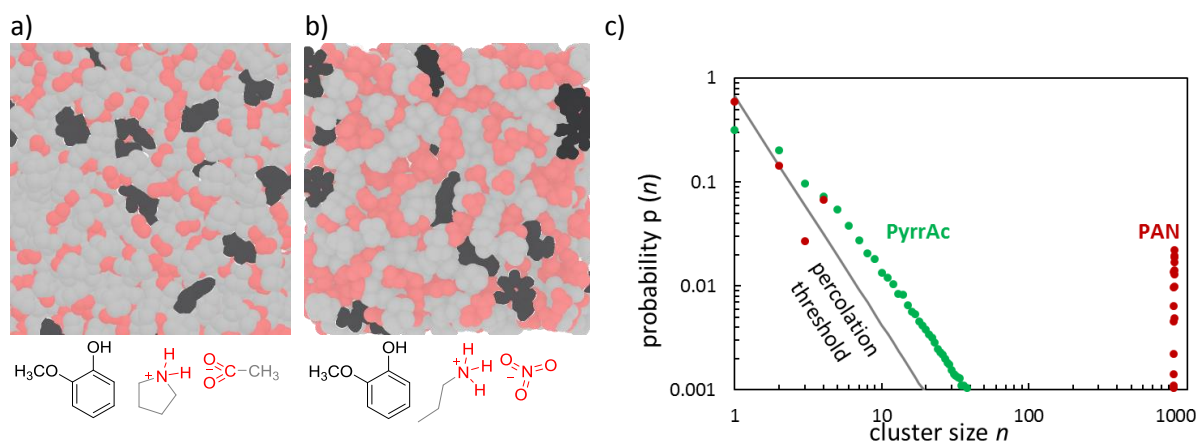


Figure 3.14 Snapshots of converged simulation boxes of a) PyrAc-guaiacol and b) PAN-guaiacol; colour coding distinguishes IL polar groups, IL apolar hydrocarbons, and guaiacol. c) Cluster analysis of IL polar groups, defined by hydrogen bond distance $< 2.8\text{\AA}$. Theoretical percolation threshold $p(n) = n^{-2.2}$, normalised to $\sum p = 1$, see reference¹⁶⁶.

3.2.5 Considerations for biomass dissolution

While solvent nanostructure is a desirable feature that provides suitable polar and apolar solvent microenvironments for guaiacol and other similar solutes with polar and non-polar groups, the details of H-bond donor and acceptor availability are also critical. Primary alkylammonium cations favour an extended H-bond network within the polar domains of the liquid which is not possible for secondary or tertiary alkylammoniums. This allows incorporation of the solute polar moieties into the polar domains without disrupting the existing solvent H-bond network. ILs can act as designer solvents because their nanostructure is driven by electrostatics, allowing H-bond availability to be tuned independently. This explains why secondary (including PyrAc) and tertiary ammonium protic ILs are more effective solvents than corresponding primary ammoniums for lignin extraction.^{41, 196}

The H-bonding capacity of the anion is also an important factor to consider. Both nitrate and acetate provide distinct acceptor sites that can simultaneously accommodate short, straight phenolic and long, bent ammonium cation H-bond donors (Figure 3.10a). Our previous study, which showed that ethylammonium thiocyanate and hydrogensulfate themselves form dense networks of short, straight cation-anion H-bonds,¹⁶² suggests that they should not be effective solvents for guaiacol, as is observed.¹⁹⁷

There is little difference between the apolar domain sizes of a cyclic secondary ammonium (PyrAc) or a primary ammonium cation (PAN). While relatively small for ILs, they are large enough to

accommodate small aromatic moieties like guaiacol. To dissolve solutes with larger non-polar groups, we anticipate that ILs with longer aliphatic chains (i.e. matched with the solute) to be better performing.⁴³ However, increasing the cation alkyl chain length leads to better-defined cation alkyl chain packing in apolar domains.¹⁷⁴ This is contrary to the disordered packing in PyrAc and is important for its solvency power. Therefore, strategies for increasing the apolar volume without increasing order such as mixtures of cations with different alkyl chain lengths¹⁹⁸ or branched chains should be pursued.

This leads to the consideration of choline amino acid-based ILs as potential lignin extraction solvents.¹⁹⁹ Based on the molecular structure of naturally occurring amino acids, it is possible to design amino acid-based ILs with desired amphiphilicity and nanoscale structure, optimising the solubility of small phenolic compounds such as guaiacol. Moreover, each amino acid-based IL contains at least one acetate group to form hydrogen bonds with the phenyl groups in lignin. The cholinium head group is sterically hindered with a minimum capacity to H-bond, and should enhance the anion-phenyl interaction and lead to a higher extraction efficiency of phenolic compounds. Details of choline amino acid ILs will be discussed in Section 3.3.

This section highlights the importance of the anion-guaiacol interaction for solubilization. Acetate is a good anion for guaiacol solubilization due to its asymmetry and site-specific interactions with the solute. To optimise the solubilization of phenolic compounds or alike, we hypothesise that reducing the number of H-donors on the cation will minimise competing interactions between the cation and phenyl groups and therefore enhance the anion-solute interaction. This hypothesis was validated using Pyr^{r+} (with fewer H-donors than PA⁺) that was found to be a more effective cation. This approach is also supported by the observation that aromatic solubilization decreases following the order of triethylammonium > diethylammonium > ethylammonium.⁴¹

Our results indicate that a matched amphiphilicity between the solvent and the solute is a minimum criterion for the solubilization of small aromatic species. For all the ILs studied, the cation determined solvent amphiphilicity. Pyrrolidinium, propyl- and branched alkylammoniums all contain a polar head group and apolar hydrocarbon tails or rings. ILs containing one of these cations can solubilise anisole-based and phenolic species, and are potential extraction solvents for aromatic polymers such as lignin. Beyond this basic amphiphilicity requirement, the extent of IL nanostructure is less relevant to the extraction efficiency based on our current observations.

3.3 Choline Amino-acid Based Ionic Liquids

Recently, Liu et al. have reported non-toxic and biodegradable ILs containing cholinium as the cation and amino acids as the anions.²⁰⁰ With up to 20% water, the delignification yield from these amino-based ILs maintains the same.¹¹⁷ This strong tolerance of ILs to moisture is critical for their cost-effective applications, as the complete removal of water from ILs and biomass requires energy and water-IL mixtures are less expensive than pure ILs. Among eight bio-based ILs that have low viscosity and high lignin selectivity at ambient temperature, cholinium lysinate (ChLys) demonstrates the highest potential as a pretreatment solvent.²⁰¹ Lignin accumulates in ChLys at a constant rate over five cycles without purification. *Sun et al.* explained the excellent performance of ChLys by the higher hydrogen bonding basicity of ILs with lysinate anions as compared to acetate ILs.¹⁹⁹ Using quantum calculations, the authors found that lysinate containing ILs have a higher binding affinity with lignin model compound than acetate ILs with the addition of water. However, how these bio-based ILs solubilise lignin and how water influences the lignin extraction process have not been explored at the nanoscale. A structural understanding of the solvent structure, solvent-solute interactions and how additional water molecules enhance solvent-solute interactions is necessary for developing subsequent novel ILs for biomass pretreatment.

In this section, we investigate the bulk structure of bio-based ILs, the relationship between ion structure and the solubility of lignin residues, key intermolecular interactions and therefore identifying a design framework to optimise extraction efficiency for future design. Cholinium lysinate (ChLys) is chosen as a promising bio-based IL for lignin extraction.¹⁹⁹ Cholinium acetate (ChAc) is chosen to compare with ChLys, contrasting the structural influence of two amine groups on the lysinate. Moreover, acetate ILs (such as the benchmark EmimAc and previously discussed PyrAc) are good extraction solvents and have been well studied.

3.3.1 How water influences the bulk structure of ILs

Starting from pure ILs, we investigate the bulk structure of ChLys and key interactions. With the addition of water, we show how an additional solute interacts with IL cations and anions, and we determine how the ChLys-H₂O (1:5 by mole) system differs from the ChAc-H₂O (1:5 by mole) system at the atomic level and at the nanoscale. We further compare quaternary ammonium ILs to previously studied primary and secondary ILs, to identify unique characteristics that are suitable for biomass processing.

Neutron diffraction with hydrogen/deuterium isotopic substitution yields multiple contrasts for each chemical system. Figure 3.15 shows atomic notations used in this section, as well as

diffraction patterns of neat ChLys, ChLys-H₂O and ChAc-H₂O systems. Contrasts in red are fully hydrogenous, contrasts in green highlight all exchangeable protons and the acetate methyl group, contrasts in blue highlight the cholinium headgroup, and contrasts in purple inversely highlight all hydrocarbons except the acetate methyl group. After simultaneously fitting to all four isotopic substitutions, all systems show good agreement between experimental data (dots) and EPSR calculation (solid lines).

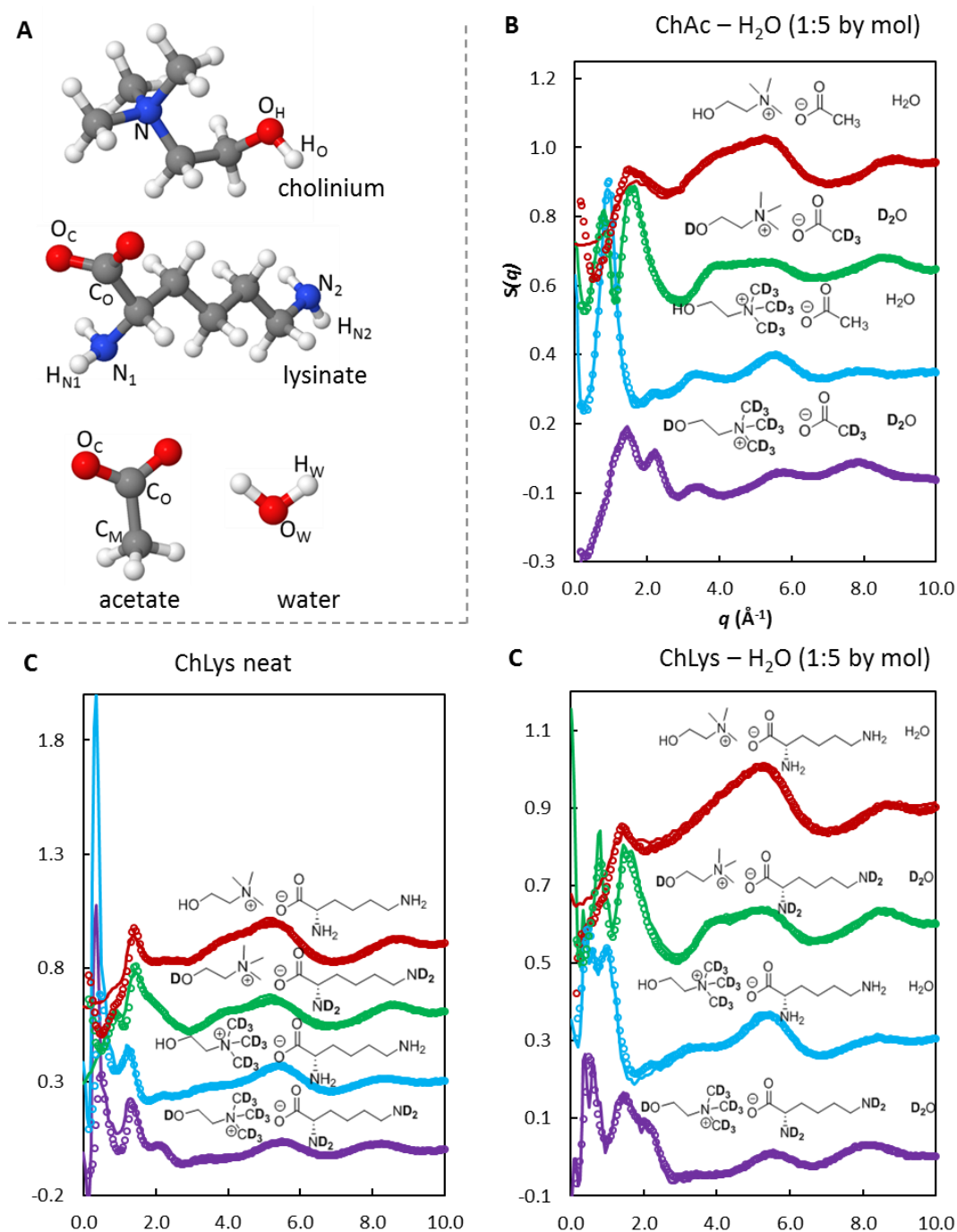


Figure 3.15 a) Components of the amino acid-based ionic liquids with atomic notations used throughout this section. b-d) Neutron diffraction (coloured data points) and EPSR fitted (coloured lines) structure factors as a function of the scattering vector, q (\AA^{-1}), at 298 K. Data are offset for clarity.

In the ChAc-H₂O system, the lowest peak in $S(q)$ is at 0.75 \AA^{-1} , in the green contrast highlighting exchangeable hydroxyl and water protons, plus the acetate methyl group. Based on Bragg's law of $d=2\pi/q$, this indicates a repeat spacing of 8.4 \AA . This is slightly larger than the cation-cation nearest neighbour distance of 6.6 \AA , calculated based on the blue contrast with a peak at 0.95 \AA^{-1} .

In neat ChLys, the blue contrast has a low-angle peak at 0.45 \AA^{-1} ($d = 14.0 \text{ \AA}$), and the purple contrast has a low-angle peak at 0.50 \AA^{-1} ($d = 12.6 \text{ \AA}$). Compared to the cation-cation nearest neighbour distance, which is indicated by the second peak in the blue contrast ($q = 1.0 \text{ \AA}^{-1}$, $d = 6.3 \text{ \AA}$), these longer repeating distances suggest that ChLys is structured at the nanoscale.

In Figure 3.15c, the EPSR fits of blue and the purple contrasts are more intense than experimental data at low angles, though the peak positions are consistent. Experimentally measured samples contain a small amount of water due to the hygroscopic nature of ChLys. As seen in the ChLys-water system in Figure 3.15d, the intensity of these peaks decreases significantly with the addition of water. This indicates that the structure of pure ChLys has a higher periodicity (though there is no crystallinity) than ChLys mixed with a small amount of water. As EPSR refines at nearest-neighbour distances, differences in intensities at the nanoscale will not influence our following interpretations.

After the simulation is refined towards experimental data, we extract atom-atom correlation functions and the spatial distribution of selected functional groups around a reference molecule. From neat ChLys (dotted lines) to the ChLys-H₂O mixture (solid lines), as shown in Figure 3.16a, we observe different responses across correlations. The addition of water increases the cation-anion electrostatic correlation distance (i.e. the peak position is right-shifted) and decreases the correlation intensity. H-bonding correlations between cations and anions show an increase in intensity, while the correlation distances remain the same. If the addition of water leads to a simple dilution process, we would expect cation-anion correlations change in the same direction, which is not what we have observed here.

Unlike most primary and secondary ammonium ILs, the electrostatic correlation between cation-anion charged groups (shown in purple) is not the strongest, because of the steric hindrance of the quaternary ammonium group. The spatial distribution of the quaternary ammonium around the carboxylate has 2-fold symmetry. The carboxylate distributes around the ammonium with 3-fold symmetry. The geometry of ion headgroups determines their spatial arrangements.

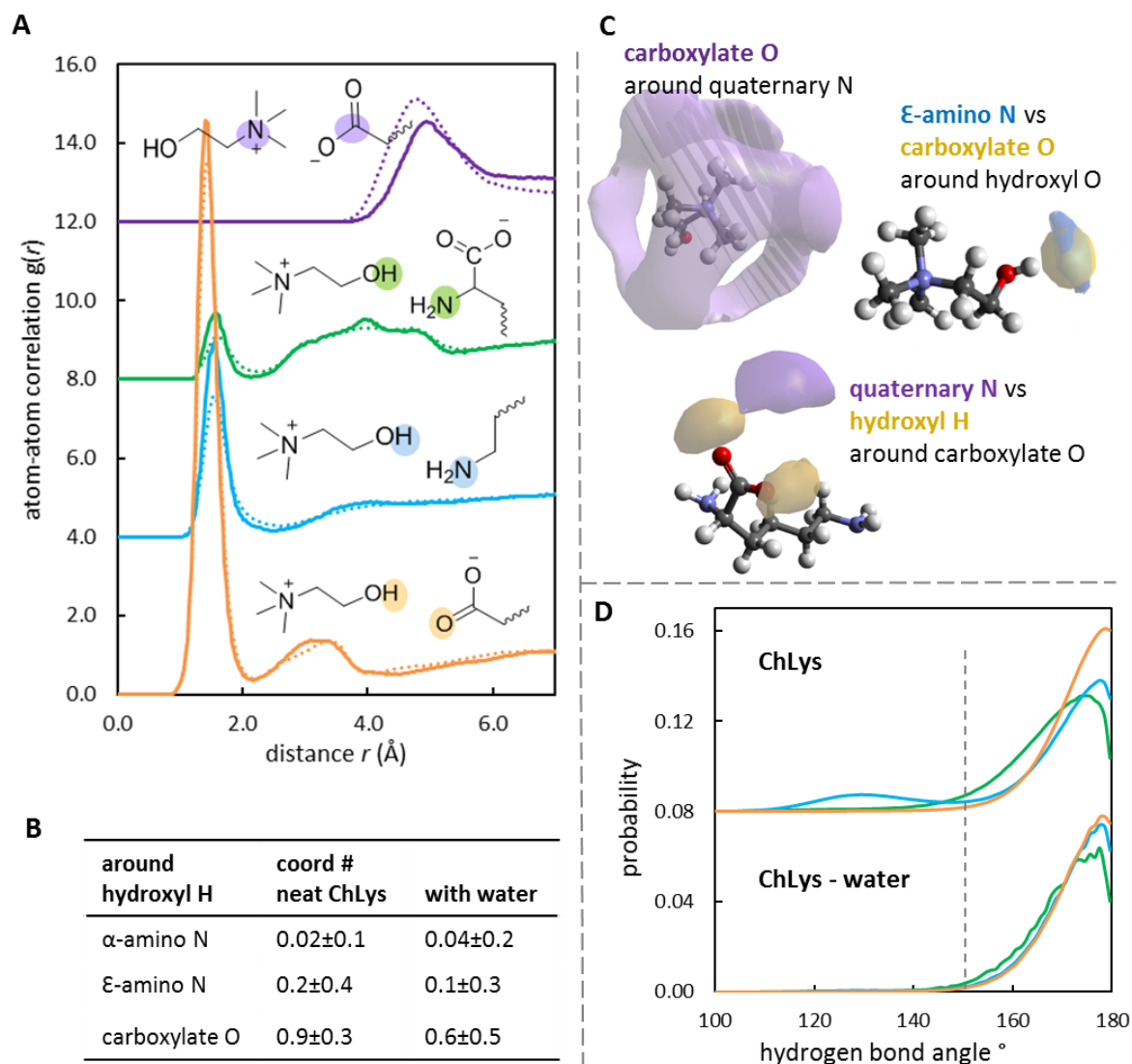


Figure 3.16 a) Atom-atom correlation functions, $g(r)$, in neat ChLys (dotted lines) and ChLys-water (1:5 by mole, solid lines). **b)** Coordination numbers around the cation hydroxyl hydrogen in neat ChLys and the ChLys-water system, defined within 0 - 2.3Å. **c)** 3D geometric plots of the ChLys system show 20% probability surfaces. **d)** hydrogen bond angle distribution in neat ChLys and the ChLys-water system. Structural labels and surfaces are colour matched with their $g(r)$ plots.

In Figure 3.16a, correlation functions show that the choline hydroxyl group can H-bond to the α -amino group, the ϵ -amino group, or the carboxylate group. Calculated coordination numbers around the hydroxyl hydrogen, shown in Figure 3.16b, indicate that the most probable interaction is with the carboxylate oxygen, evidenced from higher coordination numbers, compared to the α -amino nitrogen or the ϵ -amino nitrogen. Geometrically, Figure 3.16c shows a well-defined distribution of hydroxyl group (yellow) next to carboxylate oxygens.

In PyrAc-guaiacol mixtures discussed in Section 3.2, results showed that the amine hydrogen goes to the middle of two oxygens, forming a bent hydrogen bond; whereas the phenol hydrogen goes

to the linear positions, same as what we observed here with the choline hydroxyl group. The geometry of hydrogen-bond donating and accepting sites governs their arrangement relative to each other.

The bond angle analysis, shown in Figure 3.16d, shows that majority of H-bonds formed with the choline hydroxyl group are linear hydrogen bonds ($160\text{-}180^\circ$). Interestingly, in neat ChLys, a small proportion of hydrogen bonds formed between the cation hydroxyl group and the anion ϵ -amino group are bent hydrogen bonds ($120\text{-}140^\circ$). These bent hydrogen bonds disappeared with the addition of water.

We characterised H-bonds in the ChLys- H_2O mixture to determine the structural behaviour of water molecules in ChLys. In Figure 3.17a, atom-atom correlation functions show that a water molecule can form a hydrogen bond with another water molecule, a cation, or an anion. The water oxygen (O_w) interacts with another water molecule, or with the cation hydroxyl group. The water hydrogen (H_w) interacts with three H-bond acceptors on the lysinate anion: α -amino nitrogen (N_1), ϵ -amino nitrogen (N_2), and carboxylate oxygen (O_c). The H-bond length ranges between $1.4\text{-}1.8 \text{ \AA}$, as shown in Figure 3.17 b. Any water molecule shown in the schematic diagram could potentially be replaced by a choline hydroxyl group, as they behave alike.

Notice that the water-water correlation ($\text{H}_w\text{-O}_w$), shown in Figure 3.17a, has peak positions at 1.85 (for hydrogen bonding) and 3.15 \AA (for secondary correlations), which is similar to what was observed in pure water (1.8 and 3.3 \AA) at RT.²⁰² In Figure 3.17c, hydrogen bonding angle of water molecules (shown in purple) distributes in the $160\text{-}180^\circ$ range. This means that the hydrogen bonding formed between water molecules in the ChLys-water mixture is similar to it is in pure water.

Figure 3.17d shows the geometric distribution of H-bond donors and acceptors around water and the anion. Both the water hydrogen (H_w) and the cation hydroxyl hydrogen (H_o) are H-bond donors; they form H-bonds at multiple sites around a water molecule. Their geometric arrangement overlaps to some extent. Among three H-bond acceptors of the anion, their geometric arrangement around a water molecule completely overlaps at the linear position, meaning a spatial competition for H-bonding. Around the anion, the distribution of water hydrogen is similar to that of the cation hydroxyl hydrogen. In addition to a geometric competition between water and the cation hydroxyl group, hydrogen bond angle analysis, shown in Figure 3.17c, shows that both species form linear hydrogen bonds ($160\text{-}180^\circ$).

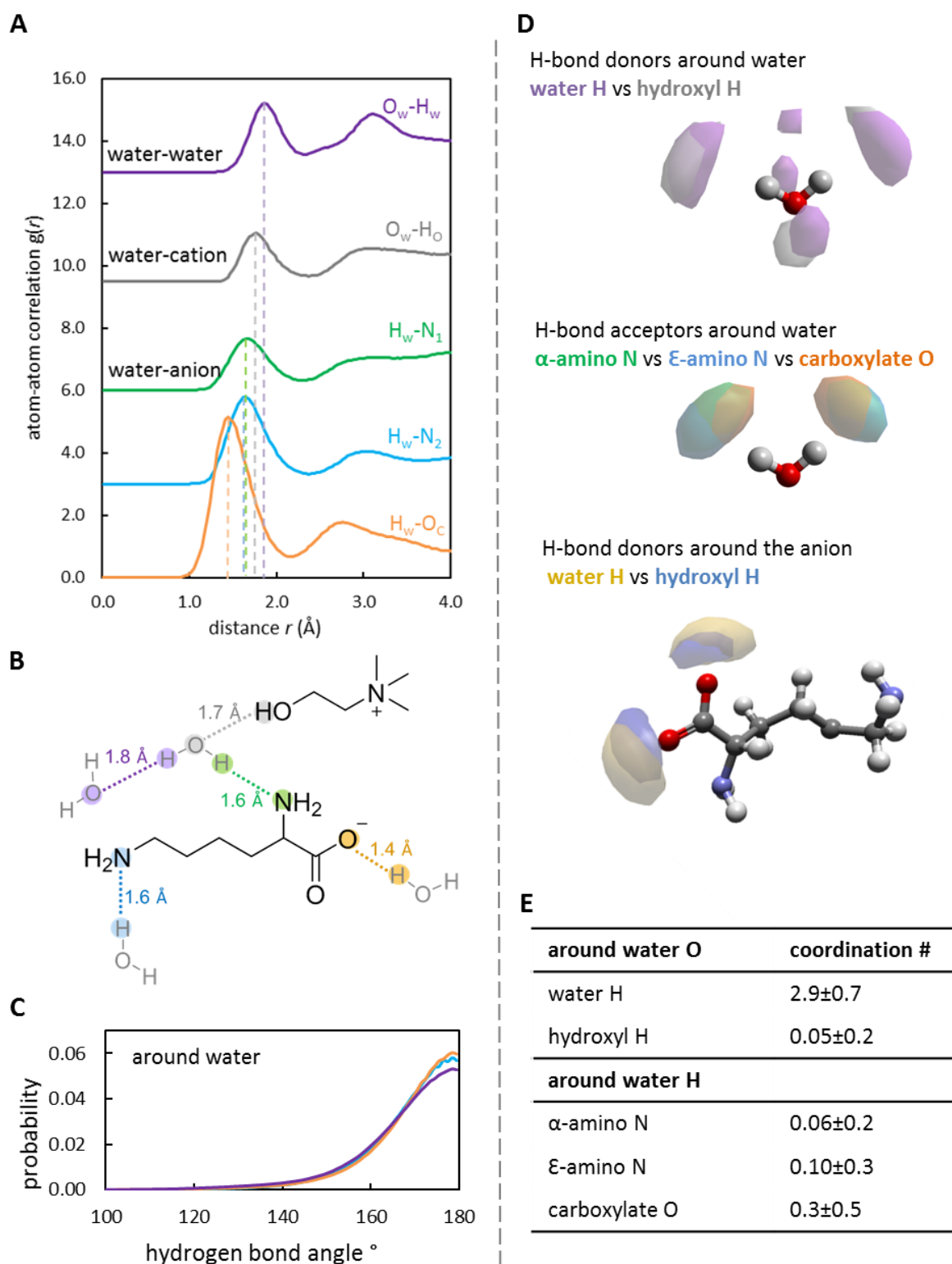


Figure 3.17 Key H-bond characteristics in the ChLys-water (1:5 by mole) system. **a)** Atom-atom correlation functions, $g(r)$. Three categories shown include interactions between water-water (top), water-cation (second top), and water-anion (the rest). **b)** A schematic diagram shows optimal H-bonding distances derived from $g(r)$ functions. **c)** Hydrogen bond angle distribution around water. **d)** 3D geometric plots show 20% probability surfaces for the *competitive* arrangement of H-bond acceptors and donors. **e)** Coordination numbers around water molecules defined within 0 - 2.3 Å. Plots and structural labels are colour matched.

Based on calculations of coordination numbers around water, shown in Figure 3.17e, water predominantly interacts with other water molecules (coordination number = 2.9 ± 0.7), with IL carboxylate oxygen to some extent (coordination number = 0.3 ± 0.5), and less with other H-bonding groups (coordination number < 0.1). The most dominant IL-water interaction is between the carboxylate oxygen and water hydrogen. This explains the decreased cation-anion coordination numbers with the addition of water (Figure 3.16b), especially between the carboxylate oxygen and the hydroxyl hydrogen (from 0.9 to 0.6).

In the ChLys-H₂O system, three H-bond acceptors on the lysinate anion interact with water molecules, and the structural behaviour of water is similar to the cholinium hydroxyl group. Water molecules are accommodated into the ionic liquid H-bonding network, without significantly changing its structure at the atomic level.

Our previous analysis on PyrAc and PyrAc-guaiacol systems has highlighted the importance of a carboxyl group for interacting with small aromatic species. To correlate our previous findings with the current choline lysinate systems, and to separate the role of the carboxylate group from the amino groups, we further look at a simplified model system, a ChAc-H₂O mixture.

Figure 3.18 shows key correlations and geometric distributions in the ChAc-H₂O system. All functions and surfaces are colour matched with their labels. The cation-anion electrostatic correlation occurs at a longer distance due to steric hindrance, as we observed in ChLys systems. Between methyls of acetates, we see a small peak at around 4 Å, indicating a solvophobic association.

There are three important hydrogen bonds. The H-bond between the choline hydroxyl group and acetate oxygen is the strongest. It has a much shorter correlation distance than the electrostatic interaction. Water can H-bond with either the acetate oxygen, or with another water molecule. Based on the correlation distance, all of them are short H-bonds, with similar peak positions at around 1.7 Å. In Figure 3.18b, hydrogen bond angle analysis shows that all three types are in the linear form (160-180°). This is quite rare for protic ionic liquids, as we often see a combination of short (linear) and long (bent) H-bonds. Moreover, water and cation hydroxyl groups are competitors. They both hydrogen bond to the acetate oxygen at short distances.

The geometric distribution of species around the anion is governed by electrostatic interaction, solvophobic association, and hydrogen bonding. In Figure 3.18c, the positively charged cholinium headgroup preferably locate on the carboxylate side of the anion. The apolar methyl group locates on the methyl side, suggesting a tail-to-tail correlation between the hydrocarbon of two anions. The calculated coordination number among methyl groups is 3.6 ± 0.8 within a radius of 5 Å, which is slightly

lower than it is in pure acetic acid (4.5 ± 1.2).²⁰³ The spatial distribution of H-bond donors (water hydrogen and hydroxyl hydrogen) overlaps right next to the carboxylate oxygens of the anion. Around water molecules, H-bond acceptors (water oxygen and carboxylate oxygen) go to the linear H-bonding position next to the hydrogens of water. Their spatial distribution overlaps completely, indicating a geometric competition.

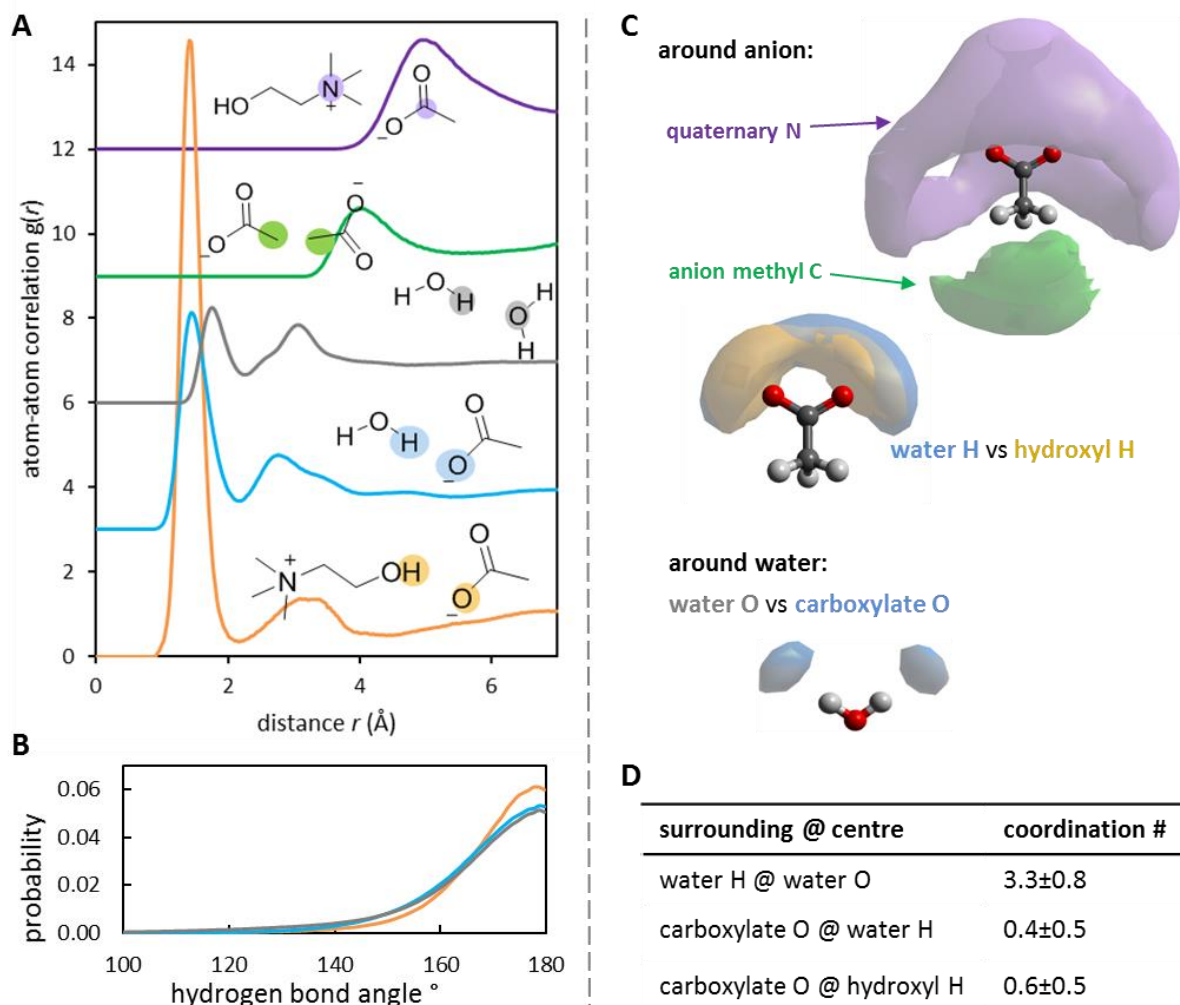


Figure 3.18 Key characteristics of the ChAc-water (1:5 by mole) system. **a)** Atom-atom correlation functions, $g(r)$. Three categories shown include cation-anion electrostatic interaction (top), anion-anion hydrophobic association (second top), and H-bonding (the rest). **b)** hydrogen bond angle distribution around water. **c)** 3D geometric plots show 20% probability surfaces. **d)** coordination numbers at hydrogen bonding sites, defined within 0 - 2.3 Å. Plots and structural labels are colour matched.

Figure 3.18d shows coordination numbers between H-bonding species in the ChAc-water system. At the nearest neighbour distances, the coordination number of water hydrogen around water nitrogen is 3.3 ± 0.8 , slightly higher than what was observed in the ChLys-water system (2.9 ± 0.7). The average number of carboxylate oxygen around water (0.4) and the hydroxyl group (0.6) in the ChAc-water system is similar to the ChLys-water system.

To visualise the structure at the nanoscale, we generate snapshots of refined simulation boxes, shown in Figure 3.19a, to visualise the distribution of IL charged groups (red), non-charged groups (grey) and water molecules (blue). In neat ChLys, there is a bi-continuous structure with IL charged groups in one phase and non-charged groups in the other phase. With the addition of water, the size of domains formed by charged and non-charged groups becomes smaller. Water molecules form segregated domains at the nanoscale. This can be explained by the hydrogen bonding among water molecules, as discussed previously. In the ChAc-H₂O system, domains are smaller than the ChLys-H₂O system. The ChAc IL is a less amphiphilic solvent environment compared to ChLys.

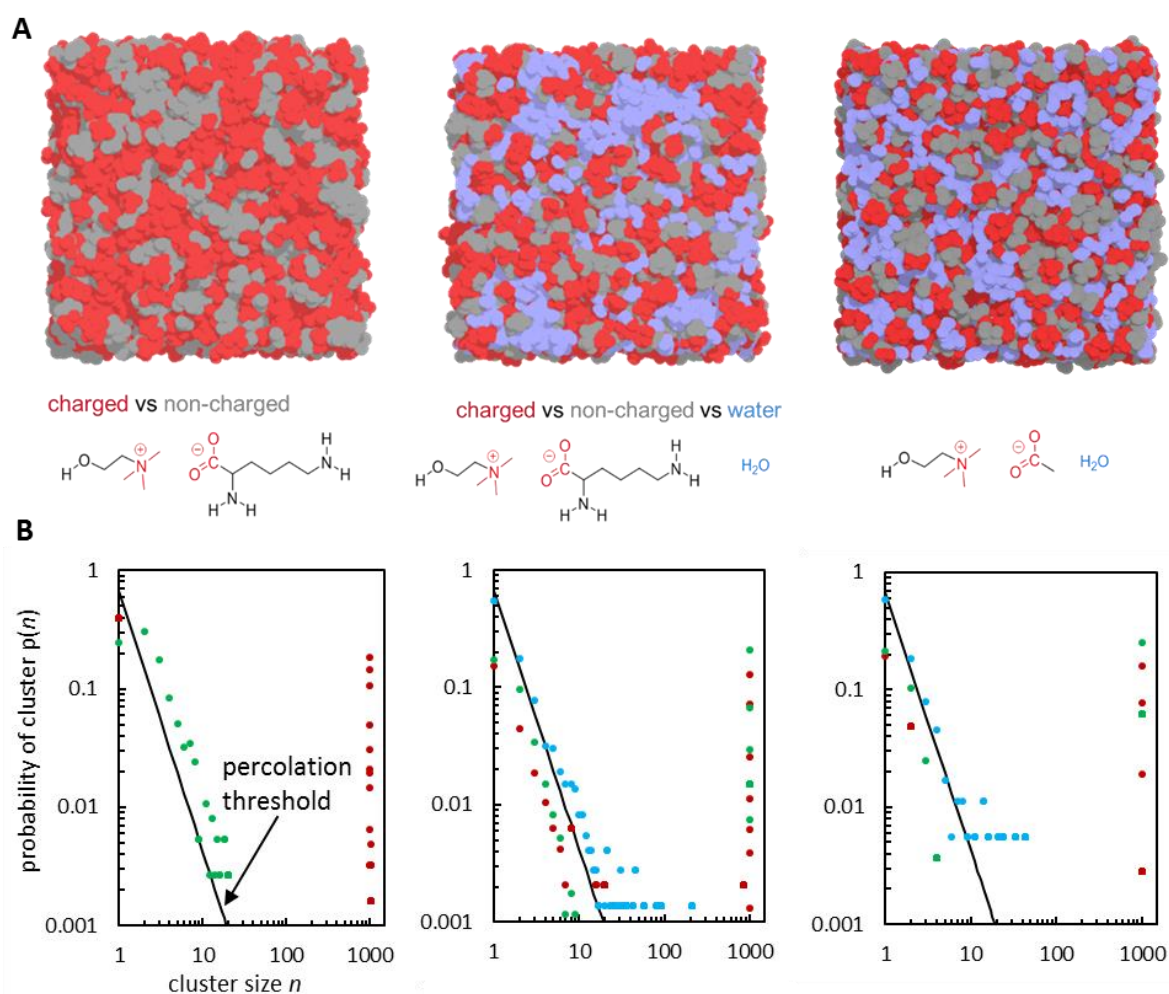


Figure 3.19 a) Snapshots of converged simulation boxes of neat ChLys (left), ChLys-water (1:5 by mole, middle), and ChAc-water (1:5 by mole, right). Colour coding distinguishes IL charged groups, non-charged groups, and water molecules. b) Cluster analysis of electrostatic interactions (N-O_c, 0-6.0Å), IL hydrogen bonding (donor-acceptor, 0-2.3 Å), and water clusters (H_w-O_w, 0-2.3Å), shows the fraction of cluster with a given size. Distance ranges are defined by the first coordination shell in $g(r)$. The theoretical percolation threshold $p(n) = n^{-2.2}$ is normalised to 1, based on reference¹⁶⁶.

In Figure 3.19b, cluster analysis calculates the normalised probability of finding clusters of a given size. We investigate three types of clusters: propagation between cations and anions through

electrostatic interactions (red), defined by nearest neighbour distances between IL charged groups; IL hydrogen bonding network (green) and water clusters (blue), defined by hydrogen bonding distances.

In neat ChLys, the only clusters found by propagating cation and anion association, shown in red, are near or equal to the size of the simulation box. This means that all charged groups are connected through electrostatic interaction, forming a continuous domain. If we consider only H-bond donors and acceptors, shown in green, the size distribution of clusters lies along the percolation threshold, which describes a randomly associated sample that starts to percolate in 3D.

Results show remarkable changes with the addition of water. While there is still a continuous network of ChLys charged groups, smaller clusters ($n = 1-30$) of charged groups appears. Clusters formed by the ChLys H-bonding groups crossed the percolation threshold, forming a continuous domain among with a low population of smaller clusters. Water molecules form clusters of small to intermediate sizes ($n = 1-200$).

In the ChAc-H₂O system, both the electrostatic network and the H-bonding network are continuous, with several small clusters that are available to hydrogen bond with water molecules. In general, the size of water clusters in ChAc ($n = 1-50$) is smaller than they are in ChLys ($n = 1-200$). Snapshots shown in Figure 3.19a have visually captured the different sizes of water clusters calculated in these two systems.

It is important to notice that, even though EPSR refines at intermolecular distances, our results show structure at the nanoscale. Using the ChLys-water system as an example, Figure 3.20 compares simulation snapshots to neutron diffraction data. For each contrast, the structural periodicity is qualitatively shown by snapshots highlighting functional groups with higher scattering length densities. Quantitative calculations of such periodicity based on the position of diffraction peaks justify simulation results. These structures do not fit into any geometric model (e.g. spheres, ellipsoids or rods), but are rather less-well defined and polydisperse.

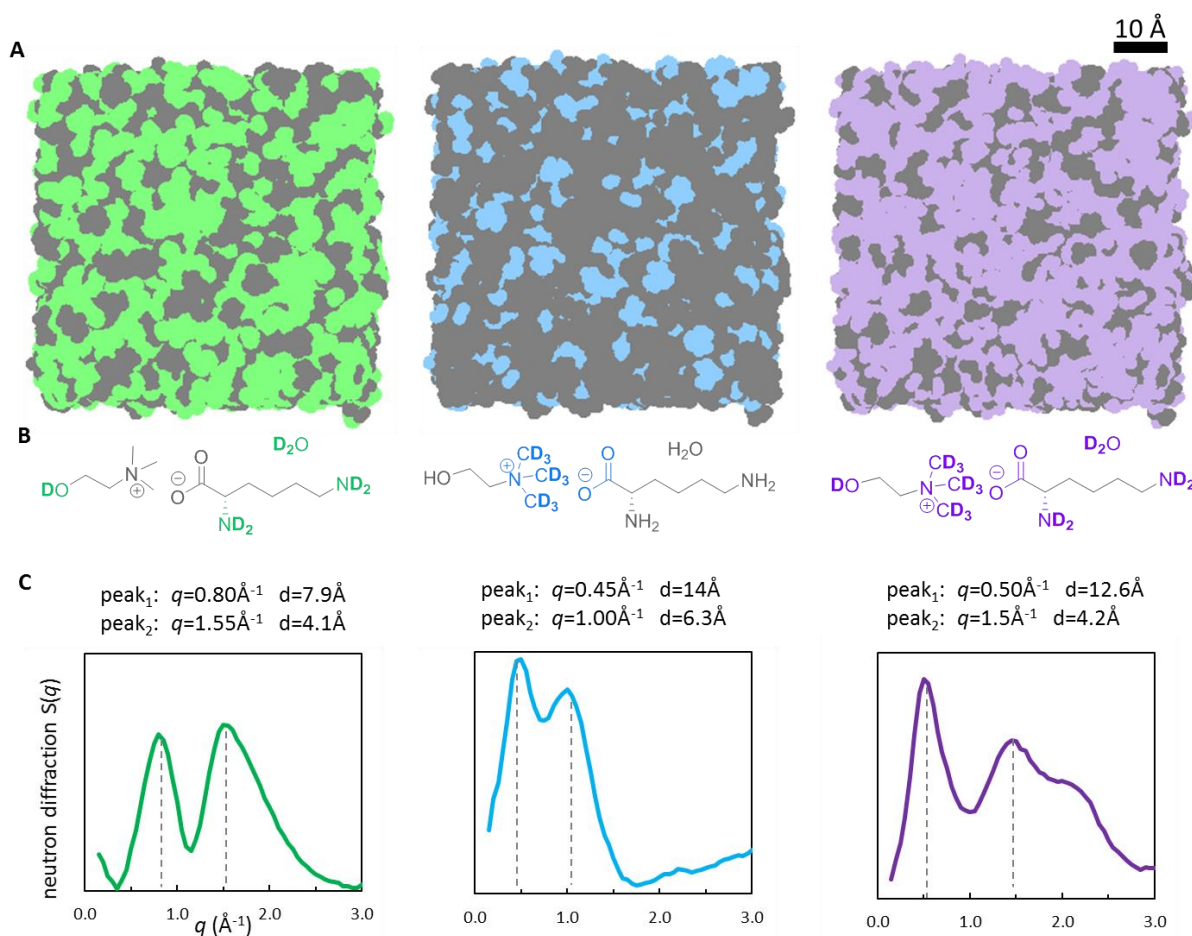


Figure 3.20 Orthogonal contrasts in the ChLys-water (1:5 by mole) system showing structure at the nanoscale. A) refined simulation snapshots contrasting high SLD functional groups with low SLD functional groups. B) colour coded molecular structures showing the position of deuteration. C) neutron diffraction patterns at low angles. Peak positions and its corresponding repeating distances were calculated based on $d = 2\pi/q$.

3.3.2 How water influences aromatic dissolution in ILs

Knowing the structure of ChLys and its water mixture, we further explore how an aromatic solute, guaiacol, interacts with the ionic solvent. As we have previously observed in PyrAc-guaiacol and PAN-guaiacol systems, hydrogen bonding with the guaiacol phenol group is the dominant solvent-solute interaction. Here in the ChLys-water-guaiacol system, after screening all atom-atom correlation functions with guaiacol molecules, we have identified that interactions with the methoxy oxygen are again negligible compared to interactions with the phenol group of guaiacol.

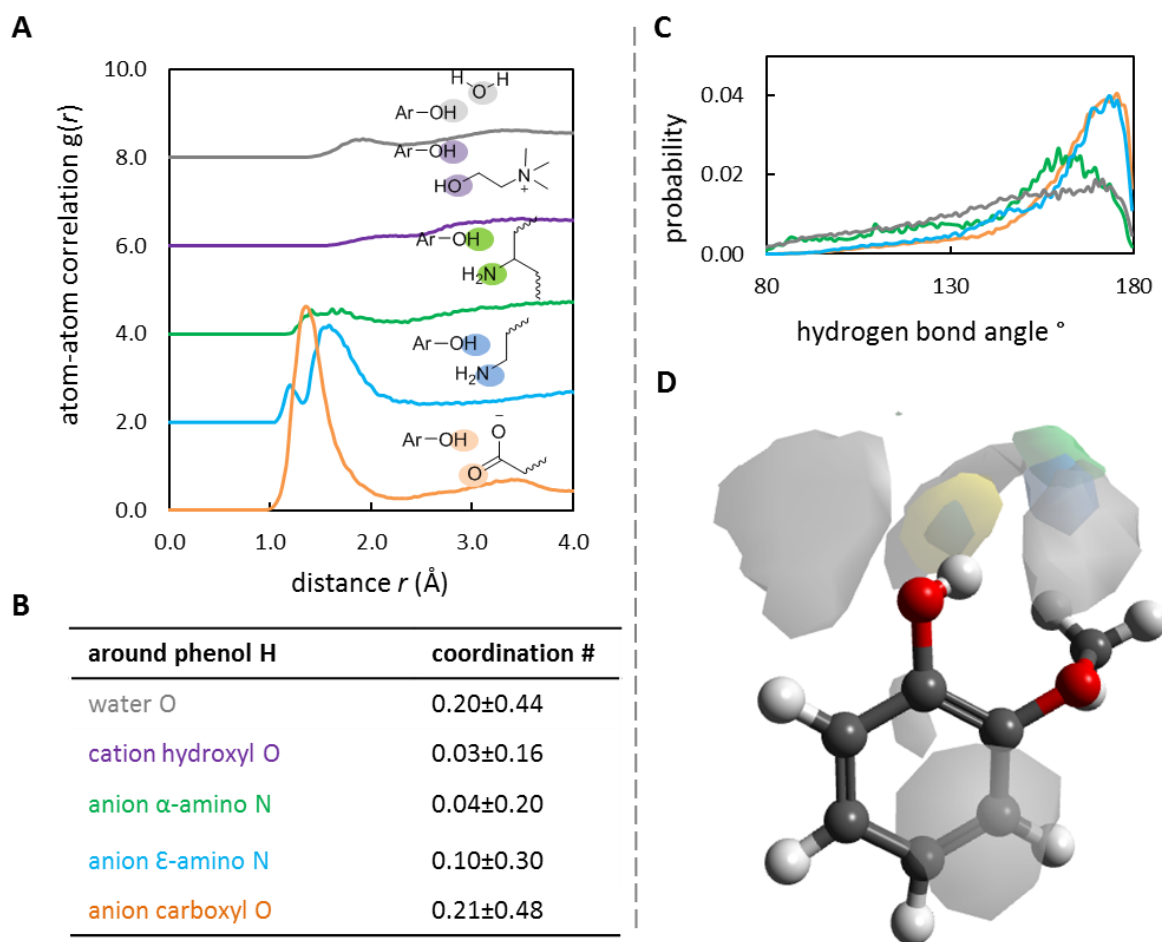


Figure 3.21 Key interactions around the phenol group in the ChLys-water-guaiacol system. **a)** Atom-atom correlation functions, $g(r)$. Three categories shown include water-guaiacol, cation-guaiacol and anion-guaiacol interactions. **b)** coordination numbers at around phenol hydrogen, defined within 0 - 2.8 Å. **c)** hydrogen bond angle distribution. **d)** 3D geometric plots show 20% probability surfaces. Plots and structural labels are colour matched.

Figure 3.21 shows how water, the cation and the anion hydrogen bonds with the phenol group of guaiacol. In figure 3.21a, atom-atom correlation functions show that the phenol group hydrogen bonds with three hydrogen bonding sites of the lysinate anion at short distances (1.0 - 2.2Å). Hydrogen bonding between the phenol group and water molecules occur at slightly longer distances (1.5 – 2.5Å). Figure 3.21b shows coordination numbers around the phenol group, to distinguish between dominant and negligible interactions at short distances. Around every phenol group, there are on average 0.20 ± 0.44 water oxygens and 0.21 ± 0.48 carboxylate oxygens within the first coordination shell. The probability of finding an α -amino or ϵ -amino nitrogen is much lower. Coordination between the cation hydroxyl and the guaiacol phenol group is negligible. The high coordination number of water around guaiacol is interesting, as guaiacol is only slightly soluble in water macroscopically. It is possible that hydrogen bonding with the lysinate anion facilitates the mixing of the immiscible.

Hydrogen bond-angle distributions around guaiacol, shown in Figure 3.21c, are generally broader than results of IL-water mixtures as previously discussed. The phenol-carboxylate hydrogen bonds are almost linear (140-180°); the phenol- ϵ -amino hydrogen bonds are mostly linear (150-175°), with a small proportion of bent hydrogen bonds (130-150°); the phenol- α -amino hydrogen bonds are mostly bent (140-160°), with a small proportion of distorted hydrogen bonds (80-130°); and the phenol-water hydrogen bond has a broad angular distribution, consisting distorted, bent and linear ranges (80-180°).

In Figure 3.21d, geometric arrangements show multiple hydrogen bonding sites around the phenol group. Carboxylate oxygens (represented by the yellow lobe) go to a near-linear position next to the phenol hydrogen. Amino nitrogens (green and blue lobes) locate at slightly bent positions. Water oxygens go to multiple sites, including near-linear positions, bent positions, or next to the aromatic ring (without hydrogen bonding with the phenol group). Both the bond angle distribution and the geometric arrangement of functional groups show a diverse range of hydrogen bonds around the guaiacol, which is different from the previously observed linear and directional interactions between guaiacol and alkylammonium ILs. In the ChLys-water mixture, there are more H-bonding capable species to interact with the guaiacol phenol group, yet these groups experience less competition geometrically.

A snapshot of the refined simulation box, shown in Figure 3.22a, helps to visualise the distribution of guaiacol molecules (coloured black) and how they influence the solvent structure. Without forming aggregates at the nanoscale, guaiacol molecules are in contact with IL charged groups (red), non-charged groups (grey) and water (blue). In Figure 3.22b, cluster analysis shows that either IL charged groups (the quaternary ammonium and the carboxylate group) or IL hydrogen bonding groups (the carboxylate group, α -amino and ϵ -amino groups) form continuous domains, just like what we have observed in the ChLys-water system. Water clusters with intermediate sizes ($n=20-200$) no longer exist with the addition of guaiacol. Instead, the size distribution of water clusters lies exactly on the 3D percolation threshold. It is remarkable to see how networks of electrostatics hydrogen bonding remain with the presence of water and guaiacol, which are two sparsely miscible components.

Choline amino-acid ILs are special for several reasons. The cation-anion electrostatic correlation distance is long due to steric hindrance. All hydrogen bonds are at short distances, which are different from conventional protic ILs. At the nanoscale, we observe continuous domains of charged and non-charged domains in ChLys. The additional water forms its own domains without changing the solvent structure significantly. Water hydrogen bonds with the anion similar to the way

in which water binds to the choline hydroxyl group. Therefore, water molecules participate in the H-bonding network of the ILs. The structural similarity between neat ChLys and its water mixture explains its high-water tolerance with preserved functionalities, such as delignification, pre-treatment of coal, extraction of carbohydrate and lipids.²⁰⁴⁻²⁰⁵

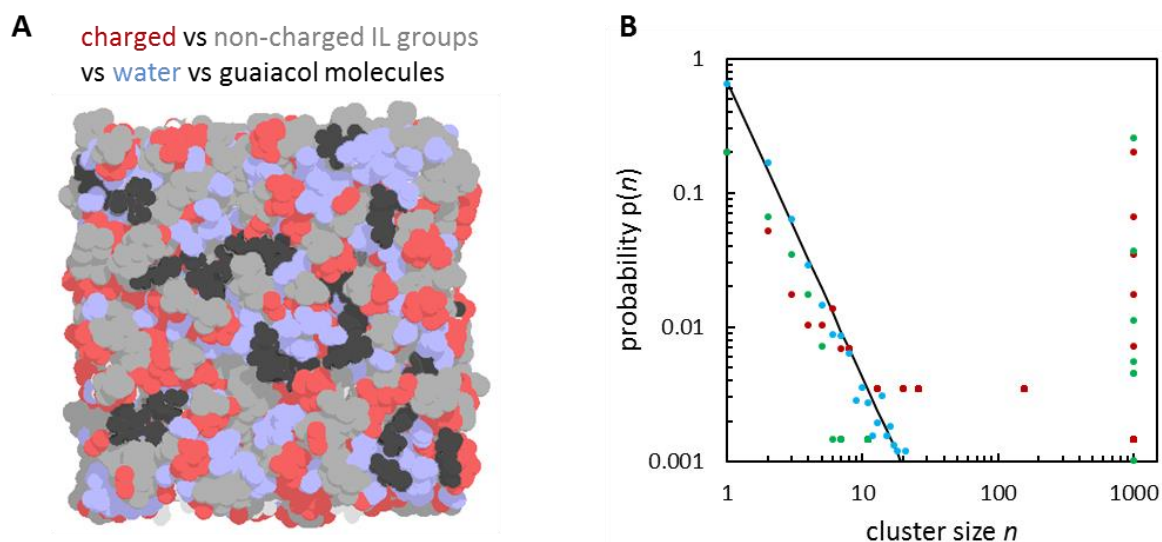


Figure 3.22 a) A snapshot of the converged simulation box of the ChLys-water-guaiacol system. Colour coding distinguishes IL charged groups, non-charged groups, water and guaiacol molecules. **b)** Cluster analysis of electrostatic interactions ($N-O_C$, 0-6.0Å), IL hydrogen bonding (donor-acceptor, 0-2.3 Å), and water clusters (H_W-O_W , 0-2.3Å), shows the fraction of cluster with a given size. Distance ranges are defined by the first coordination shell in $g(r)$. Theoretical percolation threshold (black line) is a probability function $p(n) = n^{-2.2}$ normalised to 1, based on reference¹⁶⁶.

An additional aromatic solute is accommodated into the solvent structure, without disrupting continuous networks of charged groups and hydrogen bonding species. Compared to previously studied alkylammonium and pyrrolidinium ILs, choline amino-acid ILs have at least three hydrogen bonding sites (hydroxyl, amino, and carboxylate groups) to interact with phenolic compounds. In ChLys, the solvent-solute interactions experience less geometric competition at short distances. These features of ChLys together with its amphiphilic nanostructure are important for aromatic dissolution and biomass processing. Having lignin solubilised into the non-charged domains with amino groups and possibly staying close to carboxylate groups may enhance the extraction efficiency.

Beyond liquid nanostructure and hydrogen bonding capacity, water mixtures of amino-acid based ILs are cheaper, easier to recycle and less viscous, which have been key challenges for using ionic liquids at the industrial scale.²⁰⁶ The presence of water facilitates the measurement of acidity and conductivity. These physicochemical properties of IL and their aqueous solutions are important factors to consider for catalysis, preservation of enzyme activities and electrochemical applications.²⁰

CHAPTER 4

ILS IN MICRO-EMULSIONS

Conventional microemulsions contain water and oil stabilised by a surfactant.²⁰⁷⁻²⁰⁸ Ionic liquids (ILs) as a new class of solvents can replace either the water or the surfactant component of a microemulsion, inducing molecular self-assembly at the nanoscale. We study liquid structure using three scattering techniques, as shown in Figure 4.0. Each technique provides structural information at a different length scale. We start with using small-angle X-ray scattering to screen various chemical combinations and compositions to generalise a structural trend (2-200Å). Several systems with the most interesting composition are selected for multi-contrast neutron experiments to investigate structural details. Small-angle neutron scattering combined with invariant analysis provides information on domains at the nanoscale (10-600Å). At the atomic level, neutron diffraction combined with simulation elucidates intra/intermolecular and some nanoscale features (0.5-30Å).

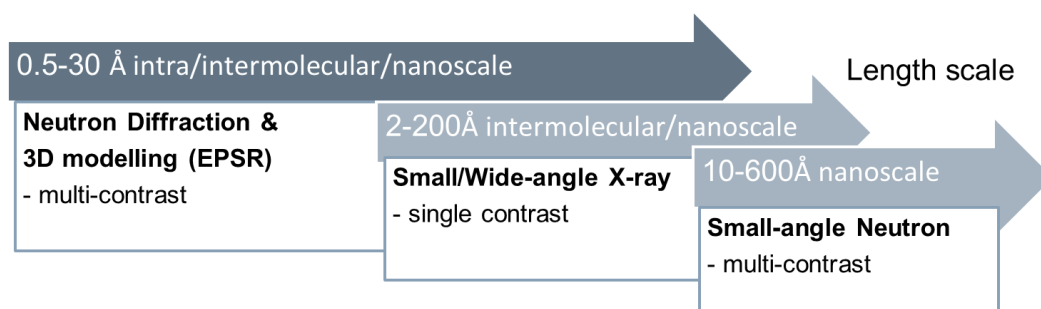


Figure 4.0 Three scattering techniques used in this work provide structural information from 0.5 to 600Å.

4.1 Introduction to Microemulsions

Microemulsions are nanostructured solutions containing hydrophilic, lipophilic and amphiphilic species, though macroscopically homogeneous and thermodynamically stable. The coexistence of polar and apolar components at the nanoscale makes microemulsions excellent nano-reactors and nano-carriers. They are key media for nano-material templating, delivering pharmaceuticals and food additives.^{93, 209-210}

Despite the original definition, the scope of microemulsions are not limited to a combination of water, oil and a surfactant. First reported in 1977, a short chain alcohol, 2-propanol, can replace the surfactant component to form a surfactant-free microemulsion in water.²¹¹ The nanostructure of the water-ethanol-octanol ternary system has been extensively studied and recently proposed as an *ultra-flexible microemulsion*, with details discussed in Chapter 1.^{97, 99, 102, 104, 106, 212} Since 1984, non-

aqueous microemulsions have been studied using small polar molecules, such as formamide, glycerol and ethylene glycol as water substitutes.²¹³⁻²¹⁵ The combination of a short-chain alcohol and a polar component creates surfactant-free water-free microemulsions.¹⁰¹ The presence of water or surfactant is no longer a necessary condition for molecules to self-organise into the nanoscale structure.

As molten salts, ionic liquids (ILs) have huge potential in material and colloid science for their tuneable properties with different combinations of cations and anions. For formulating non-conventional microemulsions, studies have used ILs as a polar component to replace water, an apolar component to replace oil, or replacing both polar and apolar components.²¹⁶⁻²¹⁹ To date, almost all studies on IL-containing microemulsions involve a surfactant, which itself can form a micellar structure in water.²¹⁹⁻²²⁰ As discussed in Chapter 1, while ILs share with water the rare ability to promote surfactant self-assembly, the fundamental yet remarkable difference is the amphiphilic character of neat ILs, which could contain both polar and apolar functional groups.^{33, 111} Unlike water and other molecular solvents, amphiphilic ILs encourage non-surfactants that are weak amphiphiles, such as alcohols, to self-assemble at the nanoscale.⁴³ An insight into the amphiphilicity of ILs will open up many opportunities, including tailored liquid nanostructure and highly functional materials.

Our current study expands the scope of amphiphilic self-assembly. We utilise ILs to formulate a matrix of microemulsions without the presence of a surfactant or water. Our systems are novel yet straightforward. All components are liquids at room temperature, thermally stable, easy to handle, non-halogenated and have low-toxicity. Two model protic ionic liquids were chosen, as shown in Figure 4.1: propylammonium nitrate (PAN) as an amphiphilic IL, and ethanolammonium nitrate (EtAN) as a non-amphiphilic IL.^{33, 173} Using phase diagrams and small-angle X-ray scattering (SAXS), we demonstrate the ability of PILs to create nanostructure, starting from binary mixtures. We further illustrate a systematic change in nanostructure by introducing a third component, and we establish a new matrix of IL-containing microemulsions with predictable structural behaviour.

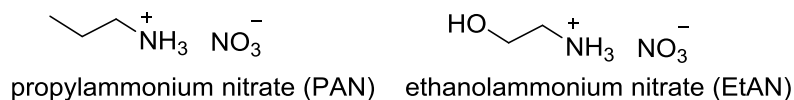


Figure 4.1. Structures of the ILs used in this work.

4.2 Amphiphilicity and Nanostructure

4.2.1 Ionic liquid – alkanol mixtures

An amphiphilic IL, such as PAN, is miscible with medium-to-long chain alkanols, such as octanol. A non-amphiphilic IL, such as EtAN, is only miscible with short-chain alcohols, such as ethanol.⁴³ To investigate structural details, Figure 4.2 shows SAXS of IL-alcohol mixtures in comparison to pure components. When mixing PAN with octanol, there is a significant increase in low- q scattering (Figure 4.2a), which is not a simple average of two pure components. Previous studies of PAN-octanol mixtures using X-ray scattering, neutron diffraction combined with simulation have shown a heterogeneous structural arrangement at the nanoscale.^{43, 53} The amphiphilic structure of PAN accommodates octanol hydroxyl groups into polar domains composed of IL charged groups, whereas non-polar domains composed of IL tails are swollen by octanol tails.

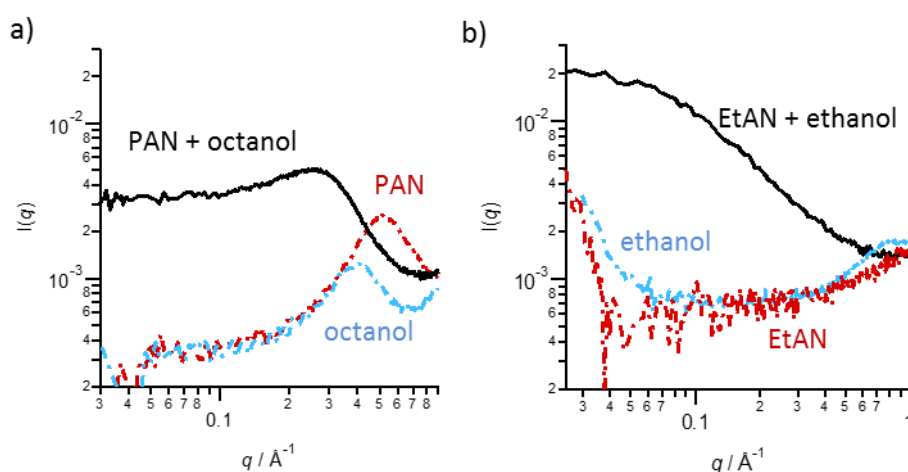


Figure 4.2 SAXS patterns of a) PAN, octanol and their binary mixture; b) EtAN, ethanol and their binary mixture at 298K, where $I(q)$ is the scattering intensity at angle q .^{43, 221}

A non-amphiphilic IL, EtAN, is only miscible with short-chain alcohols such as ethanol. Figure 4.2b shows SAXS of EtAN-ethanol mixtures in comparison to pure components. Similar to PAN-octanol, EtAN-ethanol mixture scatters intensively at low q . However, as both EtAN and ethanol are small molecules, the nanostructure is unexpected and the scattering pattern could only be explained by density fluctuation instead of polar-apolar association.²²²

To explore the role of EtAN and PAN in formulating microemulsion-type structure, we add a third component and use SAXS to screen a range of ternary mixtures containing one or two IL components. In Section 4.2.2, we compare PAN to a hydrotrope (in an aqueous environment) or a solvotrope (in a non-aqueous environment); In Section 4.2.3, we compare EtAN to water (as a polar

solvent), or a salt (as a polar additive). This leads to three different combinations with octanol as the apolar component, as shown in Table 4.1. In Section 4.2.4, we discuss an alternative approach of adding an apolar component to the PAN-octanol mixture to formulate microemulsion-type structure. Apolar molecules tested include octane, toluene and cyclohexane. We further show that octanol can be replaced by an aromatic species, guaiacol, formulating a different type of nanostructure.

Table 4.1 Ternary systems studied in this chapter using X-ray scattering.

an addition polar component	an additional apolar component	a different geometry
water-PAN-octanol	PAN-octanol-octane	
EtAN-ethanol-octanol	PAN-octanol-toluene	PAN-guaiacol-THF
EtAN-PAN-octanol	PAN-octanol-cyclohexane	PAN-guaiacol-cyclohexane

4.2.2 An amphiphilic IL as a ‘hydrotrope’

Different from surfactants, hydrotropes are amphiphilic molecules that do not form well-organised structures in water. As the solubility of a hydrotrope in water is much higher than a surfactant, hydrotropes can dramatically increase the miscibility between water and sparingly soluble organic molecules.²²³ Hydrotropes are a diverse class of molecules with different structural forms, from small aliphatic molecules to aromatic and saturated rings. One of the most common hydrotropes is ethanol, which has numerous commercial and pharmaceutical applications.²²⁴ Solutions containing alkanols show various advantages, including enhanced enzymatic activities and long lasting effect in olfaction.²²⁵⁻²²⁶ Diat et al. extensively studied the structural behaviour of the water-ethanol-octanol system, which is a model system of surfactant-free microemulsions containing a hydrotrope, as discussed in Chapter 1.^{101, 104, 106} Here we design an IL-containing system, water–PAN–octanol, to explore how IL-alcohol mixtures differ from conventional water-surfactant-oil and water-hydrotrope-oil systems.

Figure 4.3a shows the phase diagram of the water-PAN-octanol ternary system. PAN is completely miscible with either water or octanol at RT. Although water and octanol are immiscible, the presence of PAN creates a single-phase region that contains a fraction of water and octanol. In the two-phase region, tie-lines point towards the composition of separated layers at equilibrium. When using PAN as amphiphile, tie-lines are highly tilted. A sample inside of this two-phase region separates into two layers: one is octanol-rich, the other is water- and PAN-rich. In comparison, a hydrotropic system, water-ethanol-octanol, has flat tie-lines, indicating a near-equal distribution of ethanol in water and octanol layers, shown in Appendix Figure B1.1. Details of ternary phase diagrams were discussed in Section 2.2.2.

We investigate liquid nanostructure by SAXS at various compositions in the single-phase region, shown in Figure 4.3b. Without the addition of water, scattering patterns (black lines) show an increase in intensity at low angle, followed by a decrease as going from PAN-rich to the octanol-rich region. This means the nanostructure of PAN-octanol changes non-monotonically.

As water concentration increases from 5, 10 to 20wt%, there is an increase in scattering intensity across all PAN:octanol ratios. The maxima observed in PAN-octanol binary mixtures gradually disappear, merging with low-angle scattering. The nanostructure detected in the water-PAN-octanol ternary system is neither a simple average of pure components nor an average of PAN-octanol and water-PAN binary solutions. Results show a smooth transition of liquid nanostructure without any abrupt change of structural periodicity and shape. The addition of water modifies liquid nanostructure, which is different from a random distribution.

At any given water content, varying the PAN-octanol ratio results in a similar trend, a non-monotonic change, as observed in the PAN-octanol binary system. This correlation means that the formulation of the binary system, possibly the underlying liquid structure, is vital in controlling the nanostructure of ternary systems.

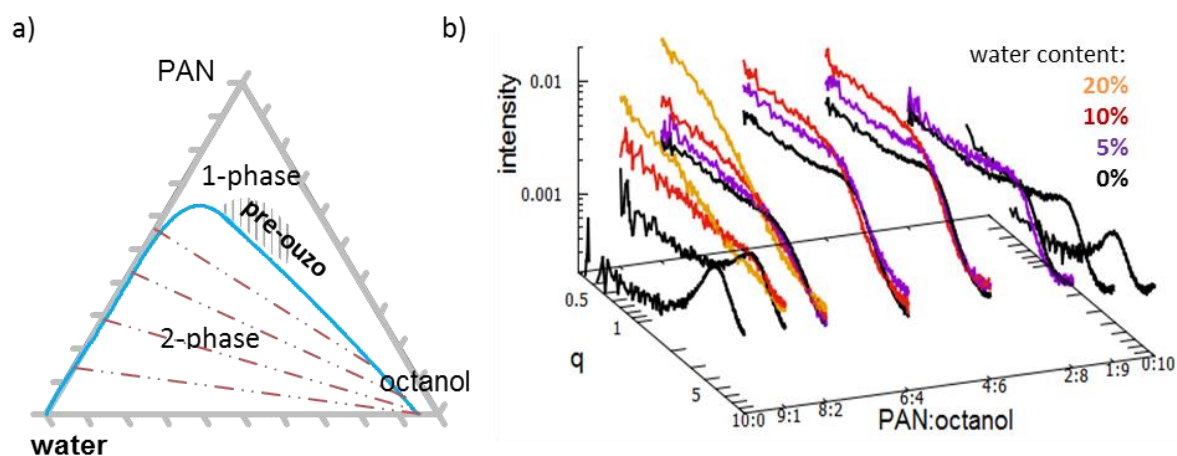


Figure 4.3 water-PAN-octanol ternary system at 298K a) Ternary phase diagram. The solid line is the phase boundary. Dotted lines in the two-phase region are tie-lines, measured by $^1\text{H-NMR}$. The shaded area is the pre-ouzo region. b) SAXS of water-PAN-octanol single-phase mixtures at various compositions. Water content increases from 0 to 20wt%. See Appendix Figure B2.1 for detailed 2D scattering and sample compositions.

In the water-ethanol-octanol system, of which ethanol is the amphiphile, SAXS and neutron scattering studies show experimental evidence of nanoscopic domains, one water-rich and one octanol-rich.²²⁷ Specific compositions that show such molecular association at the nanoscale were denoted as the pre-ouzo compositions. These compositions are in the single-phase region, lying close to the critical point where the length of tie-lines goes to zero.¹⁰⁷ Similarly, nanoscopic domains were observed in a water-free environment, when replacing water by a polar component such as glycerol

or deep eutectics. SAXS and dynamic light scattering show a monotonic change from negligible to intense low- q scattering and well-defined time-correlation functions as compositions get closer to the pre-ouzo region.¹⁰¹ These aggregate fluctuations are independent of critical fluctuations, as they occur even far from the phase boundary.

In water-PAN-octanol, we also observe the most intense low- q scattering in the pre-ouzo region, estimated according to the direction of tie-lines in Figure 4.3a. This suggests that the addition of water further modifies the liquid nanostructure from what has been determined in the PAN-octanol binary mixture. It is possible that there are water-rich and octanol-rich domains, just like what has been observed in the water-ethanol-octanol system discussed above.

4.2.3 A non-amphiphilic IL as a ‘salt’

A non-amphiphilic IL, EtAN, shares structural similarities with water as they both are polar species and lack of long-range periodicity. Therefore, we can substitute a water-containing system by EtAN, which creates non-aqueous systems. Figure 4.4 shows phase diagrams of EtAN-ethanol-octanol and EtAN-PAN-octanol systems. Ethanol-octanol is a molecular mixture, its ability to accommodate a non-amphiphilic IL is limited. In comparison, PAN-octanol is an ionic mixture; it can accommodate more EtAN than molecular solvents. A detailed comparison is shown in Appendix Figure B1.2.

To understand structural change along the phase boundary, a range of compositions and their corresponding SAXS patterns are shown in Figure 4.4. Considering the structure of corresponding binary systems, the IL-alcohol side is nanostructured, whereas the IL-IL or the alcohol-alcohol side is less structured. Moving from binary to ternary mixtures, an additional component causes a significant increase in low- q scattering, possibly due to an enhancement in molecular segregations into domains at the nanoscale. For example, adding a small amount of octanol to an EtAN-ethanol mixture (Figure 4.4a, grey) results in a higher scattering intensity at low- q , meaning a more pronounced nanoscale structure in the ternary mixture. Similarly, a small amount of octanol in an EtAN-PAN mixture (Figure 4.4b, purple) gives low- q scattering, meaning the mixture is nanostructured. These are consistent with conclusions drawn from the water-PAN-octanol, as characteristics of IL-containing microemulsion systems.

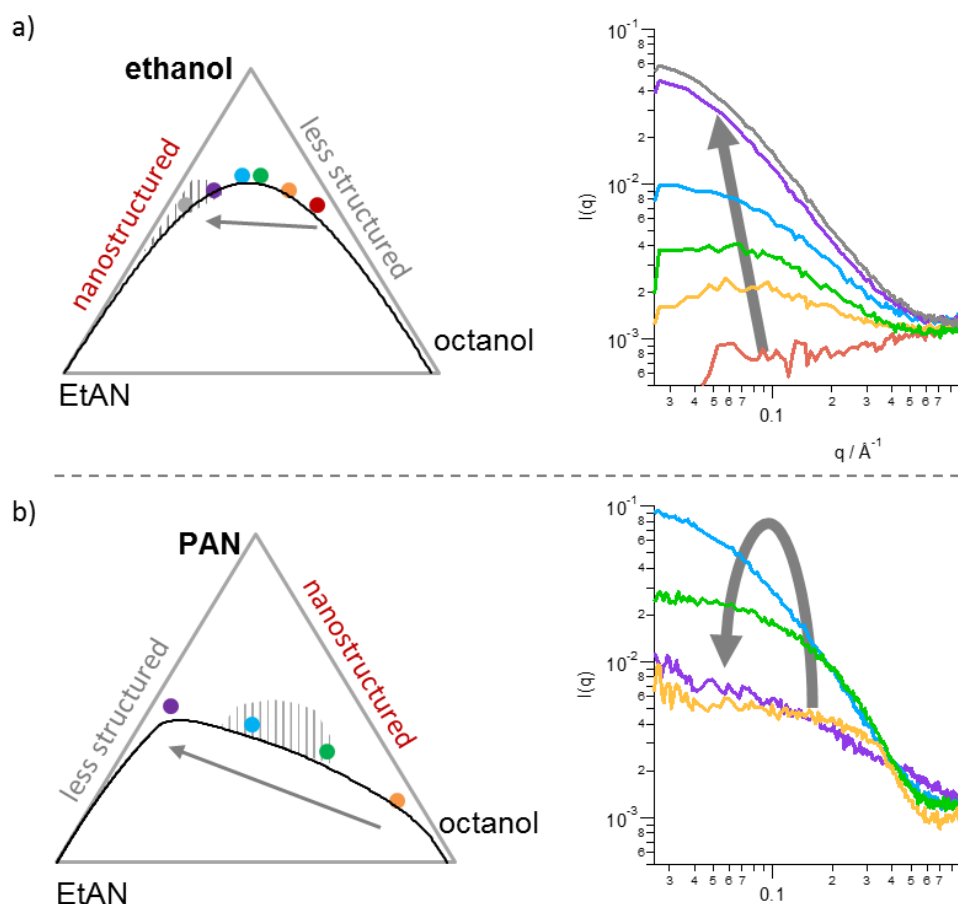


Figure 4.4 A comparison between PAN and ethanol as an amphiphile. Phase diagrams and SAXS of a) EtAN-ethanol-octanol b) EtAN-PAN-octanol along the phase boundary at 298K. Sample compositions are labelled in the corresponding phase diagram. Shaded areas indicate the pre-ouzo region with the most pronounced nanostructure.

As moving from the octanol-rich to EtAN-rich region, shown by the grey arrow, the trend in scattering is system-dependent. The scattering of EtAN-ethanol-octanol samples, as shown in Figure 4.4a, shows a monotonic change in scattering. The liquid nanostructure becomes more pronounced as moving towards the EtAN-ethanol(1:1) side. We designate this area as the pre-ouzo region, as shown in the phase diagram. This indicates highly tilted tie-lines (with positive gradients) in the two-phase region. An immiscible sample phase separates into an EtAN-rich layer and an ethanol/octanol-rich layer.

In comparison, the scattering of the EtAN-PAN-octanol system, shown in Figure 4.4b, shows a non-monotonic change in structure. The most pronounced structure has a near-equal composition of all components, labelled as the pre-ouzo region in the phase diagram. This indicates tilted tie-lines (with negative gradients) in the two-phase region. An immiscible sample separates into an EtAN/PAN-rich phase and an octanol-rich phase.

4.2.4 A matrix of IL-induced microemulsions

We can further extend our matrix by adding an apolar component, such as octane. Figure 4.5a shows the phase behaviour of the PAN-octanol-octane system, where PAN is immiscible with octane, octanol induces the miscibility between an IL and an oil. The solubilising ability of octanol is due to its amphiphilic structure, which contains a hydroxyl group that is capable of hydrogen bonding, and an alkyl chain that is solvophobic. Changing the alcohol tail length only causes slight shifts of the phase boundary, shown in Appendix Figure B1.3.

To study the structural influence of adding an apolar component, Figure 4.5b shows scattering patterns as a function of octanol: PAN ratio, with increasing octane concentration from 0, 10, 20 to 40%. Different from the water-PAN-octanol system, where water can be accommodated into PAN-rich compositions, octane can be accommodated into the octanol-rich compositions. Like the water-PAN-octanol system, the structure of ternary PAN-octanol-octane mixtures is closely related to the PAN-octanol formulation. As octane concentration increases, there is an increase in scattering intensity, meaning an enhancement in nanoscale structure.

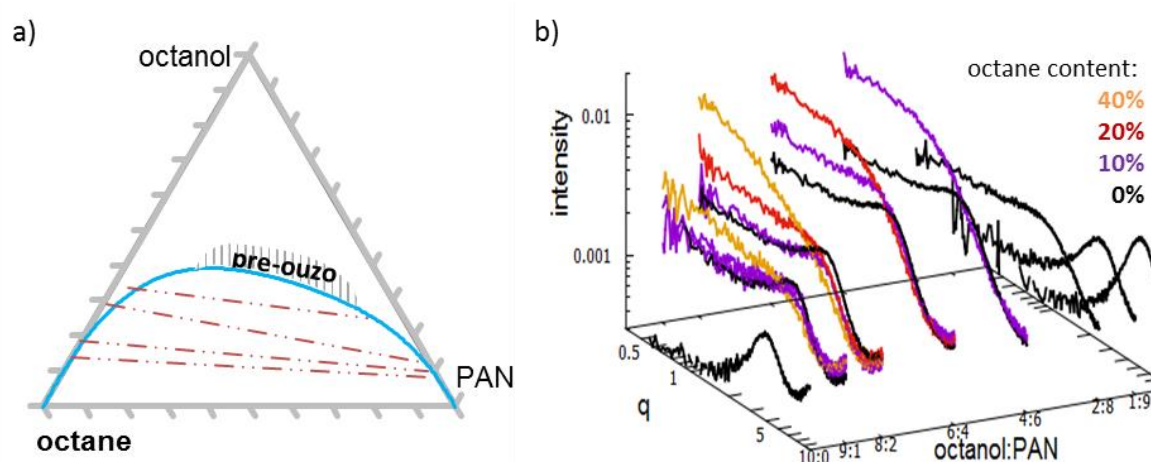


Figure 4.5 The octane-octanol-PAN system at 298K a) ternary phase diagram (wt%) b) SAXS at various octanol: PAN ratios, with increasing octane content from 0, 10, 20, 40 wt%. See Appendix Figure B2.2 for detailed 2D scattering and sample compositions.

When a non-surfactant additive induces miscibility of two immiscible components, nanostructure does not always form. Although the water-ethanol-octanol system is nanostructured in the pre-ouzo region, the solution of ethanol-octanol-octane is rather homogeneous. This means that ethanol could neither segregate to form a polar domain, nor support the segregation of octanol and octane. Our results show that IL-containing ternary systems could behave differently, such as the nanostructured **PAN**-octanol-octane system in contrast to the homogenous **ethanol**-octanol-octane.

Our SAXS results have shown that PAN supports the segregation of octanol and octane, which is a special characteristic that molecular solvents do not have.

So far, we have discussed four IL-containing systems that show systematic changes in low- q scattering as a function of the formulation. Their representative scattering patterns at pre-ouzo compositions are summarised in Figure 4.6a. Density fluctuation is an important factor to consider when interpreting low- q scattering in these systems.⁵⁴ Studies have also shown distinctions between the formation of molecular aggregates and fluctuations in molecular concentrations, though both produce Ornstein-Zernike scattering functions and diverging scattering intensities near the critical point, as discussed in Chapter 1.^{97, 107} Detailed structural studies of neat EtAN, neat PAN, EAN-water and PAN-octanol mixtures have shown hierarchical arrangement of species controlled by electrostatic interactions, hydrogen bonding, the geometry of ion headgroups and solvophobic association.^{33, 42, 53} Extended from previous studies, we hypothesise that scattering from the proposed ternary systems in this project is due to molecular segregation supported by ionic liquids, which we will validate using SANS, invariant analysis, neutron diffraction combined with simulation later in this Chapter.

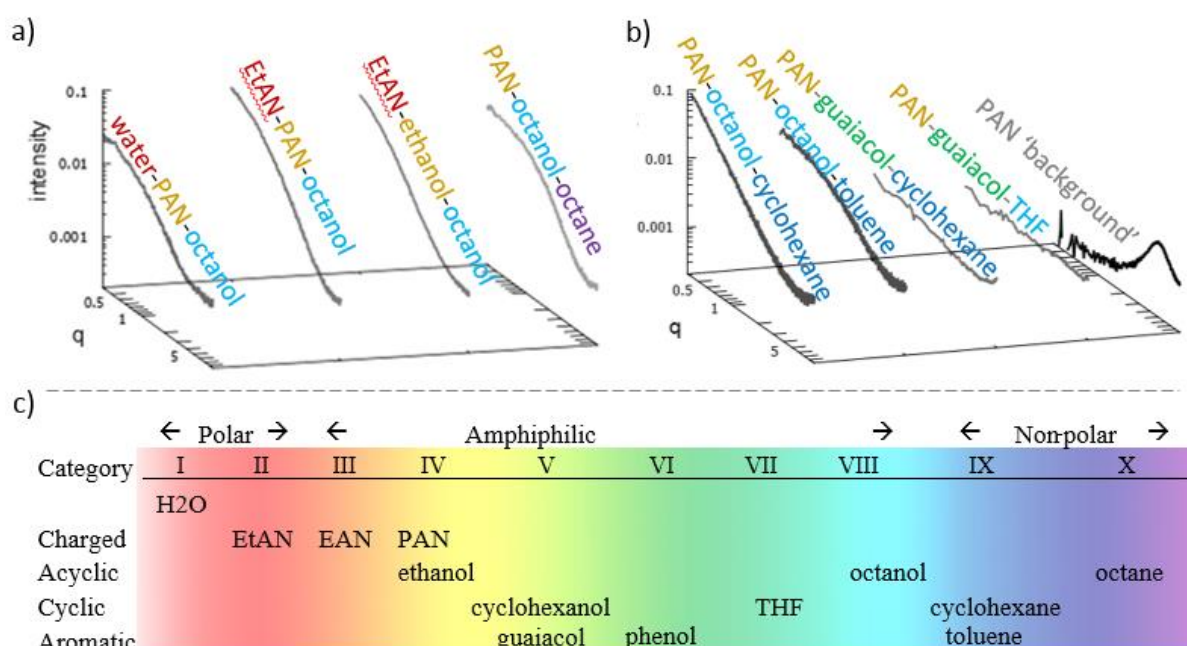


Figure 4.6 a-b) SAXS patterns of aliphatic, cyclic and aromatic systems in the pre-ouzo region. Components were colour-coded according to c) an amphiphilicity spectrum with geometric categories.

To design IL-containing nanostructured liquids, the core idea is to create polarity difference among components. This is because two immiscible components (i.e. one polar and one apolar) can potentially segregate into different domains, as it is in traditional microemulsions. Based on systems studied in this project, we propose a polarity scale that considers miscibility, amphiphilicity, electrostatic interactions, and molecular packing geometry, as shown in Figure 6c. Either water or

EtAN can act as a polar component. Either PAN or ethanol can act as an amphiphile. The amphiphilicity of octanol depends on the solvent environment – it acts as an apolar component in water-PAN-octanol, EtAN-PAN-octanol or EtAN-ethanol-octanol systems; whereas it acts as an amphiphile in the PAN-octanol-octane ternary system. Like conventional microemulsions, our ternary mixtures contain a polar component, an apolar component, and an amphiphile.

IL-induced nanostructured systems are not restricted to aliphatic compounds. Figure 4.6b shows scattering patterns of systems with cyclic or aromatic compounds. In these systems, PAN acts as the polar component; either guaiacol (2-methoxy-phenol) or octanol acts as the amphiphile; cyclohexane, toluene or THF acts as the apolar component. When replacing the aliphatic octanol with the aromatic guaiacol molecule, the resulting scattering of the PAN-guaiacol-cyclohexane system is dramatically different from the PAN-octanol-cyclohexane system. Interestingly, THF can act as the apolar component in the PAN-guaiacol-THF ternary mixture, with low- q scattering that is higher than the background (neat PAN). Depending on the molecular geometry of individual components, whether it is aliphatic (alkanols), cyclic (THF and cyclohexane) or aromatic (guaiacol), the intensity and the shape of resulting scattering curves change, meaning a change in the liquid nanostructure. To establish a comprehensive matrix of IL-containing microemulsions, it is important to categorise components based on its molecular structure in addition to the amphiphilicity scale, as shown in Figure 4.6c.

4.3 Domains at the Nanoscale with Distinct Polarities

X-ray scattering results showed intense low- q scattering in the pre-ouzo region. To distinguish between critical fluctuation and molecular segregation, we choose pre-ouzo samples for further structural studies using neutron scattering. In each system, different isotopic substitutions represent an identical chemical environment and liquid structure. Since hydrogen and deuterium have such different scattering lengths, substitution of one for the other allows selective changes in the contrast within a molecule. Combined with simultaneous analyses of multiple contrasts, this allows for selective isolation of molecular components contribution to the nanostructure. This rationale applies throughout this thesis. In this section, we qualitatively analyse neutron scattering patterns, followed by quantitative calculations using invariant analysis. Details of scattering length densities (SLDs) and invariant calculations were explained in Chapter 2.

4.3.1 PAN-octanol with an additional polar component

The water–PAN–octanol system, for example, has three contrasts. For the $D_2O-C_3H_7ND_3NO_3-C_8H_{17}OD$ contrast, exchangeable protons are deuterated to highlight polar head groups. For the $H_2O-C_3H_7NH_3NO_3-C_8D_{17}OH$ contrast, only the octanol tail is deuterated to highlight the octanol molecules. Finally for the $D_2O-C_3H_7ND_3NO_3-C_8D_{17}OD$ contrast, the exchangeable protons and octanol tails are both deuterated to reveal the behaviour of the IL tails. In SANS curves, the plateau at high q near $0.4-0.6\text{\AA}^{-1}$ is the baseline, which is mainly incoherent scattering. As the incoherent scattering length of deuterium is much lower than hydrogen, deuterium-rich samples typically give a lower baseline. A small peak at 0.5\AA^{-1} is a signature of IL nanostructure and can make it difficult to reference the baseline. Our focus, however, is within the low q region ranging from 0.01 to 0.4\AA^{-1} . Main features to notice are: 1) the difference between maxima and minima (i.e. $I(0.01) - I(0.6)$). This is known as the coherent scattering, which reveals the extent of the structure; 2) the shape of the shoulder, which indicates the structure type; and 3) the position of the shoulder, which is related to the length scale of the nanostructure.

Figure 4.7a shows SANS patterns of the PAN–octanol binary system without the addition of a polar component. Both $C_3H_7NH_3NO_3-C_8D_{17}OH$ and $C_3H_7ND_3NO_3-C_8D_{17}OD$ produce clear contrasts, indicating nano-segregations of either PAN tails or octanol tails. When adding 20wt% water to the binary system, shown in Figure 4.7b, the coherent scattering intensity of all three scattering curves increases dramatically. This suggests an enhancement in the liquid nanostructure as opposed to a dilution process. As observed previously from SAXS experiments, water and EtAN share common properties in designed ternary systems. When replacing water by EtAN, shown in figure 4.7c, the intensity of coherent scattering increases just like in the water system.

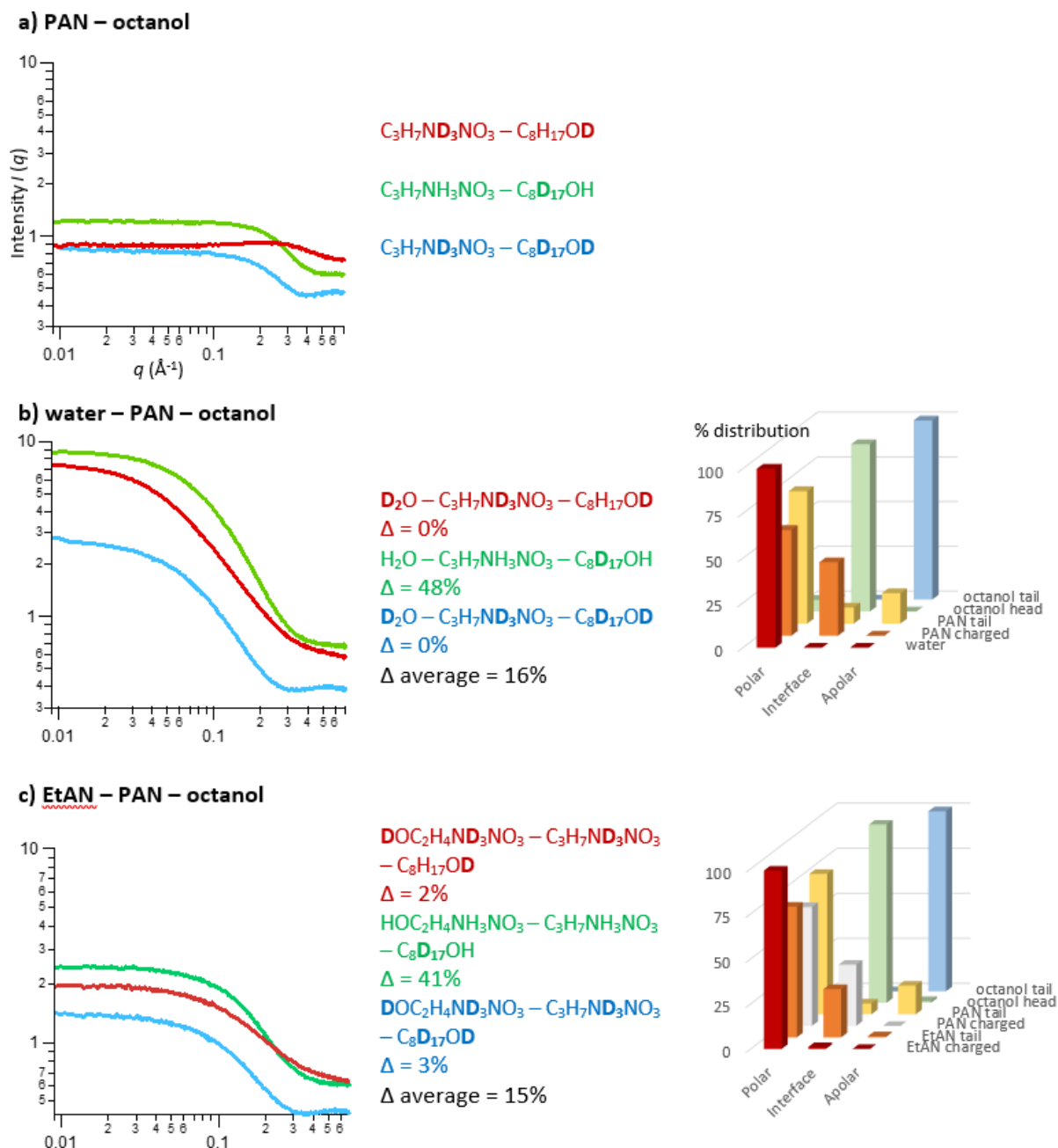


Figure 4.7 PAN–octanol with an additional polar component; SANS patterns with multiple contrasts at 298K (labels shown in colour), their corresponding Δ (% difference between experimental and theoretical invariant), and the distribution of species across domains. a) PAN–octanol (3:1), b) water–PAN–octanol (20:60:20), and c) EtAN–PAN–octanol (30:52.5:17.5). Ratios by wt. based on the fully hydrogenous sample. Deuterated samples have the same molar composition.

Qualitative analysis of scattering patterns is useful in drawing general trends of each system. As scattering patterns are two-dimensional profiles derived from three-dimensional information, it is challenging to make direct comparisons in Fourier space. Moreover, coherent and incoherent SLDs are different for each component. The resulting contrast is not linearly related to the functionality of the ‘highlighted’ component. For example, the coherent SLD of D_2O is higher than d_4 -EtAN. The fact that water–PAN–octanol pre-ouzo system produces larger contrasts does not necessarily mean a more pronounced liquid structure. Quantitative justification is required for detailed structural analysis.

Model fitting is one common method to quantitatively analyse scattering data. Although both systems show pronounced structures at the nanoscale, neither can be unambiguously resolved by geometric models. These fitting methods include polydisperse spheres, rods and bi-continuous models such as the Debye-Anderson-Brumberger method.²²⁸ Results show that each contrast could be described by several models that all yielded plausible aggregate dimensions. A single model could not systematically fit all contrasts and compositions. Examples of using the Debye-Anderson-Brumberger method to systematically fit water-PAN-octanol systems are shown in Appendix C. Moreover, the simultaneous model fitting of multiple contrasts leads to relatively large uncertainties.

The analysis of these non-conventional systems requires methods that are structure-independent. We consider two immiscible components to form separate domains, and the amphiphilic molecule is either partitioning in between (i.e. a two-domain model) or accumulating at the interface and forming its own domain (i.e. a three-domain model). This approach is inspired by scattering studies on systems containing aqueous hydrotropes.¹⁰⁴ For example, if we assume a system with only three scattering length densities, our complex fluids are simplified into three domains, denoted A, B and C.¹³⁵ This assumption allows an invariant calculation on the system, as described in Section 2.5.2, which simultaneously fits all three contrasts from SANS experiments. This model minimises the difference between experimental and theoretical invariants (Δ), generating a distribution of individual components in each domain.

The invariant analysis starts from a two-domain model with only three variables representing three components in the ternary mixture. In the case of experimental data showing strong evidence of an additional type of segregation that could not be captured by the two-domain model, we gradually increase the number of variables and consider the three-domain model to better describe SANS data. In Appendix D, we show quantitative results from both two-domain and three-domain models, with a detailed discussion of multi-variable setups, and an example system to illustrate our approach. Models that rationally fit to experimental data were summarised in Figures 4.7-9.

Figure 4.7b-c shows that invariant calculations generate a clear polarity distinction among domains, even though no such constraint is input into the model. In the water-PAN-octanol system, all water and most PAN molecules stay within the same type of domain, forming polar regions. All octanol tails and few PAN tails form a second type of domain, hence apolar regions. Over 90% of the octanol hydroxyl group and 40% of PAN charged groups form the third type of domain, denoted as interfacial regions.

Similar polarity distributions are observed in the EtAN-PAN-octanol system. Most ionic liquid species form a polar domain, while all octanol tails and few PAN tails form an apolar domain. All

octanol head groups and few ionic liquid species form the interface. We hypothesise that interactions among functional groups at the interface are essential in driving the macroscopic miscibility between polar and apolar components.

There is a good agreement between experimental and theoretical invariant, except for contrasts with deuterated octanol tails ($\text{H}_2\text{O}-\text{C}_3\text{H}_7\text{NH}_3\text{NO}_3-\text{C}_8\text{D}_{17}\text{OH}$ and $\text{HOC}_2\text{H}_4\text{NH}_3\text{NO}_3-\text{C}_3\text{H}_7\text{NH}_3\text{NO}_3-\text{C}_8\text{D}_{17}\text{OH}$). One key assumption made in invariant calculations is that species are homogeneously mixed within each domain. A 40-50% inconsistency suggests that octanol tails and PAN tails do not behave like an ideal solution in the apolar domains.

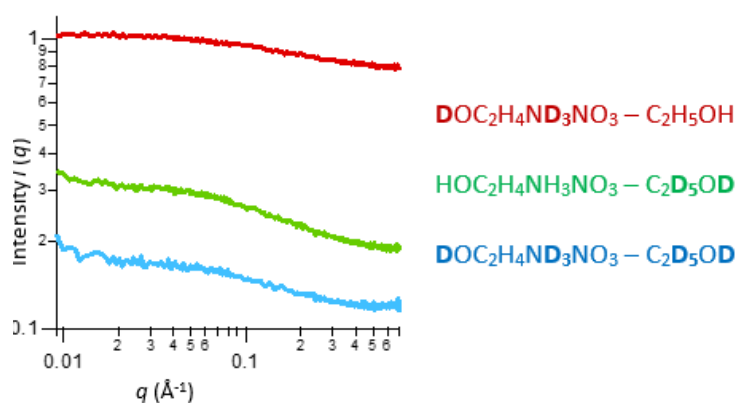
In the water-PAN-octanol system and the EtAN-PAN-octanol system, invariant analysis has shown a distinct distribution of species forming polar, interfacial and apolar domains. This is a significant step forward over X-ray scattering profiles alone. Both water and EtAN behave as polar solvents and they do not go near the apolar hydrocarbons.

4.3.2 EtAN-ethanol with the addition of octanol

The EtAN-ethanol-octanol system, shown in Figure 4.8, is an extension of hydrotropic systems. For the $\text{DOC}_2\text{H}_4\text{ND}_3\text{NO}_3-\text{C}_2\text{D}_5\text{OD}-\text{C}_8\text{H}_{17}\text{OD}$ contrast, exchangeable protons and ethanol hydrocarbons are deuterated, highlighting the octanol hydrophobic tails. For the $\text{DOC}_2\text{H}_4\text{ND}_3\text{NO}_3-\text{C}_2\text{H}_5\text{OH}-\text{C}_8\text{D}_{17}\text{OH}$ contrast, exchangeable protons on EtAN are deuterated, revealing the ethanol and EtAN tails. Finally for the $\text{HOC}_2\text{H}_4\text{NH}_3\text{NO}_3-\text{C}_2\text{D}_5\text{OD}-\text{C}_8\text{D}_{17}\text{OH}$ contrast, both ethanol and octanol are deuterated, leaving EtAN as hydrogenous.

Without the presence of octanol, three contrasts in the binary system are similar in shape (see Figure 4.8a). When scattering curves can be scaled and superimposed, the system is experiencing critical fluctuations, which are changes in molecular concentrations and often occur near the critical point of a phase diagram.¹⁰⁶ This explains the intense low- q scattering of the EtAN-ethanol system in SAXS. However, three contrasts respond differently with the addition of 10wt% octanol. Contrast $\text{HOC}_2\text{H}_4\text{NH}_3\text{NO}_3-\text{C}_2\text{D}_5\text{OD}-\text{C}_8\text{D}_{17}\text{OH}$, shows the most dramatic change. Critical fluctuation is clearly not the case for ternary systems and there is a different underlying structure at the nanoscale.

a) EtAN – ethanol



b) EtAN – ethanol – octanol

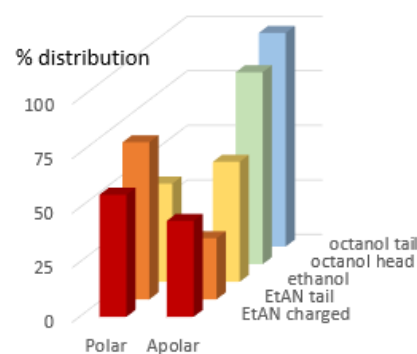
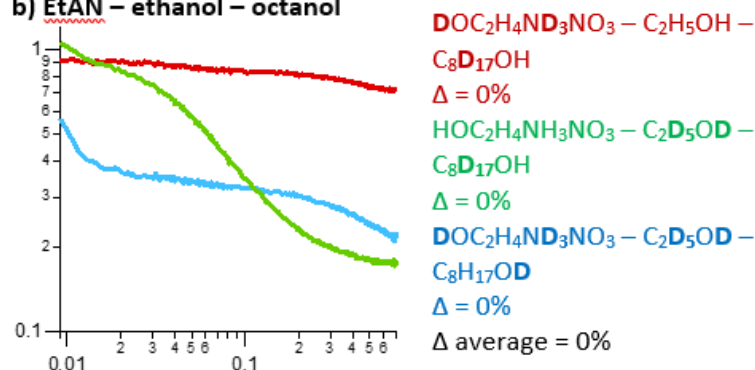


Figure 4.8 EtAN–ethanol with an additional apolar component; SANS patterns with multiple contrasts at 298K (labels shown in colour), their corresponding Δ (% difference between experimental and theoretical invariant), and the distribution of species across domains. a) EtAN–ethanol (1:2), and b)EtAN–ethanol–octanol (30:60:10. Ratios by wt. based on the fully hydrogenous sample. Deuterated samples have the same molar composition.

The invariant analysis can be described by a separation of functional groups into two domains with distinct polarity. More than half of EtAN molecules combined with some ethanol form the polar domain. Most of the octanol molecules, half of the ethanol, and a fraction of EtAN form the relatively apolar domain. Previously in the water-PAN-octanol and the EtAN-PAN-octanol systems, the invariant analysis was described by domains with distinct polarity differences. When we replace PAN with ethanol, it is surprising to see a non-negligible amount of EtAN charged groups in the same domain as the apolar hydrocarbons. It is possible that the “apolar” domain is structurally inhomogeneous. Fitting the data into with a three-domain model will not provide additional information, as the current two-domain model gives a 0% error, which could not be further reduced.

In Section 4.3.1, we have discovered that EtAN mimics the role of water by contributing to the polar domain. Here we observed that the structural response of the EtAN-ethanol mixture and the water-PAN mixture is similar to the addition of octanol as the apolar component. Both solvent environments support additional octanol molecules to aggregate into structure at a different length scale compared to the pre-existing solvent structure. The structural behaviour of PAN is similar to ethanol, which is a hydrotrope in aqueous systems. Both PAN and ethanol are amphiphilic, but neither

self-assemble into a well-defined micellar structure in water. Moreover, the original definition of 'hydrotropic' is with regards to water and most studies were conducted within the context of aqueous solutions. Our study establishes the solvotropic behaviour of ethanol and PAN in non-aqueous systems.

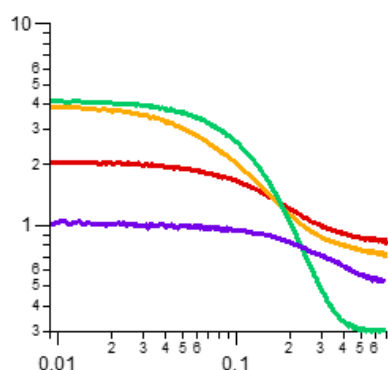
4.3.3 PAN-octanol with an additional apolar component

In Section 4.2, we screened a range of microemulsions formulated by adding an apolar component to PAN-octanol mixtures using X-ray scattering. Compounds with different geometries (e.g. linear or cyclic) led to different types of the liquid nanostructure. Here we use neutron scattering and invariant analysis to show nanoscale distributions in three systems: PAN–octanol–octane, PAN–octanol–cyclohexane, and PAN–octanol–toluene.

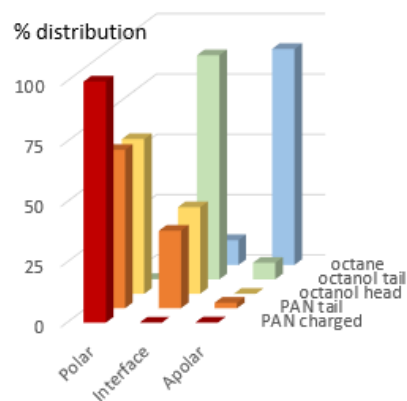
In the PAN–octanol binary system, as previously described in Figure 4.8a, there is no significant long-range order among polar groups. With the addition of octane, all four contrasts show nanoscale periodicity (Figure 4.9a). Intense low q scattering is observed for contrast C_8D_{18} – $C_8D_{17}OH$ – $C_3H_7NH_3NO_3$ and C_8D_{18} – $C_8H_{17}OH$ – $C_3H_7NH_3NO_3$. Since both samples highlight aliphatic chains, it is likely that octanol and octane aggregate to form solvophobic domains.

To find out if octanol and octane aggregate together, and if the solvophobic domain is structured in any fashion, an important feature to examine is the low contrast in sample C_8H_{18} – $C_8D_{17}OH$ – $C_3H_7NH_3NO_3$, despite the presence of 40 wt% octanol. This suggests a loose distribution of octanol, rather than aggregations by a single molecular type. Conversely, C_8D_{18} – $C_8H_{17}OH$ – $C_3H_7NH_3NO_3$ gives intense scattering at low q , indicating a likelihood of finding octane-only domains. When highlighting both octane and octanol, C_8D_{18} – $C_8D_{17}OH$ – $C_3H_7NH_3NO_3$ shows a significant enhancement in low q scattering compared to either C_8H_{18} – $C_8D_{17}OH$ – $C_3H_7NH_3NO_3$ or C_8D_{18} – $C_8H_{17}OH$ – $C_3H_7NH_3NO_3$. This leads to a conclusion that some octanol aggregates with octane. In addition, sample C_8H_{18} – $C_8H_{17}OD$ – $C_3H_7ND_3NO_3$ gives a weak contrast, possibly due to structured, but relatively discrete, polar domains.

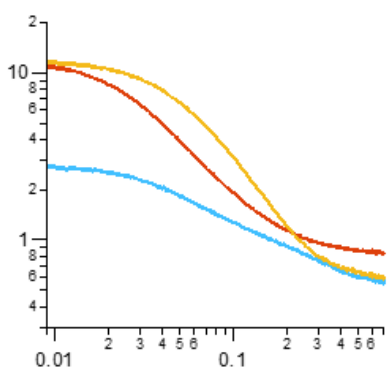
a) PAN – octanol – octane



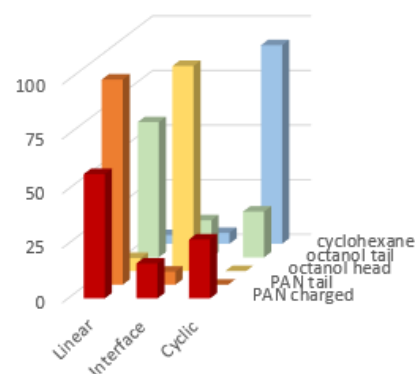
$C_3H_7ND_3NO_3 - C_8H_{17}OD - C_8H_{18}$
 $\Delta = 0\%$
 $C_3H_7NH_3NO_3 - C_8H_{17}OH - C_8D_{18}$
 $\Delta = 0\%$
 $C_3H_7NH_3NO_3 - C_8D_{17}OH - C_8H_{18}$
 $\Delta = 0\%$
 C_8D_{18}
 $\Delta = 0\%$
 $C_3H_7NH_3NO_3 - C_8D_{17}OH - C_8H_{18}$
 $\Delta = 0\%$
 Δ average = 0%



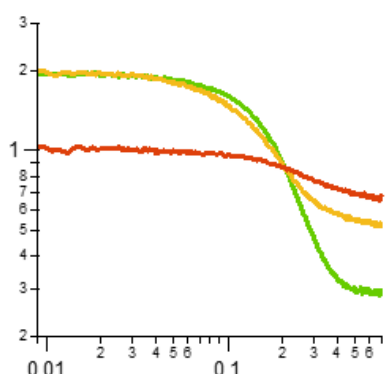
b) PAN – octanol – cyclohexane



$C_3H_7ND_3NO_3 - C_8H_{17}OD - C_6H_{12}$
 $\Delta = 0\%$
 $C_3H_7NH_3NO_3 - C_8H_{17}OH - C_6D_{12}$
 $\Delta = 0\%$
 $C_3H_7ND_3NO_3 - C_8D_{17}OH - C_6H_{12}$
 $\Delta = 0\%$
 Δ average = 0%



c) PAN – octanol – toluene



$C_3H_7ND_3NO_3 - C_8H_{17}OD - C_7H_8$
 $\Delta = 0\%$
 $C_3H_7NH_3NO_3 - C_8H_{17}OH - C_7D_8$
 $\Delta = 39\%$
 $C_3H_7NH_3NO_3 - C_8D_{17}OH - C_7D_8$
 $\Delta = 0\%$
 Δ average = 13%

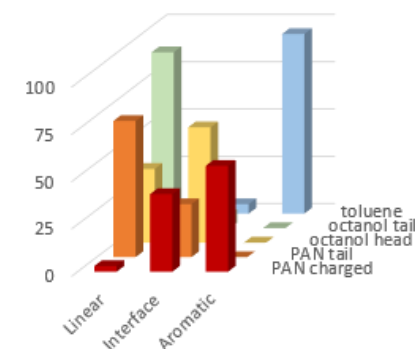


Figure 4.9 PAN–octanol with an additional apolar component; SANS patterns with multiple contrasts at 298K (labels shown in colour), their corresponding Δ (% difference between experimental and theoretical invariant), and the distribution of species across domains. a) PAN–octanol–octane (40:40:20), b) PAN–octanol–cyclohexane (34:32:34), and c) PAN–octanol–toluene (38:24:38). Ratios by wt. based on the fully hydrogenous sample. Deuterated samples have the same molar composition.

The distribution chart in Figure 4.9a shows that all PAN charged groups, most of PAN tails and octanol head groups form a polar domain. Octane molecules and a small number of octanol tails form an octane-rich apolar domain. Over 90% of octanol tails, some PAN tails and octanol headgroups form a separate domain, which could be considered as an interface or an octanol-rich apolar domain. There is a significant improvement in Δ when going from a 2-domain model (polar–apolar) to a 3-domain model (polar–interface–apolar), shown in Appendix D. Invariant analysis is consistent with our qualitative observation from SANS patterns.

Cyclohexane and toluene were added as the apolar component instead of octane, to explore how the liquid nanostructure responds to cyclic and aromatic molecules. Figure 4.9b shows scattering patterns of the PAN–octanol–cyclohexane system. Intense low q scattering is observed for contrasts $C_3H_7ND_3NO_3-C_8H_{17}OD-C_6H_{12}$ and $C_3H_7NH_3NO_3-C_8H_{17}OH-C_6D_{12}$. The first contrast highlights polar headgroups. The position of the scattering minima is low, meaning a large periodicity between polar domains. The second contrast highlights cyclohexane molecules. It is possible that this system contains a cyclohexane-rich domain.

In the PAN–octanol–toluene system, shown in Figure 4.9c, the scattering intensity is low for the $C_3H_7ND_3NO_3 - C_8H_{17}OD - C_7H_8$ contrast, which highlights polar headgroups. Different from cyclohexane, the additional toluene does not induce intense low- q scattering. The other two contrasts, $C_3H_7NH_3NO_3 - C_8H_{17}OH - C_7D_8$ and $C_3H_7NH_3NO_3 - C_8D_{17}OH - C_7D_8$, which highlight toluene and octanol respectively, both show intense low q scattering. We expect to see toluene-rich and octanol-rich domains.

The invariant analysis shows interesting distribution patterns. In the PAN–octanol–cyclohexane system, most of the octanol tail, PAN tail and some PAN head groups form one type of domain, whereas cyclohexane molecules form a separate type of domain. Instead of denoting the two types of domains based on polarity, it is more rational to classify the domains based on molecular geometry. Results show that cyclic molecules form a separate domain away from linear molecules. Similar trends were observed in the PAN–octanol–toluene system. There is a toluene-rich domain with some PAN charged groups, an octanol-rich domain with most PAN tails, and an interfacial domain with small species. Such distribution further highlights the impact of molecular geometry on the liquid nanostructure. Toluene, as an additional aromatic species, forms a separate domain away from linear octanol tails and PAN tails.

There is a good agreement between experimental and theoretical invariants, except for the $C_3H_7NH_3NO_3 - C_8H_{17}OH - C_7D_8$ contrast, which highlights toluene molecules. An important criterion of invariant calculation is to have homogenous phases; each has an averaged scattering length density. If the toluene-rich domain is layered, or composed of two types of aggregates, uncertainties arise with a large Δ value as observed.

These are remarkable experimental evidence of molecular aggregation at the nanoscale, similar to ultra-flexible microemulsions proposed by Prévost *et al.*,⁹⁶ of which the scattering curves show no peak and can be described as the sum of an Ornstein-Zernike as opposed to a Lorentzian.⁹⁹ More interestingly, these are the first systems with an alkane (or a cycloalkane) acting as the apolar component and showing microemulsion-type structure without the presence of a surfactant.⁹⁶⁻⁹⁷

4.4 Resolution at the Atomic Level

4.4.1 The water-PAN-octanol “polar” system

Pursuing an insight into atomic interaction and its effect on liquid nanostructure, we performed neutron diffraction in combination with simulation, as described in Section 2.5.4. EPSR simultaneously fits four contrasts of water–PAN–octanol system, all with an identical molar ratio. The mass ratio of water: PAN: octanol is 20:60:20 for the fully hydrogenous sample, identical to the composition chosen for SANS and invariant analysis discussed in Section 4.3. As shown in Figure 4.10a, three components of water–PAN–octanol pre-ouzo mixture and associated notations will be carried throughout this thesis.

The simulation box is composed of 2532 water molecules, 1117 PAN ion pairs, and 350 n-octanol molecules. This is equivalent to 3.7×10^4 atoms, and a cubic of length 72\AA in real space. EPSR simultaneously fits four isotopic substitutions of water–PAN–octanol at 298K (Figure 4.10b). There is an excellent agreement between the neutron diffraction data (circles) and the EPSR fits (solid lines). Limited box size and difficulties in the subtraction of the inelastic scattering is responsible for small deviation at $q < 0.3 \text{\AA}^{-1}$. Fortunately, performing neutron diffraction in addition to small-angle scattering experiments allows a combination of structural information at different length scales. The focus of EPSR is on atomic interactions and short-distance arrangements. Long-range ordering will only be described qualitatively for comparison purposes.

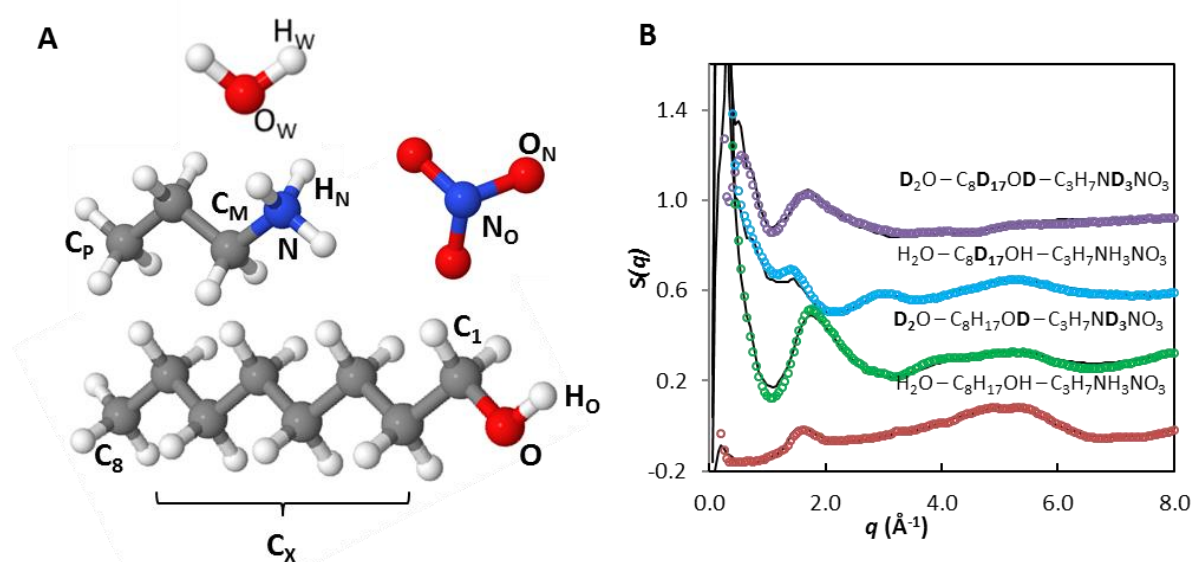


Figure 4.10 a) Components of the water–PAN–octanol system with atomic notations used throughout this thesis. Hydrocarbon hydrogens are rendered for clarity. b) Neutron diffraction (coloured data points) and EPSR fitted (black lines) structure factors as a function of the scattering vector, q (\AA^{-1}), at 298 K. Data are offset for clarity.

Previous neutron diffraction experiments show a low q signature peak at 0.54\AA^{-1} in PAN ($d = 11.6\text{\AA}$), and 0.49\AA^{-1} in 10v.v% PAN–octanol binary mixture ($d = 12.8\text{\AA}$), both representing molecular self-assembly at the nanoscale, as discussed in Chapter 1.⁵³ With the addition of water, this peak shifts further to below 0.3\AA^{-1} , which is consistent with our SANS studies.

Partial pair correlation functions, $g(r)$, inform on separations between atoms and the angles between triplets of atoms (Figure 4.11a). A peak in $g(r)$ indicates a preferred pair correlation. The intensity is generally proportional to the probability of finding such a correlation. In addition to strong electrostatic interactions between the cation and the anion, which have been previously discussed in pure ionic liquids and alcohol mixtures,^{53,173} here we highlight interactions among polar species. Water molecules (H_W and O_W), polar groups on the cation (H_N), the anion (O_N), and the octanol hydroxyl group (H_O and O), are all capable of H-bonding. Figure 4.11 compares the details of hydrogen bond arrangements in the ternary mixture.

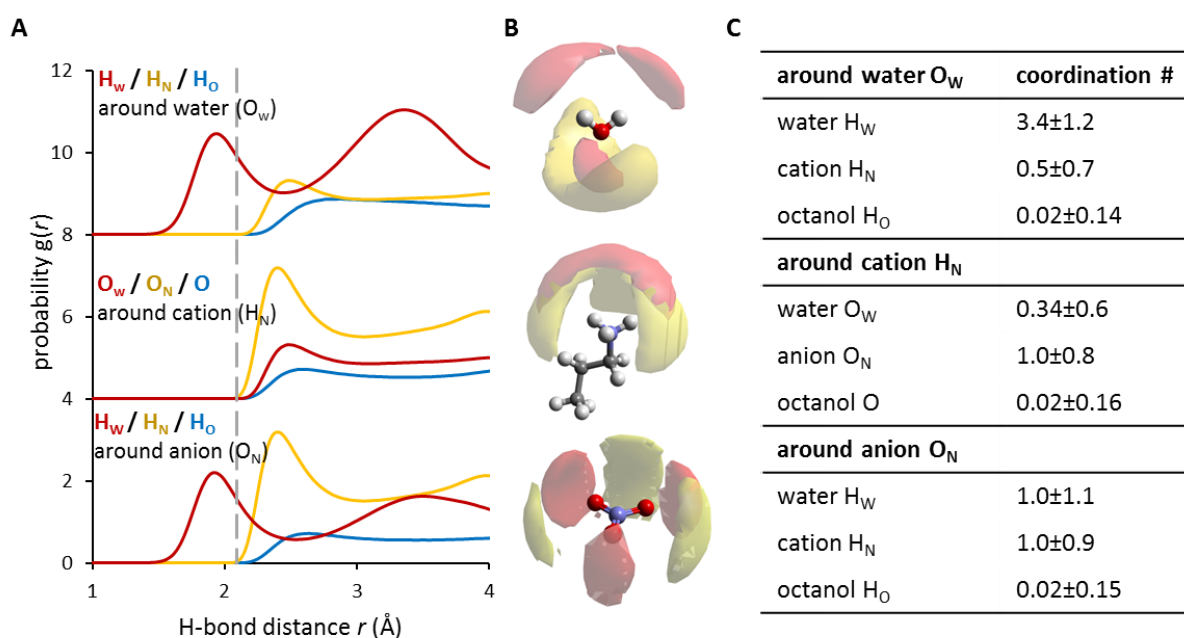


Figure 4.11 Key H-bond characteristics in the water–PAN–octanol system. Three categories shown include interactions around water (top), around cations (middle) and around anions (bottom). **a)** Atom-atom correlation functions, $g(r)$, show H-bond distances. Grey dashed lines distinguish between short and long hydrogen bonds. **b)** 3D geometric plots show 20% probability surfaces for the arrangement of H-bond acceptors and donors. **c)** coordination numbers calculated within 0–2.8 \AA .

There are two different H-bond distances in this system. Water molecules form short H-bonds with other water molecules (H_W – O_W) and with anions (H_W – O_N) at around 2.0 \AA . The rest of H-bonds observed are long, producing peaks in $g(r)$ between 2.4 and 2.5 \AA . Based on the previous study on the binary mixture of water and ethylammonium nitrate (EAN), cation–water (H_N – O_W) and cation–anion (H_N – O_N) hydrogen bonds are much shorter, with a correlation peak at 1.6 \AA .⁴² In pure EAN and PAN however,

the cation-anion hydrogen bonding distance is around 2.4\AA , which is consistent with what we observe here.¹⁶² Correlations with octanol headgroups (blue) are relatively flat. In figure 4.11c, coordination numbers of the octanol hydroxyl group are much lower than water or IL headgroups, meaning a low probability of finding the octanol hydroxyl groups around hydrogen bonding groups.

3D geometric plots, shown in Figure 4.11b, provide a visualisation of the structural arrangements in our samples. The geometric distribution of octanol hydroxyl groups is not shown because of its low probability. Water molecules (red) and PAN headgroups (yellow) all show directional distribution around other species. Their H-bonding sites around water and around the cation overlap geometrically. Interestingly, their distribution around the anion is rather different. Water (H_W) goes to the linear position next to the nitrate oxygen, whereas the cation (H_N) goes to the bent position in between two nitrate oxygens. Different from the water-EAN mixture, in which both the cation-water and the cation-anion hydrogen bonds are short and linear,⁴² it is remarkable to observe two types of hydrogen bonding with the addition of octanol.

Coordination numbers shown in Figure 4.11c reflect the amount of competition among hydrogen bonding species. Around each water oxygen, the number of water hydrogen atoms is 3.4 ± 1.2 at short distances, much higher than the number of ammonium hydrogens (0.5 ± 0.7). This means that water primarily hydrogen bonds with other water molecules. Around each cation ammonium hydrogen, the average number of anion oxygen atoms (1.0) is three times higher than water oxygen atoms (0.34). This can be explained by the cation-anion electrostatic interaction, together with geometric competition. Around each anion oxygen, the average number of cation ammonium hydrogen and water hydrogen is near equal at 1.0. In this case, the competition between the cation and water molecules are not determined by the cation-anion electrostatic interaction, as there are two separate hydrogen bonding sites (at the bent and linear positions) around the anion.

To visualise the distribution of individual components in the mixture, Figure 4.12a shows a snapshot of a simulation box converged to experimental data. PAN, shown in grey, forms a continuous domain which spans the simulation box. Most water molecules, shown in red, stay away from octanol molecules (blue). This supports our previous observation from SANS and invariant analysis, which shows the polarity distinction between a water-rich polar domain, and an octanol-rich apolar domain.

Cluster analysis, shown in figure 4.12b, is a useful tool to look at the continuity of domains formed by specific species. Here we are interested in the behaviour of species with different polarities, and their ability to form hydrophilic and hydrophobic aggregates. Cluster analysis interrogates the EPSR-generated ensembles to extract this structural information. The cluster size distribution is the fraction of species in a cluster of a given size. The 3D percolation threshold, shown in black, represents

a random distribution of clusters. Deviations above this threshold indicate cooperativity of association into either finite or continuous structures up to the number of units in the box. Details of cluster analysis were discussed in Section 2.5.4.6.

The size distribution of clusters formed by PAN headgroups (orange) and PAN tails (green) lies along the percolation threshold, as well as forming a vertical line at around $n=1000$. This means that, in addition to having a random distribution of clusters, there is a cooperative association among IL headgroups and among IL tails. The size distribution of octanol clusters (blue) lies along the percolation threshold with possibilities of finding intermediate sized clusters ($n=20-40$). In contrast, water molecules have many different-sized clusters, shown in red, up to around $n=1000$.

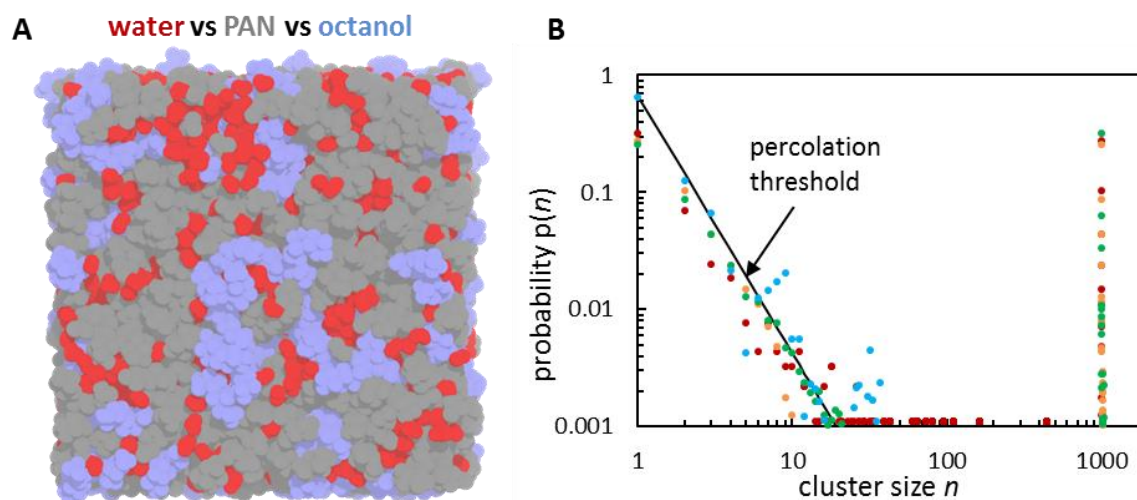


Figure 4.12 a) A snapshot of a converged simulation box of the water–PAN–octanol system; molecules were colour-coded according to the label. b) Cluster analysis of **water** (O_w-O_w , 0–3.4 Å), **PAN head groups** (N_o-N , 4,6 Å), **PAN tails** (C_M-C_p or C_p-C_p , 4.7 Å), and **octanol tails** (C_8-C_8 , C_x-C_8 or C_x-C_x , 4.7 Å). Distance ranges are defined by the first coordination shell in $g(r)$. Theoretical percolation threshold $p(n) = n^{-2.2}$, derived from probabilities, see reference¹⁶⁶.

PAN preserves its amphiphilic character, evidenced from separate domains consisting charged headgroups and non-charged propyl tails. Water molecules are distributed into PAN's charged domains as shown from H-bonding analysis, while octanol segregates to fill the voids among PAN tails.

At a microscopic level, cation-anion and water-water correlations are the dominant interactions. Their spatial arrangement is similar to that found in binary systems (i.e. water-EAN and PAN-octanol mixtures) as well as pure components. At the same time, PAN charged groups and water mimic one another, competing at possible coordination sites. The addition of water did not cause a complete structural disruption in the polar domain. Instead, water molecules cooperate in the pre-existing H-bond network with minimal changes to their local environment. The strong polar network expels octanol molecules forming its own domain. This leads to a pronounced nanostructure composed of polar and apolar domains, as observed previously from SAXS and SANS.

4.4.2 The PAN-octanol-octane “apolar” system

EPSR simulation of the neutron diffraction data further analyses the liquid structure of the PAN–octanol–octane in the pre-ouzo region. Individual components and corresponding atomic notations are shown in Figure 4.13a. The mass ratio of PAN:octanol:octane is 40:40:40 for the fully hydrogenous sample, which is the same composition explored by SANS and invariant analysis, discussed in section 4.3. The simulation box contains 607 PAN ion pairs, 570 octanol molecules and 324 octane molecules. This is equivalent to 3.5×10^4 atoms, and a cube of length 69\AA in real space. The experimental structure factor $S(q)$ is shown in comparison with EPSR fits, (Figure 4.13b). There is an excellent agreement for all isotopic substitutions across the q -range of interest, showing the consistency of the simulation model with the measured system.

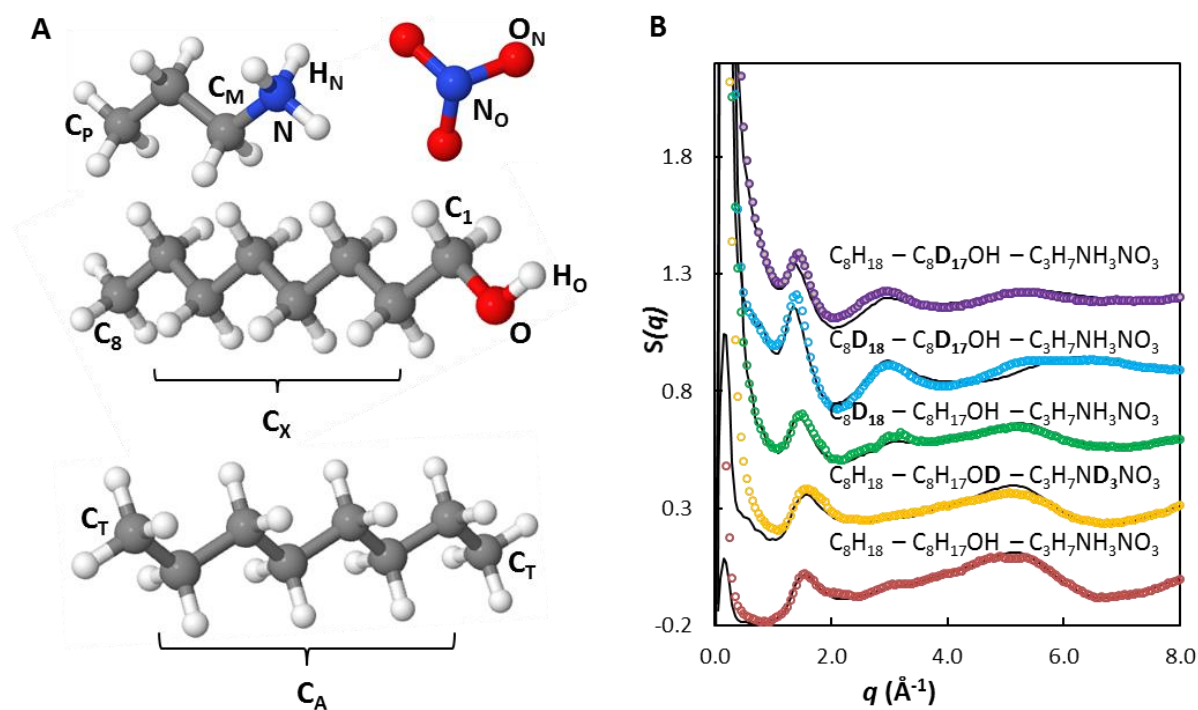


Figure 4.13 a) Components of the PAN–octanol–octane system with atomic notations used throughout this thesis. Hydrocarbon hydrogens are rendered for clarity. b) Neutron diffraction (coloured data points) and EPSR fitted (black lines) structure factors as a function of the scattering vector, q (\AA^{-1}), at 298 K. Data are offset for clarity.

Figure 4.14a shows partial correlation functions of H-bonding capable groups. All H-bonds are relatively long, ranging between 2.5 and 2.6 \AA . The cation-anion correlation (H_N-O_N) remains strong. The average coordination number of anion oxygen around cation hydrogen (and vice versa) is 1.1, as shown in Figure 4.14c. In contrast, correlations the octanol hydroxyl group are much weaker, with an average coordination number of 0.07-0.08.

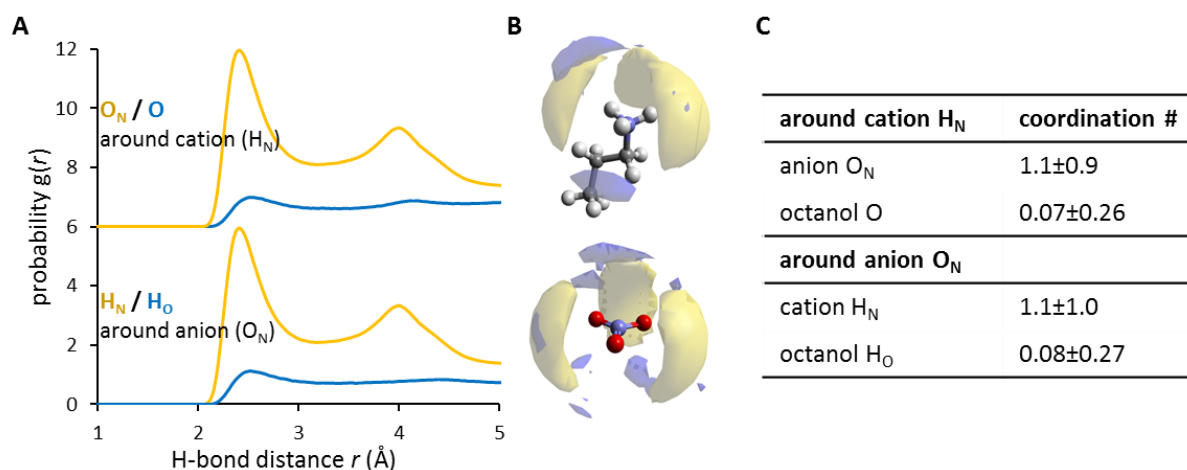


Figure 4.14 Key H-bond characteristics in the PAN–octanol–octane system. Two categories shown include interactions around cations (top) and around anions (bottom). **a)** Atom-atom correlation functions, $g(r)$, show H-bond distances. **b)** 3D geometric plots show 20% probability surfaces for the *competitive* arrangement of H-bond acceptors and donors. **c)** coordination numbers calculated within 0–2.8 Å.

In Figure 4.14b, the 3D distribution of cations around anions or vice versa is directional with a 3-fold geometry. The distribution of octanol hydroxyl groups, however, is non-directional. The H-bonding between IL head groups and octanol hydroxyl groups may not explain the formation of polar and non-polar domains observed in SANS.

Cluster analysis paired with a simulation snapshot provides an in-depth understanding of different types of segregation at the nanoscale. In Figure 4.15b, Octanol and octane molecules, shown in blue and purple, are almost all in a single cluster that is as big as the box. Multiple vertical lines of blue dots may be a result of multiple contact points as defined along the octanol tail. In contrast, PAN head groups have many different-sized clusters, shown in orange, up to and including the box size. PAN tails lie on the percolation threshold, meaning the formation of large and segregated domains. The continuous domain of octanol is visually identifiable from the simulation snapshot, shown in Figure 4.15a.

In the PAN–octanol–octane ternary system, either octanol or octane molecules can form a continuous domain. The local environment of PAN shows segregations into charged and uncharged regions. The amphiphilic character of PAN remains, despite being the most polar component in the mixture. In comparison, there is no significant correlation among hydroxyl groups of octanol molecules. Instead, octanol interleaves in the apolar domain. Therefore, it is the amphiphilicity of PAN that primarily drives the arrangement of octanol molecules. In general, octane molecules distribute near octanol-rich regions for their solvophobicity. Unlike octanol molecules, octane molecules cannot form H-bonds with IL headgroups, instead, they are isolated away from the polar region forming their own domain. High-resolution diffraction results are consistent with SANS data with invariant analysis (Figure 4.9A), where observed three types of domains: one domain consists PAN and octanol

headgroups, one domain contains mainly octanol tails, and the other domain contains mainly octane molecules.

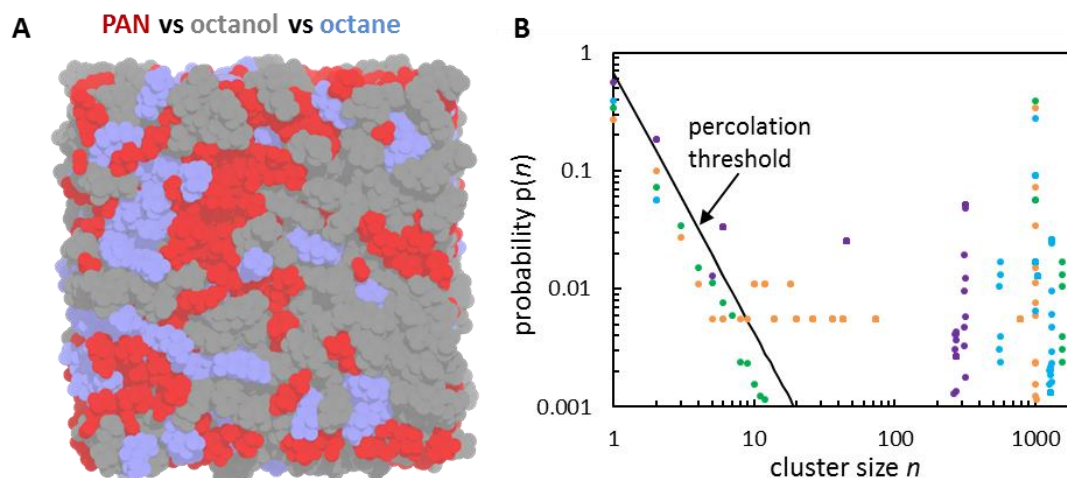


Figure 4.15 a) A snapshot of a converged simulation box of the PAN–octanol–octane system; molecules were colour-coded according to the label. b) Cluster analysis of PAN head groups (N_{O-N} , 4.6 Å), PAN tails (C_M-C_P or C_P-C_P , 4.7 Å), octanol tails (C_8-C_8 , C_X-C_8 or C_X-C_X , 4.7 Å), and octane molecules (C_A-C_A , C_A-C_T or C_T-C_T , 4.7 Å), defined within the first coordination shell. The theoretical percolation threshold $p(n)=n^{-2.2}$ is normalised to 1, derived from probabilities, see reference¹⁶⁶.

In pure protic IL, longer cation alkyl chains enhance long-range order, such as going from PAN to pentylammonium nitrate.³⁰ The Tanford model relates hydrophobic effect to micelle swelling.²²⁹ In a study of lipid bilayers, McIntosh et al. found the addition of medium-length alkanes, such as hexane and octane, increases bilayer width by partitioning between the opposing monolayers.²³⁰ Our result is consistent with these observations. That is, an additional solvophobic component goes into the apolar region of the PAN–octanol binary mixture, effectively expanding the domain size.

In this chapter, we studied ternary solutions containing two immiscible components across the polarity scale and a co-solvent that induces the miscibility in between. The absence of a surfactant leads to ill-defined structures, as opposed to conventional microemulsions with a monolayer of surfactants accumulated at the polar-apolar interface. We investigated liquid structure from the nanoscale to the atomic level using X-ray and Neutron scattering techniques combined with invariant analysis and experimentally-refined simulation. The nanostructure of IL-containing ternary mixtures is sensitive to formulation, with a similar trend to hydrotrope-containing surfactant-free microemulsions. Species distribute to form domains with distinct polarities or molecular packing geometry at the nanoscale. Electrostatic interactions and hydrogen bonding in the polar domain drive the formation of nanostructure. To rationally design surfactant-less microemulsions, we highlighted the importance of both molecular amphiphilicity and packing geometry in addition to solvent polarity.

CHAPTER 5

THE NEXT GENERATION OF ILS

The classification of ILS is diverse, as multiple labels are often appropriate for a given IL, depending on whether the cation, anion or a functional group is most important. In addition to having protic and aprotic ILS as the two most common IL types,^{15, 231} other subclasses include but not limited to chiral ILS,²³² magnetic ILS,²³³ polymeric ILS,²³⁴ fluorinated ILS,¹⁶⁹ and solvate ILS.²³⁵ The structure, nanostructure and physicochemical properties of ionic liquids tie closely to their potential applications. In this chapter, we discuss solvate ILS (with a coordinated ion) and magnetic ILS (with a paramagnetic atom) as two special classes of ILS that possess distinct structural features. The modification of the molecular structure of lithium solvate ILS leads to the formation of a liquid crystalline structure, which are potential materials for batteries and digital display. Paramagnetic ILS with tuneable formulation are useful for microfluidics, magnetic levitation, and optical devices.

5.1 Solvate Ionic liquids with an Amphiphilic Character

5.1.1 Introduction to complexation

In 1967, Pederson discovered cyclic polyethers, known as crown ethers, and their complexes with metal salts.²³⁶ The ether oxygens of the crown ethers complex with a cation. The size of the guest ion matches the cavity of the host. This leads to enhanced solubility of ionic species and selectivity by ion radii.

The chemical structure of oligoglymes and oligo(ethylene glycols) is similar to crown ethers, as shown in Figure 5.1. Breaking a carbon-carbon bond of a crown ether generates an oligoglyme, which is an aliphatic ether with terminal methyl groups. An oligoethylene glycol differs from an oligoglyme by two terminal hydroxyl groups. The oxygen atoms of these three types of ligands coordinate with a metal cation of a suitable size, forming metal complexes. For example, 12-crown-4, triglyme, and triethylene glycol each contain four oxygen atoms and preferably complexes with Li^+ rather than Na^+ or K^+ .

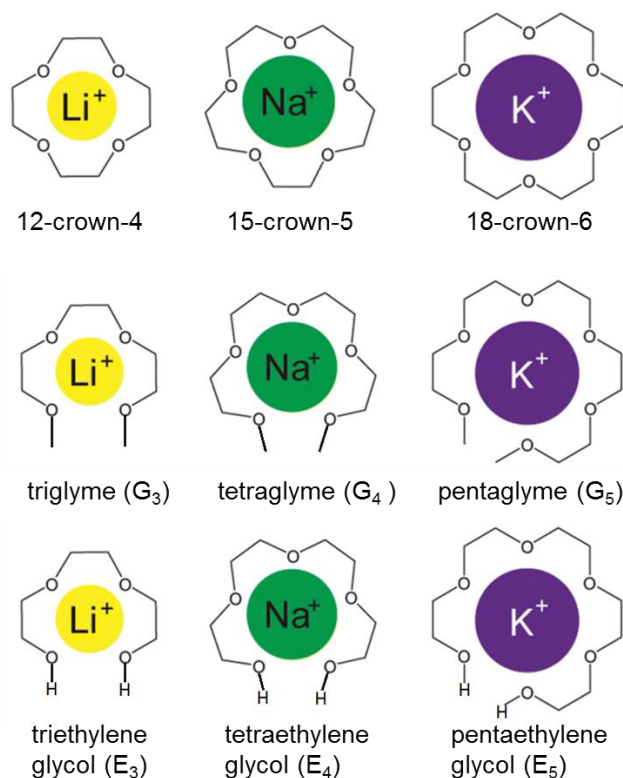


Figure 5.1 The chemical structure of three classes of ligands: crown ethers (with a cyclic structure), glymes (with terminal methyl groups) and glycols (with terminal hydroxyl groups), complexed with Li, Na, and K metal cations.

Conventional ionic liquids are solely composed of cations and anions. Watanabe *et al.* discovered that, depending on the anion property, certain glyme – lithium salt mixtures also show similar properties as ionic liquids.²³⁵ Figure 5.2 shows the solvation structure of lithium salt in triglyme, with different types of anions.

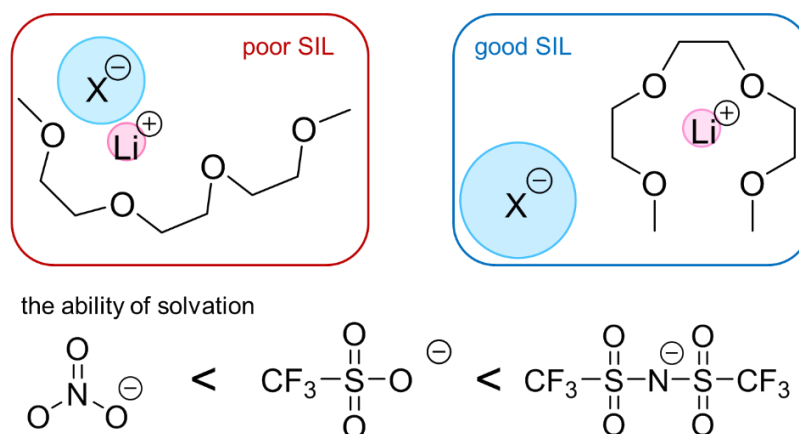


Figure 5.2 The solvation structure of Li^+ solvate ionic liquids (SILs) with a poor solvating anion versus a good solvating anion. The ability of anion solvation increases from NO_3^- , OTf^- , to TFSI^- .²³⁵

Anions and glymes compete to interact with the lithium cation. When the anion is a weak Lewis base, such as TFSI, the cation-anion interaction is relatively weak. Long-lived $[\text{Li}(\text{glyme})]^+$ complex cations form. The resulting mixture is considered as a good solvate IL, as it shows similar properties to conventional ILs composed of cations and anions.²³⁷ In contrast, if the anion is a strong

Lewis base, such as nitrate, the cation-anion interaction is strong, preventing Li^+ from interacting with oxygens on the glyme. In this case, cations are not well-solvated by glymes. It behaves more like a mixture of molecular and ionic species, rather than a complex. We classify this type of mixture as a poor solvate IL. In $\text{Li}(\text{glyme})\text{TFSI}$, Li cations predominantly coordinate with glyme oxygen atoms. In $\text{Li}(\text{glyme})\text{NO}_3$, the coordination number between Li and anion oxygen atoms is much higher.²³⁸ Based on TGA and NMR diffusion measurement, the solvation ability of common anions are ranked in the order of $\text{TFSI} > \text{OTf} > \text{NO}_3$.²³⁵ The $\text{Li}(\text{glyme})\text{TFSI}$ system has low flammability, low volatility, high lithium ion concentration, and a wide electrochemical window.²³⁹ These are desired characteristics for lithium-ion batteries, making solvate ionic liquids excellent candidates to replace conventional organic electrolyte solutions with high flammability and solid electrolytes with low power density.

5.1.2 Solvate surfactants

Replacing oligoglymes with oligoethylene glycols, we expect similar structural behaviour in coordinating with the metal cation. Although triethylene glycol (E_3) and tetraethylene glycol (E_4) have narrower electrochemical windows than glymes, studying glycol-based SILs provides insight into the role of exchangeable, acidic protons in the solvent properties of SILs. As a measure of solvent polarity, Kamlet–Taft solvation parameters of glyme and glycol-based SILs have been studied.²⁴⁰

Oligoethylene glycols have an analogous structure to the headgroup of polyoxoethylene non-ionic surfactants (C_nE_m). In C_{14}E_4 for example, there is an E_4 unit as the polar component, and a tetradecyl (C_{14}) chain as an apolar component. These C_nE_m surfactants are known to self-assemble into micellar, bilayer and liquid crystalline structures in water.²⁴¹

Figure 5.3 shows the relationship between the molecular shape of a surfactant and the type of nanostructure surfactants self-assemble into. In 1976, Israelachvili et al. proposed the packing parameter to describe an effective molecular shape.¹⁷⁵ This parameter depends on the volume of the hydrophobic chain, the interfacial area occupied by the hydrophilic headgroup and the length of the hydrophobic chain. Estimating this parameter of a surfactant allows a prediction of the molecular packing of the surfactant. When a surfactant has a large headgroup with a long tail, which could be described as cone-shaped, it has a small packing parameter and therefore self-assemble into micelles. When a surfactant has a small headgroup with a relatively short tail, which could be described as cylindrical, it has a large packing parameter and therefore self-assembles into bilayers.

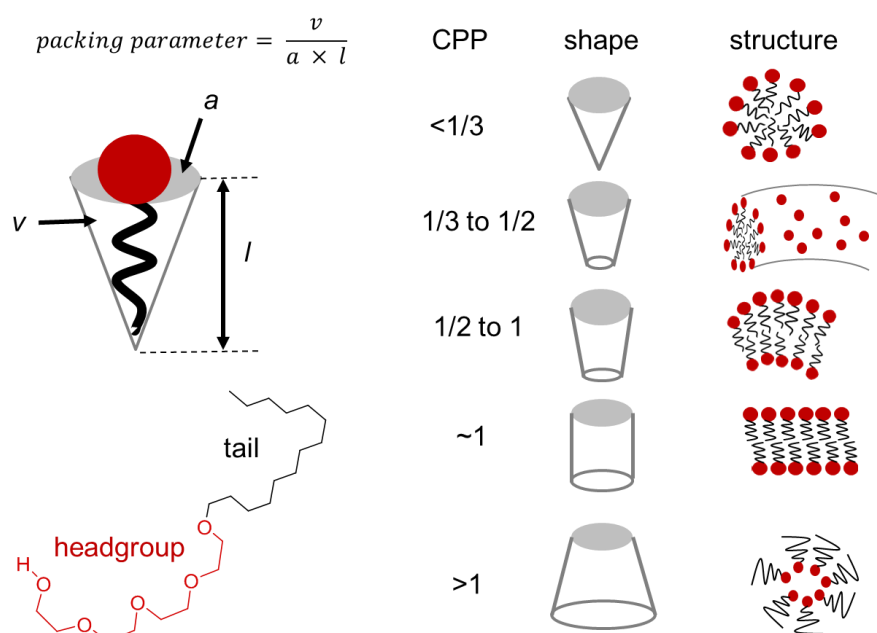


Figure 5.3 Molecular shapes and packing parameter of surfactants and the structures formed: v is the volume of the hydrocarbon core; a is the effective head group area, l is the hydrocarbon chain length.²⁴²

In this section, we propose a new family of ionic liquids, solvate surfactants (SSs), which are molten mixtures of lithium salts (LiX) and surfactants (C_nE_m) at room temperature. The presence of polar species (lithium salts and surfactant headgroups) and apolar species (surfactant tails) adds an amphiphilic character to solvate ionic liquids. Using polarising microscopy and wide-angle X-ray scattering (WAXS), we explore phase behaviour and nanostructure of solvate surfactants.

A non-ionic surfactant, $C_{14}E_4$, was mixed with water, $LiNO_3$, $LiOTf$, and $LiTFSI$ at room temperature. All lithium salts were pre-dried at high temperature under vacuum to obtain the anhydrous form. Figure 5.4 shows that all systems examined exhibited the characteristic optical texture of liquid-crystalline phases under crossed polarisers,¹²⁵ except the $C_{14}E_4$ - $LiTFSI$ mixture, which does not have any liquid crystalline phase. Details of optical properties of liquid crystals were discussed in Chapter 2. In the $C_{14}E_4$ -water mixture, the surfactant dissolves and self-assemble in an aqueous environment. In the $C_{14}E_4$ -lithium salt mixtures, however, liquid crystals form from two solids, as the melting temperature of the surfactant and the salts is above RT.

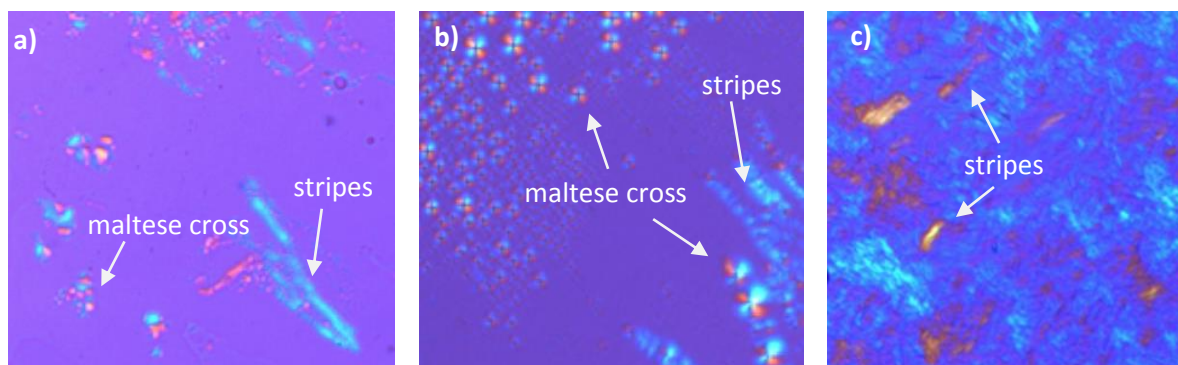


Figure 5.4 Polarising optical micrographs of $C_{14}E_4$ with the addition of a) water, b) $LiNO_3$, and c) $LiOTf$, showing the formation of vesicles and lamellar liquid crystal phases at 298K.

With the addition of water, $LiNO_3$, or $LiOTf$, micrographs show optical textures indicating a lamellar phase. Moreover, in both the $C_{14}E_4$ – water system (Figure 5.4a) and the $C_{14}E_4$ – $LiNO_3$ system (figure 5.4b), micrographs show Maltese cross textures, which are diagnostic for vesicle formation.¹²⁴ It is remarkable to see the self-assembly of $C_{14}E_4$ molecules in solid $LiNO_3$ and $LiOTf$, forming a bilayer-type structure at the nanoscale.

To study the influence of salt concentrations on the liquid nanostructure, samples with different concentrations of $LiTFSI$, $LiOTf$ and $LiNO_3$ in $C_{14}E_4$ (from 20wt% to the solubility limit of lithium salt, i.e. saturation at RT) were prepared and measured by SAXS, presented in Figure 5.5. The intensity of the scattering corresponds to the extent of the structure. A broad peak means a less-well-defined structure, whereas a sharp peak represents a liquid-crystalline structure, of which the repeating distance could be calculated by Bragg's law, $d=2\pi/q$.

As the concentration of lithium salt increases towards saturation, the scattering pattern changes with anion type. When adding $LiTFSI$ into $C_{14}E_4$, shown in figure 5.5a, the scattering curve barely changes. Since the peak position scales as volume fraction to the power $-1/3$ in isotropic samples, the negligible change of scattering patterns in the $LiTFSI$ - $C_{14}E_4$ system can be a result of a dilution process.

Schematic diagrams of proposed molecular arrangements are shown on the RHS of Figure 5.5. Li cations are well coordinated by oligoethylene groups. A cation stays close to an anion forming ion pairs. If we consider cations, anions and the oligoethylene groups as the polar part of the liquid structure, while the apolar volume and chain length remains constant, the packing parameter is inversely proportional to the polar area. The size of the anion increases in the order of $NO_3^- < OTf^- < TFSI^-$, therefore, the packing parameter of the solvate surfactant increases in the reverse order (i.e. $TFSI^- < OTf^- < NO_3^-$). The large size of $TFSI^-$ anions leads to a small packing parameter of the $LiTFSI$ - $C_{14}E_4$ solvate surfactant, lower than what is required to form a liquid crystal phase.

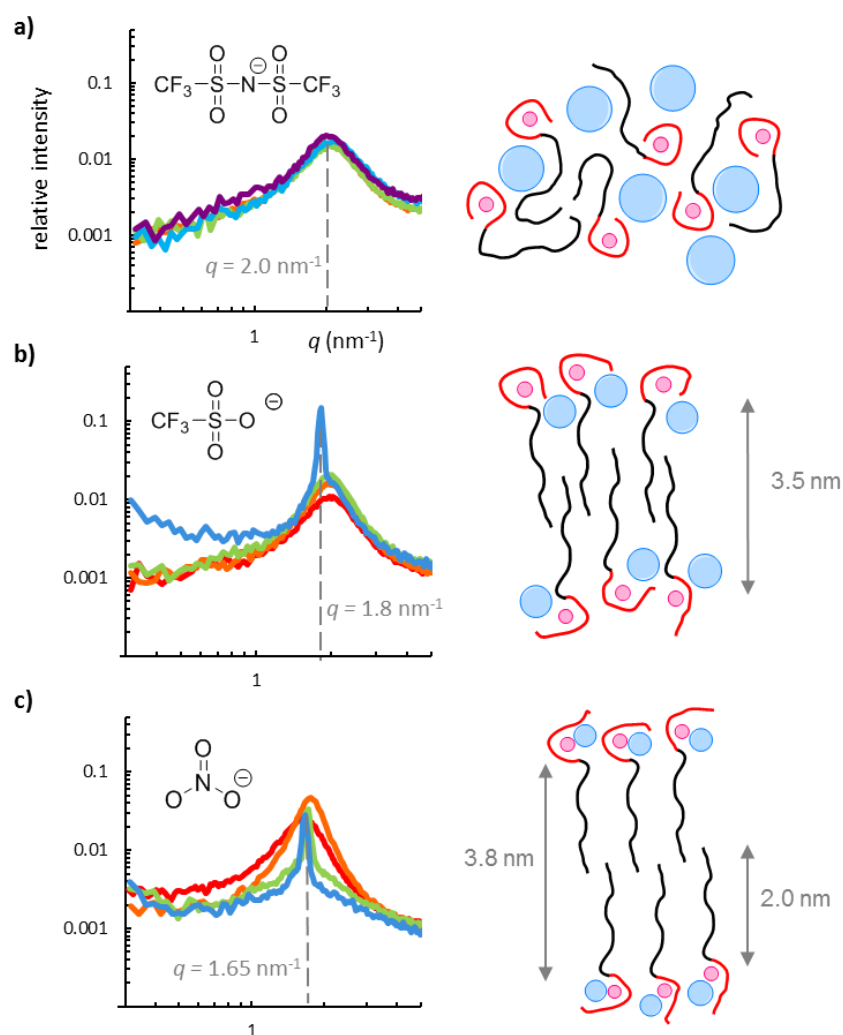


Figure 5.5 SAXS patterns of a) LiTFSI b) LiOTf and c) LiNO₃ with C₁₄E₄, from a dilute sample to saturation at RT. Data were colour coded based on the concentration of Li salts, ranging from 20, 30, 40, 50, to 60 ± 2mol%. Schematic diagrams show proposed molecular arrangements near saturation. The red circle is the lithium cation, the blue circle is the anion, the red line is the surfactant polar part, and the black line is the surfactant apolar part. This representation is consistent throughout this section.

If using a different anion, the scattering profile changes dramatically. As the LiOTf concentration increases from 20 to 40 mol%, as shown in Figure 5.5b, the peak intensity increases, meaning a slightly more defined nanostructure. When further increasing the LiOTf concentration towards saturation (near 50 mol%), a sharp peak appears at 1.8 nm⁻¹, representing the formation of a liquid crystal structure with a periodicity of 3.5 nm. This is 15% shorter than a tail-to-tail arrangement between two tetradecyl chains, indicating some degree of overlap among the alkyl chains of the surfactant.

The size of the OTf⁻ anion is half of the TFSI⁻ anion. Since the anion is less bulky, ions pack more easily. More importantly, OTf⁻ is more basic than TFSI⁻. This means that there is more competition between anions and surfactant polar groups, interacting with the cations. As shown in the schematic diagram, some Li⁺ cations are fully coordinated with surfactant polar groups; some are only partially

coordinated and forming ion pairs. The preference of anions going closer to cations leads to polar and apolar domains. This explains the liquid crystal phase at high salt concentrations.

The addition of LiNO_3 to C_{14}E_4 shows a similar structural behaviour to the addition of LiOTf , except less LiNO_3 is required to form a liquid crystal structure, as shown in Figure 5.5c. The liquid crystalline peak appears at 1.65 nm^{-1} , suggesting a periodicity of 3.8 nm. The schematic diagram shows an approximation of a tail-to-tail arrangement, forming a bilayer structure. The ability to induce C_{14}E_4 molecules to form liquid crystal structure is in the order of $\text{NO}_3^- > \text{OTf}^- > \text{TFSI}^-$, inversely correlated to the ability of solvation ($\text{TFSI}^- > \text{OTf}^- > \text{NO}_3^-$).

We further compare the liquid structure of these mixtures at a fixed concentration in the solution phase, before the formation of the liquid-crystalline phase. The scattering peak position shifts depending on the anion type. Figure 5.6 shows that the scattering peak position depends on the anion type. In neat C_{14}E_4 , there is a 3.3 nm spacing, approximately 1.5 times the C_{14} -alkyl tail length. As the schematic diagram is shown on the RHS, alkyl tails are bent, and the structure is not well-defined.

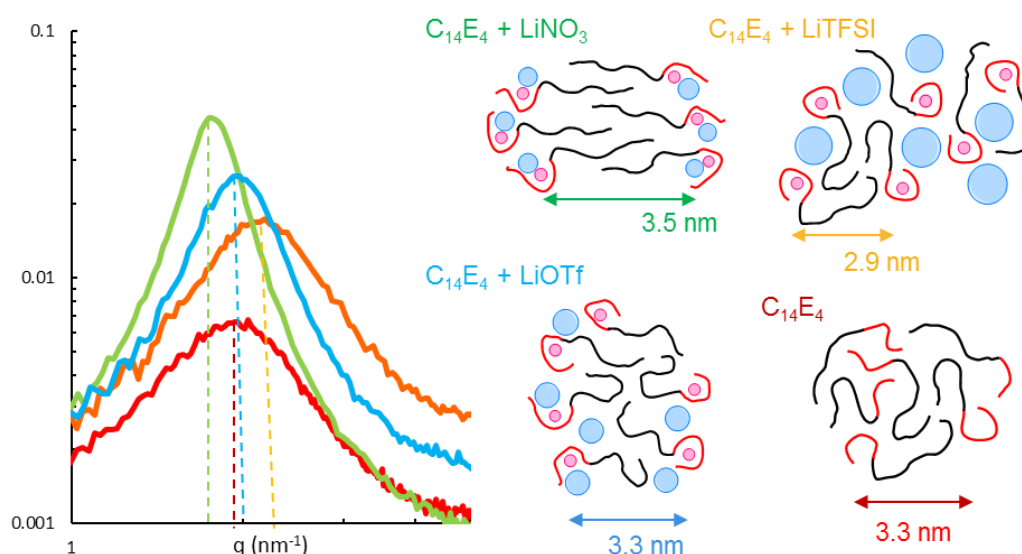


Figure 5.6 SAXS patterns of salts in C_{14}E_4 before the formation of a liquid-crystal phase (observed in figure 5.4-5.5). I.e. 56 mol% LiTFSI , 45 mol% LiOTf and 36 mol% LiNO_3 in C_{14}E_4 , compared to pure C_{14}E_4 .

With the addition of LiTFSI , the broad peak moves to a higher angle, equivalent to a reduced repeating distance from 3.3nm (in neat C_{14}E_4) to 2.9nm. With LiOTf , the peak becomes narrow and shifts to a lower angle, with the same repeating distance of 3.3nm. With LiNO_3 , the peak shifts further with a repeating distance of 3.5nm. As shown in the schematic diagrams, alkyl tails overlap to some extent in the C_{14}E_4 - LiNO_3 mixture, with a tendency of forming a bilayer structure. In general, the structure induced by nitrate anions is the most ordered compared to the rest even below the concentration of forming liquid crystals.

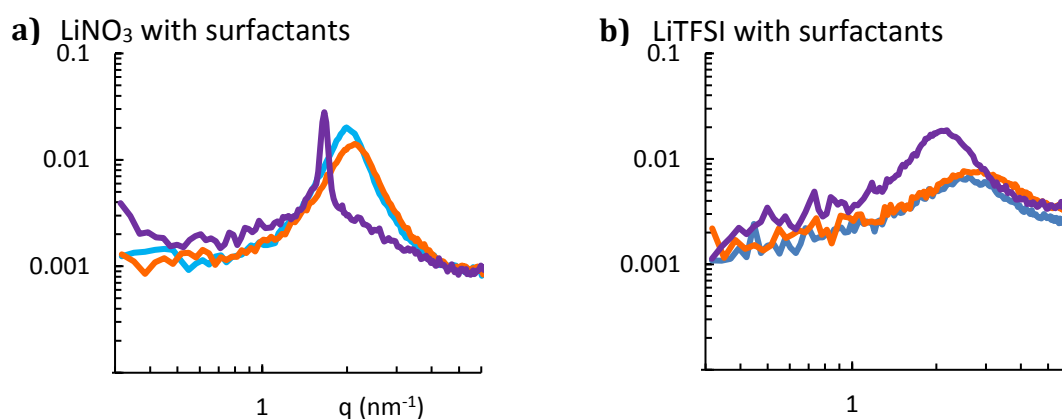


Figure 5.7 SAXS patterns of $C_{10}E_3$, $C_{10}E_4$ and $C_{14}E_4$ surfactants with a) $LiNO_3$ and b) $LiTFSI$ near saturation.

When increasing the surfactant polar group length from $C_{10}E_3$ to $C_{10}E_4$, there is no significant change in scattering. However, when increasing the surfactant apolar group length from $C_{10}E_4$ to $C_{14}E_4$, scattering peaks are left-shifted. Among three surfactants investigated, $C_{14}E_4$ leads to the most pronounced nanostructure with either salt: the $LiNO_3$ - $C_{14}E_4$ mixture has a liquid crystal phase near the solubility limit of the salt, and the nanostructure of the $LiTFSI$ - $C_{14}E_4$ mixture is more pronounced compared to using $C_{10}E_3$ or $C_{10}E_4$ surfactants. Previous studies have shown that, in both water and ethylammonium nitrate (EAN), C_{12} is the minimum alkyl chain length of a non-ionic surfactant to support the formation of lyotropic phases.²⁴³⁻²⁴⁴ The structural behaviour of a C_nE_m surfactant in a lithium salt is remarkably similar to it is in water or EAN. $C_{10}E_m$ surfactants form only micellar-type structures in all lithium salts tested, whereas $C_{14}E_m$ surfactants can form a lamellar phase in either $LiNO_3$ or $LiOTf$.

To further understand how the components are segregated, we introduce an additional polar component, either G_4 or E_4 , with an analogous structure of the surfactant headgroup. These molecules can complex with the Li^+ cation. Scattering patterns and schematic diagrams in Figure 5.8 show the structural influence of these polar species as a function of concentration.

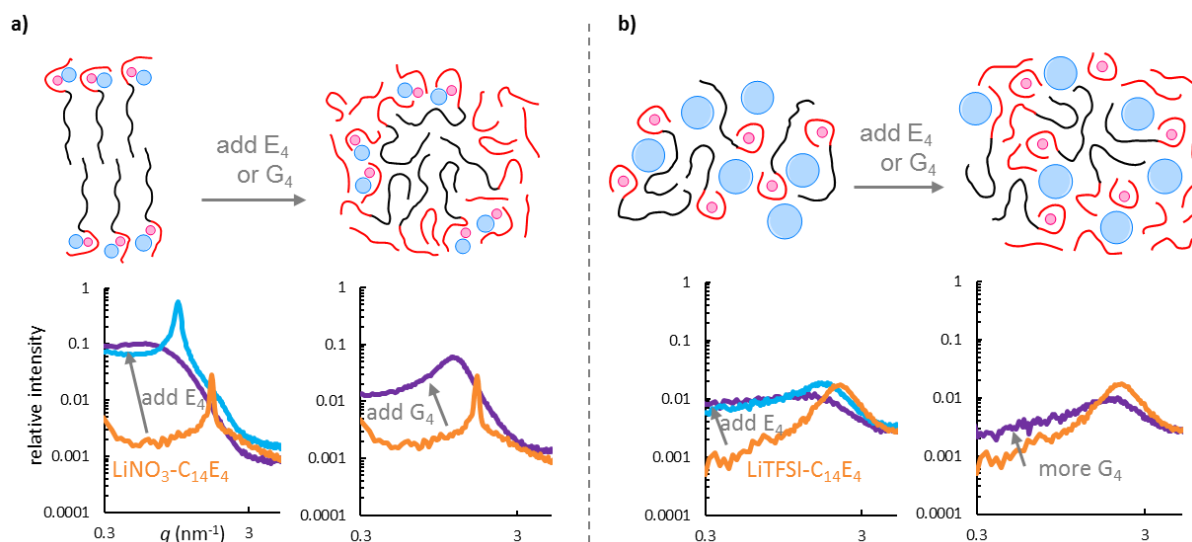


Figure 5.8 SAXS patterns of binary and ternary mixtures of Li salt – $C_{14}E_4$ – E_4/G_4 , where Li salt concentration was fixed at 50mol% and $C_{14}E_4$: E_4/G_4 ratio (by weight) changes from 50:0, 25:25 to 10:40.

Figure 5.8a shows that, at a fixed concentration of $LiNO_3$ of 50%, when moving from a $C_{14}E_4$ -rich to an E_4 -rich composition, the intensity of low- q scattering increases significantly by one magnitude. When adding 25% of E_4 , a scattering of the mixture preserves the liquid crystal peak in a combination of a microemulsion-like scattering curve. The liquid crystal peak has shifted from 1.7 nm^{-1} in the binary mixture to 1.0 nm^{-1} in the ternary mixture. This means a significant increase in periodicity from 3.7 nm to 6.3 nm. Further adding E_4 to 40%, the sharp peak disappears, and only a shoulder is present at low- q . This means the liquid crystal structure has disappeared and the mixture persists in a microemulsion-like structure. If replacing E_4 with G_4 , 25% of G_4 causes the liquid crystal peak to disappear. The resulting scattering pattern shows a broad peak at 1.2 nm^{-1} , suggesting a micellar liquid nanostructure.

In LiTFSI mixtures, as shown in Figure 5.8b, as E_4 or G_4 content increases, the general trend of increasing low- q intensity and left-shift peak positions is consistent with $LiNO_3$ -containing mixtures. The difference is that LiTFSI mixtures do not form liquid crystals, and the addition of either E_4 or G_4 causes smaller structural changes compared to $LiNO_3$ mixtures.

Cho et al. studied dendrons extended with linear polyethylene oxide (PEO) chains.²⁴⁵ These amphiphilic molecules self-assemble into a sequence of lamellar, cubic and hexagonal phases. A small amount of lithium triflate salt dissolves into the hydrophilic parts. This enables the measurement of ion conductivity, which closely relates to the type of the nanostructure.

In our systems, the nanostructure of solvate surfactants evolves as the salt-surfactant ratio changes, giving micellar and liquid-crystalline structure. The ability to induce nanostructure is different among three lithium salt anions (NO_3^- , OTf^- and $TFSI^-$) depending on the anion size and solvability. The

comparison of three surfactants ($C_{14}E_4$, $C_{10}E_4$ and $C_{10}E_3$) shows that the apolar tail length dominates the type of nanostructure. Further, the addition of either an oligoglyme or an oligo(ethylene glycol) modifies the liquid crystalline structure of solvate surfactants into micellar or microemulsion-type structure.

Unlike conventional solvents, inorganic metal salts can act as media to support surfactant self-assembly. The resulting solvate surfactants have tuneable nanostructure, which can be controlled by the concentration of the salt, the type of the anion, the length of the surfactant hydrocarbon tail and an additional solute.

Based on these trends, we anticipate that other lyotropic phases (e.g. cubic and hexagonal) could be produced with $C_{16}E_m$ or $C_{18}E_m$ surfactants in lithium salts near or slightly above RT, as observed in EAN.²⁴³ A ternary mixture of a lithium salt, a C_nE_m surfactant, and a C_n -alkanol should yield microemulsions, in which the lithium salt is immiscible with the alkanol, and the surfactant induces the miscibility in between. Other solvophobic solvents may be used to replace the alkanol component to expand the matrix of IL-containing microemulsions, as discussed in Chapter 4. Since the solvation of the lithium cation by the oligoglymes or the oligo(ethylene glycols) is not the key factor in determining structure at the nanoscale, it is possible to incorporate other metal ions (e.g. Mn^{2+} or Fe^{3+}) with alternative functionalities (e.g. magnetic properties).

5.2 Magnetic Ionic Liquids

Magnetic ILs are room-temperature ILs with paramagnetic properties, achieved by the incorporation of transition metals like iron, manganese and cobalt, or rare-earth ions like neodymium and gadolinium.²⁴⁶⁻²⁴⁷ These metal atoms may be part of the anion, the cation or both. Commonly studied magnetic ILs contains a traditional cation like [Emim], [Bmim], [P_{6,6,6,14}] or [choline], and a paramagnetic anion like $[FeCl_4]$, $[CoCl_4]$, or $[GdCl_6]$.²³³ The first magnetic IL, [Bmim][$FeCl_4$], was synthesized by mixing crystal powder of BmimCl with anhydrous $FeCl_3$ and $FeCl_3 \cdot 6H_2O$.²⁴⁸⁻²⁴⁹ Magnetic ILs based on rare-earth metals were synthesized by a metathesis procedure starting from $Ln(ClO_4)_3$, NH_4SCN , and an imidazolium IL.^{247, 250}

These transparent fluids are responsive to an external magnetic field, without the need of adding magnetic particles. Applications of magnetic ionic liquids include but not limited to, field-directed synthesis of nanomaterials, metal-based homogenous catalysis, density measurements using magnetic levitation, and environmental remediation using magnetic separation.²⁵¹

5.2.1 Paramagnetic mixtures with tunable formulations

In this section, we propose a range of simple and low-cost magnetic ionic liquids by mixing inorganic salts with either a protic ionic liquid, or with a molecular species that has a negligible vapour pressure. These room-temperature fluids have tuneable formulation, leading to controllable magnetic properties and solvent structure.

Table 5.1 shows preliminary screening of the melting temperature of a range of magnesium salts, including $\text{MnCl}_2 \cdot 2\text{H}_2\text{O}$, MnCO_3 , MnAc_2 and $\text{Mn}(\text{NO}_3)_2 \cdot 4\text{H}_2\text{O}$, and their miscibility with E_3 and G_4 . Results show that only $\text{Mn}(\text{NO}_3)_2 \cdot 4\text{H}_2\text{O}$, which has a low melting temperature of 37°C , is soluble in G_4 at room temperature in a 1:1 molar ratio. The low melting point of MnNO_3 suggests lower binding energy between Mn^{2+} and NO_3^- . This facilitates the solvation of ions by G_4 molecules via metal-oxygen chelation. Although E_3 has the same number of oxygens as G_4 , the solubility of $\text{Mn}(\text{NO}_3)_2 \cdot 4\text{H}_2\text{O}$ in E_3 is much lower, possibly because the hydroxyl group on E_3 can interact with either NO_3^- or H_2O via hydrogen bonding. This prevents E_3 from coordinating onto Mn^{2+} and therefore leads to poorer solvation of Mn salts than in G_4 , which has no hydroxyl group. Similarly, $\text{Fe}(\text{NO}_3)_3 \cdot 9\text{H}_2\text{O}$ with a low melting temperature of 47°C dissolves in G_3 .

Table 5.1 Screening of the melting temperature of common manganese salts, and their miscibility with E_3 and G_4 (1:1 molar ratio)

Salt	m.p. ($^\circ\text{C}$) of salt anhydrous	Soluble in E_3 ?	Soluble in G_4 ?
$\text{MnCl}_2 \cdot 2\text{H}_2\text{O}$	650	No	No
MnCO_3	200-300	No	N/A
MnAc_2	210	N/A	No
$\text{Mn}(\text{NO}_3)_2 \cdot 4\text{H}_2\text{O}$	37	No	Yes

As the solvation capacity of oligoglyme depends on the effective ion radii of the cation, we compare Mn^{2+} and Fe^{3+} to Li^+ . Previous studies have shown that G_3 matches well with the size of Li^+ (76 pm). Our results show that $\text{Mn}(\text{NO}_3)_2 \cdot 4\text{H}_2\text{O}$ and $\text{Fe}(\text{NO}_3)_3 \cdot 9\text{H}_2\text{O}$ are soluble in either G_3 or G_4 . Since the effective ion radii of Mn^{2+} (67 pm for low spin and 83 pm for a high spin) and Fe^{3+} (61 pm for low spin and 78 pm for a high spin) are similar to Li^+ , we hypothesize that the coordination of glyme on the metal cations and the influence of the anion is consistent with Li-based SILs.

In lithium-based SILs, NO_3^- is a poor solvate anion, therefore, G_3 only partially coordinates onto the metal cation. Although TFSI^- is a good solvate anion, which allows G_3 to fully coordinate with the metal cation, it is relatively expensive and is not suitable for low-cost applications such as magnetic levitation. In manganese-based systems, TGA results show that the $\text{Mn}(\text{TFSI})_2 - \text{G}_3$ mixture has higher thermal stability than the $\text{Mn}(\text{NO}_3)_2 - \text{G}_3$ mixture. This observation confirms our hypothesis of similarities between lithium-based and manganese-based SIL systems.

An alternative method of creating magnetic ionic liquids is to dissolve paramagnetic salts into protic ionic liquids, such as EtAN and PAN. Both $\text{Mn}(\text{NO}_3)_2 \cdot 4\text{H}_2\text{O}$ and $\text{Fe}(\text{NO}_3)_3 \cdot 9\text{H}_2\text{O}$ are soluble in either EtAN and PAN up to 1:1 molar ratio. In addition to having tunable magnetic properties via formulation, we expect to see changes in the liquid nanostructure.

Based on our previous studies, EtAN is non-amphiphilic and not nanostructured.³³ Adding Li^+ salt to EtAN is structure making, inducing a non-charged domain formed by the ethanol tail.⁴⁹ In comparison, EAN (similar to PAN but with a shorter alkyl group) is amphiphilic with polar/apolar nano-domains.³³ Adding Li^+ salt is structure breaking, slightly disrupting the alignment among the cation alkyl tail.⁴⁹

In Figure 5.9, magnetic susceptibility measurements show a linear relationship between the magnetic response of the sample and the applied field. The higher the slope, the higher the magnetic susceptibility (χ). Experimental details were discussed in Section 2.4. In general, G3-salt mixtures have a higher susceptibility than G4-salt mixtures. EtAN-salt mixtures have a higher susceptibility than PAN-salt mixtures.

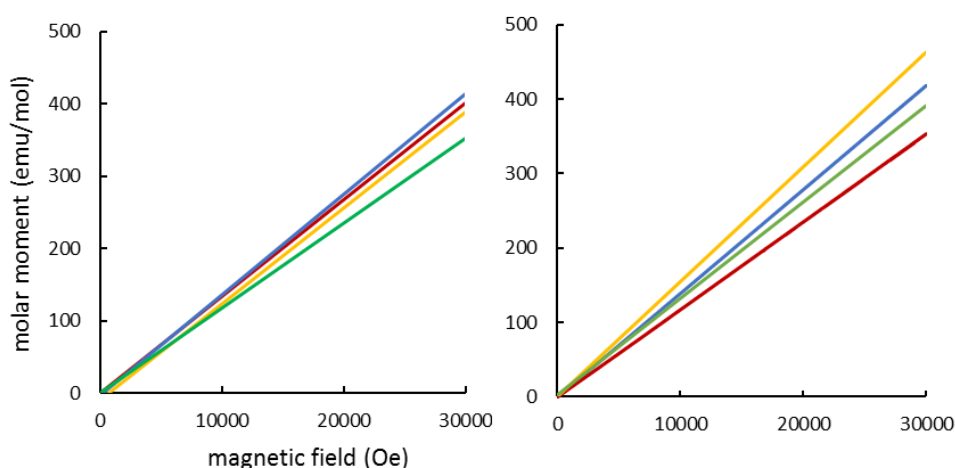


Figure 5.9 Magnetic susceptibility of a) $\text{Mn}(\text{NO}_3)_2 \cdot 4\text{H}_2\text{O}$ and b) $\text{Fe}(\text{NO}_3)_3 \cdot 9\text{H}_2\text{O}$ mixed with G3, G4, EtAN and PAN in a 1:1 molar ratio, measured under a sweeping field from -3×10^5 to $+3 \times 10^5$ Oe at 298K. Results are linear, therefore only the 0-30000 range is shown for simplicity.

Our systems are unique as the functional temperature range, sample density, and magnetic susceptibility can be tuned by formulation. Based on Table 5.2, which summarizes physical properties of paramagnetic mixtures tested, sample densities range between 1.0 and 1.6 g/cm^3 , and magnetic susceptibilities range between 0.012 to 0.014 $\text{emu}/\text{mol}\cdot\text{Oe}$, which are comparable to benchmark magnetic ILs, such as $[\text{Emim}][\text{FeCl}_4]$ and $[\text{Bmim}][\text{FeCl}_4]$.²⁵² Functional temperatures range between 0 to over 120 $^\circ\text{C}$, depending on the paramagnetic salt concentration.

Table 5.2 Properties of paramagnetic mixtures. The density range serve as a guide and are tuneable via formulation. Molar susceptibility was calculated from experimental data (Figure 5.9), based on mixtures with a 1:1 molar ratio.

	Density (g/cm ³)	susceptibility (emu/mol·Oe)
Mn(NO ₃) ₂ - G ₃	0.99-1.54	0.0138
Mn(NO ₃) ₂ - G ₄	1.00-1.54	0.0134
Mn(NO ₃) ₂ - EtAN	1.38-1.54	0.0128
Mn(NO ₃) ₂ - PAN	1.16-1.54	0.0117
Fe(NO ₃) ₃ - G ₃	0.99-1.68	0.0139
Fe(NO ₃) ₃ - G ₄	1.01-1.68	0.0118
Fe(NO ₃) ₃ - EtAN	1.38-1.68	0.0154
Fe(NO ₃) ₃ - PAN	1.16-1.68	0.0129

Paramagnetic salt solutions have been used for density-based measurement of diamagnetic objects by applying magnetic levitation.²⁵³ Magnetic ILs are potential candidates to replace aqueous solutions with advantages of having negligible vapour pressures, low melting points, and high thermal stabilities.²⁵⁴ The measuring window depends on the density of the medium, and the measuring precision depends on the magnetic susceptibility of the medium. In our systems, the densities, magnetic susceptibilities, and solvent-analyte compatibilities can be tuned over wide ranges by choosing the cation-anion pair and varying the concentration. This significantly broadens the application scope of magnetic levitation.

5.2.2 Magnetic manipulation of droplets

Microfluidics is another interesting area to apply magnetic ILs in, as the manipulation of fluid droplets is essential in micro-assays, environmental monitoring and microfluidic devices.²⁵⁵⁻²⁵⁷ Magnetic actuation has advantages of long-range forces, non-contact, controllability and negligible interaction with non-magnetic media.²⁵⁸ Traditional methods of using a dispersion of magnetic nanoparticles or encapsulating iron microparticles face challenges of evaporation and phase separation under ambient conditions.²⁵⁹ Magnetic ionic liquid droplets are chemically homogenous, and they have a negligible vapour pressure. The ability to control their movement on a hydrophobic surface offers new opportunities in microfluidics.²⁵² Using the Fe(NO₃)₃ - PAN system as an example, Figure 5.10 shows how the surface contact angle and the shape of a droplet changes with an applied magnetic field.

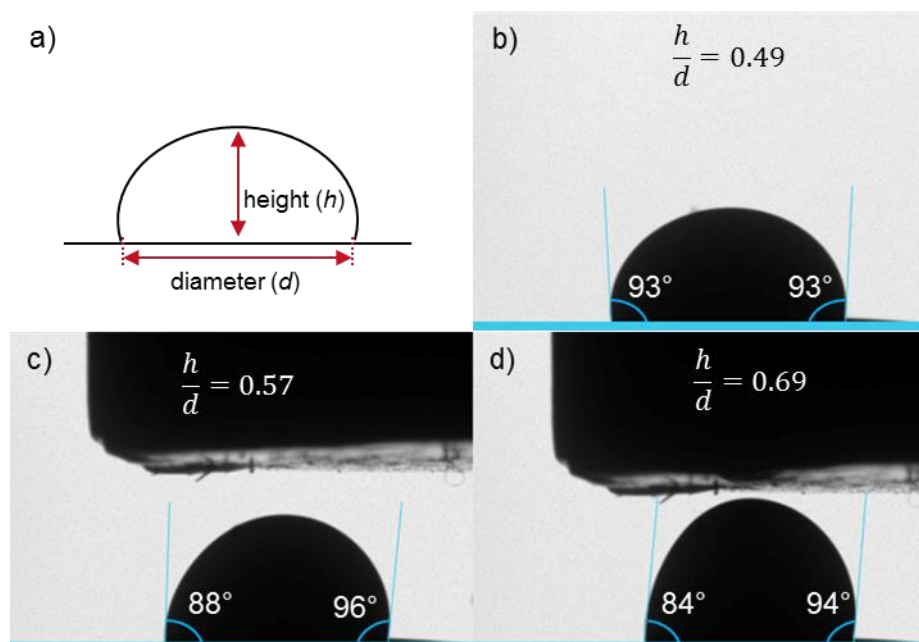


Figure 5.10 a) the shape of a droplet measured by the height-to-diameter ratio, b) a $20\mu\text{L}$ droplet of the $\text{Fe}(\text{NO}_3)_3$ - PAN mixture on a Teflon surface without the influence of a magnet. c-d) the same droplet under the influence of an external neodymium magnet bar of 0.5T . The contact angle and the shape of the droplet change as the external magnetic field shifts.

To evaluate the shape of the droplet, the ratio between the height of the droplet and the diameter at the line of contact was measured, as shown in Figure 5.10a. As an external magnet approaches to the droplet, the magnetic field experienced by the droplet strengthens. The droplet elongates along the direction of the magnetic force with an increasing height-to-diameter ratio from 0.49 to 0.69, as shown in Figure 5.10b-d. Depending on the direction of the magnetic force applied to the droplet (i.e. if it is perpendicular to the surface, or slightly tilted), the contact angle between the droplet and the Teflon surface changes accordingly. In figure 5.10c-d, the centre of the magnetic is slightly to the right of the droplet, which leads to an asymmetrical change in contact angle. In a study of aprotic magnetic ILs, He et al. has shown the shape change and the attainable speed of as a function of magnetic force in details.²⁵²

Optical transparency, high colour purity, and low volatility are major advantages of magnetic ILs over conventional magnetic fluids such as ferrofluids and magnetorheological fluids. Our results have shown the potential of magnetic ILs in fabricating soft lenses, of which their shape is tunable by an external magnet.

CHAPTER 6

CONCLUSIONS

The rational design of solvents addresses some of the most interesting problems in scientific research and many of the most challenging ones faced in industry. As designer solvents, ILs and their mixtures possess reasonably well-defined structure in the bulk phase, which underpins solvent behaviour. In this thesis, we dived into the concept of “solvent structure and nanostructure” and rationalised how one IL (or its solution) outperforms another solvent in a given process. In the context of biomass processing, we constructed a design framework of ILs to improve the dissolution of aromatic species. Utilising the amphiphilic character of ILs, we formulated a new matrix of microemulsions that are water-free and surfactant-free. Further, we discovered two new categories of ILs: one is based on the self-assembly of surfactants in inorganic salts; the other is based on the incorporation of paramagnetic salts into low-volatile solvents.

6.1 Primary and Secondary Ammonium ILs

Pyrrolidinium ILs, especially pyrrolidinium acetate (PyrrAc), have demonstrated an outstanding capacity for extracting lignin from biomass, as electrolytes for fuel cells and lithium ion batteries and as solvents for acid-catalyzed reactions. With a comparison to previously studied primary ammonium ILs, we have shown that the unusual liquid nanostructure of PyrrAc is the key to its versatility as a solvent. Neutron diffraction with multiple H/D isotopic substitutions reveals that the bulk nanostructure of PyrrAc is a bicontinuous network of interpenetrating polar and apolar domains. However, the arrangement of groups in both domains is strikingly different from that found in other ionic liquids. In the apolar regions, the pyrrolidinium rings are highly intercalated and disordered, with no preferred alignment between adjacent pyrrolidinium rings, which distinguishes it from both π - π stacking seen in imidazolium or pyridinium ionic liquids, and the tail-tail bilayer-like arrangements in linear alkylammonium ionic liquids. The H-bond network within the polar domain extends only to form finite clusters, with long bent H-bonds to accommodate electrostatics. Therefore, while PyrrAc unquestionably has well-defined amphiphilic nanostructure, the disordered arrangement of groups in the polar and apolar domains enables it to accommodate a wide variety of solutes. The combination of well-defined polar/apolar nanostructure, but disordered arrangements of groups within domains, is therefore the origin of PyrrAc's capacity for lignin extraction and as an electrolyte.

6.2 Design of ILs for Optimising Aromatic Dissolution

Certain protic ILs are potentially low-cost, high-efficiency solvents for the extraction and processing of aromatic compounds. Using neutron diffraction combined with EPSR, we compared the bulk structure of pyrrolidinium acetate (a secondary ammonium IL) and propylammonium nitrate (a primary ammonium IL) with and without an aromatic solute, guaiacol (2-methoxyphenol). Guaiacol is a common lignin residue in biomass processing, and a model compound for anisole- or phenol-based food additives and drug precursors. While a matched amphiphilicity between the solvent and the solute is a minimum criterion to facilitate the dissolution of small aromatic species, we find that the local geometry and competitive interactions between the polar groups of the cation, anion, and solute strongly influence solvation.

Hydrogen bonding is the driver for the dissolution of phenolic compounds. Primary alkylammonium cations form an extended H-bond network within the IL polar domains, whereas secondary or tertiary alkylammoniums have a higher availability of H-bond donor and acceptor to interact with a H-bonding solute. Compared to previously studied alkylammonium thiocyanate and hydrogensulfate with limited availability of H-bonding sites, the anions in both PyrAc and PAN have the short and linear H-bonding sites available to interact with a phenolic solute. Acetate is a good anion for the solubilization of phenolic compounds due to its asymmetry and site-specific interactions with the solute.

Choline amino acid-based ILs and their aqueous solutions are economically viable and environmentally friendly solvents. Choline lysinate (ChLys), an excellent solvent for lignin extraction and aromatic dissolution, was studied as a model amino acid-based IL. Unlike most primary and secondary ammonium ILs, the cation-anion electrostatic correlation occurs at a longer distance due to steric hinderance. All cation-anion hydrogen bonds are short and linear. The predominant interaction at short distances is between the choline hydroxyl group and the carboxylate acetate. Additional water molecules behave similar to the cholinium hydroxyl group, without significantly changing the arrangement of cations and anions. In both ChAc-water and ChLys-water mixtures, either charged groups or hydrogen bonding species form a continuous network. The difference is that the nanostructure of ChLys and its water mixture is much more pronounced.

We further explored the influence of water on aromatic dissolution in ChLys. Using guaiacol as a model aromatic solute, results showed a diverse range of hydrogen bonds around the phenolic group. Although ChLys consist more H-bonding capable species, the geometric competition is less severe than what is observed in alkylammonium ILs. Not only do water molecules go next to H-bonding

sites of guaiacol, they also distribute near the aromatic ring. The interaction between water and the IL facilitates the solubilisation of guaiacol, which is otherwise insoluble in water.

6.3 IL-induced Microemulsions

The amphiphilicity of protic ILs drives self-assembly of non-traditional amphiphiles at the nanoscale. Like surfactant, protic ILs induce miscibility of two immiscible components, such as water and oil. Unlike surfactant, the resulting nanostructure is relatively weak and could not be described by geometric models. In Chapter 4, we developed a strategic approach to analyse weakly-structured liquid systems. Three scattering techniques were utilised to obtain information at different length scales. Analyses include mathematical modelling and experimentally refined simulation.

PAN induces the self-assembly of octanol molecules at the nanoscale. A third component, either polar or apolar, can be accommodated into this binary system without causing phase separation. SAXS showed that liquid nanostructure is closely related to the induced miscibility. The most pronounced structures occur in the pre-ouzo region, near phase boundaries. SANS suggests that there is a polarity distinction among domains at the nanoscale. The polar domains consist mainly of IL charges groups. The apolar domains consist solvophobic groups such as alkyl tails.

An additional polar component, such as water, cooperates into the polar network. EPSR results showed that water and PAN charged groups mimic one another, as both are capable of H-bonding. With minimal changes to their local environment, two species compete at possible coordination sites. Strong polar network expels the solvophobic hydrocarbons outside, forming a relatively non-polar domain.

An additional apolar component, such as octane, partitions into the apolar region, effectively expanding the domain size. Based on SANS, octanol molecules rearrange to accommodate octane into the solvophobic domain. EPSR indicates an enhancement of correlations in the polar domain. The amphiphilicity of PAN remains strong, driving the formation of octanol-rich and octane-rich domains.

Protic IL-induced nanostructures are reminiscent of hydrotrope-containing systems. SANS illustrates that PAN and ethanol share common properties of producing *ultra-flexible microemulsions*, which contain polar and apolar domains at the nanoscale without a well-defined interface. Despite the original definition of hydrotrope, we found its amphiphilicity is not limited to aqueous environments. Water can be replaced by a non-amphiphilic protic IL, such as EtAN, without causing significant changes in the liquid nanostructure.

We proposed an amphiphilicity spectrum (Chapter 4, Figure 4.6) generalising species into three major sections: polar, amphiphilic and non-polar. Three components that are further apart in the spectrum are likely to induce pronounced liquid nanostructure. Moreover, it is important to consider the packing geometry of individual components when designing the bulk structure. Based on molecular structures, species are classified into four categories, including charged, acyclic, cyclic and aromatic. For the controlled construction of liquid nanostructure, it is important to consider solvent polarity, geometry and formulation.

6.4 Future Generations of Ionic Liquids

Extending from solvate ionic liquids, in which glymes or glycols complex onto a metal cation, we proposed a new family of ionic liquids, solvate surfactants (SSs). These are molten mixtures of lithium salts (LiX) and polyoxoethylene non-ionic surfactants (C_nE_m). The attachment of an apolar hydrocarbon tail (C_n) to the polar oligo(ethylene glycols) creates the coexistence of polar and apolar environment and therefore adding an amphiphilic character to solvate ionic liquids. Under polarising microscopy, we observed lamellar phases in $LiNO_3$ - $C_{14}E_4$ and $LiOTf$ - $C_{14}E_4$ mixtures. SAXS patterns showed the formulation of lamellar phase occurs only at high concentrations, near the solubility limit of $LiNO_3$ or $LiOTf$. In contrast, there is no liquid-crystalline phase in $LiTFSI$ - $C_{14}E_4$ mixtures in all compositions. We rationalised these observations by considering surfactant packing parameter. As the anion size increases from NO_3^- , OTf^- to $TFSI^-$, the polar area of the solvate surfactant increases, resulting in a packing parameter that is too low to form a liquid-crystalline phase. Moreover, surfactants with shorter alkyl tails, such as $C_{10}E_3$ and $C_{10}E_4$, form only micellar-type structures in all lithium salts tested. Our results are remarkably consistent with the structural behaviour of non-ionic surfactants in protic ILs, as in both cases C_{14} is the minimum alkyl-tail length required to form a lamellar phase. These trends allow us to predict the structural behaviour of solvate surfactants in formulating ternary mixtures, such as with an addition of an oil-like component to form microemulsions. It is possible to engineer solvate surfactant into cubic or hexagonal phases based on the packing parameter.

An alternative extension from solvate ionic liquids is the incorporation of paramagnetic metal cations, such as Mn^{2+} and Fe^{3+} . In Section 5.2, we formulated magnetic ionic liquids by dissolving low-melting salts, either $Mn(NO_3)_2 \cdot 4H_2O$ or $Fe(NO_3)_3 \cdot 9H_2O$, in low-volatility solvents including oligoglyme, oligo(ethylene glycols) and protic ILs. These ionic mixtures have comparable magnetic susceptibilities to conventional magnetic ILs, such as imidazolium ILs with a $FeCl_4^-$ anion. Our systems have tuneable

formulation, functional temperature range, sample density, and magnetic susceptibility. These are desirable characteristics for applications as magnetic levitation and magnetic manipulation of droplets.

ILs are not just another class of solvents. Our work has shown that even similar ILs interact differently with an additional solute (either molecular or ionic), formulating solvents that dramatically differ in structure, properties, and processing outcomes. The design of ILs as solvents is no longer limited to a *pure* salt that melts at low temperatures. Mixtures of IL-IL, IL-water, IL-inorganic salt, IL-surfactant, IL-organic solvents, and deep eutectic solvents have all emerged to meet specific physicochemical properties for process optimization.

We expect a continuing growth in the research of IL-containing solvents, especially with low-cost and biocompatible components such as water and amino acids. With an understanding of structure-property relationships, new generations of ILs will be applied to both established and emerging fields, such as energy storage, material synthesis, and biological applications. Rational design of ILs at the molecular level and at the nanoscale facilitates their cost/benefit economic analysis, enabling the innovation of solvent technology at the industrial scale.

References

1. Grand View Research (2015, August) Solvent Market Analysis By Product, By Application, And Segment Forecasts To 2020.

Retrieved from <https://www.grandviewresearch.com/industry-analysis/solvent-market>

2. Capello, C.; Fischer, U.; Hungerbuhler, K., What is a green solvent? A comprehensive framework for the environmental assessment of solvents. *Green Chem.* **2007**, 9 (9), 927-934.
3. Tanaka, K.; Toda, F., Solvent-Free Organic Synthesis. *Chem. Rev.* **2000**, 100 (3), 1025-1074.
4. Giernoth, R., Solvents and Solvent Effects in Organic Chemistry. 4th Ed. By Christian Reichardt and Thomas Welton. *Angewandte Chemie International Edition* **2011**, 50 (48), 11289-11289.
5. Holmberg, K., Organic Reactions in Microemulsions. *European Journal of Organic Chemistry* **2007**, 2007 (5), 731-742.
6. Shuai, L.; Luterbacher, J., Organic Solvent Effects in Biomass Conversion Reactions. *ChemSusChem* **2016**, 9 (2), 133-155.
7. Crick, F. H. What Mad Pursuit: A Personal View of Scientific Discovery; Basic Books: New York, 1988.
8. Bernal, J. D., A Geometrical Approach to the Structure Of Liquids. *Nature* **1959**, 183, 141.
9. Soper Alan, K., Recent water myths. In *Pure Appl. Chem.*, 2010; Vol. 82, p 1855.
10. Headen, T. F.; Howard, C. A.; Skipper, N. T.; Wilkinson, M. A.; Bowron, D. T.; Soper, A. K., Structure of pi-pi interactions in aromatic liquids. *J. Am. Chem. Soc.* **2010**, 132 (16), 5735-5742.
11. MacFarlane, D. R.; Chong, A. L.; Forsyth, M.; Kar, M.; Vijayaraghavan, R.; Somers, A.; Pringle, J. M., New dimensions in salt-solvent mixtures: a 4th evolution of ionic liquids. *Faraday Discuss* **2018**, 206 (0), 9-28.
12. Earle, M. J.; Esperanca, J. M.; Gilea, M. A.; Lopes, J. N.; Rebelo, L. P.; Magee, J. W.; Seddon, K. R.; Widegren, J. A., The distillation and volatility of ionic liquids. *Nature* **2006**, 439 (7078), 831-834.
13. MacFarlane, D. R.; Seddon, K. R., Ionic liquids - progress on the fundamental issues. *Aust. J. Chem.* **2007**, 60 (1), 3-5.
14. Earle, M. J.; Seddon, K. R., Ionic liquids: green solvents for the future. *Pure Appl. Chem.* **2000**, 72 (7), 1391-1398.
15. Angell, C. A.; Byrne, N.; Belieres, J. P., Parallel developments in aprotic and protic ionic liquids: physical chemistry and applications. *Acc. Chem. Res.* **2007**, 40 (11), 1228-1236.
16. Hayes, R.; Warr, G. G.; Atkin, R., At the interface: solvation and designing ionic liquids. *Phys. Chem. Chem. Phys.* **2010**, 12 (8), 1709-1723.
17. Endres, F., Ionic liquids: solvents for the electrodeposition of metals and semiconductors. *ChemPhysChem* **2002**, 3 (2), 145-154.
18. Welton, T., Room-temperature ionic liquids. Solvents for synthesis and catalysis. *Chem. Rev.* **1999**, 99 (8), 2071-2084.
19. Antonietti, M.; Kuang, D.; Smarsly, B.; Zhou, Y., Ionic liquids for the convenient synthesis of functional nanoparticles and other inorganic nanostructures. *Angew. Chem., Int. Ed.* **2004**, 43 (38), 4988-4992.
20. Greaves, T. L.; Drummond, C. J., Protic Ionic Liquids: Evolving Structure-Property Relationships and Expanding Applications. *Chem Rev* **2015**, 115 (20), 11379-448.
21. Belieres, J.-P.; Angell, C. A., Protic ionic liquids: Preparation, characterization, and proton free energy level representation. *J. Phys. Chem. B* **2007**, 111 (18), 4926-4937.
22. Hayes, R.; Warr, G. G.; Atkin, R., Structure and nanostructure in ionic liquids. *Chem. Rev.* **2015**, 115 (13), 6357-426.
23. Panic, M.; Radosevic, K.; Bubalo, M. C.; Curko, N.; Ganic, K. K.; Srcek, V. G.; Redovnikovic, I. R., Green solvents for green technologies. *Journal of Biotechnology* **2017**, 256, S11-S12.

24. Murphy, T.; Atkin, R.; Warr, G. G., Scattering from ionic liquids. *Curr. Opin. Colloid Interface Sci.* **2015**, *20* (4), 282-292.
25. Triolo, A.; Russina, O.; Bleif, H. J.; Di Cola, E., Nanoscale segregation in room temperature ionic liquids. *J. Phys. Chem. B* **2007**, *111* (18), 4641-4644.
26. Kashyap, H. K.; Santos, C. S.; Murthy, N. S.; Hettige, J. J.; Kerr, K.; Ramati, S.; Gwon, J.; Gohdo, M.; Lall-Ramnarine, S. I.; Wishart, J. F.; Margulis, C. J.; Castner, E. W., Jr., Structure of 1-alkyl-1-methylpyrrolidinium bis(trifluoromethylsulfonyl)amide ionic liquids with linear, branched, and cyclic alkyl groups. *J. Phys. Chem. B* **2013**, *117* (49), 15328-15337.
27. Greaves, T. L.; Kennedy, D. F.; Mudie, S. T.; Drummond, C. J., Diversity observed in the nanostructure of protic ionic liquids. *J. Phys. Chem. B* **2010**, *114* (31), 10022-10031.
28. Israelachvili, J. N.; Mitchell, D. J.; Ninham, B. W., Theory of self-assembly of hydrocarbon amphiphiles into micelles and bilayers. *J Chem Soc Farad T 2* **1976**, *72*, 1525-1568.
29. Jiang, H. J.; Imberti, S.; Atkin, R.; Warr, G. G., Dichotomous Well-defined Nanostructure with Weakly Arranged Ion Packing Explains the Solvency of Pyrrolidinium Acetate. *The Journal of Physical Chemistry B* **2017**, *121* (27), 6610-6617.
30. Hayes, R.; Imberti, S.; Warr, G. G.; Atkin, R., Effect of cation alkyl chain length and anion type on protic ionic liquid nanostructure. *J. Phys. Chem. C* **2014**, *118* (25), 13998-14008.
31. Greaves, T. L.; Kennedy, D. F.; Weerawardena, A.; Tse, N. M. K.; Kirby, N.; Drummond, C. J., Nanostructured protic ionic liquids retain nanoscale features in aqueous solution while precursor bronsted acids and bases exhibit different behavior. *J. Phys. Chem. B* **2011**, *115* (9), 2055-2066.
32. Greaves, T. L.; Kennedy, D. F.; Shen, Y.; Weerawardena, A.; Hawley, A.; Song, G. H.; Drummond, C. J., Fluorous protic ionic liquid exhibits a series of lyotropic liquid crystalline mesophases upon water addition. *Journal of Molecular Liquids* **2015**, *210*, 279-285.
33. Hayes, R.; Imberti, S.; Warr, G. G.; Atkin, R., Amphiphilicity determines nanostructure in protic ionic liquids. *Phys. Chem. Chem. Phys.* **2011**, *13* (8), 3237-3247.
34. Elbourne, A.; Voitchovsky, K.; Warr, G. G.; Atkin, R., Ion structure controls ionic liquid near-surface and interfacial nanostructure. *Chemical Science* **2015**, *6* (1), 527-536.
35. Elbourne, A.; Sweeney, J.; Webber, G. B.; Wanless, E. J.; Warr, G. G.; Rutland, M. W.; Atkin, R., Adsorbed and near-surface structure of ionic liquids determines nanoscale friction. *Chem. Commun. (Cambridge, U. K.)* **2013**, *49* (60), 6797-6799.
36. Cooper, P. K.; Wear, C. J.; Li, H.; Atkin, R., Ionic Liquid Lubrication of Stainless Steel: Friction is Inversely Correlated with Interfacial Liquid Nanostructure. *ACS Sustainable Chemistry & Engineering* **2017**, *5* (12), 11737-11743.
37. Jessop, P. G.; Jessop, D. A.; Fu, D.; Phan, L., Solvatochromic parameters for solvents of interest in green chemistry. *Green Chem.* **2012**, *14* (5), 1245-1259.
38. Ab Rani, M. A.; Brant, A.; Crowhurst, L.; Dolan, A.; Lui, M.; Hassan, N. H.; Hallett, J. P.; Hunt, P. A.; Niedermeyer, H.; Perez-Arlandis, J. M.; Schrems, M.; Welton, T.; Wilding, R., Understanding the polarity of ionic liquids. *Phys. Chem. Chem. Phys.* **2011**, *13* (37), 16831-16840.
39. Topolnicki, I. L.; FitzGerald, P. A.; Atkin, R.; Warr, G. G., Effect of protic ionic liquid and surfactant structure on partitioning of polyoxyethylene non-ionic surfactants. *ChemPhysChem* **2014**, *15* (12), 2485-2489.
40. Kirchner, B.; Holloczki, O.; Lopes, J. N. C.; Padua, A. A. H., Multiresolution calculation of ionic liquids. *Wiley Interdiscip. Rev.-Comput. Mol. Sci.* **2015**, *5* (2), 202-214.
41. George, A.; Brandt, A.; Tran, K.; Zahari, S.; Klein-Marcuschamer, D.; Sun, N.; Sathitsuksanoh, N.; Shi, J.; Stavila, V.; Parthasarathi, R.; Singh, S.; Holmes, B. M.; Welton, T.; Simmons, B. A.; Hallett, J. P., Design of low-cost ionic liquids for lignocellulosic biomass pretreatment. *Green Chem.* **2015**, *17* (3), 1728-1734.
42. Hayes, R.; Imberti, S.; Warr, G. G.; Atkin, R., How water dissolves in protic ionic liquids. *Angew. Chem., Int. Ed.* **2012**, *51* (30), 7468-71.
43. Jiang, H. J.; FitzGerald, P. A.; Dolan, A.; Atkin, R.; Warr, G. G., Amphiphilic self-assembly of alkanols in protic ionic liquids. *J. Phys. Chem. B* **2014**, *118* (33), 9983-9990.

44. Dias, A. M. A.; Cortez, A. R.; Barsan, M. M.; Santos, J. B.; Brett, C. M. A.; de Sousa, H. C., Development of Greener Multi-Responsive Chitosan Biornaterials Doped with Biocompatible Ammonium Ionic Liquids. *Acs Sustainable Chemistry & Engineering* **2013**, *1* (11), 1480-1492.
45. Hegde, G. A.; Bharadwaj, V. S.; Kinsinger, C. L.; Schutt, T. C.; Pisierra, N. R.; Maupin, C. M., Impact of water dilution and cation tail length on ionic liquid characteristics: Interplay between polar and non-polar interactions. *Journal of Chemical Physics* **2016**, *145* (6).
46. Russina, O.; Fazio, B.; Marco, G. D.; Caminiti, R.; Triolo, A., Structural Organization in Neat Ionic Liquids and in Their Mixtures. In *The Structure of Ionic Liquids*, Caminiti, R.; Gontrani, L., Eds. Springer, Cham: Switzerland, 2014; pp 39-61.
47. Murphy, T.; Hayes, R.; Imberti, S.; Warr, G. G.; Atkin, R., Nanostructure of an ionic liquid-glycerol mixture. *Phys. Chem. Chem. Phys.* **2014**, *16* (26), 13182-13190.
48. Salma, U.; Usula, M.; Caminiti, R.; Gontrani, L.; Plechkova, N. V.; Seddon, K. R., X-ray and molecular dynamics studies of butylammonium butanoate-water binary mixtures. *Phys. Chem. Chem. Phys.* **2017**, *19* (3), 1975-1981.
49. Murphy, T.; Callear, S. K.; Warr, G. G.; Atkin, R., Dissolved chloride markedly changes the nanostructure of the protic ionic liquids propylammonium and ethanolanionium nitrate. *Physical chemistry chemical physics : PCCP* **2016**.
50. Hayes, R.; Bernard, S. A.; Imberti, S.; Warr, G. G.; Atkin, R., Solvation of Inorganic Nitrate Salts in Protic Ionic Liquids. *J. Phys. Chem. C* **2014**, *118* (36), 21215-21225.
51. Aguilera, L.; Volkner, J.; Labrador, A.; Matic, A., The effect of lithium salt doping on the nanostructure of ionic liquids. *Phys. Chem. Chem. Phys.* **2015**, *17* (40), 27082-27087.
52. Araque, J. C.; Hettige, J. J.; Margulis, C. J., Modern Room Temperature Ionic Liquids, a Simple Guide to Understanding Their Structure and How It May Relate to Dynamics. *J. Phys. Chem. B* **2015**, *119* (40), 12727-12740.
53. Murphy, T.; Hayes, R.; Imberti, S.; Warr, G. G.; Atkin, R., Ionic liquid nanostructure enables alcohol self assembly. *Phys. Chem. Chem. Phys.* **2016**, *18* (18), 12797-12809.
54. Schroer, W.; Triolo, A.; Russina, O., Nature of Mesoscopic Organization in Protic Ionic Liquid-Alcohol Mixtures. *J. Phys. Chem. B* **2016**, *120* (9), 2638-2643.
55. Badgujar, K. C.; Bhanage, B. M., Factors governing dissolution process of lignocellulosic biomass in ionic liquid: Current status, overview and challenges. *Bioresource Technology* **2015**, *178*, 2-18.
56. Orr, V. C. A.; Rehmann, L., Ionic liquids for the fractionation of microalgae biomass. *Current Opinion in Green and Sustainable Chemistry* **2016**, *2*, 22-27.
57. Bryant, S. J.; Wood, K.; Atkin, R.; Warr, G. G., Effect of protic ionic liquid nanostructure on phospholipid vesicle formation. *Soft Matter* **2017**, *13* (7), 1364-1370.
58. Losada-Perez, P.; Khorshid, M.; Renner, F. U., Interactions of Aqueous Imidazolium-Based Ionic Liquid Mixtures with Solid-Supported Phospholipid Vesicles. *Plos One* **2016**, *11* (9).
59. Weber, C. C.; Masters, A. F.; Maschmeyer, T., Structural features of ionic liquids: consequences for material preparation and organic reactivity. *Green Chem.* **2013**, *15* (10), 2655-2679.
60. Weber, C. C.; Masters, A. F.; Maschmeyer, T., Pseudo-Encapsulation Nanodomains for Enhanced Reactivity in Ionic Liquids. *Angew. Chem., Int. Ed.* **2012**, *51* (46), 11483-11486.
61. Daly, R. P.; Araque, J. C.; Margulis, C. J., Communication: Stiff and soft nano-environments and the "Octopus Effect" are the crux of ionic liquid structural and dynamical heterogeneity. *The Journal of Chemical Physics* **2017**, *147* (6), 061102.
62. Hallett, J. P.; Welton, T., Room-temperature ionic liquids: solvents for synthesis and catalysis. *2. Chem. Rev.* **2011**, *111* (5), 3508-76.
63. Pensado, A. S.; Malberg, F.; Gomes, M. F. C.; Padua, A. A. H.; Fernandez, J.; Kirchner, B., Interactions and structure of ionic liquids on graphene and carbon nanotubes surfaces. *RSC Advances* **2014**, *4* (35), 18017-18024.

64. Ji, X. Y.; Zhang, Q.; Liang, F. X.; Chen, Q. N.; Qu, X. Z.; Zhang, C. L.; Wang, Q.; Li, J. L.; Song, X. M.; Yang, Z. Z., Ionic liquid functionalized Janus nanosheets. *Chemical Communications* **2014**, 50 (43), 5706-5709.
65. Fechler, N.; Fellingner, T. P.; Antonietti, M., "Salt Templating": A Simple and Sustainable Pathway toward Highly Porous Functional Carbons from Ionic Liquids. *Advanced Materials* **2013**, 25 (1), 75-79.
66. Endres, F.; Hofft, O.; Borisenko, N.; Gasparotto, L. H.; Prowald, A.; Al-Salman, R.; Carstens, T.; Atkin, R.; Bund, A.; El Abedin, S. Z., Do solvation layers of ionic liquids influence electrochemical reactions? *Phys. Chem. Chem. Phys.* **2010**, 12 (8), 1724-1732.
67. Yoo, C. G.; Pu, Y.; Ragauskas, A. J., Ionic liquids: Promising green solvents for lignocellulosic biomass utilization. *Current Opinion in Green and Sustainable Chemistry* **2017**, 5, 5-11.
68. Kirchhecker, S.; Esposito, D., Amino acid based ionic liquids: A green and sustainable perspective. *Current Opinion in Green and Sustainable Chemistry* **2016**, 2, 28-33.
69. Wang, R.; Chang, Y.; Tan, Z.; Li, F., Applications of choline amino acid ionic liquid in extraction and separation of flavonoids and pectin from ponkan peels. *Sep. Sci. Technol.* **2016**, 51 (7), 1093-1102.
70. Hou, X.-D.; Xu, J.; Li, N.; Zong, M.-H., Effect of Anion Structures on Cholinium Ionic Liquids Pretreatment of Rice Straw and the Subsequent Enzymatic Hydrolysis. *Biotechnology and Bioengineering* **2015**, 112 (1), 65-73.
71. To, T. Q.; Shah, K.; Tremain, P.; Simmons, B. A.; Moghtaderi, B.; Atkin, R., Treatment of lignite and thermal coal with low cost amino acid based ionic liquid-water mixtures. *Fuel* **2017**, 202, 296-306.
72. Karton, A.; Brunner, M.; Howard, M. J.; Warr, G. G.; Atkin, R., The high performance of choline arginate for biomass pretreatment is due to remarkably strong hydrogen bonding by the anion. *ACS Sustainable Chemistry & Engineering* **2018**.
73. Smith, E. L.; Abbott, A. P.; Ryder, K. S., Deep Eutectic Solvents (DESs) and Their Applications. *Chem. Rev. (Washington, DC, U. S.)* **2014**, 114 (21), 11060-11082.
74. Hammond, O. S.; Bowron, D. T.; Edler, K. J., The Effect of Water upon Deep Eutectic Solvent Nanostructure: An Unusual Transition from Ionic Mixture to Aqueous Solution. *Angew. Chem., Int. Ed.* **2017**, 56 (33), 9782-9785.
75. Stefanovic, R.; Ludwig, M.; Webber, G. B.; Atkin, R.; Page, A. J., Nanostructure, hydrogen bonding and rheology in choline chloride deep eutectic solvents as a function of the hydrogen bond donor. *Phys. Chem. Chem. Phys.* **2017**, 19 (4), 3297-3306.
76. Bryant, S. J.; Atkin, R.; Warr, G. G., Effect of Deep Eutectic Solvent Nanostructure on Phospholipid Bilayer Phases. *Langmuir* **2017**, 33 (27), 6878-6884.
77. Bryant, S. J.; Atkin, R.; Warr, G. G., Spontaneous vesicle formation in a deep eutectic solvent. *Soft Matter* **2016**, 12 (6), 1645-1648.
78. Chen, Z.; Ludwig, M.; Warr, G. G.; Atkin, R., Effect of cation alkyl chain length on surface forces and physical properties in deep eutectic solvents. *J. Colloid Interface Sci.* **2017**, 494, 373-379.
79. Warrag, S. E. E.; Peters, C. J.; Kroon, M. C., Deep eutectic solvents for highly efficient separations in oil and gas industries. *Current Opinion in Green and Sustainable Chemistry* **2017**, 5, 55-60.
80. Huang, K.; Chen, F. F.; Tao, D. J.; Dai, S., Ionic liquid-formulated hybrid solvents for CO₂ capture. *Current Opinion in Green and Sustainable Chemistry* **2017**, 5, 67-73.
81. Klein-Marcuschamer, D.; Simmons, B. A.; Blanch, H. W., Techno-economic analysis of a lignocellulosic ethanol biorefinery with ionic liquid pre-treatment. *Biofuels Bioprod. Biorefining* **2011**, 5 (5), 562-569.
82. Ruppert, A. M.; Weinberg, K.; Palkovits, R., Hydrogenolysis Goes Bio: From Carbohydrates and Sugar Alcohols to Platform Chemicals. *Angewandte Chemie International Edition* **2012**, 51 (11), 2564-2601.

83. Singh, S.; Simmons, B. A.; Vogel, K. P., Visualization of Biomass Solubilization and Cellulose Regeneration During Ionic Liquid Pretreatment of Switchgrass. *Biotechnology and Bioengineering* **2009**, *104* (1), 68-75.
84. Dutta, T.; Papa, G.; Wang, E.; Sun, J.; Isern, N. G.; Cort, J. R.; Simmons, B. A.; Singh, S., Characterization of Lignin Streams during Bionic Liquid-Based Pretreatment from Grass, Hardwood, and Softwood. *Acs Sustainable Chemistry & Engineering* **2018**, *6* (3), 3079-3090.
85. Ragauskas, A. J.; Beckham, G. T.; Biddy, M. J.; Chandra, R.; Chen, F.; Davis, M. F.; Davison, B. H.; Dixon, R. A.; Gilna, P.; Keller, M.; Langan, P.; Naskar, A. K.; Saddler, J. N.; Tschaplinski, T. J.; Tuskan, G. A.; Wyman, C. E., Lignin Valorization: Improving Lignin Processing in the Biorefinery. *Science* **2014**, *344* (6185).
86. Roberts, V. M.; Stein, V.; Reiner, T.; Lemonidou, A.; Li, X.; Lercher, J. A., Towards Quantitative Catalytic Lignin Depolymerization. *Chemistry – A European Journal* **2011**, *17* (21), 5939-5948.
87. Song, Q.; Wang, F.; Cai, J.; Wang, Y.; Zhang, J.; Yu, W.; Xu, J., Lignin depolymerization (LDP) in alcohol over nickel-based catalysts via a fragmentation–hydrogenolysis process. *Energy & Environmental Science* **2013**, *6* (3), 994-1007.
88. Horáček, J.; Homola, F.; Kubičková, I.; Kubička, D., Lignin to liquids over sulfided catalysts. *Catalysis Today* **2012**, *179* (1), 191-198.
89. Danielsson, I.; Lindman, B., The definition of microemulsion. *Colloids and Surfaces* **1981**, *3* (4), 391-392.
90. Taber, J. J., Research on Enhanced Oil Recovery: Past, Present and Future. In *Surface Phenomena in Enhanced Oil Recovery*, Shah, D. O., Ed. Springer US: Boston, MA, 1981; pp 13-52.
91. Lawrence, M. J.; Rees, G. D., Microemulsion-based media as novel drug delivery systems. *Advanced Drug Delivery Reviews* **2000**, *45* (1), 89-121.
92. Schroeter, A.; Engelbrecht, T.; Neubert, R. H. H.; Goebel, A. S. B., New Nanosized Technologies for Dermal and Transdermal Drug Delivery. A Review. *Journal of Biomedical Nanotechnology* **2010**, *6* (5), 511-528.
93. Ganguly, A. K.; Ganguly, A.; Vaidya, S., Microemulsion-based synthesis of nanocrystalline materials. *Chem. Soc. Rev.* **2010**, *39* (2), 474-485.
94. Eastoe, J.; Hollamby, M. J.; Hudson, L., Recent advances in nanoparticle synthesis with reversed micelles. *Adv. Colloid Interface Sci.* **2006**, *128-130*, 5-15.
95. Margulis-Goshen, K.; Magdassi, S., Organic nanoparticles from microemulsions: Formation and applications. *Curr. Opin. Colloid Interface Sci.* **2012**, (5).
96. Prévost, S.; Gradzielski, M.; Zemb, T., Self-assembly, phase behaviour and structural behaviour as observed by scattering for classical and non-classical microemulsions. *Adv. Colloid Interface Sci.* **2017**, *247*, 374-396.
97. Zemb, T. N.; Klossek, M.; Lopian, T.; Marcus, J.; Schöetl, S.; Horinek, D.; Prevost, S. F.; Touraud, D.; Diat, O.; Marčelja, S.; Kunz, W., How to explain microemulsions formed by solvent mixtures without conventional surfactants. *Proceedings of the National Academy of Sciences* **2016**, *113* (16), 4260-4265.
98. Hou, W.; Xu, J., Surfactant-free microemulsions. *Current Opinion in Colloid and Interface Science* **2016**, *25*, 67-74.
99. Prevost, S.; Lopian, T.; Pleines, M.; Diat, O.; Zemb, T., Small-angle scattering and morphologies of ultra-flexible microemulsions. *Journal of Applied Crystallography* **2016**, *49*, 2063-2072.
100. Schöetl, S.; Horinek, D., Aggregation in detergent-free ternary mixtures with microemulsion-like properties. *Curr. Opin. Colloid Interface Sci.* **2016**, *22*, 8-13.
101. Fischer, V.; Marcus, J.; Touraud, D.; Diat, O.; Kunz, W., Toward surfactant-free and water-free microemulsions. *J Colloid Interf Sci* **2015**, *453*, 186-193.

102. Schottl, S.; Touraud, D.; Kunz, W.; Zemb, T.; Horinek, D., Consistent definitions of "the interface" in surfactant-free micellar aggregates. *Colloids and Surfaces a-Physicochemical and Engineering Aspects* **2015**, *480*, 222-227.
103. Marcus, J.; Touraud, D.; Prevost, S.; Diat, O.; Zemb, T.; Kunz, W., Influence of additives on the structure of surfactant-free microemulsions. *Phys. Chem. Chem. Phys.* **2015**, *17* (48), 32528-32538.
104. Schottl, S.; Marcus, J.; Diat, O.; Touraud, D.; Kunz, W.; Zemb, T.; Horinek, D., Emergence of surfactant-free micelles from ternary solutions. *Chemical Science* **2014**, *5* (8), 2949-2954.
105. Klossek, M. L.; Touraud, D.; Kunz, W., Eco-solvents - cluster-formation, surfactantless microemulsions and facilitated hydrotropy. *Phys. Chem. Chem. Phys.* **2013**, *15* (26), 10971-10977.
106. Diat, O.; Klossek, M. L.; Touraud, D.; Deme, B.; Grillo, I.; Kunz, W.; Zemb, T., Octanol-rich and water-rich domains in dynamic equilibrium in the pre-ouzo region of ternary systems containing a hydrotrope. *Journal of Applied Crystallography* **2013**, *46*, 1665-1669.
107. Klossek, M. L.; Touraud, D.; Zemb, T.; Kunz, W., Structure and Solubility in Surfactant-Free Microemulsions. *ChemPhysChem* **2012**, *13* (18), 4116-4119.
108. Neuberg C. Hydrotropic phenomena. *Biochem Z* 1916;76:107-76.
109. Kunz, W.; Holmberg, K.; Zemb, T., Hydrotropes. *Current Opinion in Colloid and Interface Science* **2016**, *22*, 99-107.
110. Evans, D. F.; Yamauchi, A.; Roman, R.; Casassa, E. Z., MICELLE FORMATION IN ETHYLAMMONIUM NITRATE, A LOW-MELTING FUSED SALT. *J Colloid Interf Sci* **1982**, *88* (1), 89-96.
111. Atkin, R.; Bobillier, S. M. C.; Warr, G. G., Propylammonium Nitrate as a Solvent for Amphiphile Self-Assembly into Micelles, Lyotropic Liquid Crystals, and Microemulsions. *J. Phys. Chem. B* **2010**, *114* (3), 1350-1360.
112. Eastoe, J.; Gold, S.; Rogers, S. E.; Paul, A.; Welton, T.; Heenan, R. K.; Grillo, I., Ionic liquid-in-oil microemulsions. *J. Am. Chem. Soc.* **2005**, *127* (20), 7302-7303.
113. Wellens, S.; Thijs, B.; Binnemans, K., How safe are protic ionic liquids? Explosion of pyrrolidinium nitrate. *Green Chem.* **2013**, *15* (12), 3484-3485.
114. Achinivu, E. C.; Howard, R. M.; Li, G. Q.; Gracz, H.; Henderson, W. A., Lignin extraction from biomass with protic ionic liquids. *Green Chem.* **2014**, *16* (3), 1114-1119.
115. Zhang, Q.; Benoit, M.; De Oliveira Vigier, K.; Barrault, J.; Jérôme, F., Green and Inexpensive Choline-Derived Solvents for Cellulose Decrystallization. *Chemistry – A European Journal* **2012**, *18* (4), 1043-1046.
116. Petkovic, M.; Ferguson, J. L.; Gunaratne, H. Q. N.; Ferreira, R.; Leitão, M. C.; Seddon, K. R.; Rebelo, L. P. N.; Pereira, C. S., Novel biocompatible cholinium-based ionic liquids—toxicity and biodegradability. *Green Chem.* **2010**, *12* (4), 643-649.
117. Ren, H.; Zong, M.-H.; Wu, H.; Li, N., Efficient Pretreatment of Wheat Straw Using Novel Renewable Cholinium Ionic Liquids To Improve Enzymatic Saccharification. *Industrial & Engineering Chemistry Research* **2016**, *55* (6), 1788-1795.
118. Vitale, S. A.; Katz, J. L., Liquid droplet dispersions formed by homogeneous liquid-liquid nucleation: "The ouzo effect". *Langmuir* **2003**, *19* (10), 4105-4110.
119. Shimizu, S.; Matubayasi, N., Hydrotropy and scattering: Pre-ouzo as an extended near-spinodal region. *Phys. Chem. Chem. Phys.* **2017**, *19* (39), 26734-26742.
120. Bauduin, P.; Testard, F.; Zemb, T., Solubilization in alkanes by alcohols as reverse hydrotropes or "Lipotropes". *J. Phys. Chem. B* **2008**, *112* (39), 12354-12360.
121. Oldenbourg, R., Polarized Light Microscopy: Principles and Practice. *Cold Spring Harbor Protocols* **2013**, *2013* (11), pdb.top078600.
122. Pelzl, G.; Hauser, A., Birefringence and phase transitions in liquid crystals. *Phase Transitions* **1991**, *37* (1), 33-62.
123. R. Carlton, in *Pharmaceutical Microscopy*, Springer New York, 2011, DOI: 10.1007/978-1-4419-8831-7_2, ch. 2, pp. 7-64.

124. Rosevear, F. B., The microscopy of the liquid crystalline neat and middle phases of soaps and synthetic detergents. *Journal of the American Oil Chemists' Society* **1954**, 31 (12), 628-639.
125. Laughlin, R. G., The role of swelling methods in surfactant phase science: past, present, and future. *Adv. Colloid Interface Sci.* **1992**, 41, 57-79.
126. Hyde, A. J.; Langbridge, D. M.; Lawrence, A. S. C., Soap + water + amphiphile systems. *Discussions of the Faraday Society* **1954**, 18 (0), 239-258.
127. O'Handley, R. C., *Modern Magnetic Materials: Principles and Applications*. Wiley: 1999.
128. Edward, J. T.; Farrell, P. G.; Shahidi, F., PARTIAL MOLAL VOLUMES OF ORGANIC-COMPOUNDS IN CARBON-TETRACHLORIDE .1. ALKANES - CONFORMATIONAL EFFECTS. *J. Phys. Chem.* **1978**, 82 (21), 2310-2313.
129. Gruen, D. W. R., A model for the chains in amphiphilic aggregates. 1. Comparison with a molecular dynamics simulation of a bilayer. *The Journal of Physical Chemistry* **1985**, 89 (1), 146-153.
130. <http://www.ncnr.nist.gov/resources/activation/>
131. Gilbert, E. P.; Schulz, J. C.; Noakes, T. J., 'Quokka' - the small-angle neutron scattering instrument at OPAL. *Physica B* **2006**, 385-86, 1180-1182.
132. Kline, S. R., Reduction and analysis of SANS and USANS data using IGOR Pro. *Journal of Applied Crystallography* **2006**, 39, 895-900.
133. Porod, G., DIE RONTGENKLEINWINKELSTREUUNG VON DICHTGEPACKTEN KOLLOIDEN SYSTEMEN .1. *Kolloid-Zeitschrift and Zeitschrift Fur Polymere* **1951**, 124 (2), 83-114.
134. Porod, G., DIE RONTGENKLEINWINKELSTREUUNG VON DICHTGEPAKTEN KOLLOIDEN SYSTEMEN .2. *Kolloid-Zeitschrift and Zeitschrift Fur Polymere* **1952**, 125 (1), 51-57.
135. de Campo, L.; Varslot, T.; Moghaddam, M. J.; Kirkensgaard, J. J. K.; Mortensen, K.; Hyde, S. T., A novel lyotropic liquid crystal formed by triphilic star-polyphiles: hydrophilic/oleophilic/fluorophilic rods arranged in a 12.6.4. tiling. *Phys. Chem. Chem. Phys.* **2011**, 13 (8), 3139-3152.
136. Enderby, J. E., NEUTRON-DIFFRACTION, ISOTOPIC-SUBSTITUTION AND THE STRUCTURE OF AQUEOUS-SOLUTIONS. *Philos. Trans. R. Soc. Lond. Ser. B-Biol. Sci.* **1980**, 290 (1043), 553-566.
137. Soper, A. K., Inelasticity corrections for time-of-flight and fixed wavelength neutron diffraction experiments. *Molecular Physics* **2009**, 107 (16), 1667-1684.
138. Soper, A. K.; Howells, W. S.; Hannon, A. C., *ATLAS : analysis of time-of-flight diffraction data from liquid and amorphous samples*. Rutherford Appleton Laboratory: Didcot, 1989.
139. Soper, A. K., Joint structure refinement of x-ray and neutron diffraction data on disordered materials: application to liquid water. *J. Phys.-Condes. Matter* **2007**, 19 (33), 18.
140. Soper, A. K., Empirical potential Monte Carlo simulation of fluid structure. *Chem. Phys.* **1996**, 202 (2-3), 295-306.
141. Soper, A. K., Partial structure factors from disordered materials diffraction data: An approach using empirical potential structure refinement. *Phys. Rev. B* **2005**, 72 (10).
142. Soper, A. K., Tests of the empirical potential structure refinement method and a new method of application to neutron diffraction data on water. *Molecular Physics* **2001**, 99 (17), 1503-1516.
143. Guillaume, E.; László, P., Reverse Monte Carlo modelling of the structure of disordered materials with RMC++ : a new implementation of the algorithm in C++. *Journal of Physics: Condensed Matter* **2005**, 17 (5), S1.
144. Pusztai, L. In *Reverse Monte Carlo Modelling of Diffraction Data : Structural Studies of Amorphous Ices*, Dordrecht, Springer Netherlands: Dordrecht, 2004; pp 237-256.
145. McGreevy, R. L., Reverse Monte Carlo modelling. *Journal of Physics: Condensed Matter* **2001**, 13 (46), R877.
146. Ballentine, L. E.; Jones, J. C., Relationship between Pair Potentials and Liquid Structure. *Canadian Journal of Physics* **1973**, 51 (17), 1831-1839.
147. Svishchev, I. M.; Kusalik, P. G., STRUCTURE IN LIQUID WATER - A STUDY OF SPATIAL-DISTRIBUTION FUNCTIONS. *Journal of Chemical Physics* **1993**, 99 (4), 3049-3058.

148. Gray, C. G.; Gray, C. G.; Gubbins, K. E.; Joslin, C. G., *Theory of Molecular Fluids: I: Fundamentals*. OUP Oxford: 1984.
149. Towey, J. J.; Soper, A. K.; Dougan, L., Molecular insight into the hydrogen bonding and micro-segregation of a cryoprotectant molecule. *The journal of physical chemistry. B* **2012**, *116* (47), 13898-904.
150. T. Youngs, <https://www.projectaten.com/dlputils>
151. George, A.; Tran, K.; Morgan, T. J.; Benke, P. I.; Berruoco, C.; Lorente, E.; Wu, B. C.; Keasling, J. D.; Simmons, B. A.; Holmes, B. M., The effect of ionic liquid cation and anion combinations on the macromolecular structure of lignins. *Green Chem.* **2011**, *13* (12), 3375-3385.
152. Shi, J.; Thompson, V. S.; Yancey, N. A.; Stavila, V.; Simmons, B. A.; Singh, S., Impact of mixed feedstocks and feedstock densification on ionic liquid pretreatment efficiency. *Biofuels* **2013**, *4* (1), 63-72.
153. Çetinkol, Ö. P.; Dibble, D. C.; Cheng, G.; Kent, M. S.; Knierim, B.; Auer, M.; Wemmer, D. E.; Pelton, J. G.; Melnichenko, Y. B.; Ralph, J.; Simmons, B. A.; Holmes, B. M., Understanding the impact of ionic liquid pretreatment on eucalyptus. *Biofuels* **2010**, *1* (1), 33-46.
154. Anouti, M.; Caillon-Caravanier, M.; Dridi, Y.; Galiano, H.; Lemordant, D., Synthesis and characterization of new pyrrolidinium based protic ionic liquids. Good and superionic liquids. *J. Phys. Chem. B* **2008**, *112* (42), 13335-13343.
155. Anouti, M.; Timperman, L., A pyrrolidinium nitrate protic ionic liquid-based electrolyte for very low-temperature electrical double-layer capacitors. *Phys. Chem. Chem. Phys.* **2013**, *15* (17), 6539-6548.
156. Vogl, T.; Menne, S.; Kuhnel, R. S.; Balducci, A., The beneficial effect of protic ionic liquids on the lithium environment in electrolytes for battery applications. *J. Mater. Chem. A* **2014**, *2* (22), 8258-8265.
157. Araque, J. C.; Yadav, S. K.; Shadeck, M.; Maroncelli, M.; Margulis, C. J., How is diffusion of neutral and charged tracers related to the structure and dynamics of a room-temperature ionic liquid? Large deviations from Stokes–Einstein behavior explained. *J. Phys. Chem. B* **2015**, *119* (23), 7015-7029.
158. Kashyap, H. K.; Annapureddy, H. V. R.; Raineri, F. O.; Margulis, C. J., How Is Charge Transport Different in Ionic Liquids and Electrolyte Solutions? *J. Phys. Chem. B* **2011**, *115* (45), 13212-13221.
159. Hall, H. K., Correlation of the base strengths of amines. *J. Am. Chem. Soc.* **1957**, *79* (20), 5441-5444.
160. Walba, H.; Isensee, R. W., Acidity constants of some arylimidazoles and their cations. *J. Org. Chem.* **1961**, *26* (8), 2789-2791.
161. Evans, D. F.; Chen, S.; Schriver, G. W.; Arnett, E. M., Thermodynamics of solution of nonpolar gases in a fused salt. Hydrophobic bonding behavior in a nonaqueous system. *J. Am. Chem. Soc.* **1981**, *103* (2), 481-482.
162. Hayes, R.; Imberti, S.; Warr, G. G.; Atkin, R., The nature of hydrogen bonding in protic ionic liquids. *Angew. Chem., Int. Ed.* **2013**, *52* (17), 4623-4627.
163. Greaves, T. L.; Drummond, C. J., Solvent nanostructure, the solvophobic effect and amphiphile self-assembly in ionic liquids. *Chem.Soc.Rev.* **2013**, *42*, 1096-1120.
164. Ray, A., Solvophobic Interactions and Micelle Formation in Structure Forming Nonaqueous Solvents. *Nature* **1971**, *231* (5301), 313-315.
165. Kashyap, H. K.; Hettige, J. J.; Annapureddy, H. V.; Margulis, C. J., SAXS anti-peaks reveal the length-scales of dual positive-negative and polar-apolar ordering in room-temperature ionic liquids. *Chem Commun (Camb)* **2012**, *48* (42), 5103-5.
166. Jan, N., Large lattice random site percolation. *Physica A* **1999**, *266* (1-4), 72-75.
167. Anouti, M.; Vigeant, A.; Jacquemin, J.; Brigouleix, C.; Lemordant, D., Volumetric properties, viscosity and refractive index of the protic ionic liquid, pyrrolidinium octanoate, in molecular solvents. *J. Chem. Thermodyn.* **2010**, *42* (7), 834-845.

168. Amith, W. D.; Hettige, J. J.; Castner, E. W.; Margulis, C. J., Structures of ionic liquids having both anionic and cationic octyl tails: lamellar vacuum interface vs sponge-like bulk order. *J. Phys. Chem. Lett.* **2016**, *7* (19), 3785-3790.
169. Shen, Y.; Kennedy, D. F.; Greaves, T. L.; Weerawardena, A.; Mulder, R. J.; Kirby, N.; Song, G. H.; Drummond, C. J., Protic ionic liquids with fluorinated anions: physicochemical properties and self-assembly nanostructure. *Phys. Chem. Chem. Phys.* **2012**, *14* (22), 7981-7992.
170. Hettige, J. J.; Araque, J. C.; Margulis, C. J., Bicontinuity and multiple length scale ordering in triphasic hydrogen-bonding ionic liquids. *J. Phys. Chem. B* **2014**, *118* (44), 12706-12716.
171. Youngs, T. G. A. DLPUTILS: Calculate properties from molecular dynamics trajectories. <https://www.projectatn.com/dlputils> (accessed December 2016).
172. Matthews, R. P.; Welton, T.; Hunt, P. A., Competitive pi interactions and hydrogen bonding within imidazolium ionic liquids. *Phys. Chem. Chem. Phys.* **2014**, *16* (7), 3238-3253.
173. Hayes, R.; Imberti, S.; Warr, G. G.; Atkin, R., Pronounced sponge-like nanostructure in propylammonium nitrate. *Phys. Chem. Chem. Phys.* **2011**, *13* (30), 13544-13551.
174. Hayes, R.; Imberti, S.; Warr, G. G.; Atkin, R., Effect of Cation Alkyl Chain Length and Anion Type on Protic Ionic Liquid Nanostructure. *J. Phys. Chem. C* **2014**, *118*, 13998-13998.
175. Israelachvili, J. N.; Mitchell, D. J.; Ninham, B. W., Theory of self-assembly of hydrocarbon amphiphiles into micelles and bilayers. *J. Chem. Soc., Faraday Trans. 2* **1976**, *72*, 1525-1568.
176. Israelachvili, J. N.; Marcelja, S.; Horn, R. G., Physical principles of membrane organization. *Q. Rev. Biophys.* **1980**, *13* (2), 121-200.
177. Zemb, T. N.; Hyde, S. T.; Derian, P. J.; Barnes, I. S.; Ninham, B. W., Microstructure from X-ray scattering - the disordered open connected model of microemulsions. *J. Phys. Chem.* **1987**, *91* (14), 3814-3820.
178. Strey, R., Microemulsion microstructure and interfacial curvature. *Colloid Polym. Sci.* **1994**, *272* (8), 1005-1019.
179. Chen, V.; Warr, G. G.; Evans, D. F.; Prendergast, F. G., Curvature and geometric constraints as determinants of microemulsion structure - evidence from fluorescence anisotropy measurements. *J. Phys. Chem.* **1988**, *92* (3), 768-773.
180. Bowron, D. T.; D'Agostino, C.; Gladden, L. F.; Hardacre, C.; Holbrey, J. D.; Lagunas, M. C.; McGregor, J.; Mantle, M. D.; Mullan, C. L.; Youngs, T. G., Structure and dynamics of 1-ethyl-3-methylimidazolium acetate via molecular dynamics and neutron diffraction. *J. Phys. Chem. B* **2010**, *114* (23), 7760-7768.
181. Chundawat, S. P. S.; Beckham, G. T.; Himmel, M. E.; Dale, B. E., Deconstruction of lignocellulosic biomass to fuels and chemicals. In *Annual Review of Chemical and Biomolecular Engineering, Vol 2*, Prausnitz, J. M., Ed. 2011; Vol. 2, pp 121-145.
182. Binder, J. B.; Raines, R. T., Simple chemical transformation of lignocellulosic biomass into furans for fuels and chemicals. *J. Am. Chem. Soc.* **2009**, *131* (5), 1979-1985.
183. Brandt, A.; Grasvik, J.; Hallett, J. P.; Welton, T., Deconstruction of lignocellulosic biomass with ionic liquids. *Green Chem.* **2013**, *15* (3), 550-583.
184. Varanasi, P.; Singh, P.; Auer, M.; Adams, P. D.; Simmons, B. A.; Singh, S., Survey of renewable chemicals produced from lignocellulosic biomass during ionic liquid pretreatment. *Biotechnology for Biofuels* **2013**, *6*.
185. Stärk, K.; Taccardi, N.; Bösmann, A.; Wasserscheid, P., Oxidative Depolymerization of Lignin in Ionic Liquids. *ChemSusChem* **2010**, *3* (6), 719-723.
186. Xu, C.; Arancon, R. A.; Labidi, J.; Luque, R., Lignin depolymerisation strategies: towards valuable chemicals and fuels. *Chem Soc Rev* **2014**, *43* (22), 7485-500.
187. Zhang, K.; Pei, Z. J.; Wang, D. H., Organic solvent pretreatment of lignocellulosic biomass for biofuels and biochemicals: A review. *Bioresource Technology* **2016**, *199*, 21-33.
188. Brandt, A.; Hallett, J. P.; Leak, D. J.; Murphy, R. J.; Welton, T., The effect of the ionic liquid anion in the pretreatment of pine wood chips. *Green Chem.* **2010**, *12* (4), 672-679.

189. Sun, N.; Rahman, M.; Qin, Y.; Maxim, M. L.; Rodriguez, H.; Rogers, R. D., Complete dissolution and partial delignification of wood in the ionic liquid 1-ethyl-3-methylimidazolium acetate. *Green Chem.* **2009**, *11* (5), 646-655.
190. Pinkert, A.; Goeke, D. F.; Marsh, K. N.; Pang, S., Extracting wood lignin without dissolving or degrading cellulose: investigations on the use of food additive-derived ionic liquids. *Green Chem.* **2011**, *13* (11), 3124-3136.
191. Jiang, H. J.; Atkin, R.; Warr, G. G., Nanostructured ionic liquids and their solutions: Recent advances and emerging challenges. *Current Opinion in Green and Sustainable Chemistry* **2018**, *12*, 27-32.
192. Binder, J. B.; Gray, M. J.; White, J. F.; Zhang, Z. C.; Holladay, J. E., Reactions of lignin model compounds in ionic liquids. *Biomass and Bioenergy* **2009**, *33* (9), 1122-1130.
193. Jiang, H. J.; Imberti, S.; Atkin, R.; Warr, G. G., Dichotomous Well-defined Nanostructure with Weakly Arranged Ion Packing Explains the Solvency of Pyrrolidinium Acetate. *J. Phys. Chem. B* **2017**, *121* (27), 6610-6617.
194. Jiang, H. J.; FitzGerald, P. A.; Dolan, A.; Atkin, R.; Warr, G. G., Amphiphilic self-assembly of alkanols in protic ionic liquids. *J. Phys. Chem. B* **2014**, *118* (33), 9983-90.
195. Greaves, T. L.; Kennedy, D. F.; Kirby, N.; Drummond, C. J., Nanostructure changes in protic ionic liquids (PILs) through adding solutes and mixing PILs. *Phys. Chem. Chem. Phys.* **2011**, *13* (30), 13501-13509.
196. De Gregorio, G. F.; Weber, C. C.; Grasvik, J.; Welton, T.; Brandt, A.; Hallett, J. P., Mechanistic insights into lignin depolymerisation in acidic ionic liquids. *Green Chem.* **2016**, *18* (20), 5456-5465.
197. George, A.; Brandt, A.; Tran, K.; Zahari, S. M. S. N. S.; Klein-Marcuschamer, D.; Sun, N.; Sathitsuksanoh, N.; Shi, J.; Stavila, V.; Parthasarathi, R.; Singh, S.; Holmes, B. M.; Welton, T.; Simmons, B. A.; Hallett, J. P., Design of low-cost ionic liquids for lignocellulosic biomass pretreatment. *Green Chem.* **2015**, *17* (3), 1728-1734.
198. Chen, Z. F.; Greaves, T. L.; Warr, G. G.; Atkin, R., Mixing cations with different alkyl chain lengths markedly depresses the melting point in deep eutectic solvents formed from alkylammonium bromide salts and urea. *Chem. Commun. (Cambridge, U. K.)* **2017**, *53* (15), 2375-2377.
199. Sun, N.; Parthasarathi, R.; Socha, A. M.; Shi, J.; Zhang, S.; Stavila, V.; Sale, K. L.; Simmons, B. A.; Singh, S., Understanding pretreatment efficacy of four cholinium and imidazolium ionic liquids by chemistry and computation. *Green Chem.* **2014**, *16* (5), 2546-2557.
200. Liu, Q.-P.; Hou, X.-D.; Li, N.; Zong, M.-H., Ionic liquids from renewable biomaterials: synthesis, characterization and application in the pretreatment of biomass. *Green Chem.* **2012**, *14* (2), 304-307.
201. Hou, X.-D.; Smith, T. J.; Li, N.; Zong, M.-H., Novel renewable ionic liquids as highly effective solvents for pretreatment of rice straw biomass by selective removal of lignin. *Biotechnology and Bioengineering* **2012**, *109* (10), 2484-2493.
202. Soper, A. K., The radial distribution functions of water and ice from 220 to 673 K and at pressures up to 400 MPa. *Chem. Phys.* **2000**, *258* (2-3), 121-137.
203. Imberti, S.; Bowron, D. T., Formic and acetic acid aggregation in the liquid state. *J. Phys.-Condes. Matter* **2010**, *22* (40).
204. Hou, X.-D.; Li, N.; Zong, M.-H., Facile and Simple Pretreatment of Sugar Cane Bagasse without Size Reduction Using Renewable Ionic Liquids–Water Mixtures. *ACS Sustainable Chemistry & Engineering* **2013**, *1* (5), 519-526.
205. To, T. Q.; Procter, K.; Simmons, B. A.; Subashchandrabose, S.; Atkin, R., Low cost ionic liquid-water mixtures for effective extraction of carbohydrate and lipid from algae. *Faraday Discuss* **2018**, *206*, 93-112.
206. Haghghi Mood, S.; Hossein Golfeshan, A.; Tabatabaei, M.; Salehi Jouzani, G.; Najafi, G. H.; Gholami, M.; Ardjmand, M., Lignocellulosic biomass to bioethanol, a comprehensive review with a focus on pretreatment. *Renewable and Sustainable Energy Reviews* **2013**, *27*, 77-93.

207. Hoar, T. P.; Schulman, J. H., Transparent water-in-oil dispersions the oleopathic hydro-micelle. *Nature* **1943**, 152, 102-103.
208. Schulman, J. H.; Stoeckenius, W.; Prince, L. M., Mechanism of formation and structure of micro emulsions by electron microscopy. *J. Phys. Chem.* **1959**, 63 (10), 1677-1680.
209. Flanagan, J.; Singh, H., Microemulsions: A potential delivery system for bioactives in food. *Critical Reviews in Food Science and Nutrition* **2006**, 46 (3), 221-237.
210. Kogan, A.; Garti, N., Microemulsions as transdermal drug delivery vehicles. *Adv. Colloid Interface Sci.* **2006**, 123, 369-385.
211. Smith, G. D.; Donelan, C. E.; Barden, R. E., Oil-continuous microemulsions composed of hexane, water, and 2-propanol. *J Colloid Interf Sci* **1977**, 60 (3), 488-496.
212. Zemb, T.; Kunz, W., Weak aggregation: State of the art, expectations and open questions. *Curr. Opin. Colloid Interface Sci.* **2016**, 22, 113-119.
213. Fletcher, P. D. I.; Galal, M. F.; Robinson, B. H., Structural study of aerosol-OT-stabilized microemulsions of glycerol dispersed in n-heptane. *Journal of the Chemical Society-Faraday Transactions I* **1984**, 80, 3307-3314.
214. Rico, I.; Lattes, A., Waterless microemulsions. *Nouveau Journal De Chimie-New Journal of Chemistry* **1984**, 8 (7), 429-431.
215. Friberg, S. E.; Sun, W. M., A nonaqueous microemulsion system of ethylene-glycol, sodium dodecyl-sulfate, toluene, and decanol. *Colloid Polym. Sci.* **1990**, 268 (8), 755-759.
216. Atkin, R.; Warr, G. G., Phase behavior and microstructure of microemulsions with a room-temperature ionic liquid as the polar phase. *J. Phys. Chem. B* **2007**, 111 (31), 9309-9316.
217. Cheng, S. Q.; Zhang, J. L.; Zhang, Z. F.; Han, B. X., Novel microemulsions: ionic liquid-in-ionic liquid. *Chemical Communications* **2007**, (24), 2497-2499.
218. Gao, Y.; Li, N.; Zheng, L. Q.; Zhao, X. Y.; Zhang, S. H.; Han, B. X.; Hou, W. G.; Li, G. Z., A cyclic voltammetric technique for the detection of micro-regions of bmimPF(6)/Tween 20/H₂O microemulsions and their performance characterization by UV-Vis spectroscopy. *Green Chem.* **2006**, 8 (1), 43-49.
219. Kunz, W.; Zemb, T.; Harrar, A., Using ionic liquids to formulate microemulsions: Current state of affairs. *Curr. Opin. Colloid Interface Sci.* **2012**, 17 (4), 205-211.
220. Figueira-González, M.; García-Río, L.; Parajó, M.; Rodríguez-Dafonte, P., Properties of Ionic Liquid-Based Microemulsions. In *Ionic Liquid - Based Surfactant Science*, 2015.
221. Greaves, T. L.; Kennedy, D. F.; Kirby, N.; Drummond, C. J., Nanostructure changes in protic ionic liquids (PILs) through adding solutes and mixing PILs. *Physical chemistry chemical physics : PCCP* **2011**, 13 (30), 13501-9.
222. Russina, O.; Sferrazza, A.; Caminiti, R.; Triolo, A., Amphiphile Meets Amphiphile: Beyond the Polar-Apolar Dualism in Ionic Liquid/Alcohol Mixtures. *J. Phys. Chem. Lett.* **2014**, 5 (10), 1738-1742.
223. Hodgdon, T. K.; Kaler, E. W., Hydrotropic solutions. *Curr. Opin. Colloid Interface Sci.* **2007**, 12 (3), 121-128.
224. Zana, R., Aqueous surfactant-alcohol systems - a review. *Adv. Colloid Interface Sci.* **1995**, 57, 1-64.
225. Drapeau, J.; Verdier, M.; Touraud, D.; Krockel, U.; Geier, M.; Rose, A.; Kunz, W., Effective Insect Repellent Formulation in both Surfactantless and Classical Microemulsions with a Long-Lasting Protection for Human Beings. *Chemistry & Biodiversity* **2009**, 6 (6), 934-947.
226. Zoumpantoti, M.; Karali, M.; Xenakis, A.; Stamatis, H., Lipase biocatalytic processes in surfactant free microemulsion-like ternary systems and related organogels. *Enzyme and Microbial Technology* **2006**, 39 (4), 531-539.
227. Diat, O.; Klossek, M. L.; Touraud, D.; Deme, B.; Grillo, I.; Kunz, W.; Zemb, T., Octanol-rich and water-rich domains in dynamic equilibrium in the pre-ouzo region of ternary systems containing a hydrotrope. *Journal of Applied Crystallography* **2013**, 46 (6), 1665-1669.
228. Debye, P.; Anderson, H. R.; Brumberger, H., Scattering by an Inhomogeneous Solid. II. The Correlation Function and Its Application. *Journal of Applied Physics* **1957**, 28 (6), 679.

229. Tanford, C. A. *The Hydrophobic Effect: Formation of Micelles and Biological Membranes*, 2nd ed.; Wiley: New York, 1980.
230. McIntosh, T. J.; Simon, S. A.; Macdonald, R. C., THE ORGANIZATION OF NORMAL-ALKANES IN LIPID BILAYERS. *Biochimica Et Biophysica Acta* **1980**, *597* (3), 445-463.
231. Greaves, T. L.; Drummond, C. J., Protic ionic liquids: Properties and applications. *Chem. Rev.* **2008**, *108* (1), 206-237.
232. Ding, J.; Armstrong, D. W., Chiral ionic liquids: synthesis and applications. *Chirality* **2005**, *17* (5), 281-92.
233. Santos, E.; Albo, J.; Irabien, A., Magnetic ionic liquids: synthesis, properties and applications. *Rsc Advances* **2014**, *4* (75), 40008-40018.
234. Mecerreyes, D., Polymeric ionic liquids: Broadening the properties and applications of polyelectrolytes. *Progress in Polymer Science* **2011**, *36* (12), 1629-1648.
235. Ueno, K.; Yoshida, K.; Tsuchiya, M.; Tachikawa, N.; Dokko, K.; Watanabe, M., Glyme-Lithium Salt Equimolar Molten Mixtures: Concentrated Solutions or Solvate Ionic Liquids? *J. Phys. Chem. B* **2012**, *116* (36), 11323-11331.
236. Pedersen, C. J., Cyclic polyethers and their complexes with metal salts. *J. Am. Chem. Soc.* **1967**, *89* (26), 7017-7036.
237. Mandai, T.; Yoshida, K.; Ueno, K.; Dokko, K.; Watanabe, M., Criteria for solvate ionic liquids. *Phys. Chem. Chem. Phys.* **2014**, *16* (19), 8761-8772.
238. Murphy, T.; Callear, S. K.; Yepuri, N.; Shimizu, K.; Watanabe, M.; Canongia Lopes, J. N.; Darwish, T.; Warr, G. G.; Atkin, R., Bulk nanostructure of the prototypical 'good' and 'poor' solvate ionic liquids [Li(G4)][TFSI] and [Li(G4)][NO]. *Physical chemistry chemical physics : PCCP* **2016**.
239. Tamura, T.; Hachida, T.; Yoshida, K.; Tachikawa, N.; Dokko, K.; Watanabe, M., New glyme-cyclic imide lithium salt complexes as thermally stable electrolytes for lithium batteries. *J. Power Sources* **2010**, *195* (18), 6095-6100.
240. Dolan, D. A.; Sherman, D. A.; Atkin, R.; Warr, G. G., Kamlet-Taft Solvation Parameters of Solvate Ionic Liquids. *ChemPhysChem* **2016**, *17* (19), 3096-3101.
241. Strey, R., I. Experimental Facts: Water-Nonionic Surfactant Systems, and the Effect of Additives. *Berichte der Bunsengesellschaft für physikalische Chemie* **1996**, *100* (3), 182-189.
242. Israelachvili, J. N., 19 - Thermodynamic Principles of Self-Assembly. In *Intermolecular and Surface Forces (Third Edition)*, Israelachvili, J. N., Ed. Academic Press: San Diego, 2011; pp 503-534.
243. Araos, M. U.; Warr, G. G., Self-assembly of nonionic surfactants into lyotropic liquid crystals in ethylammonium nitrate, a room-temperature ionic liquid. *J. Phys. Chem. B* **2005**, *109* (30), 14275-14277.
244. Mitchell, D. J.; Tiddy, G. J. T.; Waring, L.; Bostock, T.; McDonald, M. P., Phase behaviour of polyoxyethylene surfactants with water. Mesophase structures and partial miscibility (cloud points). *Journal of the Chemical Society, Faraday Transactions 1: Physical Chemistry in Condensed Phases* **1983**, *79* (4), 975-1000.
245. Cho, B. K.; Jain, A.; Gruner, S. M.; Wiesner, U., Mesophase structure-mechanical and ionic transport correlations in extended amphiphilic dendrons. *Science* **2004**, *305* (5690), 1598-1601.
246. Del Sesto, R. E.; McCleskey, T. M.; Burrell, A. K.; Baker, G. A.; Thompson, J. D.; Scott, B. L.; Wilkes, J. S.; Williams, P., Structure and magnetic behavior of transition metal based ionic liquids. *Chemical Communications* **2008**, (4), 447-449.
247. Nockemann, P.; Thijs, B.; Postelmans, N.; Van Hecke, K.; Van Meervelt, L.; Binnemans, K., Anionic Rare-Earth Thiocyanate Complexes as Building Blocks for Low-Melting Metal-Containing Ionic Liquids. *J. Am. Chem. Soc.* **2006**, *128* (42), 13658-13659.
248. Satoshi, H.; Hiro-o, H., Discovery of a Magnetic Ionic Liquid [bmim]FeCl₄. *Chemistry Letters* **2004**, *33* (12), 1590-1591.
249. Sitze, M. S.; Schreiter, E. R.; Patterson, E. V.; Freeman, R. G., Ionic liquids based on FeCl(3) and FeCl(2). Raman scattering and ab initio calculations. *Inorganic chemistry* **2001**, *40* (10), 2298-304.

250. Mallick, B.; Balke, B.; Felser, C.; Mudring, A.-V., Dysprosium Room-Temperature Ionic Liquids with Strong Luminescence and Response to Magnetic Fields. *Angewandte Chemie International Edition* **2008**, 47 (40), 7635-7638.
251. Joseph, A.; Zyla, G.; Thomas, V. I.; Nair, P. R.; Padmanabhan, A. S.; Mathew, S., Paramagnetic ionic liquids for advanced applications: A review. *Journal of Molecular Liquids* **2016**, 218, 319-331.
252. Xiaodong, H.; Wenbin, Q.; Jianbing, W.; Qunfeng, S.; Pengfei, C.; Lin, C.; Xiaoping, Z.; Youquan, D., Manipulation of magnetic ionic liquid droplets and their application in energy harvesting. *Journal of Physics D: Applied Physics* **2017**, 50 (46), 465002.
253. Mirica, K. A.; Shevkoplyas, S. S.; Phillips, S. T.; Gupta, M.; Whitesides, G. M., Measuring Densities of Solids and Liquids Using Magnetic Levitation: Fundamentals. *J. Am. Chem. Soc.* **2009**, 131 (29), 10049-10058.
254. Bwambok, D. K.; Thuo, M. M.; Atkinson, M. B. J.; Mirica, K. A.; Shapiro, N. D.; Whitesides, G. M., Paramagnetic Ionic Liquids for Measurements of Density Using Magnetic Levitation. *Anal. Chem.* **2013**, 85 (17), 8442-8447.
255. Foudeh, A. M.; Fatanat Didar, T.; Veres, T.; Tabrizian, M., Microfluidic designs and techniques using lab-on-a-chip devices for pathogen detection for point-of-care diagnostics. *Lab Chip* **2012**, 12 (18), 3249-3266.
256. Berge, B.; Peseux, J., Variable focal lens controlled by an external voltage: An application of electrowetting. *The European Physical Journal E* **2000**, 3 (2), 159-163.
257. Zhao, Y.; Fang, J.; Wang, H.; Wang, X.; Lin, T., Magnetic Liquid Marbles: Manipulation of Liquid Droplets Using Highly Hydrophobic Fe₃O₄ Nanoparticles. *Advanced Materials* **2010**, 22 (6), 707-710.
258. Lehmann, U.; Hadjidj, S.; Parashar, V. K.; Vandevyver, C.; Rida, A.; Gijs, M. A. M., Two-dimensional magnetic manipulation of microdroplets on a chip as a platform for bioanalytical applications. *Sensors and Actuators B: Chemical* **2006**, 117 (2), 457-463.
259. Zhang, S.; Zhang, Y.; Wang, Y.; Liu, S.; Deng, Y., Sonochemical formation of iron oxide nanoparticles in ionic liquids for magnetic liquid marble. *Phys. Chem. Chem. Phys.* **2012**, 14 (15), 5132-5138.
260. Moriyoshi, T.; Sakamoto, T.; Uosaki, Y., (liquid+liquid) Equilibria of (water plus ethanol plus a C₈ alkanol) from 0.1 to 200 mpa at 298.15K. *J. Chem. Thermodyn.* **1989**, 21 (9), 947-954.

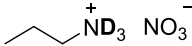
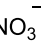
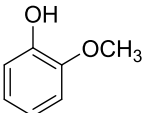
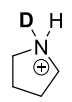
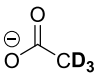
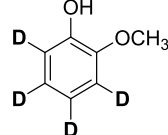
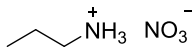
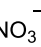
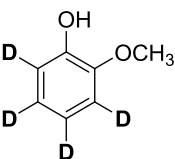
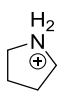
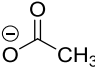
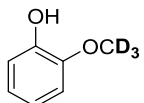
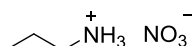
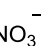
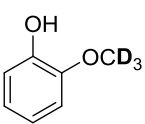
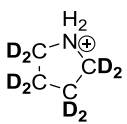
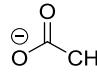
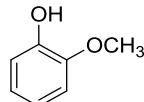
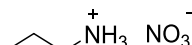
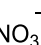
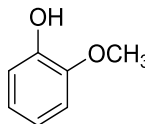
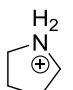
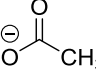
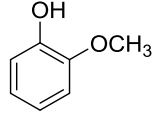
APPENDICES

Appendix A. ILs for Aromatic Dissolution (EPSR Details)

A1. Isotopic substitution – hydrogenated (H) and deuterated (D) samples

Three sets of mixtures, 10wt% guaiacol in propylammonium nitrate (PAN), 10wt% and 25wt% guaiacol in pyrrolidinium acetate (PyrrAc), were prepared with isotopic substitutions. Listed in Table A1, each set includes four chemically identical but isotopically different samples. H-PAN is fully hydrogenous, D₃-PAN is partially deuterated for all exchangeable protons. H-PyrrAc is fully hydrogenous, D₄-PyrrAc is partially deuterated on the acetate methyl group and exchangeable protons, and D₈-PyrrAc is deuterated on the cation ring. H-guaiacol is fully hydrogenous, D₃-guaiacol is partially deuterated on the methoxy group, and D₄-guaiacol is partially deuterated on the aromatic ring. This selective deuteration method is known as contrast variation, which highlights molecular regions of interest in the neutron diffraction experiment.

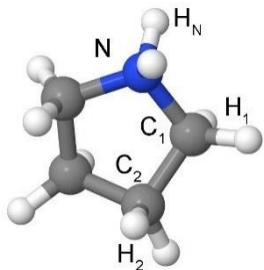
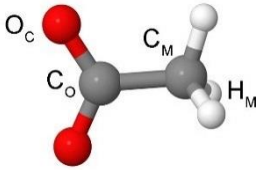
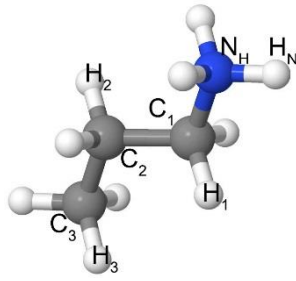
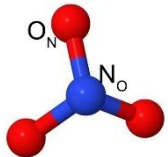
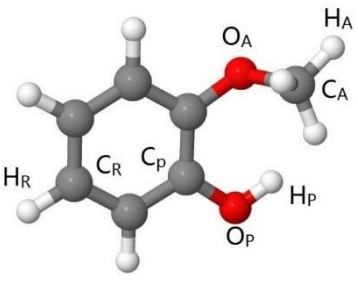
Table A1. Isotopic substitutions (H/D) used for neutron diffraction experiments

	PAN – guaiacol (10wt%)		PyrrAc – guaiacol (10 or 25wt%)			
D ₃ -PAN H-guaiacol				D ₄ -PyrrAc D ₄ -guaiacol	 	
H-PAN D ₄ -guaiacol				H-PyrrAc D ₃ -guaiacol	 	
H-PAN D ₃ -guaiacol				D ₈ -PyrrAc H-guaiacol	 	
H-PAN H-guaiacol				H-PyrrAc H-guaiacol	 	

A2. Modelling parameters – Empirical Potential Structure Refinement (EPSR)

EPSR performs a Monte Carlo simulation governed by Lennard-Jones potentials listed in Table A2, atom-centered point charges as well as chemical and physical constraints such as molecular structure and liquid density.

Table A2. Lennard–Jones and Coulombic charge parameters used in the EPSR model

Atom		ϵ (kJ mol ⁻¹)	σ (Å)	q (e)
pyrrolidinium cation				
N _H		0.711	3.25	-0.060
H _N		0.126	2.50	0.310
C ₁		0.276	3.50	-0.170
C ₂		0.276	3.50	0.010
H ₁		0.126	2.50	0.130
H ₂		0.126	2.50	0.060
acetate anion				
C _O		0.500	3.50	0.700
O _C		0.655	3.17	-0.800
C _M		0.500	3.50	-0.280
H _M		0.200	2.50	0.060
propylammonium cation				
N _H		0.711	3.25	-0.734
H _N		0.126	2.50	0.421
C ₁		0.276	3.50	0.108
C ₂		0.276	3.50	-0.037
C ₃		0.276	3.50	-0.653
H ₁		0.126	2.50	0.118
H ₂		0.126	2.50	0.095
H ₃		0.126	2.50	0.209
nitrate anion				
N _O		0.711	3.25	0.845
O _N		0.879	2.96	-0.615
guaiacol				
C _R		0.293	3.55	-0.115
C _O		0.293	3.55	0.135
H _R		0.126	2.52	0.115
H _A		0.065	1.80	0.005
O _A		0.711	3.00	-0.385
O _P		0.711	3.07	-0.585
H _P		0.000	0.00	0.435
C _A		0.711	3.80	0.250

A3. Hydrogen bonds

Table A3.1 summarises key hydrogen bond properties in PyrrAc-guaiacol and PAN-guaiacol systems. There are multiple types of hydrogen bonds involved for each correlation, listed in Table A3.2. Although both the cation and the anion interact with the solute, the type of hydrogen bond formed is different. Cation-guaiacol H-bond is long, bent and complex. Anion-guaiacol H-bond is short, linear and simple with the majority in the single and bidentate form.

Table A3.1 Hydrogen bond properties

	donor: acceptor	Length (Å)	Angle	coord # (0-3 Å)
cation-anion				around anion
Pyrr-Ac	2:2	2.4	Bent	1.4
PA - N	3:3	2.4	Bent	2.2
cation-guaiacol				around guaiacol
Pyrr-O _p /O _m	2:2	2.5	Bent	0.5/0.3
PA-O _p /O _m	3:2	2.5	Bent	0.7/0.6
guaiacol-anion				
H _p -Ac	1:2	1.7	Linear	0.9
H _p -N	1:3	1.8	Linear	1.5

Table A3.2 Hydrogen bond types shown in percentage distribution

	single	bidentate	bifurcated	bridge	multi
cation-anion					
Pyrr-Ac	41.5%	16.0%	21.5%	1.0%	20.0%
PA - N	-	-	-	-	-
cation-guaiacol					
Pyrr-O _p /O _m	58.0%	14.0%	17.0%	1.5%	9.5%
PA-O _p /O _m	43.5%	8.0%	23.0%	3.5%	22.0%
guaiacol-anion					
H _p -Ac	66.0%	34.0%	-	-	-
H _p -N	41.0%	22.0%	-	-	37.0%

Appendix B. Ternary Phase Diagrams and Scattering Patterns

B1. Phase diagrams

The phase behaviour of the water-PAN-octanol system is similar to conventional hydrotropic systems, such as the water-ethanol-octanol system, shown in Figure B1.1. Hydrotropes, such as ethanol, are industrial solubilisers for organic solutes in water. Compared to surfactants, they are weakly amphiphilic with a smaller hydrophobic region. As a result, solubilisation of insoluble normally requires high hydrotrope levels. PAN is comparable to ethanol as both are small amphiphiles. The difference is that water-PAN-octanol has a wider two-phase region and its phase boundary is more asymmetric than water-ethanol-octanol. Tie-lines in water-PAN-octanol are highly tilted, whereas tie-lines in water-ethanol-octanol are relatively flat. When using ethanol as the amphiphile, there is a near-equal distribution of ethanol in water and octanol.

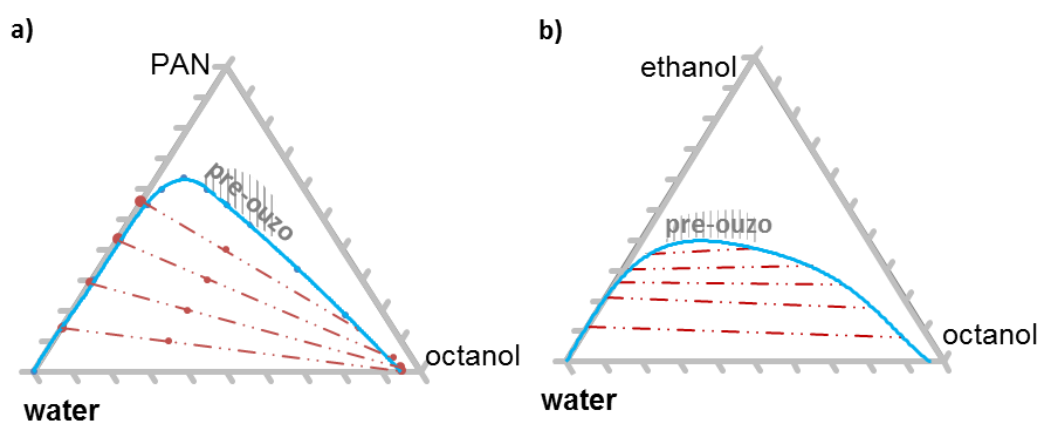


Figure B1.1 Ternary phase diagrams of a) water-PAN-octanol and b) water-ethanol-octanol (ref 21) at 298K. ^{260 260 259 259 258 257 256 255 255 1 1} Solid lines represent the phase boundary, dotted lines represent tie-lines in the two-phase region.

Figure B1.2 shows four systems with either water or EtAN as the polar component, and with either ethanol or PAN as the amphiphile. The phase boundary shifts depending on the combination. Shown in a), if starting from ethanol-octanol molecular mixtures, the system can accommodate more water than EtAN. Similar to a salting-out effect, the addition of a non-amphiphilic ionic liquid decreases miscibility. Shown in b), if starting from PAN-octanol mixtures, which is an ionic environment, the system can better accommodate an additional ionic liquid, EtAN, than water.

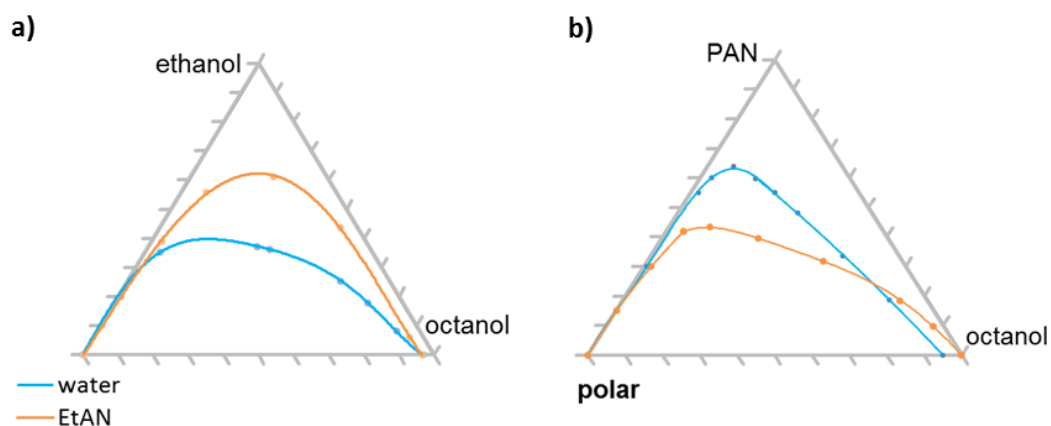


Figure B1.2 Ternary phase diagrams (wt%) of polar–n-octanol–amphiphile systems at 298K. A comparison between water and EtAN ternary systems. a) using ethanol as the amphiphile, b) using PAN as the amphiphile. — water as the polar component; — EtAN as the polar component.

By varying the alcohol chain length, as shown in Figure B1.3a, results demonstrate the influence of alcohol amphiphilicity on its ability as a solubiliser. Short chain alcohols such as butanol (C4OH) is better at solubilising IL than oil. Therefore the phase boundary of PAN-butanol-octane is left-skewed. As the alkyl chain length increases, the alcohol solvophobicity increases and becomes better at solubilising oil than IL, therefore the phase boundary of PAN-decanol-octane is right-skewed.

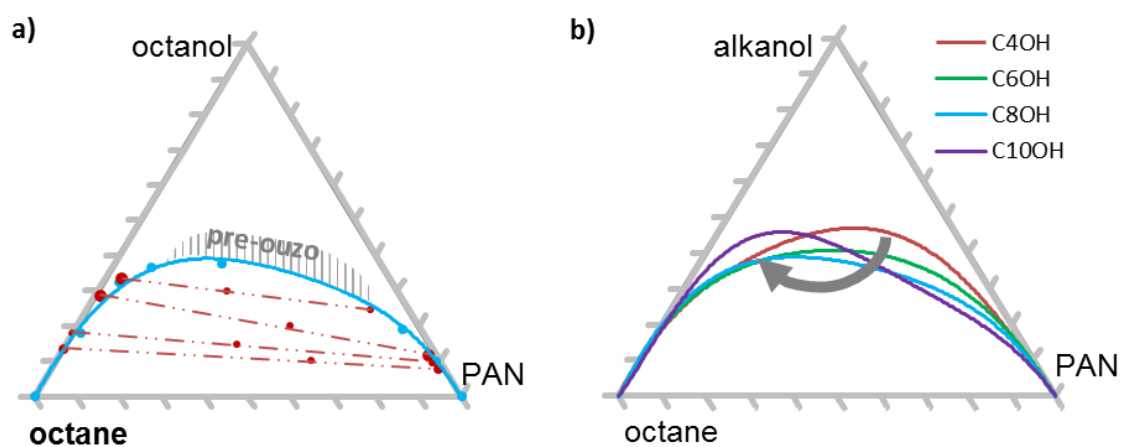


Figure B1.3 Ternary phase diagrams (wt%) of octane-alkanol-PAN systems at 298K. a) octane-octanol-PAN ternary system with tie-lines. b) octane-alkanol-PAN systems, as a function of the alkyl chain ratio. Experimental errors are represented by the radius of data points.

B2. Scattering Patterns and Sample Compositions

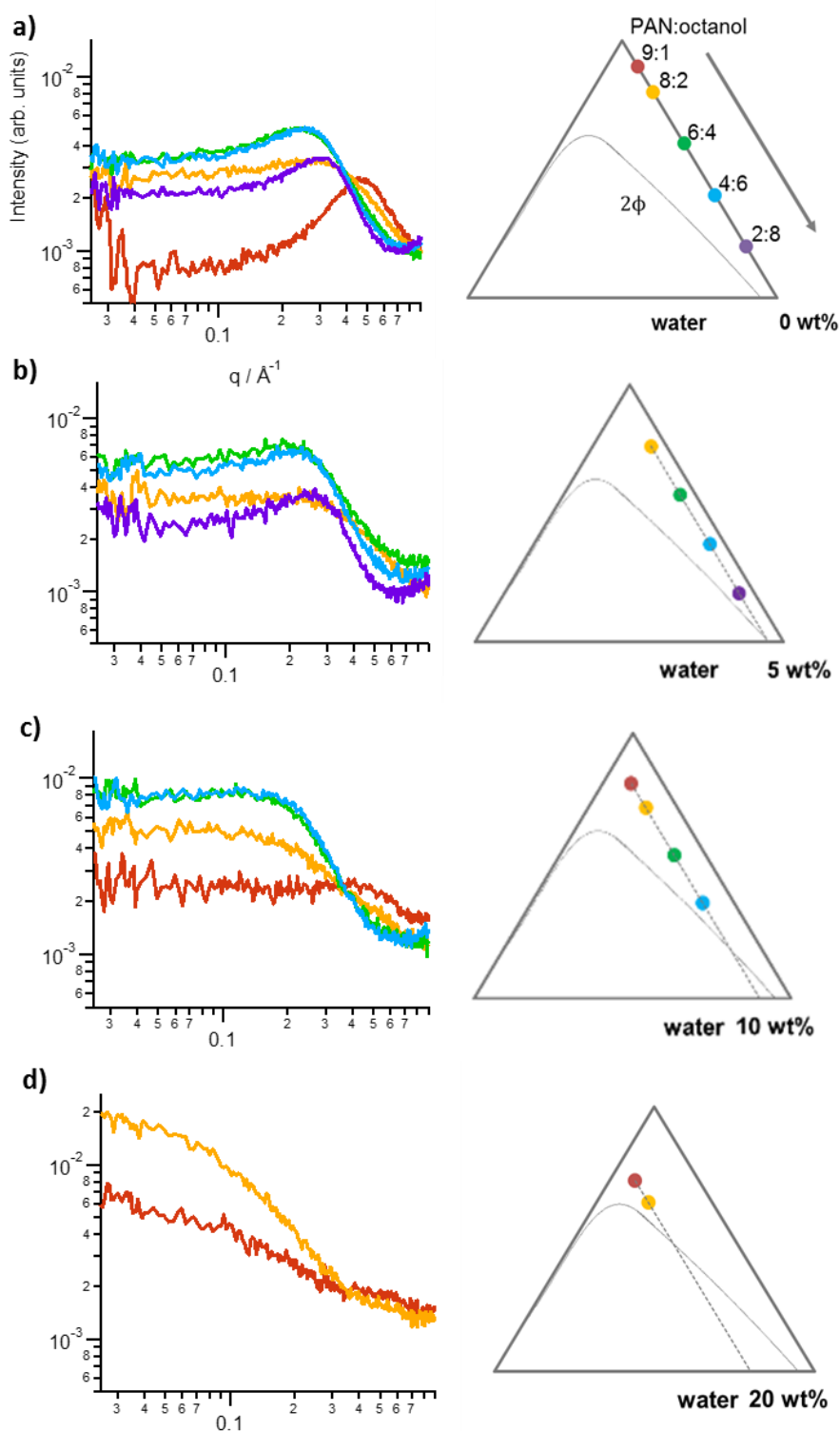


Figure B2.1 SAXS of water–PAN–octanol mixtures at various compositions at 298K. Water content increases from 0, 5, 10 to 20wt% (top to bottom); At any given water content, PAN:octanol ratio varies as labelled on its corresponding phase diagram.

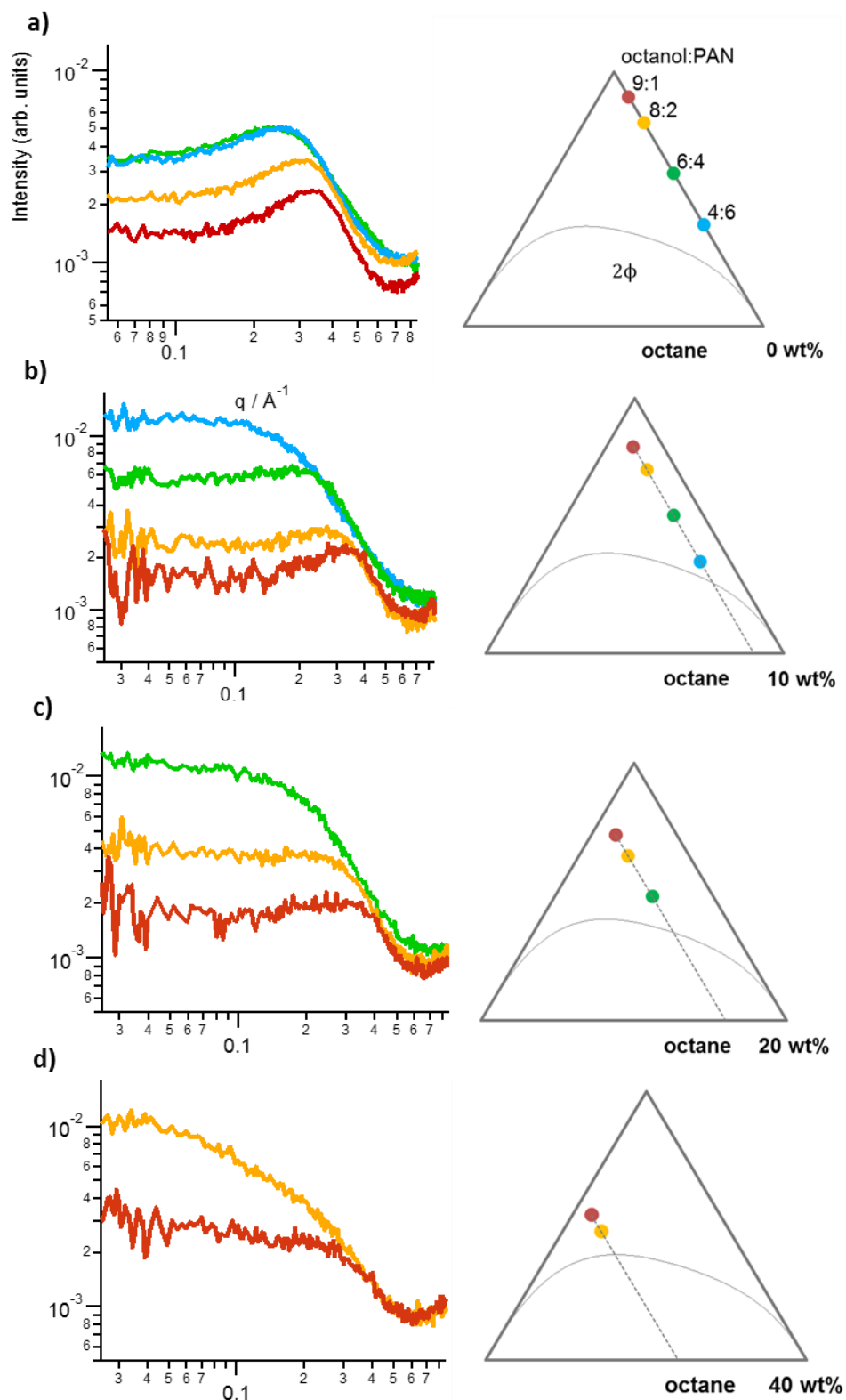


Figure B2.2 SAXS of octane–n-octanol–PAN mixtures at various compositions at 298K. Octane content increases from 0, 10, 20 to 40wt% (left to right); At any given octane content, PAN:octanol ratio varies as labelled on its corresponding phase diagram.

Appendix C. Geometric Model Fitting of SANS data

The Debye-Anderson-Brumberger (DAB) model calculates the scattering from a randomly distributed two-phase system. This model is originally designed for scattering by inhomogeneous solids. However, it can also fit the scattering by liquid systems. The DAB model assumes a sharp interface between two domains. This model characterises a two-domain system by a single length scale. The correlation length represents the average spacing between region of domain A and domain B.

The DAB model defines:

$$I(q) = I_0 \frac{1}{(1 + (q \cdot a)^2)^2}$$

where a is the correlation length in Å, $I(q)$ is the scattering intensity, and q is the scattering vector.

The value of χ^2 indicates how good a fit is. It is based on a Gaussian distribution in his context. For our systems in general, a fitting with $\chi^2 < 20$ is acceptable, and $\chi^2 < 5$ gives a good fit.

Here we use the DAB model to systematically fit all contrasts and compositions of water-octanol-PAN and octanol-PAN systems. As shown in Table C, results show that this model applies to some contrasts, while relatively large uncertainties occur for other contrasts. With 20wt% of water, the $\text{D}_2\text{O}-\text{C}_8\text{H}_{17}\text{OD}-\text{C}_3\text{H}_7\text{ND}_3\text{NO}_3$ contrast has a χ^2 value of more than 200, which is beyond the acceptable range. The correlation length in the $\text{C}_8\text{H}_{17}\text{OD}-\text{C}_3\text{H}_7\text{ND}_3\text{NO}_3$ contrast is 1.5 Å, which is not physically plausible.

Table C. DAB model fitting of water-PAN-octanol systems.

20wt% water in octanol-PAN(1:3 by wt)			
Contrast	H ₂ O- C ₈ D ₁₇ OH- C ₃ H ₇ NH ₃ NO 3	D ₂ O- C ₈ D ₁₇ OH- C ₃ H ₇ ND ₃ NO 3	D ₂ O- C ₈ H ₁₇ OD- C ₃ H ₇ ND ₃ NO 3
<i>q</i> -range (Å ⁻¹)	0.00914 - 0.34	0.00914 - 0.26	0.00914 - 0.35
Background <i>d</i>	0.65	0.339	0.7
Scale	0.0206	0.0038	0.0073
Length (Å)	7.3	8.44	9.34
Chi ²	21.6	10.8	218

10wt% water in octanol-PAN(1:3 by wt)			
Contrast	H ₂ O- C ₈ D ₁₇ OH- C ₃ H ₇ NH ₃ NO 3	D ₂ O- C ₈ D ₁₇ OH- C ₃ H ₇ ND ₃ NO 3	D ₂ O- C ₈ H ₁₇ OD- C ₃ H ₇ ND ₃ NO 3
<i>q</i> -range (Å ⁻¹)	0.00914 - 0.4	0.014 - 0.32	0.012 - 0.5
Background <i>d</i>	0.434	0.23	0.567
Scale	0.05	0.0204	0.0545
Length (Å)	3.28	3.4	2.397
Chi ²	59	8	12.1

octanol-PAN(1:3 by wt)			
Contrast	C ₈ D ₁₇ OH- C ₃ H ₇ NH ₃ NO 3	C ₈ D ₁₇ OH- C ₃ H ₇ ND ₃ NO 3	C ₈ H ₁₇ OD- C ₃ H ₇ ND ₃ NO 3
<i>q</i> -range (Å ⁻¹)	0.00914 - 0.45	0.014 - 0.35	0.00914 - 0.7012
Background <i>d</i>	0.488	0.301	0.688
Scale	0.05	0.035	0.0689
Length (Å)	2.5	2.5	1.5
Chi ²	66	12.2	34.6

Appendix D. Invariant Analysis of SANS data

Table D1 and D2 show representative invariant models and applied to ternary mixtures discussed in Chapter 4. Theories behind invariant analysis were described in Chapter 2. The analysis starts from a simple model with a small number of variables and rationally moves to a complex model to better describe SANS data when necessary. Here we use the EtAN-PAN-octanol system, shown in Table D1b, as an example to illustrate our overall approach.

Based on a two-domain, three-variable model, invariant calculations generate a clear polarity distinction between two domains, even though no such constraint is input into the model. Over 90% of EtAN and PAN molecules go into one domain (denoted as the polar domain), while 80% octanol molecules go into another domain (denoted as the apolar domain). With only three variables, the percentage difference between the experimental and theoretical invariant is 54% per contrast. These variations are likely caused by an over-simplification of the model. If PAN is the amphiphilic component, it is unlikely for its polar and apolar groups to have an equal distribution in a single domain. To understand the surfactant-like behaviour of PAN, introducing an additional variable is necessary.

With a four-variable model, the percentage error has been significantly reduced to 43% per contrast. General features from three-variable calculations have been preserved. Results further show a distribution difference between PAN charged groups and tails. This four-variable model captures most of the important features in the liquid system. Since the HPAN-D17octanol-HEtAN contrast shows the most inconsistency (96%) between theoretical and experimental invariants, we further include the amphiphilicity of n-octanol molecules and consider possibilities of octanol tails segregating into its own domain. We introduced a three-domain five-variable model by separately consider the distribution of the polar and apolar part of octanol. This effectively reduces the average error down to 15% per contrast.

Table D1. Invariant analysis of “polar” ternary mixtures using two-domain and three-domain models.

a)	water	PAN charged	PAN tail	octanol head	octanol tail	% diff	HPAN-D17oct-H2O	D3PAN-D17oct-D2O	D3PAN-D1oct-D2O
2-domain	100	93	45	67	1	31	94	0	0
5-variable	0	7	55	33	99				
3-domain	100	59	74	7	0	16	48	0	0
5-variable	0	41	9	94	0				
	0	0	17	0	100				

b)	EtAN charged	EtAN tail	PAN charged	PAN tail	octanol head	octanol tail	% diff	HPAN-D17oct-HEtAN	D3PAN-D17oct-	D3PAN-D1oct-D4EtAN
3-variable	91	91	93	93	20	20	54	52.65	9	99
4-variable	9	9	7	7	80	80				
4-variable	100	100	100	47	0	0	43	96	0	32
5-variable	0	0	0	53	100	100				
3-domain	99	72.6	66	78	0	0	15	41	2.7	2.3
5-variable	1	26.8	34	6	99	0				
	0	1	0	16	1	100				

c)	EtAN charged	EtAN tail	ethanol head	ethanol tail	octanol head	octanol tail	% diff	D4EtAN-D6eth-D1oct	D4EtAN-Heth-D17oct	HEtAN-D6eth-D17oct
3-variable	3	3	70	40	32	32	9	22	5.2	0.1
4-variable	97	97	30	60	68	68				
4-variable	78	78	4	22	56	56	0	0.57	0.19	0.001
5-variable	22	22	97	78	44	44				
5-variable	56	72	45	45	15	2	0	0.003	0.02	0.009
	44	28	56	56	85	98				

Table D2. Invariant analysis of “apolar” ternary mixtures using two-domain and three-domain models.

a)	PAN charged	PAN tail	octanol head	octanol tail	octane	% diff	D3PAN-D1oct-Hoctane	HPAN-Hoct-D18octane	HPAN-D17oct-D18octane	HPAN-D17oct-Hoctane
2-domain	100	75	80	6	5	53	3.5	97	3	56
5-variable	0	25	20	94	95					
3-domain	1	1	11	11	100	27	82	7	0	0
3-variable	99	99	31	31	0					
3-variable	0	0	58	58	0					
3-domain	100	66	64	0	0	0	0	0	0	0
5-variable	0	32	36	93	10					
	0	2	0	7	90					

b)	PAN charged	PAN tail	octanol head	octanol tail	cyclohexane	% diff	D3PAN-D1oct-Hcyclo	HPAN-Hoct-D12cyclo	HPAN-D17oct-D12cyclo
2-domain	0.1	95.5	100	100	28.1	25	72.6	2.8	0
4-variable	99.9	4.5	0	0	71.9				
2-domain	3	97	3	73	2	0	0.04	0.01	0.04
5-variable	97	3	97	27	98				
3-domain	16	6	94	17	5	0	0	0	0
5-variable	57	94	6	62	4				
	27	0	0	22	91				

c)	PAN charged	PAN tail	octanol head	octanol tail	toluene	% diff	D3PAN-D1oct-Htol	HPAN-Hoct-D8tol	HPAN-D17oct-D8tol
2-domain	77	1	49	6	94	17	0.68	50.5	1.1
5-variable	23	99	51	94	6				
3-domain	3	72	39	93	0	13	0	38.6	0
5-variable	41	28	61	7	0				
	56	0	0	0	100				